I. Crystallization and Morphological Studies of ICI's Intermediate Temperature Semicrystalline (ITX) Polymer and II. The Influence of Deformation (Shear Strain) During Bond Formation on Adhesive Bond Strength

by

Pamela Anne Percha

Dissertation submitted to the Faculty of the Virginia Polytechnic Institute and State University in partial fulfillment of the requirements for the degree of
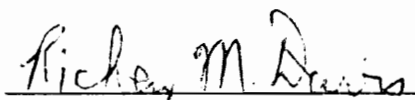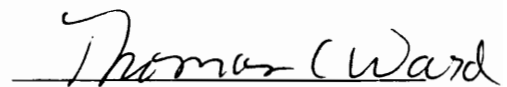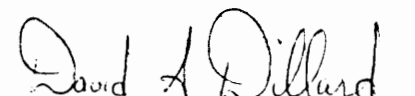
DOCTOR of PHILOSOPHY
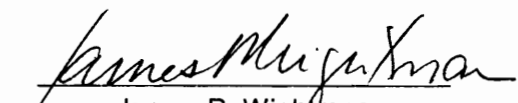
in

MATERIALS ENGINEERING SCIENCE

APPROVED:

Garth L. Wilkes, Chairman

Richey M. Davis

Thomas C. Ward

David A. Dillard

James P. Wightman

August, 1995
Blacksburg, VA

I. CRYSTALLIZATION AND MORPHOLOGICAL STUDIES OF ICI'S INTERMEDIATE TEMPERATURE SEMICRYSTALLINE (ITX) POLYMER AND II. THE INFLUENCE OF DEFORMATION (SHEAR STRAIN) DURING BOND FORMATION ON ADHESIVE BOND STRENGTH

by

Pamela Anne Percha

Dr. G. L. Wilkes, Chairman
Materials Engineering Science

(ABSTRACT)

Results for two unrelated studies are included in this dissertation. The primary investigation focused on evaluation of the crystallization conditions utilized in commercial consolidation of ICI's semicrystalline "ITX" polymer. Manipulating the initial polymer melting temperature and time was seen to influence the crystallization behavior and final morphology of the material. Variations in the crystallization kinetics, nucleation density, and crystalline texture of ITX were observed as a function of melt history. Experimental evidence suggests that ITX, like several other rigid-chain high-performance semicrystalline materials, is melt sensitive in that its nucleation density greatly decreases as a function of time and temperature in the melt. Melt degradation does not appear to strongly influence the crystallization behavior of ITX under normal processing conditions; however, spherulitic growth rates were seen to decrease after melting under the most severe conditions indicating that some degradation may be present. Unlike polyetheretherketone, ITX which was previously melted at the processing window high temperature limit can regenerate crystalline nuclei within the material via thermal

treatments. Cooling and reheating the material to a lesser temperature increases the level of crystallinity generated such that it is equivalent to that found in material treated to less harsh conditions. Wide angle x-ray diffraction and the method of Hermans and Weidinger were utilized to calculate a theoretical heat of fusion of 180 J/g for ITX, and show that absolute crystallinity decreases by ~5% within the ICI recommended processing range.

The second dissertation topic discusses the effect of adhesive deformation during bond preparation on the mechanical performance of two commercial hot-melt adhesives, Dow DAF® 821 and Du Pont Surlyn® 1601. Lap shear bonds were sheared (// or ⊥ to load) during preparation to induce molecular orientation within the adhesive, before the mechanical properties were evaluated. The measured DAF 821 tensile strengths were similar, however, the Surlyn bond strengths varied in that sheared bonds were weaker than control bonds. Linear dichroism was used to quantify the level of orientation present within similarly prepared adhesive films. The technique indicated that there was no measurable preferential orientation in either adhesive.

Dedicated to:

Leonard Joseph Percha, Jr. … my father…

> … who wanted to study history, but who's football scholarship was lost to injury and there was no money … so he did his best at whatever he did … and became one of the best in his field

Marjorie Jane Kuznicki Percha … my mother …

> … who wanted to study nursing, but there was no money … so she did her best at whatever she did … and became the original "Dr. Mom"

Leonard Joseph Percha, Sr. … my paternal grandfather …

> … who wanted to be a physician, but there was no money … so he would hurry through his deliveries and then sit in his truck cab to read and learn …

Julia Ann Schepke Kuznicki … my maternal grandmother …

> … who wanted to finish high school, but there was no money … and so she went to work to help support her family as a maid when she was still a child … and read for the rest of her life …

… to all of you … thank you for teaching me that money is not important, but that education and dedication to a dream are … this is for all of us.

ACKNOWLEDGMENTS

was greatly appreciated., as were technical discussions with Dr. G. Hoh of Du Pont and Mr. S. Imfeld of Dow. The second and major investigation, the ITX crystallization study was aided by the following sources. The Boeing Commercial Airplane Group, ICI Fiberite and the NSF-Science and Technology Center at Virginia Tech contributed technical assistance to this work, and in addition, ICI Fiberite contributed the ITX powder used in this evaluation. I would like to acknowledge the Chemical Engineering department staff for their contributions to this project as well, especially Mr. B. Williams and Mr. W. Brown. Also, many thanks to Ms S. Simpkins for the everyday, but oh so important help that she always so professionally provides.

Finally, I would like to thank several friends and colleagues who have helped me with portions of this work. Several members of Dr. Wilkes research group helped with the collection of the WAXS data discussed here including D. K. Brandom, S. Srinivas and B. G. Risch. Thanks also to Dr. J. W. Chin for colllecting, analyzing, and discussing the ESCA data completed as part of the molecular orientation project. Lastly, I appreciate the assistance of M. A. Brown in collecting part of the thermal stability DSC data for the ITX project.

TABLE of CONTENTS

CHAPTER 3   MATERIALS and EXPERIMENTAL METHODS

CHAPTER 4   CRYSTALLIZATION and MORPHOLOGICAL STUDIES of ITX

CHAPTER 6   RECOMMENDATIONS

LIST of FIGURES

List of Figures

List of Figures

LIST of TABLES

CHAPTER 1

INTRODUCTION

1.1   Organization of this Document

The research presented in this dissertation arises from work on two separate research projects as is noted in the title. The first, and more in-depth project, is a study of the crystallization behavior and morphology of a high-performance polymer from ICI that will hereafter be referred to as "ITX" for Intermediate Temperature Semicrystalline polymer. The majority of this dissertation will summarize the results for this work, with the other topic summarized in a separate chapter. The second project discussed here looks at the effects of deformation induced molecular orientation during cure on the strength of adhesive bonds prepared from two commercial hot-melt adhesives, and will not be the main focus of this dissertation.

The organization scheme for this document will now be outlined. As mentioned above, the majority of this dissertation will address the crystallization and

morphological studies completed on ITX. For this reason, the introduction, the literature review that follows in Chapter 2, and the general format of this paper will focus on ITX. Chapter 3 will describe ITX and the experimental methodology that was used in its evaluation. Next, Chapter 4 will present the bulk of the experimental results and discussion on the crystallization and morphological studies completed for this project. The emphasis of Chapter 5 will then diverge to the second topic "The Influence of Deformation (Shear Strain) During Bond Formation on Adhesive Bond Strength." This chapter will stand alone in that it will contain a separate introduction, a brief literature review as well as a discussion of the research completed. Finally, Chapter 6 will first summarize the ITX conclusions, and finish with recommendations for additional future research.

1.2   Introduction to this Research

Continuous fiber reinforced composites, a high-performance subset within the general class of organic matrix composites, were originally developed for the aerospace industry to provide superior structural material properties unattainable with only homogeneous structural materials [1-5]. To supply sufficient strength and stiffness, high strength, high modulus reinforcing fibers are typically a substantial volume fraction (~60 %) of the composite structure, consequently the choice of original component materials, their morphology, and the resultant interfacial region will all contribute significantly to the final properties of the composite [2, 6].

When the chosen composite matrix material is a semicrystalline thermoplastic polymer, processing history is particularly important since many of these high performance resins begin to degrade near their respective melting temperatures. A

fundamental understanding of the processing-property relationships for the matrix material is essential as the properties of semicrystalline thermoplastics are strongly influenced by processing history [7-19]. Variations in processing conditions can induce sufficient temperature gradients that morphological inhomogeneities may result. The melting temperature, the time a polymer remains in the melt and the number of thermal cycles can all influence the nucleation behavior, and therefore the final morphology which develops [6, 12, 20, 21]. These variations in morphology can induce stress concentrations and mechanical property differences from region to region. Microstructural fluctuations in the degree of crystallinity, spherulite size, lamella thickness and spherulite organization can have a profound effect on the ultimate properties of a composite structure [22-24].

This investigation focused on identifying the appropriate crystallization conditions most likely to enhance the development of crystallinity in a specific semicrystalline thermoplastic matrix material. Work with ICI's intermediate temperature semicrystalline "ITX" polymer has shown that manipulating the initial polymer melting temperature and melt residence time will influence the crystallization behavior and final morphology that develops in neat specimens. Variations in crystallization kinetics, nucleation density, and the type of crystalline morphology which develop as a function of melt temperature and time were systematically investigated. This study characterizes how fluctuations even within the ICI recommended processing profile can affect the fundamental crystallization behavior and final morphology of ICI's semicrystalline ITX resin, as well as ITX in the presence of carbon fibers. The results define a processing "window" for ITX as a function of thermal history that will provide for more consistent crystallization behavior and ultimately more consistent physical properties in the final product.

CHAPTER 2

LITERATURE REVIEW

2.1   Introduction

The purpose of this chapter is to provide background information for the study of the high-performance semicrystalline polymeric material, ITX, under investigation. Due to restrictions on the publication of the chemistry, and limited access to information regarding the chemical microstructure and molecular weight of the material, literature on ITX is minimal. In fact, as of this time only limited publications have been submitted which address "ITX" as such, and they evaluate the physical and chemical aging of the material as a function of environment, and reprocessibility [25, 26, 27]. To deal with this restriction, and still provide relevant background information for this research, another similar arylene ether ketone high-performance semicrystalline polymer, poly (ether ether ketone),(PEEK), will be used as a model for discussion of the majority of topics

addressed including the thermal properties, mechanical performance and crystallization behavior of ITX during the literature survey. Information on both PEEK resin, and PEEK/carbon-fiber composites will be reviewed, even though the majority of the research presented here focuses on neat ITX with less emphasis on its composites.

PEEK was chosen as a model semicrystalline material due to the similarity of its thermal characteristics with that of ITX, and the fact that it has been well studied, both as the neat resin and in its composite form [4-9, 11-18, 20-22, 24, 28, 29-78]. Blends of PEEK, particularly with PES (poly (ether sulfone)), have also been studied [79-83]. Over the course of this research, it was noted that ITX displayed additional similarities to PEEK in its crystallization behavior, and melt sensitivity. As a basis for comparison, ITX displays a glass transition temperature (T_g) at approximately 180 °C, and a melting point (T_m) about 360 °C in contrast to PEEK whose T_g and T_m are circa 140 and 340 °C respectively [12, 30, 31]. The higher T_g typical of ITX expands the potential application temperature window upwards, making it a candidate for such applications as the High Speed Civil Transport (HSCT) composite commercial aircraft [32].

2.1.1 Advantages of High-Performance Thermoplastic Matrix Composites

Thermoplastic materials such as PEEK have two particular advantages over thermosets as matrix materials in that 1) they have a longer shelf life, and 2) they are more efficient to prepare since they only require heat, not heat and alterations in chemistry through cross-linking in processing [2, 5]. A third potential advantage thermoplastics have over thermosets is that the materials are potentially recyclable; regrind material can be reprocessed as with other thermoplastics, and parts are

potentially repairable [2, 4, 78]. Additional advantageous properties semicrystalline polymers provide include:

- resistance to organic solvents and hot water,
- resistance to dynamic fatigue,
- increased temperature applications when fiber-reinforced,
- retention of ductility on short-term heat aging, and
- orientation and crystallinity can generate higher strength as in fibers [2, 78].

In addition, thermoplastic composites can potentially overcome some of the property limitations associated with thermoset matrix composites including brittleness, solvent susceptibility, and chemical reactivity. Since thermoplastics are not chemically reacted during processing, their properties are not a function of the degree of cure, and parts are potentially repairable in contrast to thermosets. High temperatures and pressures are required in the processing of many thermoplastic materials however, and high-productivity automated systems have been instituted to economically process these materials in high volume [3].

2.1.2 Properties of High-Performance Thermoplastics and Reinforcing Fibers

Thermoplastic polymers constitute the majority of the polymers produced in the United States, with the rest made up of predominately thermosetting materials [3]. The trend is the opposite however with organic matrix composites, where thermosetting resins hold a majority of the market. In the composites industry, thermoplastic resins are predominately seen in short-fiber-reinforced injection molding compounds, and thermosetting polymers are largely in long- or continuous-fiber-reinforced composites, with the application determining the matrix resin choice. Long- or continuous-fiber-reinforced composites are particularly well suited to applications where the polymer is

impregnated into the fibers since they are low viscosity liquids that can be handled at room temperature will relative ease [3].

The 1980's have seen growth in the use of thermoplastic composite parts, and this has spurred growth particularly in the area of long- or continuous-fiber-reinforced thermoplastic advanced composites. This type of composite typically consists of a high temperature polymer with an oriented fiber-reinforcement structure. Carbon fibers are the preferred reinforcement material in advanced composites because of their higher modulus as compared to glass fibers. Table 2.1a-c lists the properties of semicrystalline polymers, amorphous polymers and synthetic reinforcing fibers frequently utilized in thermoplastic composites.

A wide variety of thermoplastic polymers have been considered for applications requiring advanced composites [3]. These include: poly (ether ether ketone) or PEEK as noted earlier, poly (phenylene sulfide) or PPS, polysulfone (PSF), polyamideimide (PAI), thermoplastic polyimides (TPI or PI), and poly (phenyl sulfone). Several of these materials were evaluated by Hartness for suitability in aerospace applications, and it was noted that amorphous polymers (polysulfone and poly (phenyl sulfone)) showed excessive susceptibility to solvent attack, while semicrystalline polymers did not [3]. The semicrystalline materials considered included: poly(ethylene terephthalate), poly (butylene terephthalate), PPS and PEEK. Both PPS and PEEK are resistant to most aviation fluids, and a comparison of their fracture toughness (Table 2.2) in both neat and composite form shows that they are considerably tougher than several thermoset systems as noted. While carbon-fiber reinforced PEEK and PPS are being evaluated for advanced composite applications, overall, thermoplastic matrix materials constitute only a small (8%) portion of the advanced composite market.

Properties of a) semicrystalline polymers, b) amorphous polymers and c) synthetic reinforcing fibers respectively frequently utilized in thermoplastic composites [3].

a) Properties of Semicrystalline Polymers

Polymer	Code	Density (g/cm^3)	Strength (MPa)	Modulus (GPa)	T_g (°C)	T_m (°C)
High density polyethylene	HDPE	0.96	34	1.23	−20	132
Polypropylene	PP	0.91	31	1.50	−10	176
Polyvinylidene fluoride	PVDF	1.78	50	2.90	−30	178
Polyoxymethylene	POM	1.42	68	3.56	−65	180
Polybutylene terephthalate	PBT	1.32	52	2.50	40	228
Nylon-6	Ny 6	1.14	79	1.20	65	228
Polyethylene terephthalate	PET	1.38	70	3.10	80	255
Nylon-6,6	Ny 66	1.14	82	1.20	78	260
Polyphenylene sulfide	PPS	1.34	83	3.28	93	288
Polyetheretherketone	PEEK	1.36	95	3.85	143	338

b) Properties of Amorphous Polymers

Polymer	Code	Density (g/cm^3)	Strength (MPa)	Modulus (GPa)	T_g (°C)
Polyvinyl chloride	PVC	1.35	60	4.10	85
Polystyrene	PS	1.04	80	4.10	108
Styrene-acrylonitrile	SAN	1.10	80	3.15	108
Acrylonitrile-butadiene-styrene	ABS	1.06	48	2.40	108
Polyphenylene oxide[a]	PPO	1.06	66	2.60	145
Polycarbonate	PC	1.20	65	2.40	150
Polyurethane	PU	1.05	25	0.50	160
Polysulfone	PSF	1.24	70	2.69	190
Polyetherimide	PEI	1.33	105	2.95	217
Polyether sulfone	PES	1.37	85	2.60	223
Polyimide[b]	PI-K	1.31	102	3.76	250
Polyamideimide	PAI	1.40	63	4.60	275

[a] General Electric Company's Noryl (referenced blend contains 50% polystyrene).
[b] Du Pont's Avimid K-III.

c) Properties of Synthetic Reinforcing Fibers

Property	Glass E	Glass S	Carbon T-300	Carbon AS-4	Aramid Kevlar-49
Density, g/cm^3	2.55	2.48	1.75	1.77	1.45
Diameter, μm	13.5	7.0	8.0	8.0	12.0
Strength, GPa	2.40	4.60	3.10	3.98	3.60
Modulus, GPa	69	85	220	241	124
Elongation, %	3.5	2.75	1.25	1.65	2.9

Kevlar is a registered tradename for Du Pont aramid fibers.

Table 2.2   Comparison of the Mode I Fracture Toughness of Advanced Polymers and Composites [3].

Polymer	Polymer		Composite	
	G_{Ic} (J/m^2)	Ref.	G_{Ic} (J/m^2)	Ref.
Thermosets				
Epoxy (conventional, T_g = 238°C)	54	67	140	88
Bismaleimide	400	94	300	94
Epoxy (toughened, T_g = 285°C)	250	67	230	68
Polyimide (PMR-15)	200	72	—	—
Thermoplastics				
Polysulfone	3200	72	1130	69
Polyphenylene sulfide	—	—	1370	69
Polyether sulfone	1900	93	—	—
Polyetherimide	3300	93	1020	69
Polyetheretherketone	5000	71	3230	69
Aromatic polyamide (J-1 polymer)[a]	1900	71	2020	69
Polyamideimide	3400	72	1750	93
Polyimide (Avimid K-III)	1900	92	1800	92

[a] Du Pont semicrystalline polymer based on bis(para-amino cyclohexyl) methane.

2.2   Poly (Ether Ether Ketone)

2.2.1   Material Description

Poly (ether ether ketone) or PEEK is a highly aromatic, high-temperature, semicrystalline thermoplastic material which has seen wide-spread application in the areas of electrical and electronic parts, military equipment, wires and cables in nuclear facilities, as well as in advanced structural composites for the aircraft industry [4]. Figure 2.1 shows the structure of PEEK, and Figure 2.2 shows the chain conformation and crystal structure of PEEK which is orthorhombic [12, 30, 69].

2.2.2   Mechanical Properties and Processing Parameters for PEEK

A summary of the standard properties and characteristics of PEEK is provided in Table 2.3. PEEK can be compression-molded, injection molded and extruded using conventional equipment after drying [78]. The melt-processing temperatures required for PEEK are high, with typical barrel temperatures of 340-400 °C and mold temperatures of 140-180°C. However, since these temperatures are within the heating capabilities of conventional processing equipment, any additional equipment expenditure is not necessary [78]. In addition, the combination of PEEK with continuous carbon or other high-performance fibers provides high-strength, high-temperature composites [2, 4, 7, 69].
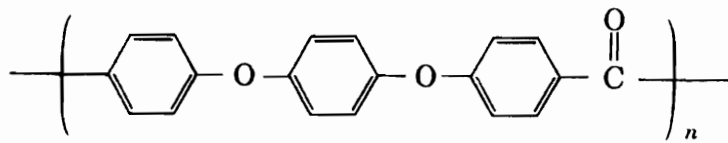
Figure 2.1 Microstructural repeating unit of poly (oxy-1,4-phenyleneoxy-1,4 phenylene carbonyl-1,4-phenylene), i. e. PEEK [69].
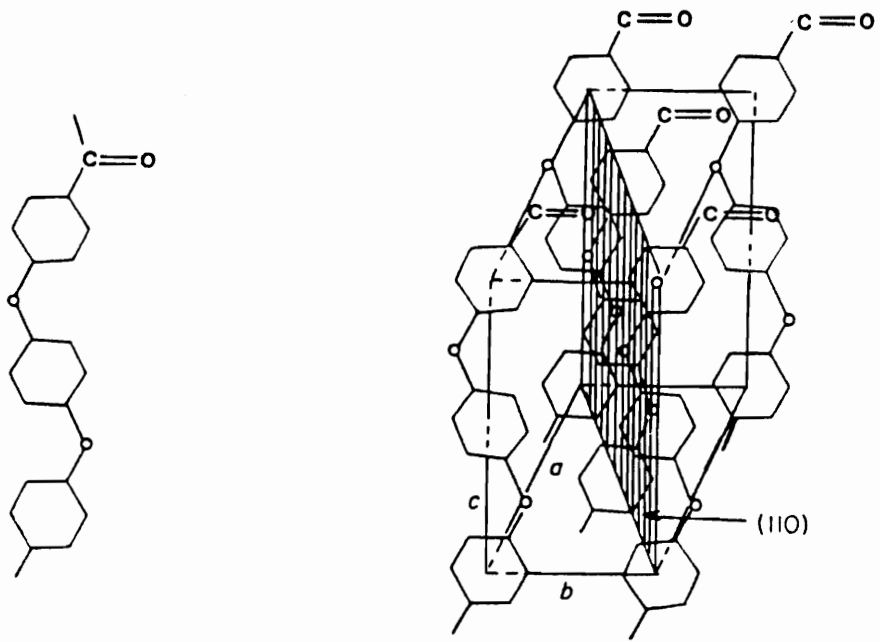
Figure 2.2   Extended chain conformation and crystal structure of PEEK [69].

Table 2.3   Standard properties of PEEK [5, 78, 84].

Property	PEEK
Appearance	Gray/opaque
Density	1.32 g/cm^3
Tensile Strength (psi)	14,500
Fracture Mode	Yielding or shear banding [4]
Elongation to Break (%)	> 100
Flexural Modulus (psi X 10^5)	5.5
Heat Distortion Temperature (°C)	165
Glass Transition Temperature (°C)	140
Melting Temperature (°C)	334
Chemical Resistance	Excellent
Flammability and Smoke Emission	Very Low

2.2.3   Thermal and Radiation Stability of PEEK

One of the most significant restraints on the adoption of thermoplastics by the aerospace industry has been the difficulty of combining, within one polymer, a sufficiently high glass transition temperature and resistance to aviation fluids [2]. In addition, a high degree of thermal stability is required of the matrix material in order to see increased demand for thermoplastic resins. Prime and Seferis have reported that PEEK possesses exceptional thermal stability, exhibiting only minimal weight loss up to 500 °C when heated in air [47]. PEEK decomposition products in air include: phenol, diphenyl ether, benzophenone and benzoquinone, with the presence of copper increasing the decomposition rate and the evolution of the latter component by 4 to 5 times at 375 °C [47].

The thermal stability of PEEK has been investigated by Jonas and Legras as a function of melt holding time and temperature in both air and inert environments [11]. Their work revealed that PEEK thermal degradation, both in air or vacuum, was characterized by a progressive branching mechanism and cross-linking. The diffusion of oxygen into molten PEEK was cited as one of the degradation controlling mechanisms. They determined that the thermal degradation of PEEK results in an increase in the M_W and M_Z, but not M_n values measured, and the emission of volatile materials, with the rate of degradation increasing in air. They propose a degradation mechanism which consists of a homolytic random chain scission process which produces radicals that attack nearby polymer chains to form branches, and ultimately cross-links. The lifetime of the radicals is thought to be sufficiently long to permit the branching reaction before termination since no decrease in M_n is observed. In this scenario, volatile emission will only occur after scission very near a chain end, when the radical cannot attack another molecule. The

authors offer this explanation to account for the observed reduction in crystallization kinetics and ultimate crystalline content in PEEK even when processed at temperatures less than the measured degradation temperature determined by thermogravimetric analysis.

Another area of basic PEEK research, that of radiation stability, has also reported the presence of a branching mechanism during degradation. The stability of PEEK in the presence of high energy electron beam radiation has also been evaluated for applications in nuclear industry instrumentation in a radiation environment [48, 49]. PEEK has been reported to not suffer significant damage after absorbing up to 100 Gy of gamma radiation [3].

Sasuga and Hagiwara have reported that irradiating amorphous PEEK results in the formation of structures which inhibit crystallization, i. e. structural changes including cross-links and/or short branching in the main chain during irradiation as a result of chain scission [49]. Studying semicrystalline PEEK, they found that semicrystalline material is more sensitive to radiation damage than is amorphous material due the susceptibility of the interface between phases to attack [48]. The inferior radiation resistance of semicrystalline versus amorphous PEEK is assigned to the preferential disintegration of the tie-molecules between crystalline and amorphous phases. As a result of this work, it appears that amorphous PEEK would be more applicable to electron beam radiation environments than would semicrystalline PEEK.

Kumar, et al. also evaluated the electron beam radiation damage to determine the dose required to damage different polymers such that the intensity of diffraction was reduced by a factor of $1/e$, defining this value as D^*. The D^* value for PEEK was determined to be approximately an order of magnitude greater than for polyethylene, with the result that PEEK is more stable to electron microscopy evaluation [12].

2.2.4   Crystalline Structure and Morphological Characteristics of PEEK

Since the introduction of PEEK, and subsequently its commercial continuous fiber composite prepreg, Aromatic Polymer Composite (APC-1) in 1982, numerous researchers have studied its crystalline structure and morphology [2, 12, 21, 29, 30, 33, 35, 36, 37].   This section will discuss the characteristic crystalline structure and semicrystalline morphology observed for neat PEEK resin, and section 2.3 will address that of the composite.

2.2.4.1   Crystalline Structure of PEEK

Two studies on the crystalline structure of PEEK will be briefly reviewed.   The first, by Hay, et al., was completed in 1984 on PEEK polymerized with the typical 1,4 para-linked aromatic rings [29].   The work is an x-ray diffraction study of partially crystalline PEEK which used the diffraction pattern to substantiate the crystal structure of the polymer utilizing a procedure introduced originally by Rietveld for neutron scattering studies.   Oriented and isotropic semicrystalline specimens of PEEK were prepared and annealed before examination by x-ray and for density determination.

Wide angle x-ray scattering (WAXS) patterns were collected for PEEK as shown in Figure 2.3, and used to determine the degree of crystallinity from the ratio of the areas under the respective curves.   The results for the degree of crystallinity determined ranged from 0 to 35.0 ± 1.5% via density measurements, and from 0 to 30.0 ± 5% from the WAXS data.

The unit cell and the crystalline density of a 100% crystalline specimen were also determined.   The unit cell for PEEK is described by the dimensions:
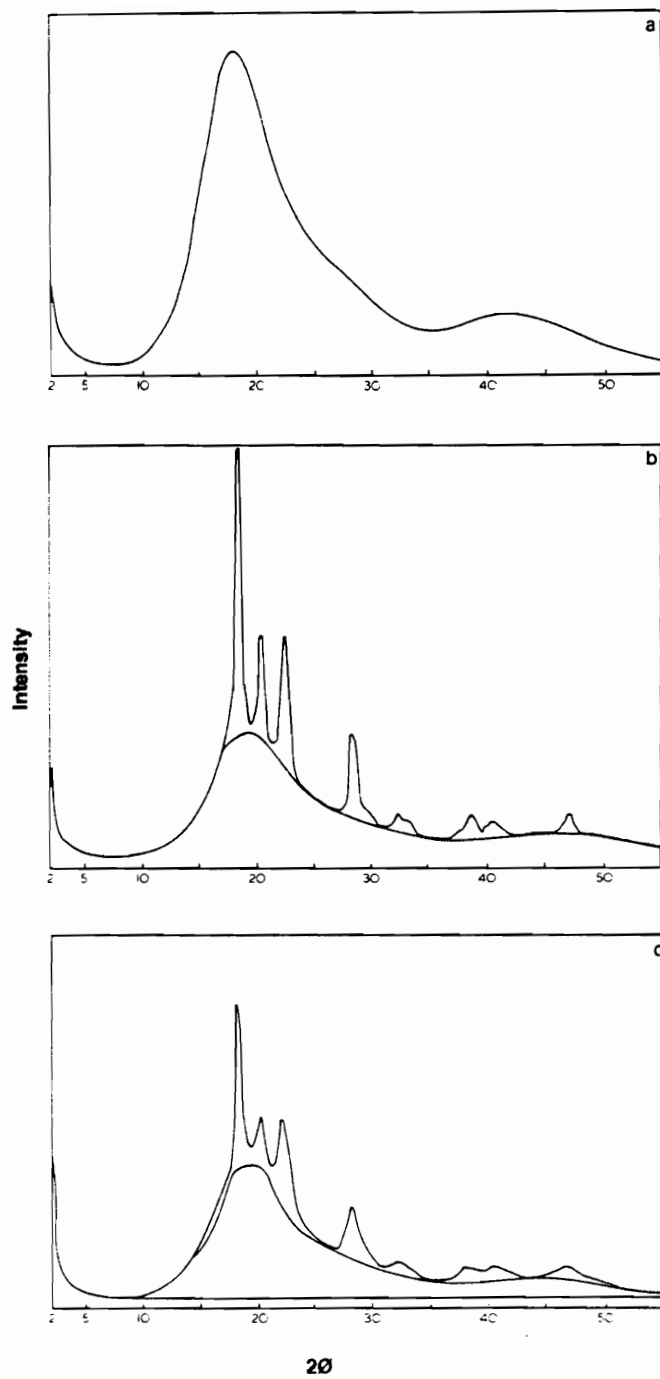
Figure 2.3   Typical wide angle x-ray scattering (WAXS) patterns for PEEK:
a) amorphous, b) crystallized at 155 °C, followed by annealing at
200 °C, and c) crystallized at 325 °C [29].

$$a = 7.781 \pm 0.009 \text{ Å},$$
$$b = 5.922 \pm 0.010 \text{ Å, and}$$
$$c = 10.056 \pm 0.014 \text{ Å}.$$

The crystalline density was determined at ambient temperature to be 1.378 ± 0.005 g/cm^3, while that for the quenched amorphous material was 1.264 g/cm^3. The WAXS patterns in Figure 2.3 are very similar to those determined for ITX as will be seen later in Chapter 5.

The second reference on crystalline structure in PEEK by Blundell reports information on the conformation and packing of the case where meta-phenyl linkages occur at regularly spaced internals [35]. The addition of meta-linkages is reflected in the unit cell dimension reported for ambient temperatures:

$$a = 7.71 \text{ Å},$$
$$b = 6.05 \text{ Å, and}$$
$$c = 39 \text{ Å}.$$

The deduced lateral dimension of the unit cell are similar to PEEK, as is typical for other all-para-phenyl polymers.

2.2.4.2   Morphological Characteristics of PEEK

The morphology of PEEK has been experimentally evaluated by several researchers, and their work will be summarized briefly in this section [12, 21, 30, 33, 36, 37]. Early work on PEEK was completed by Blundell and Osborne in 1983 on the morphology and related properties which will be discussed further in section 2.2.5. In this study, the authors examined the morphology of PEEK crystallized in the DSC to directly relate their observed morphologies to the crystallization studies [33]. Their optical micrographs revealed a spherulitic growth habit, with positively birefringent

spherulites. Also evaluated in this study, and summarized in Table 2.4 are: 1) an estimate of the average spherulite size, L, 2) the primary nucleation density, N, 3) the average measured spherulite radius, r, and 4) the radial growth rate, G, all as a function of crystallization temperature (T_C) and crystallization time (t_C).

Olley, Bassett and Blundell also examined the morphology of PEEK utilizing transmission electron microscopy (TEM) and an etchant technique in 1986 [37]. Their work revealed three types of morphologies designated as microspherulitic with areas of larger spherulites, uniformly spherulitic, and very densely nucleated material with corresponding crystalline contents ranging from 19 to 37% as described in the previous paper. In might be noted here that all three types of spherulitic morphologies, microspherulitic with areas of larger spherulites, uniformly spherulitic, and very densely nucleated material, were observed for ITX as well over the course of the project addressed in this dissertation.

Electron microscopy was also utilized by Lovinger and Davis in 1985 to examine the morphology of melt-crystallized from ultrathin polymer films cast from α-chloronaphthalene and benzophenone [30]. Crystallization from thin films resulted in negatively birefringent spherulites in contrast to the work of Blundell and Osborn just reported. Spherulitic growth was observed with a unique orientation, the b-axis radial, and the molecular c-axis tangential to in the plane of the film. The a-axis was noted as tangential normal to the spherulitic plane. Narrow lamellae were observed as a characteristic growth habit for PEEK, with the majority of the lamellae tending toward edge-on crystallization. The growth habit just described for PEEK is illustrated in Figure 2.4, along with that observed more typically with polymer spherulites. The authors suggest that the growth habit is related to the PEEK chain conformation, which would impart an aniosmetric cross-section to the molecule. Overall, the growth habit of PEEK

Table 2.4   Spherulite growth data for PEEK as a function of crystallization temperature (Tc) and time (tc) [33].

T_c (°C)	t_c (s)	$\bar{L}$ (μm)	N (m^{-3})	r (μm)	G (nm s^{-1})
287	136	29.2	2.3×10^{13}	21.9	161
277	71	25.0	3.6	18.75	264
260	28	20.3	6.8	15.2	540
240	13	16.9	11.7	12.7	980

(a)
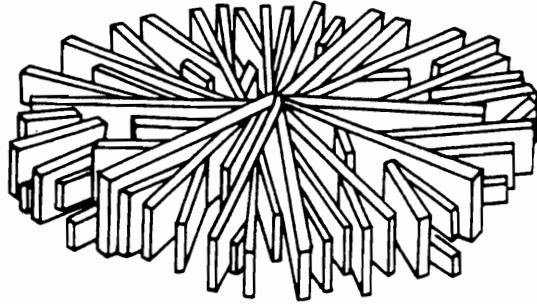
(b)
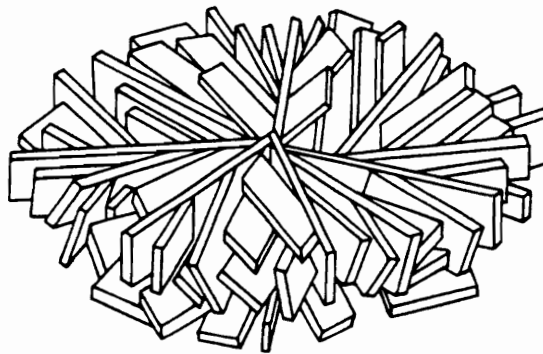
Figure 2.4   (a) Atypical growth habit observed for PEEK, as well as (b) that observed more generally for polymer spherulites [30].

is described as reminiscent of branched polyethylene, polyacrylonitrile and polyphenylenesulfide.

Kumar, Anderson and Adams also studied the crystallization and morphological features of PEEK in their work reported in 1986, in this case as a function of processing parameters [12]. In their work they related the nucleation density, and therefore the subsequent spherulite size observed for PEEK to melt history. Linear growth rates of $0.045 \mu m/sec$ at 320°C, and 0.32 $\mu m/sec$ at 300°C were evaluated for negatively birefringent spherulites. Nucleation density was observed to fall off exponentially with increasing melt temperature between 380 and 420 °C, and was interpreted as the result of self-nucleation of incompletely melted crystals, or the presence of impurities in the melt. The refractive indices of PEEK crystals along the three crystallographic axes, a, b, and c were 1.77, 1.48 and 1.97 respectively. The b crystal axis was again observed in a radial position in this study, with (110) as the preferred growth plane.

One additional study completed in 1986 examines the solution crystallization behavior of PEEK [57]. Lovinger and Davis studied PEEK crystallized from α-chloronaphthalene and benzophenone. The spherulites and single crystals examined in this work were seen to possess very narrow, elongated growth habits. The preferred growth direction corresponded to the b crystallographic axis, and the molecules were normal to the lamellar surfaces, as was observed with melt-grown PEEK.

Recently, additional research has centered on the morphological characteristics of PEEK spherulites with the observation of two melting transitions in DSC results [21, 36]. Marand and Prasad reported the existence of a morphological transition from spherulitic to crystal-aggregate-like (I→II) structures during isothermal crystallization in 1992. As crystallization temperature is increased, and longer times are allowed for crystal reorganization, the population of the second state, which has the same crystal

structure is seen to increase [21]. Work also published in 1992 by Zhang and Zeng describes the presence of negatively birefringent spherulites for PEEK, which can thermally rearrange [36]. The process is described as reversible, and dependent on the heating process, i. e. a slow heating rate is necessary to observe the rearrangement procedure. The partial melting of the spherulites is considered to be reason why one form of spherulite changes into the second structure.

2.2.5 Crystallization Behavior

The crystallization behavior of PEEK has also been well characterized by a number of researchers, some of whose work will be briefly summarized here in chronological order of its appearance in the literature [5, 9, 12, 20, 28, 55, 56, 58-61, 68].

ICI researchers Chalmers, Gaskin and Mackenzie utilized infrared reflection spectroscopy in a 1984 study of the crystalline content in PEEK plaques, to estimate and correlate, the level of crystallinity with WAXS results [56]. They found that the multiple internal reflection (MIR) spectrum could be used to provide comparable crystallinity estimates to WAXS values for determined for PEEK specimens by sampling the first 1-2 μm of the surface.

Morphological studies on PEEK completed in 1986 by Kumar at al., were described in the previous section. The crystallization studies portion of that work will be described now [12]. In their publication, Kumar and coworkers correlated processing parameters with morphology, and ultimately the properties exhibited by PEEK. Their work was one of the first studies to attribute melt sensitivity to PEEK, ascribing its final nucleation density and hence the spherulitic size exhibited by the material to the thermal

history used in processing. They found that the natural log of the nucleation density was a linear function of the melt temperature utilized before crystallization, i. e. ln N decreased as melt temperature increased. In addition, they determined that the linear growth rate, (G), of PEEK spherulites was <u>independent</u> of melt temperature, and reported to be 0.045 and 0.32 μm/sec. respectively when experimentally evaluated at 320 and 300 °C. Viscosity increases for increasing dwell times in air during viscosity measurements were noted however, and attributed to cross-linking or chain extension. The authors observed that melting and recrystallization over several cycles during the optical microscopy studies resulted in reproducible spherulite sizes and growth rates, therefore they suggested that significant degradation did not occur under these conditions. Overall, they determined that even though significant differences were observed in the nucleation density of PEEK as a function of melt temperature, other parameters such as degree of crystallinity, crystallite size and disorder were not similarly affected.

Also published in 1986 were two crystallization studies on PEEK by Nguyen and Ishida, and Cebe and Hong [28, 59]. Nguyen and Ishida investigated the crystallization behavior of PEEK as a function of annealing using FTIR spectroscopy [59]. Their research identified two distinct molecular rotation mechanisms that occur preceding crystallization when amorphous PEEK is annealed. The first is a relaxation mechanism that occurs between 50-140 °C involving the partial bond rotation of the ether linkages to 1) release steric strain, and 2) align the diphenyl ether groups into ordered regions. The second mechanism takes place above the glass transition temperature when the benzophenone linkages rotate moving the entire chain. The authors also completed an analysis of the crystallization kinetics of PEEK following bands at 1601 and 1286 cm^{-1} which are associated with skeletal in-plane vibrations of the phenyl rings in the

crystalline phase. An Avrami exponent of n=1.05 and k=0.04 were determined for crystallization at 140 °C.

The study completed by Cebe and Hong included crystallization behavior evaluations of PEEK utilizing isothermal and non-isothermal crystallization methods. The Avrami analysis of both cold and melt crystallized material yielded "n" values of approximately three, suggesting heterogeneous nucleation, and spherulitic growth. Non-isothermal studies revealed that the relative level of crystallinity which develops before the inflection point in the heat flow curve decreases with increasing cooling rate, where the kinetics change to a slower process. The authors also attributed PEEK crystallization behavior to thermal history, noting that repetitive heating at successively higher temperatures resulted in the development of lower temperature (310 °C) melting crystals in contrast to the majority of the material which melts at 355 °C. This was similar to the work reported by Blundell and Osborn [33]. Finally, the authors used the Ozawa non-isothermal crystallization analysis method to compare crystallization data at selected temperatures and various heating rates. They found that instead of determining a set of parallel lines of equal slope when plotting log (-ln(1-[conversion at a temperature])) versus log (heating rate) as expected when the Ozawa analysis is appropriately modeling crystallization, the plots were curved, which they interpreted as an indication of secondary crystallization.

The existence of a double-melting peak for PEEK has been studied by several researchers, as was noted earlier, and in the study by Cebe and Hong as well. Lee and Porter completed a differential scanning calorimetry (DSC) crystallization study in 1987 which examined this behavior also [55]. Their work evaluated the crystallization behavior of amorphous PEEK, and PEEK that was melt crystallized at low supercooling. Their conclusions were that the double-melting peak arises from four contributions to the

heat flow signal generated due to a crystalline reorganization process on heating. The low-temperature endotherm is the melting of crystals that were originally present in the material, convoluted with their melting and recrystallization over the course of the DSC scan. The higher melting peak is then interpreted as the signal generated by melting the recrystallized material, along with that of any residual crystalline material that had not previously melted. This was considered reasonable, as a Hoffman-Weeks analysis of the equilibrium melting temperature determined a T_m° of 389 ± 4 °C for PEEK. In addition, they found that wide angle-x-ray scattering patterns found only one crystal structure for both the melt and cold-crystallized specimens, indicating that the two melting endotherms did not represent two morphologically different crystals.

Due to its commercial importance, and controversial crystallization behavior, PEEK continues to be an interesting research topic. In 1988 an additional crystallization study was published by Basset, Olley and Raheil in which the authors described a third explanation for the observed melting behavior of PEEK, the existence of low melting material organized between individual primary lamellae [9]. They suggest that PEEK crystalline morphology is characterized by a framework of dominant lamellae which form first, and are higher melting. Interleaved between the dominant lamellae is subsidiary lamellar growth material which crystallizes in increasingly restricted circumstances, and subsequently melts at lower temperatures. In addition, etching and microscopy studies indicate that the internal texture of PEEK is based on branching and splaying of individual lamella, however, fractional crystallization appears not to play a significant role.

Two final crystallization studies will now be reviewed which focus on the effect of thermal history and thermal stability on the crystallization behavior of PEEK. In October 1989 Deslandes, et al. published a DSC and optical microscopy study investigating the

effect of the thermal history of the melt on the crystallization of a commercial film sample of PEEK [20]. This work is significant in that it addresses the crystallization of PEEK after melt treatments corresponding to typical processing temperatures and times, unlike most of the previously discussed studies where the specimens were melted quickly at relatively low temperatures before evaluation. PEEK crystallization from the glass was studied after melting the PEEK specimens at 420 °C for between 0-800 min. Under these conditions, both the crystallization temperature and the shape of the crystallization peak were observed to change. As the hold time in the melt increased, the crystallization peak temperature decreased, and the heat of fusion decreased as well. Isothermal crystallization experiments were also completed after melting PEEK at 420 °C for times ranging from 5 to 120 minutes, and a corresponding increase was noted in the crystallization half time from approximately 250 to 1500 sec. respectively. Nucleation density was also seen to decrease as time in the melt increased, as did linear growth rate by a factor of three. Their findings were in contrast to those of Kumar and associates whose paper noted no change in growth rate as a function of thermal history. Finally, they felt that the observed changes in crystallization behavior, i. e. the decrease in the area of the crystallization peak, were "irreversibly cumulative". Melting and recrystallizing the material a second time resulted in similar data to that generated when a specimen was melted once for an equivalent length of time. Once the material was melted at high temperature, no increase in crystallinity was observed on further thermal treatment.

The final paper that will be reviewed regarding the crystallization behavior of PEEK was completed in 1991 by Jonas and Legras, and is an in-depth review on the thermal stability and crystallization behavior of PEEK [11]. In this research, the molecular weight distribution of PEEK was measured as a function of the melt holding

temperature and time, both in air, and in an inert atmosphere. Three melt times (5, 15 and 30 minutes) were used, and four melt temperatures (385, 400, 420 and 440 °C) for their study. From the molecular weight data, a branching mechanism related to polymer degradation was identified which occurred under typical melt processing conditions. The mechanism consists of progressive branching through random homolytic chain scission which leads to eventual cross-linking. This process was observed to be more rapid in air than in nitrogen.

The influence of material degradation was to decrease the crystallization rate and level of crystallinity which developed in PEEK. The decrease in crystallization rate was associated with decreased molecular mobility accompanying the molecular weight increase as seen via an increase in molecular viscosity. A decrease in the level of crystallinity generated was associated with the structural defects introduced along the chain by the branching process, i. e. as chain symmetry decreased, crystallinity also decreased.

Also discussed as part of the study was the self-nucleation and growth rate behavior of the PEEK. It was noted that in order to eliminate self-nucleation as a result of the presence of minute crystalline seeds, PEEK must be melted at temperatures greater than 385 °C where degradation is already occurring. Accompanying the decrease in nucleation density, which decreases the crystallization rate, is a decrease in the linear growth rate due to the increase in the entanglement density or true chemical (covalent) cross-links generated during the degradation process.

The authors summarize their work with the conclusion that "there are no ideal melt conditions " for PEEK. Degradation is already present under processing conditions, but can be minimized. Melting PEEK for 5 minutes at 400 °C before processing in nitrogen will result in suppressed self-nucleation, and minimal degradation.

2.2.6 Summary

In summary, since its commercial introduction in the early 1980's, PEEK has been of considerable interest to numerous researchers. Initially, it was thought that the crystallization behavior or the material was not a function of its thermal history, but subsequent studies revealed that the material was in fact sensitive to thermal processing. Ultimately, it was revealed by Jonas, et al. that simply melting PEEK is sufficient to initiate a slow, but definite chain scission and cross-linking mechanism that will affect its crystallization behavior.

Since one of the main applications of PEEK is as a semicrystalline matrix material in a high-performance composite, it is appropriate to continue this literature review now with a discussion of the crystallization behavior of PEEK in that form. Again the discussion will be in chronological order, and will highlight the microstructure, properties, and crystallization behavior of PEEK composites.

2.3   Carbon-Fiber Composites with PEEK

Depending on the thermoplastic utilized as the matrix material in a composite, the mechanical, chemical and thermal properties can be tailored for the application [84]. Matrix materials can be chosen from a wide range of polymeric materials including: nylons (polyamides PA), polypropylene PP, and many advanced "engineering" thermoplastics such as polyphenylene sulphide PPS, polyetherimide PEI, polyethersulfone PES, and polyetheretherketone PEEK. The mechanical properties, strength and modulus, will be largely controlled by the fiber choice, its volume fraction and the arrangement selected. Chemical and thermal properties however, are controlled by the matrix material, and it is therefore important to consider the thermal and melt

stability of a thermoplastic during the design stage [84]. This section will briefly review the typical mechanical properties, crystallization behavior, and morphological features observed in PEEK/carbon-fiber composites, and the influence of processing history on those characteristics.

2.3.1 Mechanical Properties

The mechanical properties of PEEK and its composites have been more widely evaluated than many other continuous-fiber reinforced composites [3]. The polymer is generally impregnated into the reinforcing fibers to form a prepreg of 50-65 vol. % fibers, the prepreg plies are laid up in specific orientations, and as a last step consolidated into a sheet or the finished part using heat and pressure. Table 2.5 lists the commercial product forms and manufacturers of continuous-fiber-reinforced polyketone matrix composites. The typical thickness of an individual ply is approximately 100-150 μm.

As was noted earlier, commercial PEEK composites have been well characterized, and typical characterization values are readily available in the literature [3]. A summary of representative property values will be included in the following tables and figures. The physical and thermal properties of several commercial ICI Victrex PEEK molding compounds are summarized in Table 2.6. Next, Table 2.7 lists the physical and thermal properties of consolidated APC-2/AS4 PEEK/carbon fiber composites, and Table 2.8 contains a summary of the mechanical properties of APC-2 PEEK composites when prepared with a variety of reinforcing carbon fibers. Figure 2.5 completes this brief summary with information on a) the tensile strength of both neat and reinforced thermoplastics, and b) information on the effect of temperature on the 0° strength of APC-2/AS4 PEEK-carbon fiber composites [3].

Table 2.5   Continuous-fiber-reinforced composite product forms and manufacturers [3].

Manufacturer	Trade Name	Matrix Polymer	Composite Form
ICI	APC-2	PEEK	Fully impregnated tape and tow
DuPont	—	PEEK	Fully impregnated tape and tow
		PEKK	Long-discontinuous-fiber tape
BASF	—	PEEK	Commingled polymer fibers and reinforcing fibers; tapes and fabrics
		PEKEKK	Powder impregnated tape and fabrics
Courtaulds Heltra	FILMIX	PEEK	Spun staple yarn of discontinuous reinforcing and polymer fibers; tapes and fabrics

Table 2.6   The physical and thermal properties of several commercial ICI Victrex PEEK molding compounds [3].

Property	ASTM Test Methods	Units	PEEK 450G	PEEK 450GL20[a]
General Properties				
Fiber reinforcement	—	—	Glass	Glass
Fiber content	—	%	20	30
Density (crystalline)	D792	g/cm^3	1.32	1.43
(amorphous)			1.265	—
Typical level of crystallinity	—	%	35	35
Processing temperature range	—	°C	350–380	360–400
Mold shrinkage	—	%	1.1	0.7[b]–1.4
Water absorption				
24 hours @ 23°C	D570	%	0.5	—
Equilibrium @ 23°C	D570	%	0.5	—
Thermal Properties				
Melting point	DSC	°C	334	334
Glass transition temperature	DSC onset	°C	143	143
Specific heat	—	cal/g·°C	0.32	—
Heat distortion temperature, 1.82 MPa	D648	°C	160	285
Coefficient of thermal expansion	D696	mm/mm·K $\times 10^{-6}$	47	24
Thermal conductivity	C177	W/m·°C	0.25	0.41
Maximum continuous service temperature (Estimated UL-based test)	—	°C	250	250

[a] These materials are anisotropic, and properties will vary according to the direction of measurement.
[b] Lower figure refers to shrinkage in the fiber orientation direction.

Table 2.7   Physical and thermal properties of consolidated APC-2/AS4
PEEK/carbon fiber composites [3].

Property	Units	APC-2–AS4	
Physical Properties			
Fiber type	—	Hercules AS4 Continuous Carbon	
Fiber volume	%	61	
Density	g/cm^3	1.60	
Standard fiber areal weight	g/m^2	145	
Standard consolidated ply thickness	mm	0.132	
Thermal Properties			
Processing temperature range	°C	380–400	
		LONGITUDINAL	TRANSVERSE
Thermal diffusivity, 23°C	m^2/S	28×10^{-7}	3.4×10^{-7}
Thermal conductivity, 23°C	W/m·°C	4.92	0.611
Enthalpy, 23°C	kJ/kg	32	32
Coefficient of linear thermal expansion			
−55°C	mm/mm·K $\times 10^{-6}$	0.012	27
23°C	mm/mm·K $\times 10^{-6}$	0.28	30
121°C	mm/mm·K $\times 10^{-6}$	0.5	44
232°C	mm/mm·K $\times 10^{-6}$	1.0	75

Table 2.8   Mechanical properties of APC-2 PEEK composites when prepared
with a variety of reinforcing carbon fibers [3].

Property	Units	Carbon Fibers				Glass S-2
		AS4	IM6	IM7	IM8	
0° Tension						
Strength	MPa	2068	2689	2896	2689	1172
Modulus	GPa	138	169	169	187	55
0° Compression (IITRI)						
Strength	MPa	1206	1103	1103	1172	1103
0° Flexure						
Strength	MPa	1999	1999	1999	1999	1551
Modulus	GPa	125	155	155	169	55
90° Flexure						
Strength	MPa	138	156	167	141	110
Open hole tension[a]						
Strength	MPa	387	517	535	474	—
Open hole compression[a]						
Strength	MPa	327	301	303	282	—
Compression after impact[a]						
6.68 J/mm Strength	MPa	338	363	375	324	—

[a] Quasi-isotropic layups.

a)
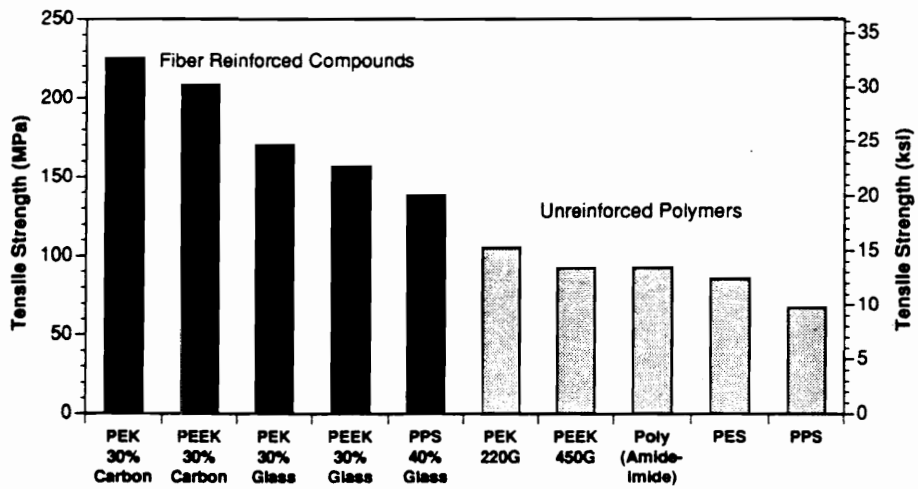
b)
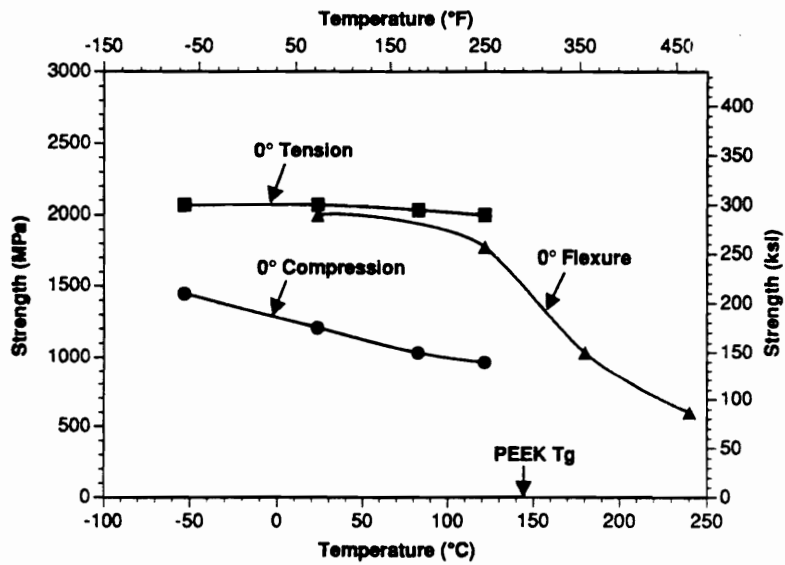
Figure 2.5   a) Tensile strength of both neat and reinforced thermoplastics, and b)
Effect of temperature on the 0° strength of APC-2/AS4 PEEK-carbon
fiber composites [3].

2.3.2 Crystallinity in PEEK Composites

Understanding the crystallization process in PEEK and PEEK composites is important because the level of crystallinity present enhances solvent resistance and modulus while decreasing toughness. In general, polyaryletherketones are semicrystalline materials, however some may have melting points in excess of the onset of degradation for the material so melting is not readily observed. Other factors may affect crystallinity in PEEK as well, such as incorporation of non-crystallizable backbone units such as sulfone that can impede and reduce the crystallization process [3]. In neat PEEK, crystallinity can range from 0-40%, and from 20-40% in a composite [3, 7]. The purpose of this next section is to review, in chronological order, several literature references which address the microstructure, crystalline content and related physical properties of PEEK composites .

In a 1983 ICI review, published soon after the 1982 commercial introduction of ICI's Aromatic Polymer Composite (APC-1) prepreg, Cogswell discussed the microstructure and properties of PEEK composite [2]. The microstructure of the composite was addressed via its three principal components: the organization of the fibers, the crystalline texture of the resin, and the interface. The organization of the fibers within the composite were classified as "regular", "random" and "bundle" with the resin thickness typically observed for each organization scheme increasing respectively. Examination of specimens revealed that the organization type within APC-1 composites was uniformly random, leading to a 7 μm resin phase, which is on the same order of magnitude as the fiber. The texture of the resin phase was reported as crystalline, with approximately 2 μm spherulites observed, which is smaller than the resin phase thickness. It was also noted that if the composite was cooled from the melt between 20-

200 °C, the morphology was not significantly dependent on processing history. Finally, the nature of the fiber-matrix interface was described. Intense nucleation along the fiber surface was observed only for very slow cooling cycles, and not as the dominate morphology within the composite. Cogswell concluded that surface nucleation "testified to the excellent adhesion between resin and fiber and ... that the resin can be considered an extension of the fiber".

Blundell, Chalmers, Mackenzie and Gaskin, also of ICI, published their results on a 1985 crystallization study on APC-2 composites [7]. In their work they estimated the crystalline content within the composite utilizing a combination of x-ray diffraction and infrared reflection spectroscopy. They found that crystallinity varied systematically with cooling rate, crystallization temperature, and annealing time (between 200-300 °C) over a range of 20-40 % of the matrix. Very slow cooling (0.5 °C/min.) resulted in a slightly higher value of ~35 % crystallinity. It was also observed that transcrystalline growth was present, and could be monitored via x-ray if a unidirectional lay-up was examined. Crystallization of the composite either by post annealing, or by rapid cooling generated essentially a random crystallite orientation, however, relatively slow cooling rates emphasized the nucleation of transcrystallinity as was noted earlier.

An additional crystallization study on PEEK in the presence of carbon fibers was published by Lee and Porter in 1986 [6]. The research described in this paper focused on evaluating the nucleation behavior of PEEK in the presence of carbon fibers as a function of thermal history. In this work, the crystallization behavior of PEEK was a function of fiber content. As fiber content increased, the level of supercooling needed to initiate crystallization decreased, indicating that the Thornel 300 PAN-based fibers were a nucleating agent for PEEK. In addition, repeated melting (396 °C for 0, 20, 20, 50, and 20 min. cycles) of the PEEK resin was found to decrease the nucleation density in the

polymer, resulting in subsequently higher relative nucleation off the carbon fiber surface. The higher surface nucleation resulted in the generation of a pronounced transcrystalline region. Transverse tensile test and strain-to-failure results for the transcrystalline material were reported to be twice those for the less strenuous melt history material which did not include the transcrystalline morphology. Greater matrix adhesion was also observed by SEM for the transcrystalline material. The authors concluded that crystallization nucleated off the surface of the carbon fiber generated a stronger interfacial bond between the PEEK matrix and the fiber.

Nguyen and Ishida reviewed PEEK and PEEK advanced composites in a 1987 review article [4]. This reference discusses synthesis, molecular weight determination, solution properties, morphology and mechanical properties of PEEK and PEEK composites. In the summary, the authors noted that previous thermal history is very influential on the melting and crystallization behavior of PEEK, which is in agreement with other authors [11, 12, 20, 59].

Annealing effects on the crystallinity in PEEK composites were addressed in the next two references [64, 65]. Work completed in 1987 by Ostberg and Seferis evaluated the degree of crystallinity in PEEK composites by DSC and density gradient column [65]. This study is unique in that it involved "freezing" PEEK specimens at various positions along the DSC heating profile and evaluating the percent crystallinity via density gradient column (DG). It was seen that the results for both DSC and DG were further apart for specimens with lower levels of crystallinity, and in good agreement at higher crystalline contents. The authors concluded that PEEK, like other polymers continues to crystallize during the DSC scan once the material is heated above the glass transition temperature. Partial melting, recrystallization, and crystal perfection occur which lead to an increase in the level of crystallinity observed and generated a second endothermic peak. Similar

results were determined for PEEK composite in the DSC, however, high void content in the composite prohibited its crystalline content evaluation by density gradient column during this study.

The second annealing study was completed by Ma, et al. in 1989, and investigated the effect of annealing on the properties of carbon fiber reinforced PEEK composites [64]. PEEK composites were prepared from 5 mil thick ICI PEEK films and carbon fiber woven cloth consolidated at 390 °C and 200 psi. All specimens were then annealed at 250 °C for times ranging from 20 min. to 10 hours. It was found that the higher the annealing temperature, the higher the crystallinity present in the composite, which in turn increased the observed Tg and flexural strength. The work in this reference was in agreement with the previous paper, annealing was seen to increase composite properties. The authors also suggested that longer times were equivalent to higher annealing temperatures in their effects on composite crystallization.

A 1990 publication discusses the effects of cooling rate during processing on the mechanical properties of APC-2 composites [18]. AS4/PEEK composite laminates were prepared using cooling rates ranging from 1 to 20 °C/min. to examine the effect on crystalline content and the impact resistance of the material. Wide angle x-ray scattering was utilized to measure crystalline contents of 37 and 30 %, respectively, for the cooling rate extremes just noted. For unidirectional coupons, mechanical properties were essentially unchanged by the increase in crystallinity which accompanied the slower cooling rate. Only a very slight increase was noted for transverse tensile strength and modulus, while longitudinal tensile strength and modulus were unchanged. Impact resistance was seen to be sensitive to cooling rate for the samples evaluated. Toughness decreased as crystallinity increased, with an increase in cumulative damage within the composite observed by C-SCAN for the more slowly cooled specimen.

A second review, based largely on PEEK and its composites, was published in 1991 by Schultz.. In this article, the mechanical behavior of semicrystalline polymer matrix materials was addressed as being dependent on three levels of microstructure: intracrystalline, crystallite-level and spherulite level as seen in Figure 2.6a. On a spherulitic level, research determined that PEEK was composed of lath-like crystals as seen in Figure 2.7a. Figure 2.7b illustrates the general process of spherulitic growth which is thought to occur in PEEK starting from the initial crystal, and continuing by the regular creation of new crystallites at the new growth front. New growth splays at the growth front to eventually generate a spherically symmetric system. Microstructure at the spherulite level has little effect on the stiffness or chemical properties of the material, however it may influence the ultimate properties including mechanical and electrical failure. On the crystallite level, organization and orientation of spherulitic structures within a crystalline material can affect the tensile modulus of a spherulitic material, which is normally dominated by the amorphous phase. One example is the case of rapid crystallization under high strain where a microstructure of oriented rod-like crystals within an amorphous matrix can generate a classical "fiber composite" system with far different properties than an unoriented material of similar crystalline content. Figure 2.6b summarizes how various microstructures can influence stiffness. Finally, Schultz summarizes the effects of intracrystalline microstructure, i. e. chain packing and mobility. These factors are reflected in the thermal transitions that a material displays, as well as in the permeability and diffusivity of small molecules within the material as a result of the packing density and perfection. Elastic behavior in semicrystalline materials is also affected by the degree of chain alignment, modulus is higher along the chain then across

a)
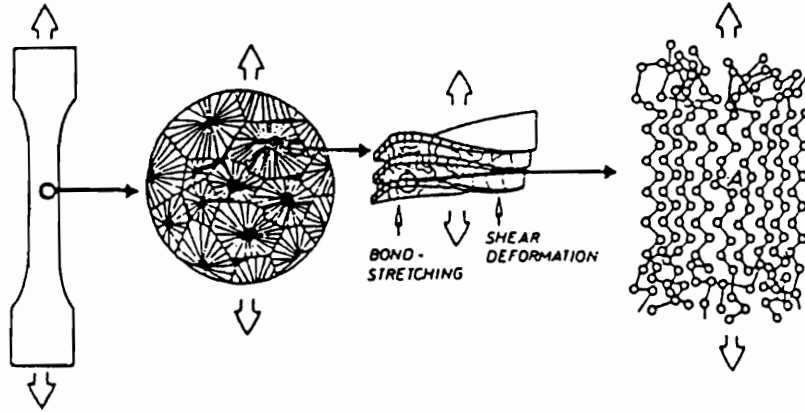
b)

Microstructure type	Axial tensile modulus
Fibrillar crystals, oriented amorphous	$E = v_c E_{cc} + (1 - v_c)\, E_{ac}$
Row structure, with oriented amorphous	$1/E = v_c/E_{cc} + (1 - v_c)/E_{ac}$
Fibrillar crystals, relaxed amorphous	$E = v_c E_{cc} + (1 - v_c)\, E_{ar}$
Row structure, with relaxed amorphous	$1/E = v_c/E_{cc} + (1 - v_c)/E_{ar}$
Spherulite	$1/E = v_c/E_{cav} + (1 - v_c)/E_{ar}$

v_c = volume fraction crystallinity; E_{cc} = crystalline tensile modulus in the chain direction; E_{ac} = oriented amorphous modulus in the chain direction; E_{ar} = relaxed amorphous tensile modulus; E_{cav} = crystalline modulus averaged [47] over all directions.

Figure 2.6   a) Levels of microstructure to be considered for their influence on mechanical properties including: intermolecular structure, crystalline and amorphous layer organization, crystalline morphology (spherulitic etc.). b) Contribution of various types of microstructure to axial stiffness. [69].

a)
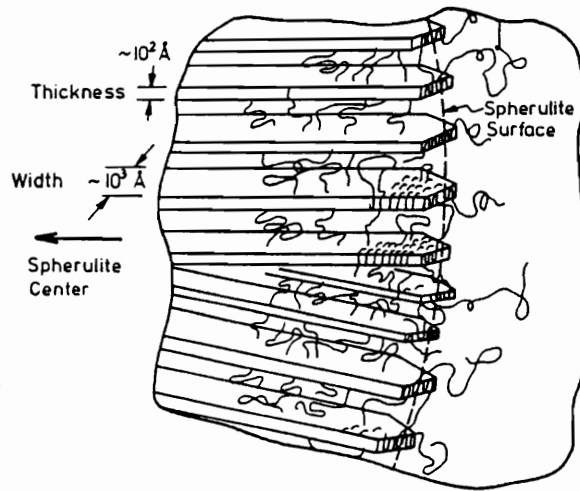
b)
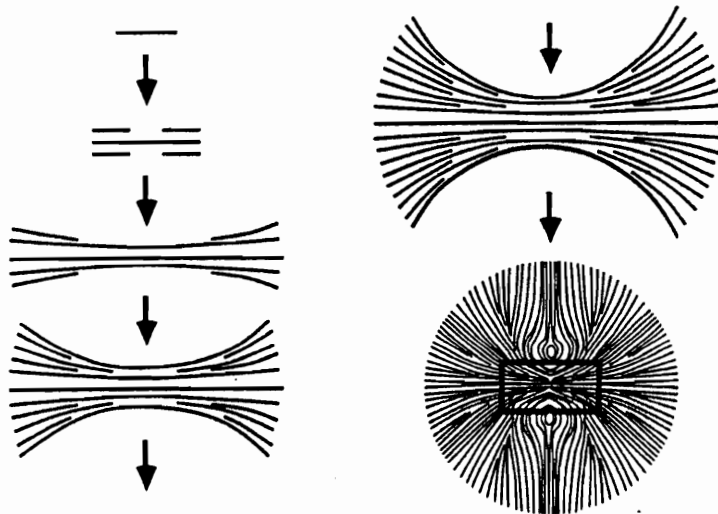
Figure 2.7   a) PEEK internal spherulitic microstructure showing radially arrayed fibrils composed of lathlike crystallites separated by amorphous layers. b) Schematic illustration of spherulitic growth encompassing: 1) nucleation from a lathlike crystal, 2) growth through multi layer sheaves, and 3) the final spherulitic form [69].

the chain, and shear moduli is highest at large angle to the chain direction for unoriented materials.

One final reference that will be discussed which addresses the structure-property relationship between crystalline morphology and processing conditions in PEEK composites was completed by Jar et al. in 1991 [16]. In this work the authors look at the effect of thermal history and processing on the microstructure of the composite material. Specifically, they examined how the mechanical behavior varied for APC-2 composites with different crystal morphologies generated as a function of thermal history. Specimens were prepared by heating to 350, 370 or 390 °C for 30 min., and then annealed at 300 °C for 3 hrs., followed by a slow (1 °C/min.) cool to room temperature. The crystalline morphology of each specimen was examined by optical microscopy, and was seen to vary with melt temperature. The specimens melted at low (350 °C) temperature had a fine spherulitic texture, as did the 370 °C material, however the nucleation density of the latter was reduced. The 390 °C microstructure contained large spherulites (some > 20 μm) and some transcrystalline structures. The variation in crystalline texture was attributed to self-seeding of nuclei on incompletely melted material. Some of the specimens were then fractured in tension at 90 ° to the fiber direction, and the fracture surfaces examined. Clear differences exist in the fracture surfaces of the low and high temperature melt treatment fracture surfaces. The finer texture material generated after melting at 350 °C displayed some plastic deformation and cracking at rupture, with the crack traveling around the spherulites, with the spherulites stretching and aligning in the direction of the stress. In contrast, the larger spherulitic structure which resulted from the higher temperature melt treatment temperature (*390 °C) was observed to crack through the spherulites, with little plastic drawing. The authors noted that although well defined differences in the fracture

behavior were noted for the different morphologies, the observations did not clarify whether the mechanical properties were affected by thermal history as the results on similarly treated consolidated panels were not complete.

The previous sections summarized results on observed differences in crystallization behavior, mechanical properties, and morphological features that have been noted for PEEK/carbon-fiber composites in the literature. One morphological feature that was observed within several systems was transcrystalline growth off the surface of the reinforcing fiber. At this point, this topic will be addressed in further detail.

2.3.3 Transcrystallinity

Researchers have noted the presence of transcrystalline growth initiating off the surface of carbon fibers in PEEK composites, and in other materials as well, and have been interested in both the cause and effect of this phenomena on material properties [2, 4, 7, 6, 20, 22, 38, 71, 75, 85-95]. Several papers on this topic will be briefly reviewed in this section.

Well before the commercial introduction of PEEK in the early 1980's, the effect of transcrystallinity on mechanical properties was already of scientific interest. One example, a paper published by Frisch in 1971, discussed the effects of transcrystallinity on adhesion [91]. The author, whose goal was to investigate the contribution of morphology and spherulite orientation (transcrystallinity) on mechanical properties, commented that transcrystallinity has been described in the literature in polyamides, polyurethanes, and polyolefins as far back as the 1950's. The focus of the paper was in determining if in thin films, such as adhesive layers where the surface zone is a substantial portion of the total volume, whether the transcrystalline region may

significantly affect overall properties of the bond. Films of various thicknesses of transcrystalline polyethylene and polypropylene were prepared on aluminum and copper, and the dynamic Young's modulus measured. The results suggested that the modulus of the transcrystalline regions was higher than that of the bulk material, and the author suggested that it might positively affect adhesive strength.

Work by Folkes and Hardwick in 1987 also addressed the properties of the transcrystalline region in polypropylene, in this case against poly(ethylene terephthalate) fibers by measuring tensile and shear properties of a transcrystalline tape [71]. Their results were in agreement with Frisch, the transcrystalline sheets were found to be stiffer (but more brittle) as compared to their spherulitic counterparts. However, their interpretation of the data differed with the previous work in that they thought that the influence of transcrystallinity would not be entirely positive. They suggested that composites with transcrystalline zones might fail at lower strain values than spherulitic material, and that cracks would propagate more readily along the highly oriented transcrystalline zones. In contrast, they also noted that the higher shear strengths (20.8 versus 13.1 MPa respectively) measured for the transcrystalline material might increase matrix shear strength and increase the efficiency of stress transfer from the matrix to the reinforcing fiber. Overall, they thought that the presence of transcrystallinity may have a net reinforcing effect, however, that some deleterious effects might exist as well.

He and Porter also looked at transcrystallinity in polyolefins in their 1988 work on polyethylene [92]. They investigated the crystallization process, as opposed to the effect of transcrystallinity on mechanical properties. Their results suggested that the surface of high-modulus PE fibers was a more efficient nucleating agent than was the bulk PE crystallizing around the fiber. As fiber content increased, nucleation density therefore increased, and the 2-3 μm thick transcrystalline zone was observed by DSC to crystallize

at higher temperatures (~2.5°C) than the bulk material. With 50 wt. % fiber present, isothermal crystallization was observed to be a two-step process for the transcrystalline, and subsequently bulk materials as well.

Work by Blundell, Crick, Fife, Peacock, Keller, and Waddon published in 1989 examined the crystalline morphology and nucleation sites of PEEK/carbon-fiber composites [38]. They reported the existence of different morphologies as a function of crystallization conditions. At lower temperatures, nucleation within the matrix was favored, and no evidence of transcrystalline growth was observed. In addition, nucleation from fiber surfaces was associated at fiber-fiber contact points was observed, arising, the authors suggest, from local shearing or differential contraction stresses. Nucleation at free fiber-polymer interfaces and within the matrix were also observed, with the relative proportion of each nucleation mechanism varying as a function of crystallization conditions. Based on scanning electron microscopy studies, the authors conclude that the growth habits in normally prepared composite specimens appear to be identical to those found in the pure polymer. The authors attribute transcrystalline morphologies observed by other researchers to experimental artifacts, e. g. interaction between single carbon fibers and the glass hot-stage slides during crystallization.

A study addressing the interfacial morphology of carbon-fiber/PEEK composites by Saiello, et al. was published in 1990, and it also investigated the effects of transcrystallinity on composite properties [75]. Earlier work by Lee and Porter with transverse tensile tests on composites prepared at different isothermal temperatures had indicated that those which contained transcrystallinity at the carbon fiber surface displayed considerably higher strength values than the matrix indicating that the specimens exhibited a strong interfacial bond between the resin and fiber. These authors attempted to correlate the fracture surfaces of like specimens with their

properties and found that fracture surfaces did vary with morphology. Amorphous specimen fracture surfaces were characterized by clean fibers protruding from the matrix, and no resin deformation or fracture. On the other hand, semicrystalline composite specimens showed evidence of matrix material still attached to the fibers, particularly in the case of material with higher levels of crystallinity, and the presence of some transcrystallinity. The authors suggested that these difference might reflect increasing composite properties, and therefore considered this to be a positive influence.

Work completed in 1989 by Carvalho, et al. also found differences in properties in specimens with transcrystallinity versus those without transcrystalline regions in polyethylene and polypropylene/carbon-fiber composites [89]. Here also the effect was interpreted as a potential positive influence on composite properties as inter-laminar shear strengths were seen to increase with the increase in thickness of the transcrystalline region and its uniformity. Another set of authors whose research suggested that transcrystallinity was a positive influence on composite properties were Caramaro et al who looked at the crystallization kinetics of PPS/carbon-fiber composites in 1991 [85]. They suggested that the presence of a well-crystallized structure with a transcrystalline phase around the fiber helped to optimize mechanical properties. Cohesive failure was noted for short beam shear strength test specimens prepared within the thermal window where transcrystallinity was present, with adhesive failure generally noted elsewhere.

Several researchers looked at the effect that fiber characteristics and shear had in initiating transcrystallinity in addition to such factors as thermal history [86, 88]. Desio and Rebenfeld also worked with poly (phenylene sulfide), and reported in 1990 that utilizing crystallization half-times, differing crystallization rates were observed for different fiber containing composites [88]. After normalization for fiber surface area, PPS was

seen to crystallize most rapidly in the presence of aramid fibers as opposed to carbon or glass fibers in that order, and the level of crystallinity was also seen to be lower in the latter two fiber systems with respect to neat PPS. Lopez and Wilkes also studied PPS crystallization and reported in 1991 that the crystallization temperature, molecular weight, and surface treatment of carbon fibers affected the crystallization behavior of the material [86]. Low crystallization temperatures, slow cooling rates and external stresses were seen to favor the generation of transcrystallinity. PPS specimens isothermally crystallized at 180, 200, 225 and 245 °C all nucleated on the carbon-fiber surface, however, only at 180 and 200 °C was the nucleation density sufficiently high to generate transcrystallinity. This is unusual behavior in that lower crystallization temperatures generally enhance bulk nucleation, which might be expected to diminish the prevalence of fiber-surface nucleation. The authors suggest that this behavior is the result of the difference in the thermal conductivity between the fiber and matrix materials. This difference may generate a thermal gradient at the fiber-matrix interface during cooling, with the effect being most pronounced at lower crystallization temperatures where a stress gradient could arise and promote nucleation. In contrast, increasing the polar component of the fiber surface through anodization was seen to decrease the nucleating ability of T300U carbon fibers, as did increasing the molecular weight of the PPS.

Other researchers looked at the effects of fiber characteristics and shear on transcrystallinity in polyolefin materials [87, 90, 93, 94]. Devaux and Chabert studied transcrystallinity in polypropylene/glass-fiber composites and reported in 1991 that controlling crystallization conditions, i. e. temperature and shear generated transcrystalline morphology in isotactic polypropylene on glass fibers. Ishida and Bussi published results in 1991 regarding surface-induced crystallinity of high-density polyethylene on ultrahigh-modulus polyethylene fiber [90]. In their work they noted that

polyethylene fibers were good nucleating agents for the polyethylene matrix and subsequent transcrystalline growth. Thomason and Van Rooyen also studied transcrystallinity in polypropylene, and reported their work in 1992 [93, 94]. They observed that transcrystallinity was generated in polypropylene in the presence of high-modulus carbon fibers and aramid fibers, but not for high-strength carbon nor glass fibers. Interestingly, even those fibers that actively nucleated transcrystallinity only did so when crystallization temperatures below 138 °C were utilized, unless shear stress was induced. When stress was induced at the fiber-matrix interface, a wider range of fibers and crystallization temperatures evaluated generated transcrystalline morphologies in polypropylene. The authors suggested that thermally induced stress gradients were related to nucleation at the fiber-matrix interface. Transcrystallinity is influenced by: 1) the axial thermal coefficient of expansion of the fiber (i. e. the greater the mismatch between fiber and matrix, the lower the cooling rate needed to generate transcrystallinity), 2) the sample cooling rate, 3) the fiber length and position (tips more active than fiber center) and 4) the polymer molecular weight. Like Wilkes and Lopez who also proposed stress-induced crystallization effects at the fiber surface, Thomason and Van Rooyen noted that transcrystallinity was reduced for higher molecular weight materials when crystallized at the same temperatures, however, they noted that higher crystallization temperatures could in fact generate transcrystallinity in higher molecular weight materials.

2.3.4 Summary

Studies addressing the interrelationship between thermal history, processing parameters and semicrystalline morphology in several organic matrix composites have been briefly addressed in this section. Additional understanding of the structure-property

relationships in PEEK composites has evolved since Cogswell's initial work where it was reported that composite morphology was not significantly dependent on processing history [2]. Currently, it is accepted that thermal history does affect the final morphology of PEEK, and therefore its properties [4, 6, 11, 12, 20, 59].

Cogswell also noted in his early ICI report that surface nucleation resulted in excellent adhesion between resin and fiber, and work has continued to elucidate this specific research area [2]. The development of a transcrystalline phase adjacent to the reinforcing fiber within the matrix has been reported by numerous researchers, however the effect of this microstructure remains controversial. Thermal history, including such parameters as melt treatment temperature, crystallization temperature, and cooling rate have been reported to influence the size of spherulitic radii, nucleation density, and ultimately the structure of the matrix including the development of transcrystallinity. Once the mechanism responsible for the generation of transcrystallinity is clarified, the properties of composites containing these "controlled" morphologies can be more readily interpreted, and the effect of its existence on composite mechanical properties generalized, as is not currently possible.

2.4   Polymer Crystallization

The properties of semicrystalline polymers are a function of the chemical structure, molecular weight distribution, and the crystallization conditions under which the material solidifies. The crystallization conditions, and therefore the mechanisms involved in crystallization under those conditions, have a substantial influence on the properties of the resultant material. Controlling the crystallization process can directly influence the final properties of the material through its repercussions on the size of the

crystallites, the degree of crystallinity, the morphology of the lamellar crystallites and their associated interfacial or amorphous regions [3]. Therefore understanding the crystallization process, and subsequently optimizing it for each specific material, is fundamental in ensuring that consistent mechanical properties develop during industrial crystallization processes.

Under the appropriate conditions of temperature, pressure, stress or in the presence of solvents a spontaneous ordering of flexible chain molecules of sufficient structural regularity can occur. In this process, the chain bonds assume energetically favorable rotationally oriented states, and long range three-dimensional order develops such that crystalline contents ranging from 30 to 90% are achieved [96]. Even though the crystallization process is rarely complete as with low molecular weight materials, similarities do exist between the crystallization behavior of polymers and low molecular weight materials. Some important principles that are relevant to both small molecule, and longer chain polymer molecule crystallization include:

- Normal small molecule bond distances, bond angles and other structural elements are the general rule in polymer crystals as well.

- The chemical repeating unit in polymer crystals plays a role that is analogous to that of small molecules in crystals of low molecular weight organic compounds.

- A complete molecule is not typically present within one polymer crystal unit cell, in fact it is not uncommon to find more than one chain passing through the crystalline unit cell [97].

The transformation of a polymer from the amorphous molten to the ordered semicrystalline state is not instantaneous. In fact, this ordering involves two processes including the initiation of the crystalline phase, and its subsequent development, which

are termed nucleation and growth respectively. A discussion of the theory behind these two processes is included next.

2.4.1 Thermodynamics of Primary Nucleation

The transformation process from liquid to solid semicrystalline polymer begins with the formation of a very small amount of crystalline material, which emerges from the molten parent phase by fluctuation processes, and can lead to the growth of a stable crystal. This process is termed nucleation, i. e. homogeneous or self-nucleation, in contrast to heterogeneous nucleation in the presence of a second phase or material [98, 99]. The initial origination of a crystal phase from the parent phase is denoted "primary nucleation" in contrast to surface nucleation on a growth plane which occurs as part of crystal growth, and is known as "secondary nucleation".

Nucleation involves an activation process leading to the formation of unstable intermediate states known as embryos. A critical embryo which is sufficiently stable to go on to form a crystal is termed a nucleus. A nucleus differs from an equal number of disperse molecules in that it posses sufficient excess surface energy to produce the new phase in the presence of the parent phase. A thermodynamic description of the crystallization process can be written as:

$$\Delta G = G_{crystal} - G_{melt} \qquad (2.1)$$

$$\Delta G = \Delta H - T \Delta S \qquad (2.2)$$

where ΔG is the Gibbs free energy of crystallization and ΔH and ΔS are the enthalpy and entropy of crystallization. Equation 2.2 applies to the overall macroscopic transformation, where theoretically crystallization becomes possible as soon as ΔG

assumes negative values, and crystals are randomly distributed throughout the volume of material at the melting temperature (T_m). In reality, polymer melts and solutions crystallize by growing from a nucleus, and initiate growth only at much lower temperatures (T_c) than T_m where ΔG equals zero, i. e. they supercool.

Polymer crystals begin with a large specific surface area whose overall free energy can be written as:

$$G_{crystal} = G_{bulk} + \sum \gamma A \qquad (2.3)$$

where G_{bulk} is the free energy of the crystal disregarding surface effects, γ is the specific surface free energy, and A is the corresponding surface area [100]. On crystallization, the free energy change is defined as:

$$\Delta G = \Delta Gc + \sum \gamma A \qquad (2.4)$$

where ΔG_c describes the bulk free energy change, and the specific surface energies are positive for the crystallization temperatures. Once temperatures less than T_m are reached, ΔG 1) rises, 2) exhibits a maximum, and 3) then decreases through zero as a function of embryo size as a stable growing crystal is formed within the amorphous melt. This process is called primary nucleation as noted earlier, and is described schematically in Figure 2.8.

The process of primary nucleation illustrated in Figure 2.8 includes several processes denoted by various terms. Moving from left to right of the diagram along the curve: 1) a thermodynamically stable crystal of sufficient size grows to form a nucleus from an embryo due to random fluctuations of order within the melt, 2) the primary nucleus reaches sufficient size to be "critical" at the maximum of the ΔG versus size
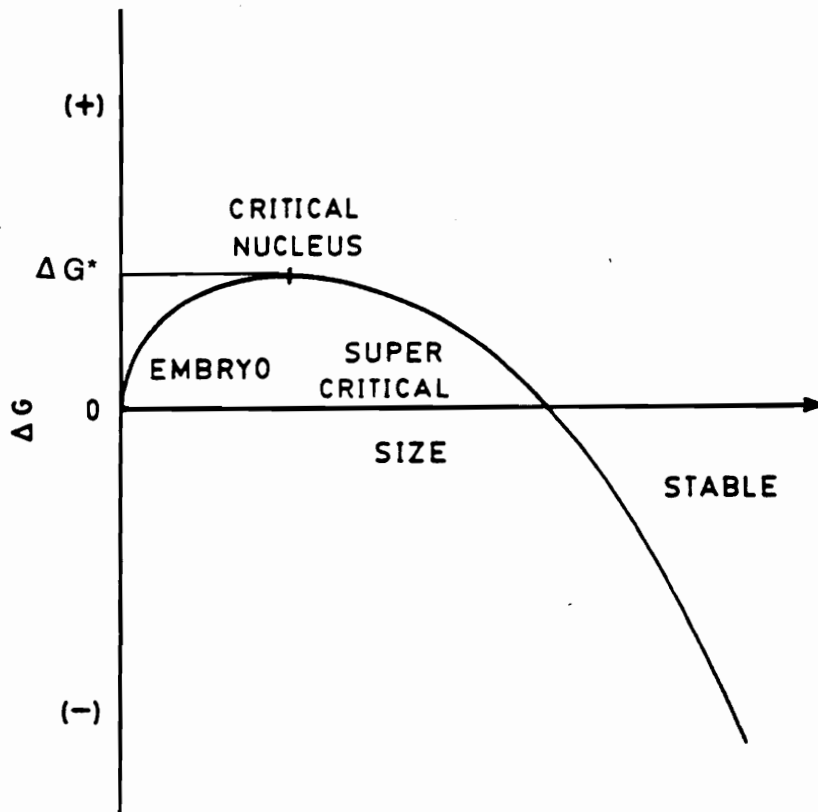
Figure 2.8   Schematic representation of the change in free energy occurring during the primary nucleation process in polymer crystallization [100].

curve, and finally 3) the nucleus size continues to increase upwards from the supercritical point until once again ΔG is negative. At this point, small crystals exist within the amorphous material. Once their crystalline radius is greater than the critical radius, r_c, ΔG decreases, and eventually further growth of the fragment is spontaneous [99, 100].

The previous discussion centered on the free energy changes associated with primary nucleation. Additional work on nucleation in condensed systems has been completed addressing the rate of nucleation. The steady-state nucleation rate per unit volume and time has been derived by Becker and Doring (1935), Fisher and Turnbull (1949), and Hoffman et al (1958-66), and is given by the expression in Equation 2.5 [96, 97, 102, 103]:

$$N = N_0 \exp \left[\left(-E_D / RT \right) - \left(\Delta G_n^* / RT \right) \right] \qquad (2.5)$$

where at constant pressure and temperature: N_0 is generally considered a constant, E_D is the energy of transport in the solid-liquid interface, ΔG_n^* is the free energy of formation of a critical nucleus, T is absolute temperature, and R is the universal gas constant. Wunderlich describes the preexponential term as the approximate transmission coefficient for the crystallizing element [100]. The temperature dependence of this term is generally considered negligible compared to the exponential terms, and for data analysis it is usually treated as a constant [103]. Two additional terms are also included within the exponential term, and the contribution each makes will be described next.

The expression noted in Equation 2.5 to describe the steady-state rate of nucleation includes two exponential terms describing different influences on nucleation

rate. The first term enclosed within brackets, ($-E_D / RT$), describes the temperature dependence of the rate of diffusive transport of the molecules in the melt, and is known as the transport factor [103]. Work by Hoffman et al. has suggested that $-E_D$ is not a constant, and instead that the diffusive transport in a melt should be described by a WLF (Williams-Landel-Ferry) function in a similar manner to that used when describing the viscoelastic deformations in a glassy polymer melt near the glass transition temperature. The general form of the WLF expression used by Hoffman to approximate the effect of molecular weight on the transport term below T_g is noted in Equation 2.6 [103]:

$$E_D / RT \approx [(C_1) / R (C_2 + T - T_g)] \qquad (2.6)$$

where T_g is the glass transition temperature, and C_1 and C_2 are universal constants (C_1 = 17.2 kJ/mol or 4.12 kcal/mol and C_2 = 51.6 K). Except for cyclic polymers, the molecular weight dependence is monitored through the T_g term, where the relationship between T_g and molecular weight is reflected in the Flory-Fox equation:

$$T_g = T_g^\infty - k / \bar{M}_n \qquad (2.7)$$

where T_g^∞ is the glass transition temperature for the infinite molecular weight polymer, and k is a constant. The expression in Equation 2.6 has also been used considering C_1 and C_2 as adjustable parameters [96]. Hoffman's approximation is approximately true at temperatures in the neighborhood of the glass transition temperature, but does not hold in the region of the optimum rate of crystallization [103]. Van Krevelen has proposed the semi-empirical correlation noted in Equation 2.8:

$$E_D / R \approx (C_D) [(T_m^2) / (T_m - T_g)] \qquad (2.8)$$

where $C_D \approx 5$ as calculated utilizing experimental activation energies determined by Mandelkern for a series of polymers [103]. An additional approximation of the transport term has been proposed by Vogel, which expresses the temperature dependence of the viscosity of supercooled liquids. This approximation writes the transport term as:

$$E_D / RT \approx [B / R (T - T_\infty)] \qquad (2.9)$$

where B is a temperature-independent constant, and T_∞ is the temperature at which the viscosity reaches an infinite value. The relationship between the Vogel and WLF parameters is: $B = C_1 / R$, and $C_2 = T - T_\infty$.

The second exponential term within the brackets of Equation 2.5, ($\Delta G^* / RT$), is known as the nucleation factor. The expression for the free energy of formation of a critical nucleus, ΔG^*, is composed of two contributions: the bulk free energy of fusion, and of opposite sign are terms that represent the excess surface free energies contributed by the interfaces present, and which are a function of the shape of the nucleus. Flory determined the critical conditions for three-dimensional homogeneous nucleation for pure polymer chains of infinite molecular weight to include:

$$\Delta G^* = 8 \pi \sigma_u \sigma_e / \Delta G_u^2 \qquad (2.10a)$$

$$\rho^* = 4 \pi \sigma_u / \Delta G_u^2 \qquad (2.10b)$$

$$\zeta^* = 4 \sigma_e / \Delta G_u \qquad (2.10c)$$

where: ΔG^* is the free energy of nucleation, ΔG_u is the bulk free energy of fusion per mole of repeat unit, σ_e is the excess interfacial free energy per repeat unit as it emerges from the crystal face normal to the chain direction, ζ^* is the number of repeat units in the

chain in the crystalline array, and ρ^* are the number of sequences in cross section [96]. Variations in molecular weight, particularly in the low molecular weight region, and of diluents result in significant differences in the critical dimensions of the nuclei, and of their corresponding free energy of nucleation.

In polymers, the fact that the crystals are exceedingly thin relative to their other dimensions, allows the determination of one of the principal surface free energies from the free energy of formation of a single chain-folded crystal. The free energy of formation of a single chain-folded crystal can be described in Equation 2.11 as:

$$\Delta \phi_{crystal} = 4 \, x \, l \, \sigma = 2 \, x^2 \, \sigma_e - x^2 \, l \, (\Delta f) \qquad (2.11)$$

where l is the thin dimension or lamellar thickness of the crystal, x is the large or lateral dimension, σ_e is the fold surface interfacial free energy, and σ is the lateral surface interfacial free energy (see Figure 2.9) [104]. Equation 2.11 defines σ and σ_e for a chain-folded crystal. The quantity Δf is the bulk free energy of fusion, and is approximated near the melting point by assuming that the heat of fusion is independent of temperature as noted in Equation 2.12:

$$\Delta f = \Delta h_f - T \Delta S_f = \Delta h_f - T \, (\Delta h_f) / T_m^\circ = \Delta h_f (\Delta T) / T_m^\circ \qquad (2.12)$$

where Δh_f is the heat of fusion per unit volume of the crystal, T_m° is the melting point of a crystal of infinite molecular weight, i. e. with very large thickness, l, and ΔT is the undercooling $T_m^\circ - T$. At the melting point of the crystal, $\Delta \phi_{crystal} = 0$, and since $x \gg l$ [104]:
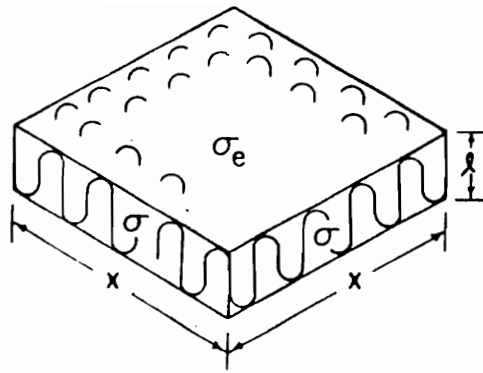
Figure 2.9   Schematic representation of a thin chain-folded crystal showing σ_e and σ [104].

$$T_m = T_m° [1 - 2 \sigma_e / (\Delta h_f) l] \qquad (2.13)$$

Equation 2.13, which is known as the classical Gibbs-Thomson expression, shows that the observed melting point, T_m, for a thin platelet is depressed below that of an infinite crystal by an amount $2 \sigma_e T_m° / (\Delta h_f) l$ [104]. For high molecular weights, this expression represents the relationship between melting temperature and crystallite thickness, l [97]. By plotting T_m versus $1/l$, the slope is $-2 \sigma_e T_m° / \Delta h_f$ and the intercept is $T_m°$. Once Δh_f is known, σ_e can be determined using this relationship.

2.4.2 Types of Nucleation

Nucleation in polymers is influenced by the presence or absence of a second phase in the melt, and can be affected by external influences such as orientation as well. The following main types of nucleation are distinguished from each other, and are defined in the literature [98].

- *Heterogeneous nucleation* is nucleation due to the presence of a second phase, and occurs at the interface between the second phase and the parent phase. Often heterogeneous nucleation reduces the nucleus size needed for crystal growth since the creation of the interface between the polymer crystal and the substrate is more readily completed than generating free polymer crystal surface due to a drop in the interfacial free energy. Nucleation may be the result of a special fit of the crystalline phase onto the substrate, due to the effects of hydrogen bonding groups or parallel ridges on the surface of a nucleating agent, or may often remain obscure.

- *Homogeneous nucleation* is crystal nucleation in the absence of a second phase, or in the presence of a second phase which does not affect crystallization. Homogeneous nucleation may occur through external influences such as orientation.

- *Spontaneous nucleation* is the term used to describe nucleation under no other influence than supercooling or supersaturation of the parent phase, and is often incorrectly used interchangeably with homogeneous nucleation where outside influences can play a role. Spontaneous nucleation generally requires greater supercooling than other nucleation mechanisms, and therefore is not normally observed in the crystallization of bulk materials. The material will previously have nucleated off the surface of impurities in the melt as it is not generally possible in practice to purify the polymer sufficiently that heterogeneities are ineffective under typical conditions.

- *Orientation-induced nucleation* is nucleation within the polymer melt due to some degree of alignment of the liquid molecules. This type of nucleation is almost specific for polymers, as opposed to low molecular weight materials, and it occurs as a result of shearing the melt or solution.

- *Nucleants or nucleating particles* are foreign particles which induce heterogeneous nucleation, and are not nuclei themselves. In the presence of nucleating agents, the actual crystallization nuclei are formed at the surface of the nucleating particles.

Nucleation in polymers can also be influenced by the presence of additives such as nucleants as was just mentioned, or by seeding and breeding, or by diluents or liquid additives [98]. When small crystals of the phase to be crystallized are added to the crystallizing material the phenomenon is known as seeding, and is not true nucleation. In contrast, breeding is the generation of a greater number of crystallization sites than were added as a result of fragmentation of the growing crystals. Diluents (solvents) can induce crystallization in polymers by swelling the glassy phase. Swelling drops the glass transition temperature of the material, increases molecular mobility, and facilitates molecular reorganization. Liquid additives can have the opposite effect to diluents, and in fact in low viscosity systems suppress crystallization via different mechanisms such as increasing viscosity, influencing the hydrogen-bonding and polarity of the materials and inducing coprecipitation of the additive-polymer pair which in general retards crystal

nucleation and influences growth. This effect is not observed in high molecular weight polymers except in cases where large amounts of diluents can reduce growth rates [98].

2.4.3 Thermal and Processing History Effects on Nucleation

Nucleation and crystal growth are dependent on numerous variables including time, temperature, pressure, mechanical action, pretreatments, concentration, and additives. In many cases, the influence of crystallization conditions on the final morphology is seen to be the result of changes in nucleation, rather than in changes in crystal growth. For this reason, this section will discuss and summarize the influence of thermal history and the rate of cooling used before crystallization on the nucleation behavior of polymers [98].

- **Quenching** or fast cooling of the melt to generate a large degree of supercooling before crystallization can result in two extreme cases, i. e. the material can solidify into a glass, or the number of nucleating sites can increase rapidly with an increasing degree of supercooling with a fine-grained crystalline morphology resulting. The nucleating ability of the particles in the melt is thought to increase with increasing supercooling, with the finer texture resulting.

- **Reheating from the glassy state** is another method to generate a high nucleation density as nucleation will be at a maximum near the glass transition temperature (T_g) when a material is quenched to a glass, and then reheated to slightly above T_g. Several explanations exist for this behavior: 1) nucleation may have occurred on cooling without perceptible crystal growth, 2) when the material is supercooled, nearly all types of solid impurities can begin to actively nucleate crystals heterogeneously, and 3) impurities in the glass may have precipitated at a far lower temperature than needed for the material to crystallize, and can nucleate crystal growth.

- **Preheating conditions** such as the time and temperature of preheating above the melting point can have a profound effect on the crystallization

behavior of some polymers as summarized from Binsbergen's review [98]. Figure 2.10 schematically illustrates two types of premelting history.

Case a) illustrates heating a material to above the melt temperature, holding and then subsequently cooling to an isothermal crystallization temperature, or cooling at a rate during crystallization. Frenkel introduced the theory of heterophase fluctuations to explain nucleation under these clusters of molecules at T_1 that are similar to those of the stable phase at T_2. According to this theory, fast cooling to T_2 would produce a set of embryos which represent the clusters already present at T_1. The lifetime of the clusters is long relative to the cool-down period, hence the generation of a stable nucleus. If T_1 is increased, the smaller the number of initial clusters, and the lower the subsequent T_2 required to generate stable nuclei from fluctuations in the clusters. Only for long times at T_2 would a sufficient number of fluctuations occur to form new nuclei if no clusters were present. This results in a correspondence between T_1, the premelting temperature, and the number of nuclei present at T_2, the crystallization temperature. Not all polymers show this dependence of nucleation density on premelting temperature.

Case b) in Figure 2.10 illustrates the situation where recrystallization occurs after incomplete melting of a polymer, such that the nucleation density present is the result of incompletely melted crystalline material. Semicrystalline polymeric materials lack sharp melting points, but instead display a melting range that is a function of crystalline content, molecular-weight distribution, lamellar thickness and lattice perfection. If a material is heated to a temperature T_1 at which the material is not completely melted, it will retain some regions of order. If instead of melting at a higher temperature to remove this residual order, the material is cooled again, the material will start to crystallize at those ordered regions, possibly retaining the features of the original texture as was illustrated by Magill with poly(tetramethyl-p-phenylene siloxane) [105]. In this case also, the number of crystalline nuclei present is a function of T_1, the melt treatment temperature.

- **Orientation** of a polymer melt or solution can also induce crystallization in cross-linked, crystallizable elastomers and in non-crosslinked polymer melts and solutions. Nucleation, in the form of nucleation lines, can be induced via shear or tensile strains at lower levels of supercooling than is typically required.

Nucleation can also be promoted in polymers via irradiation with x-rays or γ-rays, in a few cases by very high electric field strengths, by agitating a crystal suspension, and

a)

● ISOTHERMAL
○ AMBIENT COOLING

b)

T_2 = CRYSTALLIZATION TEMPERATURE
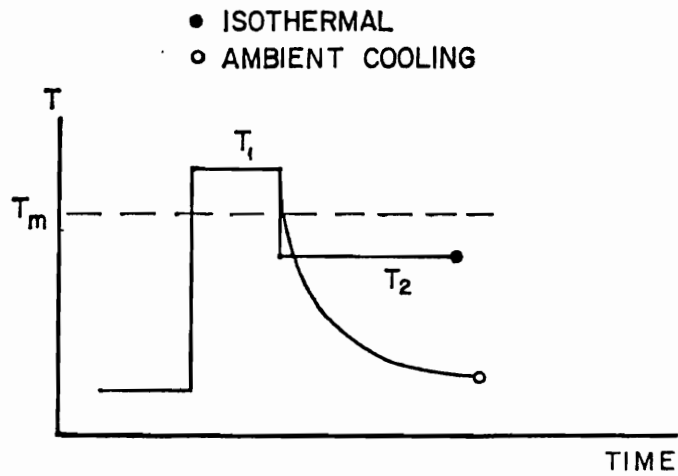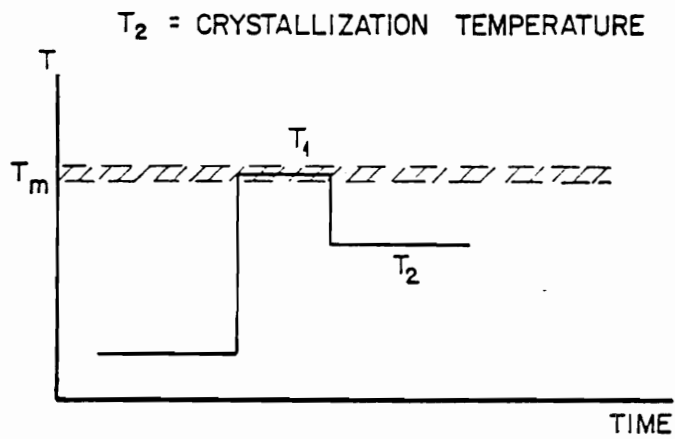
Figure 2.10   Schematic representation of two recrystallization procedures: a) normal crystallization procedure where a substance is heated from below T_m to a temperature T1>Tm for some time, and then cooled to either an isothermal crystallization temperature T2, or at a rate "a" or b) recrystallization after incomplete melting [98].

possibly by ultrasonic irradiation [98]. These cases will not be discussed here however, as they are not the most influential factors affecting crystallization in the two projects discussed in this dissertation. Cooling rate, thermal history, premelting conditions and conditions. He suggested that there are "fluctuations" or "time-dependent orientation effects are the key parameters relevant to examination of the crystallization behavior of ITX and the semicrsytalline adhesives under scrutiny.

2.4.4 Crystal Growth Rate of Chain-Folded Lamellar Spherulites

Even though the influence of crystallization conditions on the final morphology is seen to be more frequently the result of changes in nucleation rather than in changes in crystal growth, crystal growth mechanisms are still important in that they affect the microstructure that will be generated. After a nucleus is formed, a new layer grows upon the surface after secondary nucleation, i. e. nucleation on the surface of the crystalline layer just formed. Studies of the temperature coefficient of the overall crystallization rate, in bulk and from solution, have established that polymer crystallization is a nucleation controlled process, irrespective of the form, structure or chain disposition within the nucleus [96]. This indicates that the spherulitic growth rate, G, can be described by an equation identical in form to that for nucleation discussed earlier. The spherulitic growth rate is denoted in Equation 2.14 as:

$$G = G_0 \exp \left[\left(-E_D / RT \right) - \left(\Delta G^* / RT \right) \right] \qquad (2.14)$$

where ΔG^* is the critical free energy for nucleation, E_D is the energy of transport at the interface as discussed earlier, G_0 is a preexponential factor, R is the universal gas

constant, and T is absolute temperature. The general shape of the growth rate curve modeled by this expression is shown in Figure 2.11 as a function of crystallization temperature. For polymeric systems which have been studied over an extended temperature range, a maximum is observed in the plot of the growth rate versus crystallization temperature. However, in many polymers, the maximum is not experimentally attainable because of the limited regions in which it is possible to measure spherulite growth rates.

2.4.5   Isothermal Crystallization Kinetics

The emphasis of the following portion of the literature review is on the methodology utilized in this dissertation for evaluating polymer isothermal crystallization kinetics, focusing especially on the well known Avrami Equation. After a brief discussion regarding the origin of the methodology and theory, section 2.4.5.2 will discuss the assumptions involved in the process, and the experimental variations that have been observed when this analysis technique was applied to polymer crystallization.

2.4.5.1   The Avrami Method of Analysis

In order to monitor the crystallization of polymers, a relationship for calculating the overall crystallization rate as a function of time from the linear growth rate and the primary nucleation rate for three dimensional spherulitic crystal growth was developed by several researchers including Kolmogoroff (1937), Johnson and Mehl (1939), Avrami (1939, 1940, 1941) and Evans (1945) [100]. The relationship, based on descriptions of the problem of expanding waves created by raindrops on a pond, can be stated as: if
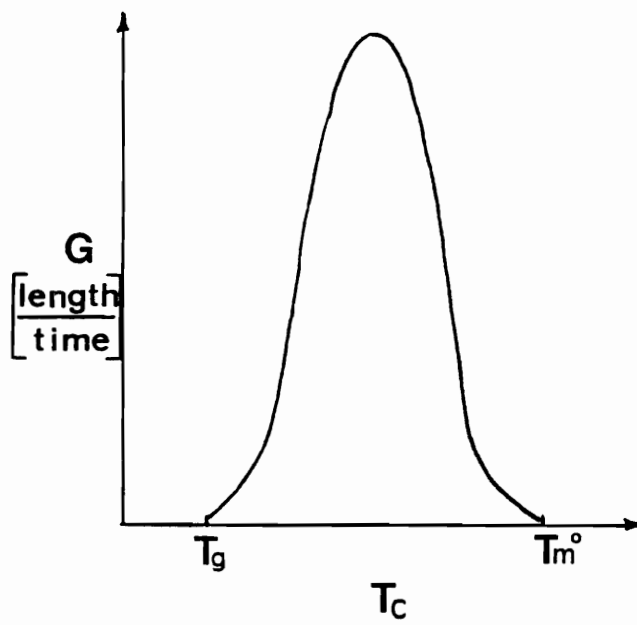
Figure 2.11   Schematic representation of spherulite linear growth rate as a function of crystallization temperature between the glass transition and equilibrium melting temperature.

raindrops fall randomly on a surface of water creating one leading expanding circular wave each, what is the chance that the number of waves, n, which pass over a representative point P up to time t is exactly n? This concept was translated to polymer crystallization by Avrami, by assuming that nucleation occurs according to a certain probability function P(t) as defined in Equation 2.15, and that growth of the nuclei is two-dimensional and linear with time:

$$P_n(t) = \exp^{-E}(E^n/n!) \qquad (2.15)$$

and that E is the expected number of waves or growth fronts [100, 106-108]. Eventually, the growth of a real crystal is assumed to be retarded as it encounters other regions of transformed or crystallized material, and impingement occurs. If the probability that no front will cross a point, i. e. the material will not crystallize (n = 0), is considered then Equation 2.15 becomes [100]:

$$P_0(t) = \exp^{-E} = 1 - X(t) \qquad (2.16)$$

where X(t) is the volume fraction of the material crystallized. If $P_0(t)$ is considered as the volume fraction of amorphous material, 1 - X(t), and E is the volume of crystalline material at a time, V(t), then Equation 2.16 can be written as:

$$\exp^{-V(t)} = 1 - X(t) \qquad (2.17)$$

which leads to:

$$V(t) = \pi N r^2 t^2 \qquad (2.18)$$

from the raindrop analogy to express the transformed fraction as a function of time for the two dimensional case of N nuclei of radius r.

For the case of three-dimensional growth, the volume of "converted" or crystalline material at a time *t* must be evaluated for two cases: first, instantaneous or athermal nucleation, and secondly, thermal or sporadic nucleation in time. Again, the number of nuclei present are denoted as N, with constant linear spherulitic growth rate G, and spherulite radius r. The volume increase in crystallinity for each case is treated below in Equations 2.19 and 2.21 respectively.

Athermal or instantaneous nucleation:

In athermal or instantaneous nucleation, the number of nuclei, N, are considered to be constant with time. In this situation the transformed fraction as a function of time is described as :

$$V(t) = 4/3\, \pi\, r^3\, t^3\, N \qquad\qquad (2.19)$$

or substituting in linear growth rate, G, for r:

$$V(t) = 4/3\, \pi\, G^3\, N\, t^3 \qquad\qquad (2.20)$$

which describes the transformation of amorphous to crystalline material via three-dimensional growth.

Thermal or sporadic nucleation:

In thermal or sporadic nucleation, the number of nuclei, N or sometimes I*, is considered to increase linearly with time, and the volume transformation can be written as [100]:

$$V(t) = \pi \, I^* \, r^3 \, t^4 / 3 \qquad (2.21)$$

or substituting G again for spherulitic radius yields:

$$V(t) = \pi \, N \, G^3 \, t^4 / 3 \qquad (2.22)$$

for three dimensional growth.

A general form of the expression in Equation 2.15 is noted in Equation 2.23, and is commonly called the Avrami equation. The Avrami expression follows the crystallization process as a function of time as:

$$1 - X(t) = \exp[-V(t)] = \exp[-K \, t^n] \qquad (2.23)$$

where K is a bulk conversion rate constant at a temperature containing numerical and growth rate information, e. g. $K = 4 \pi \, N \, G^{n}/3$ with corresponding units of $1/\sec^n$ for three dimensional growth and heterogeneous nucleation. The term n is the Avrami coefficient, which is characteristic of the growth geometry and nucleation mode. Here n = 4 for homogeneous nucleation, and spherical crystal growth, but n = 3 for heterogeneous nucleation and three-dimensional growth [100]. Experimental values for K and n are determined graphically from crystallization data which is explained in greater

detail in Chapter 3. With the final expression noted in Equation 2.23 Avrami has established a method for quantitatively monitoring the transformation from the amorphous to the crystalline state isothermally as a function of time in semicrystalline polymers. Next, some of the limitations to this technique will be reviewed.

2.4.5.2   Assumptions and Variations in the Avrami Analysis Results

Experimental application of the Avrami technique to semicrystalline materials has illustrated that the derivation of the Avrami expression for the overall change in crystallinity contains a number of simplifications which do not necessarily all apply to the crystallization of macromolecules. These complications to the Avrami analysis include the following errors [100].

1) The volume does not stay constant on crystallization as was initially assumed.

2) Under certain circumstances, the linear growth rate is not constant with time.

3) The number of nuclei may not increase continuously, but may reach a limiting level.

4) The crystalline morphology may not conform exactly to a spherical, circular, rod-like growth habit.

5) The crystalline microstructure frequently branches, instead of growing only in one direction.

6) Crystallization can be a two-stage process.

7) Crystals may perfect their organization after the initial crystallization is completed.

The effect of these complications, and others, have been addressed by several researchers since the introduction of the analysis method in 1939. Price discussed the effect of the first complication noted above, the inconstant volume during crystallization, in a 1965 publication [109]. He noted that the Avrami expression was "only a first approximation to the correct relation and that the use of this equation to interpret data and to calculate precise values of K and n^3 can lead to considerable error." [109] Price reported that error of 0.15 to 0.25 in n are easily obtainable if weight fraction data is used in the analysis in place of volume fraction data. Variations of 0.72 for n = 3, and 0.57 for n = 4 were noted. In addition, he noted that only at low levels of conversion, when impingement was negligible could values of n smaller than 3 be interpreted as growth of rods, disks etc.

The complication to the Avrami analysis as a result of non-linear growth rates with time would be reflected in the evaluation of the expected number of crystals present in the specimen [100]. Instead of G being only a function of T, for the case of crystallization under transport control, a decrease in growth rate would lead to a $t^{(1/2)}$ dependency of n, e. g. n = 3/2 for athermal nucleation and three-dimensional growth.

The third limitation to the Avrami analysis is that the number of nuclei is not constant, but instead varies for thermal nucleation. The fourth limitation regarding non-spherical growth habits is addressed by adjustments to the description of the transforming volume to more reasonably reflect the actual shape. Complication number five relates to branching, and again similar adjustments to the volume description are suggested. Branching has been seen to increase the experimentally observed n value.

Complications to the Avrami analysis due to two-stage spherulitic crystallization have been addressed by Price (1965), Hillier (1965) and Hoshino, et al. (1965) [100]. This correction to the analysis includes considering the crystallization process as

incorporating two Avrami-type expressions, the second of which is assumed to have $n = 1$, and considered to add to the level of crystallinity generated in the first expression. The final level of crystallinity for a two-step process is then the sum of the two processes at long times. Standard deviations of approximately 5% have been observed utilizing this technique. The last limitation presented in Wunderlich's review regards crystal perfection occurring after the initial growth front has passed, and is similar to the one just described in that a second expression is incorporated in the analysis, but not of the Avrami type. Instead this type of deviation can frequently be considered utilizing a log time dependence. Both the two-step crystallization process and the crystal perfection allowance to the analysis are corrections to the assumption that growth ceases at impingement.

Other publications also address limits to the Avrami analysis, including work by Grenier and Prud'Homme from 1980 [110]. These authors address errors in the analysis that arise from experimental parameters, particularly the choice of determining "time zero" for the analysis, and overestimation of the ΔH values used in evaluating crystallization kinetics by differential scanning calorimetry. They noted that positive errors in t resulted in a decrease in the calculated n values, while negative errors had the opposite effect. A 5% error in estimating t was judged sufficient to generate a non-integral value of n. Cheng and Wunderlich (1988) suggest several modifications to the Avrami treatment to account for the nucleus volume fraction and mobility reduction effects at the crystal-melt interface inducing non-linear growth rates [111].

Several other references address volume effects on the Avrami analysis as well. Escleine, et al., Billion, et al. and Billion and Haudin each look at different aspects of the problem [112-114]. Escleine, et al. (1984) used an analytical model to determine that for a volume limited by two parallel infinite planes, specimen thickness only becomes

relevant when the thickness is of the order of or smaller than the average spherulite radius [112]. When thickness decreases, crystallization kinetics are seen to slow, and the Avrami exponent also decreases. Billion et al. (1989) also looked at crystallization in a thin film, here by modifying Evan's approach to calculate transformation across the film thickness [113]. Finally, Billion and Haudin (1989) addressed the overall crystallization kinetics of thin films by introducing a factor, f, to correct for the reduction in spherical surface area resulting from truncations [114].

A recent publication (1995) by Mehl and Rebenfeld applied 3-D computer simulation methods to the Avrami analysis of neat and fiber filled PPS specimens noted variations in the Avrami data in the presence of fibers [115]. Experimental values were measured for the growth rate, bulk nucleation density, volume fraction of fibers and fiber diameter. These variables were input into the program, and then fiber surface nucleation was allowed to vary in the simulation. Experimental crystallization data were then compared to the simulation results, and a best fit chosen for the nucleation mode which represented the experimental results. The Avrami rate constant, K, was seen to be higher for fiber-reinforced systems than for neat systems. The Avrami exponent for the reinforced systems was seen to be lower for all cases, presumably due to spherulitic growth being truncated by the constraining network of fibers.

2.4.5.3 Summary

Overall, though the Avrami crystallization kinetics analysis method was not originally designated for the evaluation of polymers, numerous research projects have successfully incorporated this analysis method into their polymer studies. Corrections to the theory, and limitations to its application have restricted the precision of Avrami data,

but this trend appears to be changing as refinements to the expressions are published in the literature. Recent work employing computer simulations of the crystallization process will also help clarify deviations in experimental data from the expected results.

CHAPTER 3

MATERIALS and EXPERIMENTAL METHODS

3.1   Material Description

The ITX evaluated in this research was supplied by ICI Fiberite Advanced Composites as a semicrystalline, white powder. The chemical composition of ITX is not available for publication at this time, however, the material is a high-performance semicrystalline polymer somewhat similar in character to PEEK (poly (ether ether ketone)) as is shown in Figure 3.1. ITX was designed as an intermediate temperature semicrystalline composite matrix material for use in higher temperature applications than could be satisfied by a PEEK matrix. The material displays a glass transition temperature (T_g) at approximately 180 °C, and a melting point (T_m) about 360 °C in contrast to PEEK whose T_g and T_m are circa 140 and 340 °C respectively [12, 28, 29]. The higher T_g typical of ITX expands the potential application temperature window upwards, making it a candidate for such applications as the High

- **"Victrex" PEEK (semi-crystalline)**
  $T_g = 143$, $T_m = 343$ °C
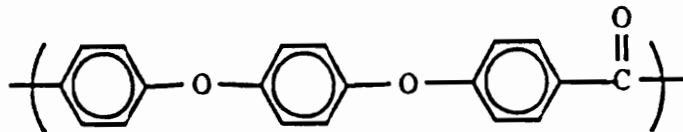
- **ITX $T_g = 180$, $T_m = 360$ °C**

Figure 3.1   Microstructural and thermal characteristics of PEEK and, thermal characteristics of ITX.

Speed Civil Transport (HSCT) composite commercial aircraft. ICI supplied the typical processing profile for consolidation of a composite composed of ITX resin, and this profile is shown in Figure 3.2.

An approximate density value of ~1.3 g/cc was supplied by ICI for ITX "polymer" [116]. This value, which is slightly greater than that of PEEK, was later confirmed experimentally by density gradient column. The densities of the as received semicrystalline powder and an amorphous melt-pressed film were determined to be 1.391 and 1.329 g/cc respectively, which is in reasonable agreement with the ICI value just noted. In contrast, the value for the amorphous density of PEEK has been measured as 1.263-1.264 g/cc [28, 29].

3.2   Experimental Apparatus Utilized

3.2.1 Thermal Characterization

3.2.1.1   Differential Scanning Calorimetry (DSC)

The initial thermal characterization of ITX was completed using a Seiko 5040 Thermal Analysis System with an attached DSC 210 Differential Scanning Calorimeter (DSC). However, due to the instability of the heating system design in that instrument when operated against liquid nitrogen cooling as required for rapid cooling, only the initial screening work for ITX was finished with that system. Instead, the majority of the thermal characterization work was completed using either a Perkin-Elmer DSC-4 or DSC-7 with its appropriate analysis computer. Calibration for temperature and heat flow
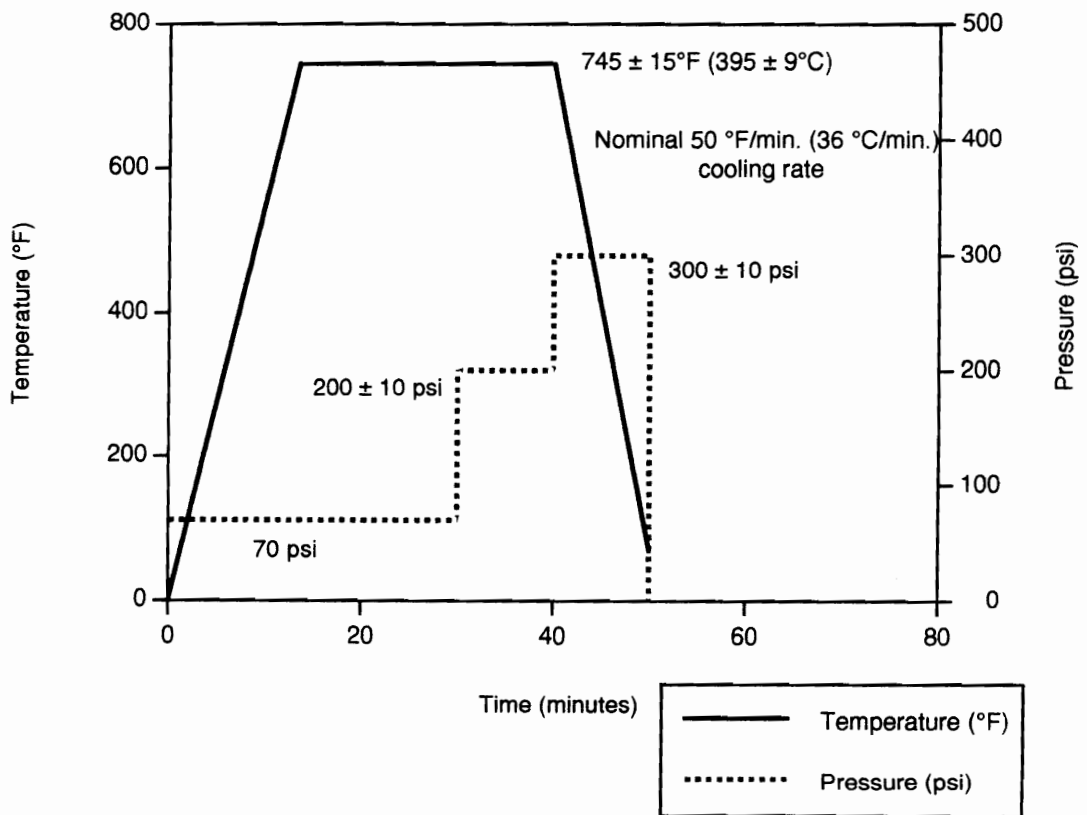
Figure 3.2 ICI recommended typical experimental processing profile for consolidation of ITX composites [116].

was accomplished with either indium or indium and zinc respectively. Greater experimental detail is described for each type of experiment in the following sections.

3.2.1.1.1 Dynamic Experiments

As was mentioned previously, the initial thermal stability work on ITX was completed using the Seiko DSC. Most of this work was designed to determine if ITX was in fact melt sensitive, and therefore was composed of a series of dynamic experiments that involved heating specimens to either: 1) successively higher temperatures, or 2) holding ITX in the melt for increasingly longer times at a specific temperature before crystallizing the material. The crystallization exotherms were then inspected for changes in shape, and integrated to evaluate variations in the heat of crystallization observed. The onset of crystallization as determined by software extrapolation and crystallization peak temperatures, in addition to the corresponding melt information, were all monitored as well. Typical specimen weights ranged from 5-12 mg. All dynamic melting endotherms were collected at a scan rate of 10 °C/min., and the cooling data were taken at 5 °C/min. A nitrogen purge of 50 ml/min. was typically used for these DSC experiments.

In addition to the screening work, dynamic scan experiments were also performed at the latter stages of this study to mimic the processing conditions (melt @ 395 ± 9 °C/hold ~20 min.) recommended for composite consolidation. A systematic crystallization study was completed using the Perkin-Elmer DSC-7 system at scan rates of 36 °C/min. to establish the behavior of ITX as a function of time and temperature [f(t, T_f)] in the melt. The DSC-7 was able to reproducibly melt the specimens at 3 degree intervals against an ice bath, and provide controlled cooling over the entire temperature

range of interest unlike the Seiko system. Powder specimens were subjected to a thermal history designed to replicate that used in the actual ICI-recommended ITX-carbon fiber composite preparation profile as follows:

1) heat @ 36 °C/min. to a Tf between 380-410 °C,
2) hold for between 1-30 minutes @ Tf, and
3) cool @ 36°C/min. to 100 °C,

while following the extent of crystallinity generated via the heat of crystallization, ΔH_C. Seventy-seven distinctly different specimens were evaluated, and data collected for each of four variables studied: crystallization onset and peak temperatures, crystallization peak breadth and heat of crystallization under a nitrogen purge of ~ 20 ml/min. A much smaller series of experiments were completed with an air purge at the same rate. All the data reported are from separate specimens.

The reproducibility of the temperature and heat of crystallization values noted was evaluated by running replicate specimens under the same conditions, and by performing multiple analyses on the same file. Typical variations in the temperature values were ±0.01 °C and ±0.20 °C when the files were either reanalyzed or the experiments repeated, respectively. The heat of crystallization values varied by ±0.2 to ±0.5 J/g when the data were evaluated repeatedly, or a new specimen tested as described above.

3.2.1.1.2 Isothermal Experiments

The isothermal quiescent crystallization behavior of ITX was characterized using the Perkin-Elmer DSC-4 attached to a TADS data analysis computer. The switch to the

DSC-4 occurred after the Seiko system demonstrated that it was unable to reproducibly achieve the programmed melt temperatures requested, leading to inconsistent kinetics data. [This is not entirely negative, in fact, resolving this inconsistency played a key role in identifying the melt sensitive nature of ITX.] Again, specimen weights ranged from 5-12 mg for these experiments. All specimens were preheated to an initial melt treatment temperature, (T_f), at the maximum machine rate, nominally 200 °C/min. [the machine heating rate slows as set-point is reached] that was chosen to bound the processing temperature window for this polymer. A hold time of 15 minutes was chosen to mimic a typical time that this thermoplastic might see at the maximum temperature during composite processing. At the end of the hold period, the samples were quenched to T_c, the crystallization temperature range accessible by DSC, by calling for the fastest DSC cooling rate, 320°C/min. to the crystallization temperature. Calling for a cooling rate of 320 °C/min. actually turns off all heating until set-point is approached, giving a faster cooling rate than would be possible if heating to the system is simply reduced. A nitrogen purge rate of 25 ml/min. was used for all Perkin-Elmer DSC experiments. The Perkin-Elmer systems were calibrated using indium and zinc, or indium alone for the DSC-7 and DSC-4 models respectively, at either 10 or 20 °C/min. heating rates.

The series of analyses described above were carried out for two melt treatment temperature extremes chosen to simulate the ITX composite processing window extremes, 386 and 404 °C. Lower (373 °C) temperature data sets were also collected to verify these results. The data were analyzed, and the results for the bulk conversion rate constant, ln K, as a function of crystallization temperature and thermal history were evaluated. Additional details on the evaluation methods used to examine this data are described in Section 3.3.1.

3.2.1.2 Thermogravimetric Analysis (TGA)

Thermal stability results for ITX were determined via the Seiko thermal analysis system mentioned earlier using a Thermogravimetric-Differential Thermal Analyzer (TG-DTA) 200 combined module. TG-DTA at a heating rate of 2 °C/min. in both air and nitrogen atmospheres with a purge rate of 50 ml/min. The data were analyzed using the extrapolated onset of degradation temperature calculated with the Seiko software system.

3.2.2 Polarized Optical Microscopy (POM)

The morphology and crystallization behavior of ITX were studied using polarized optical microscopy (POM). A Linkam Scientific Instruments Ltd. TH600 hot stage was connected to a Zeiss Axioskop transmission polarizing optical microscope for these studies. Specimens were prepared by scattering a thin layer of ITX powder on a glass slide, and then covering the powder with a second slide. The samples were heated at 50 °C/min., under a 20 cc/min. nitrogen purge, to melt treatment temperatures within the range mentioned earlier, 386-404 °C. Several studies were also completed at a lower treatment temperature of 373 °C as well. The samples were held for 15 minutes at T_f, and then quench cooled to the selected crystallization temperature. Crystallization was observed either as a function of time or temperature. Optical micrographs were taken using a 35 mm Zeiss camera.

The magnifications and dimensions noted on the micrographs were calibrated by photographing a 0.001" calibration grid at the same magnification used for the data

collection. More detail on this procedure is provided in section 3.3.2 where the determination of the linear spherulitic growth rate is described.

3.2.3 Wide Angle X-Ray Scattering (WAXS)

The absolute crystalline content of ITX powder was determined via wide angle x-ray diffraction (WAXD) using the method of Hermans and Weidinger for determining percent crystallinity in a semicrystalline material [117-123]. The WAXD data were obtained using a Nicolet/Seimens Model STOE/V2000 Transmission mode wide angle x-ray diffractometer equipped with a STOE Bragg-Brentano type goniometer operating at 40 kV and 30 mA. Copper (Cu-Kα/1.54 Å) x-rays were passed through a graphite monochrometer before final collimination. Data were collected at 0.05°/step increments, holding for 10 seconds/step. The goniometer was stepped through the angles of 5 and 40 ° for each experiment.

Specimens were prepared for WAXD analysis from amorphous films of ITX. To prepare the films, ITX powder was melted in the press at ~ 404°C and 50 psi for 15 minutes and then quenched into an ice bath. Disks of the transparent film were cut with a paper punch, and then thermally treated in the DSC-7 to generate incrementally increasing levels of crystallinity. The DSC was held isothermally at 300 °C, and the specimens were placed into the oven chambers for various times including 1, 5, 10, 15, 30, 60, 90, 120, 1800 and 3600 seconds. The specimens were then tested as described previously.

Data collection and the initial analysis were performed using the Seimens Polycrystalline Software Package. After smoothing using the Seimens routines, the data were analyzed using two different methods. First, the Seimens integration package was

used to integrate and manipulate the data to ratio peak areas and approximate the crystalline fraction as a function of the total peak area. No corrections or normalization routines were applied to the data. The second analysis method utilized was more rigorous. The data were transferred from the Seimens system, and integrated using the method of Hermans and Weidinger for determining percent crystallinity. Corrections were made for beam intensity, optical density, and all data were normalized following the procedures summarized by Alexander [124]. More detail on the procedures utilized can be found in section 3.3.4.

3.3   Data Collection and Analysis Methods Utilized

3.3.1   Avrami Analysis

3.3.1.1   DSC Data Collection

The isothermal quiescent crystallization behavior of ITX was characterized using the Perkin-Elmer DSC-4 or DSC-7 system, and the well known Avrami isothermal crystallization kinetics analysis method [106-108]. The instrument changeover occurred due to the failure, and replacement of the DSC-4 with a new DSC-7 during the course of the study. The Avrami analysis follows the normalized crystalline content within a material, collected at a fixed temperature, as a function of time. For the majority of this work, the data collected were (x, y) pairs consisting of the millivolt (mv) signal for the heat flow within the system, and the time (t) respectively.

The DSC data were collected in this atypical fashion for two reasons: 1) instrumental programming restrictions and 2) the inherent rapid crystallization nature of

ITX. Specimens were heated to the melt treatment temperature selected, held for 15 minutes, and then quench cooled to the crystallization temperature. Quench cooling, cooling with no applied control heating is possible in the Isothermal Program mode, unlike the Standard Data Collection program where the instrument attempts to control cool even when the maximum cooling rate is selected. The quench cooling option was necessary as ITX crystallizes rapidly, and the start of the crystallization data were lost in the typical "start-up" hook for the vast majority of the crystallization temperatures selected, leaving only a very narrow crystallization window accessible for study. By utilizing the Isothermal Data Collection Program in this manner, a wider range of data was collected covering the crystallization behavior of ITX.

As was just noted, using the DSC-4 in the Isothermal Data Collection Program expanded the range of data available for analysis, but it also complicated the overall analysis process since the Perkin-Elmer "Partial Areas Program" was designed to only analyze data collected in the Standard Program, and the data files were inaccessible for transfer to another computer for manual integration as well due to a software restriction. In order to overcome these restrictions, the data were collected in the Isothermal Data Collection Program Mode as noted, but the actual computer file was never accessed. Instead, as soon as the DSC-4 entered the isothermal data collection mode, the mv and minute values displayed on the screen were manually copied into a data book throughout the course of the crystallization experiment. This was possible as the interval between data pairs collected is a function of the time range selected for the entire experiment. By selecting a final hold time of 30 minutes, the DSC-4 divided the set number of data pairs by the selected time to default to a six-second regular interval between data pairs. With practice, it was feasible to copy the data pairs real-time into a

data book for collection, and then integration in a spreadsheet as described in the next section 3.3.1.2.

The majority of the Avrami isothermal kinetics data for this study were collected in the "paper and pencil" manner just described. After the DSC-4 was replaced by the DSC-7 however, it was possible to convert the data collected over the same type of temperature profile into an ASCII data file that could be accessed by Excel$^{®}$. This considerably sped up the data collection for the crystallization studies from that point on.

3.3.1.2   Data Integration Method

After collection, the DSC data were transferred to a Mac IIci for numerical integration using Simpson's Rule since the DSC-4 TADS software was incapable of evaluating data collected in the isothermal program mode as explained earlier. The formula for Simpson's Rule is noted in Equation 3.1 as well as its restrictions [125].

$$\int_a^b f(x)\,dx \approx \frac{b-a}{3n}\left[\, f(x_0) + 4\,f(x_1) + 2\,f(x_2) + 4\,f(x_3)\,\ldots \right.$$
$$\left. + 2\,f(x_{n-2}) + 4\,f(x_{n-1}) + f(x_n)\,\right] \qquad \text{Equation 3.1}$$

where f is a continuous function on [a, b], n is an even integer, and the
partitions are regular [125].

Partial integrals were calculated and normalized to the total area under the crystallization peak versus time using a spreadsheet and Excel$^{®}$ version 3.0 or 4.0 for Macintosh. The data was entered into Excel as (x, y) pairs, and then the two endpoints chosen for integration by inspection. The data were then shifted along the y-axis to zero by subtracting a line through the minim, i. e. subtracting a linear baseline. From the partial area data, the extent of conversion as a function of time was then

calculated as shown graphically in Figure 3.3. An example set of data analyzed using this procedure is shown in Figure 3.4, including the Avrami analysis, which was completed in Cricket Graph version 1.3.2 or 1.5.2. The extent of conversion or crystallization data (weight fraction amorphous material as a function of time) were then analyzed using the standard linear form of the Avrami expression:

$$\ln\left[-\ln\left(1-X_C(t)\right)\right] = \ln K + n \ln t \qquad (3.2)$$

where: $X_C(t)$ or X = the normalized crystalline fraction as $f(t)$
K = the bulk crystallization rate constant,
n = the Avrami dimensionality exponent, and
t = time.

Using the expression in this form (Equation 3.2) allows graphical determination of the ln K (intercept) and n (slope) variables as shown in Figure 3.5, with the bottom graph in Figure 3.4 serving as an actual example data set. The bulk crystallization constant, K, determined in this manner contains information on the temperature dependent nucleation density (N) and the linear growth rate (G) for the material. The Avrami exponent, n, often carries information on the dimensionality of the crystal growth under those conditions. More discussion on K can be found in section 3.3.3 where the procedure used to estimate the nucleation density for ITX is described.

3.3.1.3   Effect of Integration Method on Reproducibility

As described in the previous section, 3.3.1.2, the integration method for the raw crystallization data involved inspecting the crystallization peak to determine if the entire crystallization was "captured", choosing the start and stop points for the integration

$$X_C^{(t)} = \frac{\int_o^t \left(\frac{dH}{dt}\right) dt}{\int_o^\infty \left(\frac{dH}{dt}\right) dt}$$

Figure 3.3   Schematic illustration of an ideal crystallization exotherm showing the method utilized to numerically integrate the DSC data and calculate the normalized crystalline content [126].

	A	B	C	D	E	F	G	H	I	J	K	L	M
1	Raw Time (min.)	Raw mv signal	Time (min.)	mv signal	SUM(all terms)	Partial Sums	Sum (%)	Time (sec.)	ln(t)	ln(-ln(1-X(t))		Crystallization @ 280 °C (404 °C melt/ 15 min. hold)	
2	15.66	5.37	0.00	-9.98									
3	15.72	14.00	0.06	-1.35									
4	15.78	15.24	0.12	-0.11									
5	15.84	15.35	0.18	0.00	0.00000	0.00000	0.00	0					
6	15.90	15.29	0.24	-0.06	-0.00002	-0.00002	0.12	4					
7	15.96	15.13	0.30	-0.22	-0.00004	-0.00006	0.33	7					
8	16.02	14.92	0.36	-0.43	-0.00014	-0.00020	1.16	11					
9	16.08	14.66	0.42	-0.69	-0.00011	-0.00031	1.83	14					
10	16.14	14.36	0.48	-0.99	-0.00033	-0.00064	3.74	18					
11	16.20	14.02	0.54	-1.33	-0.00022	-0.00087	5.03	22					
12	16.26	13.65	0.60	-1.70	-0.00057	-0.00143	8.31	25	3.23	-2.44			
13	16.32	13.25	0.66	-2.10	-0.00035	-0.00178	10.34	29	3.36	-2.21			
14	16.38	12.85	0.72	-2.50	-0.00083	-0.00262	15.17	32	3.48	-1.80		ITX: Extent of Crystallization vs Time (Tx = 280°C)	
15	16.44	12.46	0.78	-2.89	-0.00048	-0.00310	17.97	36	3.58	-1.62			
16	16.50	12.09	0.84	-3.26	-0.00109	-0.00418	24.27	40	3.68	-1.28			
17	16.56	11.77	0.90	-3.58	-0.00060	-0.00478	27.73	43	3.77	-1.12			
18	16.62	11.50	0.96	-3.85	-0.00128	-0.00606	35.17	47	3.85	-0.84			
19	16.68	11.31	1.02	-4.04	-0.00067	-0.00674	39.08	50	3.92	-0.70			
20	16.74	11.21	1.08	-4.14	-0.00138	-0.00812	47.08	54	3.99	-0.45			
21	16.80	11.19	1.14	-4.16	-0.00069	-0.00881	51.10	58	4.05	-0.33			
22	16.86	11.26	1.20	-4.09	-0.00136	-0.01017	59.01	61	4.11	-0.11			
23	16.92	11.42	1.26	-3.93	-0.00065	-0.01083	62.80	65	4.17	-0.01			
24	16.98	11.64	1.32	-3.71	-0.00124	-0.01207	69.98	68	4.23	0.18			
25	17.04	11.93	1.38	-3.42	-0.00057	-0.01264	73.28	72	4.28	0.28			
26	17.10	12.26	1.44	-3.09	-0.00103	-0.01367	79.25	76	4.33	0.45			
27	17.16	12.61	1.50	-2.74	-0.00046	-0.01412	81.90	79	4.37	0.54			
28	17.22	12.96	1.56	-2.39	-0.00080	-0.01492	86.52	83	4.42	0.70			
29	17.28	13.31	1.62	-2.04	-0.00034	-0.01526	88.49	86	4.46	0.77			
30	17.34	13.65	1.68	-1.70	-0.00057	-0.01583	91.78	90	4.50	0.92		ITX: Avrami Crystallization Kinetics (Tx = 280 °C)	
31	17.40	13.95	1.74	-1.40	-0.00023	-0.01606	93.13	94	4.54	0.99			
32	17.46	14.23	1.80	-1.12	-0.00037	-0.01643	95.30	97	4.58	1.12			
33	17.52	14.46	1.86	-0.89	-0.00015	-0.01658	96.16	101	4.61	1.18			
34	17.58	14.65	1.92	-0.70	-0.00023	-0.01681	97.51	104	4.65	1.31			
35	17.64	14.82	1.98	-0.53	-0.00009	-0.01690	98.02	108	4.68	1.37			
36	17.70	14.95	2.04	-0.40	-0.00013	-0.01704	98.80	112	4.71	1.49			
37	17.76	15.06	2.10	-0.29	-0.00005	-0.01708	99.08	115	4.75	1.54			
38	17.82	15.14	2.16	-0.21	-0.00007	-0.01715	99.48	119	4.78	1.66			
39	17.88	15.20	2.22	-0.15	-0.00002	-0.01718	99.63	122	4.81	1.72			
40	17.94	15.24	2.28	-0.11	-0.00004	-0.01722	99.84	126	4.84	1.86			
41	18.00	15.28	2.34	-0.07	-0.00001	-0.01723	99.91	130	4.86	1.94			
42	18.06	15.31	2.40	-0.04	-0.00001	-0.01724	99.99	133	4.89	2.18			
43	18.12	15.33	2.46	-0.02	0.00000	-0.01724	100.00	137					
44	18.18	15.35	2.52	0.00	0.00000	-0.01724	100.00	140					
45	18.24	15.36	2.58	0.01	0.00000	-0.01724	100.00	144			Avrami		
46	18.30	15.38	2.64	0.03							Exponents:	* n = 2.7142	
47	18.36	15.39	2.70	0.04								* ln K = -11.300	
48	18.42	15.40	2.76	0.05									
49	18.48	15.41	2.82	0.06							Filename:	Kinetics (280C).1	
50	18.54	15.41	2.88	0.06							Data Source:	Perkin-Elmer II032.IS	
51	18.60	15.42	2.94	0.07								27-Jan-93	
52	18.66	15.41	3.00	0.06									
53	18.72	15.42	3.06	0.07									
54	18.78	15.43	3.12	0.08									
55	18.84	15.44	3.18	0.09									

Figure 3.4 Example data set illustrating the analysis procedure utilized for the integration and Avrami analysis of ITX.

Figure 3.5   Schematic illustration of the Avrami isothermal crystallization procedure utilized to calculate n and ln K from the DSC data.

and finally choosing a baseline and subtracting that value from all the data before the actual numerical integration takes place. The Avrami analysis results are therefore sensitive to each of those steps in the procedure, and the effect each would have on the calculated values of n and K were also examined.

3.3.1.3.1 *Crystallization Peak Shape Variation Effects*

Due to standard DSC instrument limitations, very fast (lower T_c) and very slow (higher T_c) crystallization data are experimentally inaccessible. That is, very rapid crystallization occurs at the lower temperature limit due to the high nucleation densities encountered, and the crystallization data are lost in the initial quench phase machine drift as seen in the example in Figure 3.6a. Higher temperature crystallization is slower, but still problematic in that data collection is limited by the longer residence times needed at higher temperatures. Two factors are important in this situation. First, long times at higher temperatures may induce possible chemical reactions (crosslinking) or degradation in the polymer which will affect the kinetics data collected. Secondly, longer data collection times also spread out the data over a broader time frame, decreasing the signal to noise ratio, and masking some of the signal in baseline drift at the beginning and end of the crystallization peak (Figure 3.6b). The peak shapes shown in these two figures illustrate why isothermal crystallization could only be monitored by DSC for experiments between 270-290 °C and 304-319 °C for the high and low melt treatment temperatures respectively. All data collected were from curves intermediate to the extreme cases just described.

In addition to capturing the entire crystallization process at the beginning of the crystallization peak, it was also noted that variations in the end of crystallization peak
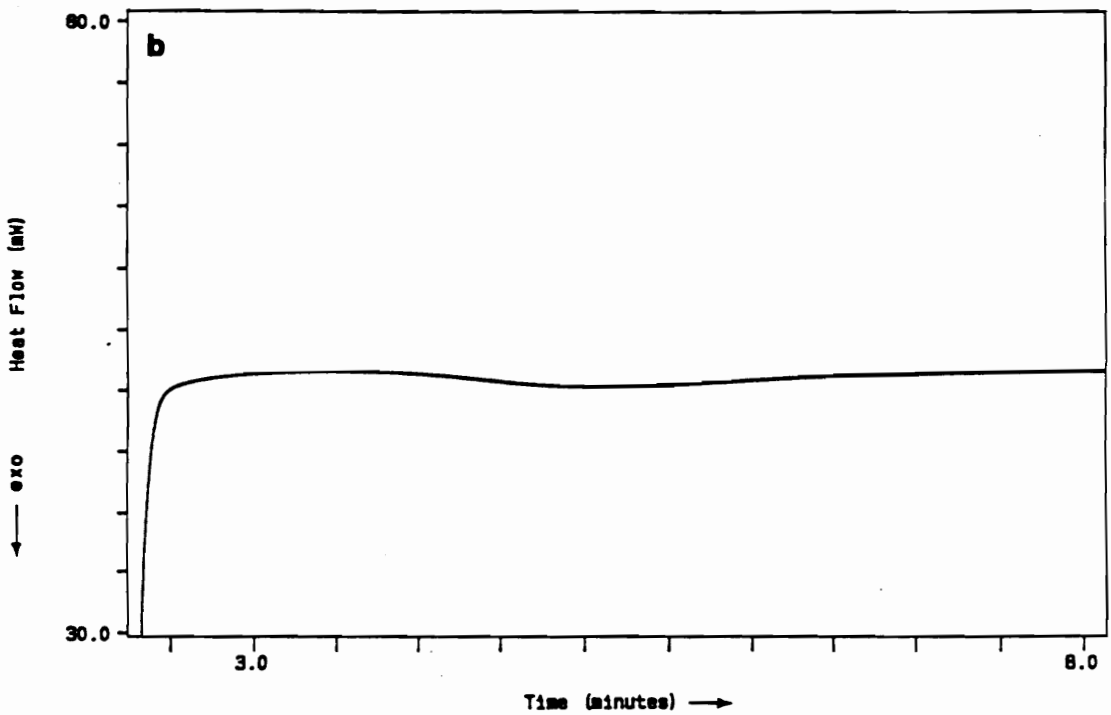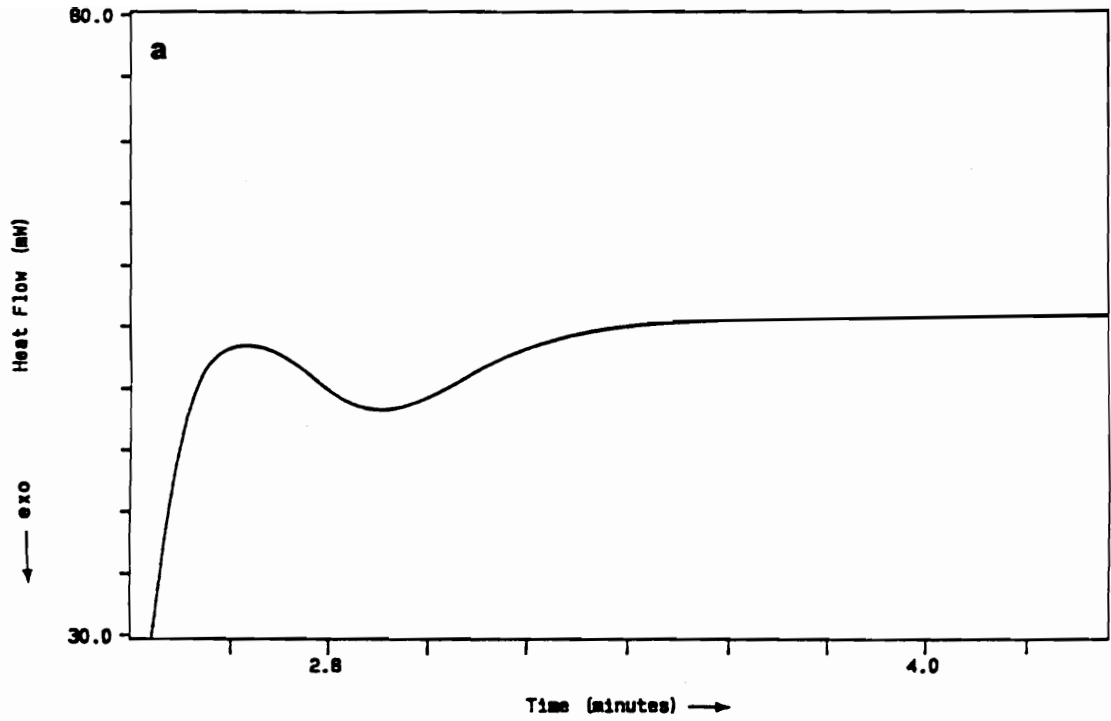
Figure 3.6a & b   Examples of instrumental isothermal data collection limitations for the DSC: a) low (280°C) temperature very fast crystallization data and b) higher (312°C) temperature slow crystallization example.

"tail" also affected the numerical integration result determined, and ultimately the n and K values evaluated for a data set. As the experimentally observed crystallization temperature increases, a typical DSC broadens, and flattens out with the longer time "tail" region of the peak increasing. Several data sets were evaluated by deliberately taking the end integration limit at several places. The results for these reproducibility analyses are found in Chapter 4.

3.3.1.3.2   Baseline Selection Effects

Variations in the DSC crystallization peak shape also affect the reproducibility of the Avrami analysis in one additional manner, i. e. by influencing the validity of the baseline correction applied when the data is integrated. When the crystallization data was collected on either the DSC-4 or DSC-7 the automatic baseline correction was applied to correct for any systematic system drift. This usually resulted in DSC data that was approximately horizontal, beginning and ending on a straight line. The other typical type of data that was observed during this study were data sets where the baseline drifted or curved slightly upwards or downwards during collection. Data such as this is generated when the baseline correction is not perfect, i. e. when the signal begins to drift as the ice in the icebath melts. This effect can be minimized by running new baselines frequently, and maintaining a constant supply of ice in the bath, but it was not possible to completely eliminate this curvature in all the scans.

Since it was not practical to completely eliminate the curvature in the baseline of the crystallization data collected for ITX, an additional analysis was performed to determine how variations in the baseline affected the final Avrami results. This was accomplished by subtracting two different types of baselines from the peaks, a linear and

a third-order polynomial curve as follows. The data points in the peak "onset" and "end" regions were defined as the region where the curve first deviates from the baseline. After inspecting the curve and designating these baseline points, a tangent was drawn to the curve and then the points were transferred to a Cricket Graph file for curve fitting. The "best" baseline selection was accomplished by fitting several curves to the points adjacent to the onset and end. If the entire beginning and end regions looked "reasonable", that is the baseline was a replicate of the experimental data points, it was used for the next step in the integration procedure, subtraction from the file to shift the curve to y = zero.

After determining the equation for the baseline curve, the value for the baseline at each x was subtracted from each experimental point. This subtraction "shifted" the data, such that the area under the curve between the experimental curve and the x-axis could be integrated. Simpson's Rule was used for the integration as described earlier, and then the Avrami analysis completed. The actual baseline comparison is accomplished by completing this entire process for the two baseline types which are shown in Figure 3.7. Avrami exponents, n and K, were calculated as a function of integration start and stop limits and as a function of baseline correction applied. These results will be discussed in Chapter 4.

3.3.2 Linear Growth Rate (G) Determination

The linear growth rate for ITX spherulites as a function of temperature was determined using Polarized Optical Microscopy (POM) for a series of crystallization temperatures. POM specimens were prepared as described earlier, with the exception

a

$y = 0.39394 - 0.65657x \quad R^2 = 1.000$
(0.60 to 2.58 min.)

b

$y = 3.7262 - 8.7866x + 4.7999x^2 - 0.84335x^3 \quad R^2 = 1.000$

▲ Baseline mv signal
• DSC mv signal
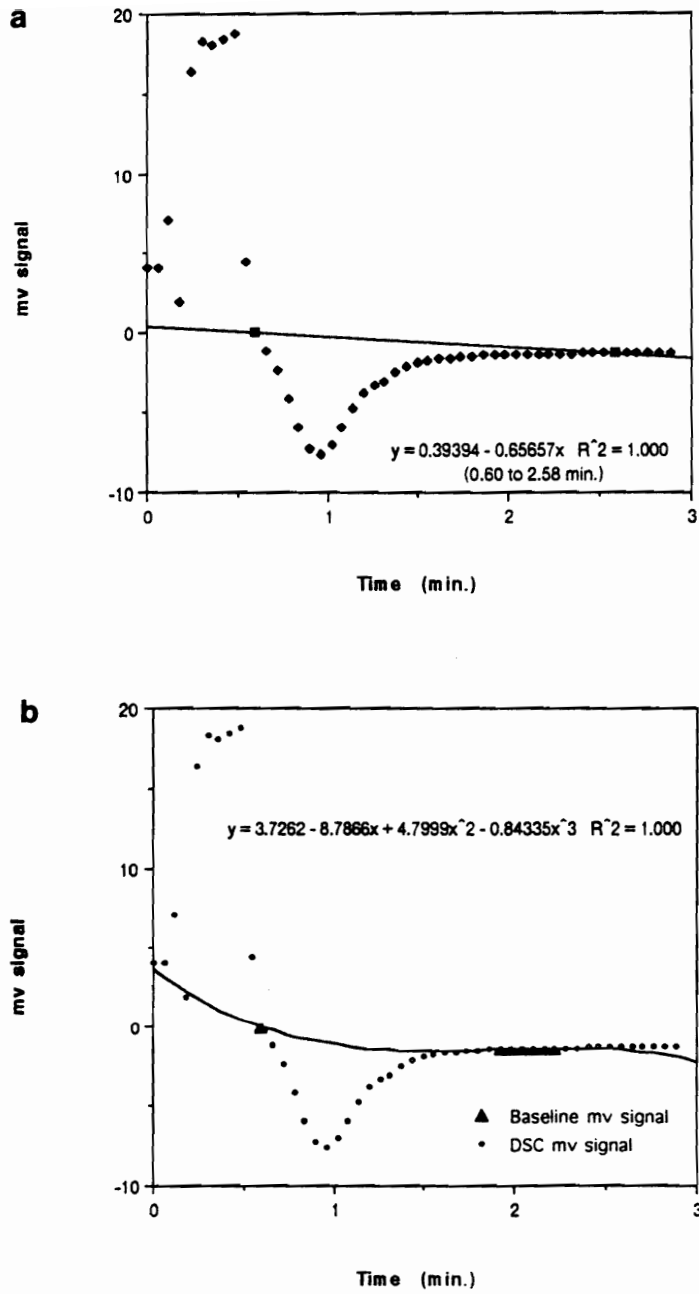
Figure 3.7   DSC crystallization peak illustrating the two baseline choices used, a) linear and b) 3° polynomial fit.

that each specimen was melted twice. The powder specimens were heated at 50 °C/min. to 360 °C, and immediately cooled back to room temperature at the same rate. This "first melt" served two purposes. It simulated a first melt that a powder specimen might see during a composite thermal prepregging process, and it gave all specimens a similar initial thermal history. After the specimens returned to room temperature, they were reheated to the high melt treatment temperature used in this study, 404°C. [The lower melt treatment temperature (373 °C) noted in the morphological studies section was not used in this series of studies; the nucleation density remaining after a lower temperature melt treatment was too high to follow nucleation and growth over a sufficiently long time frame for the evaluation of the growth rate.] Each specimen was held for 15 minutes at the treatment temperature, and then quench cooled (~90 °C/min.) to an isothermal crystallization temperature. Crystallization was monitored through crossed polarizers to follow the nucleation and subsequent growth of the ITX spherulites. ITX spherulitic growth was photographed using a 35 mm camera, and the photomicrographs were used for the growth rate determinations.

The data were analyzed graphically to determine the growth rate in μm/sec for each isothermal temperature evaluated. A Mitutoya micrometer was used to measure either the radius or the diameter of a set of developing spherulites for each crystallization temperature photograph. The measured spherulite dimensions were averaged at each time. The "inch" measurements from the photographs were converted to microns using a calibration factor. The calibration factor was derived from a calibration grid that was photographed and analyzed in the same manner. An average of ten measurements was taken to determine the conversion factor. The time values for the corresponding experimental radii were normalized to the start time, i. e. the time when the controller

reached the programmed isothermal temperature. A example data set illustrating the steps involved in these calculations is shown in Table 3.1.

After collection and tabulation, the growth rate data were plotted as the average spherulite radius versus normalized time. The slope of the line fit to the data in Cricket Graph® gives the linear growth rate for each isothermal crystallization temperature as shown in Figure 3.8.

Growth rate determinations were not possible for ITX melted at the lower melt treatment temperatures using this procedure. The number of nucleating sites at the start of crystallization was so high that it was not possible to visually follow the growth of any individual spherulites following these methods. In addition, crystallization occurred almost instantaneously for the lower melt temperature treatment specimens, leaving insufficient time for a series of photographs.

3.3.3 Nucleation Density (N) Estimation

Once the linear growth rate is known as a function of temperature, and if three-dimensional growth is assumed, it is possible to quantitatively estimate the nucleation density of the polymer and determine if melt treatment is affecting the number of initial nucleating sites. This estimation is possible using the Avrami expression noted earlier. For the case of heterogeneous nucleation with three dimensional-growth, the nucleation density, N, is related to G and K as expressed in Equation 3.3:

$$\ln K = \ln N + 3 \ln G + \ln \left(\frac{4\pi}{3} \right) \qquad (3.3)$$

where G is obtained experimentally for each crystallization temperature of interest as described in the previous section 3.3.2. The ln K values needed for the estimation of the

Table 3.1 Example data set illustrating the procedure utilized in determining the linear growth rate for ITX spherulites.

Temperature (°C)	Raw Time (min:sec)	X1 (in.)	X2 (in.)	X3 (in.)	X4 (in.)	X5 (in.)
282 °C	2:42	0.255	0.251	0.283	0.302	0.285
	2:55	0.305	0.292	0.337	0.338	0.337
	3:16	0.376	0.330	0.391	0.403	0.401
	3:32	0.410	0.408	0.456	0.482	0.462
	3:44	0.456	0.425	0.491	0.504	0.504
	3:54	0.494	0.459	0.529	0.561	0.533
	4:13	0.547	0.519	0.613	0.628	0.616
	4:22	0.567	0.555	0.661	0.665	0.665
	4:47	0.660	0.645	0.719	0.778	0.766
	5:19	0.786	0.819	0.921	0.896	0.924
	5:52	0.908	0.966	1.061	1.024	
	6:32				1.210	

Normalized Time (sec)	R1 (μm)	R2 (μm)	R3 (μm)	R3 (μm)	R3 (μm)	Average Spherulite Radius (um)
42	4.782	4.707	5.308	5.664	5.345	5.161
55	5.720	5.476	6.320	6.339	6.320	6.035
76	7.052	6.189	7.333	7.558	7.521	7.131
92	7.689	7.652	8.552	9.040	8.665	8.320
104	8.552	7.971	9.209	9.452	9.452	8.927
114	9.265	8.608	9.921	10.521	9.996	9.662
133	10.259	9.734	11.497	11.778	11.553	10.964
142	10.634	10.409	12.397	12.472	12.472	11.677
167	12.378	12.097	13.485	14.591	14.366	13.383
199	14.741	15.360	17.273	16.804	17.329	16.302
232	17.029	18.117	19.899	19.205		18.562
272				22.693		

G (μm/sec) = 0.075
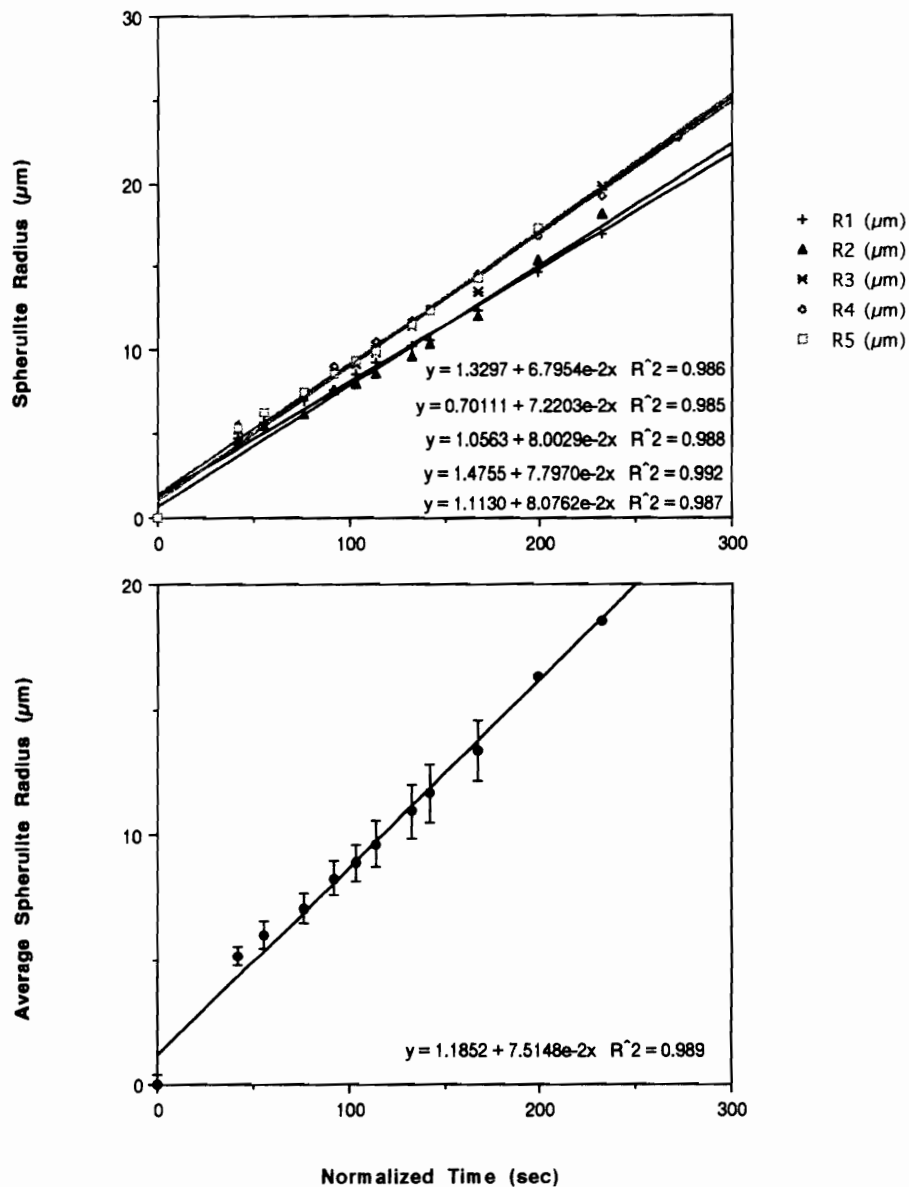
Figure 3.8   ITX growth rate determination data (Thold = 404°C/Tc = 282 °C): top) individual spherulite data, bottom) line fit to the average spherulite radii including the standard deviation of the data.

nucleation density as a function of temperature were obtained from the DSC Avrami analysis data just described.

3.3.4 Hermans and Weidinger Analysis

The wide angle x-ray scattering (WAXS) data collected for the Hermans and Weidinger determination of the percent crystalline content in a semicrystalline specimen was analyzed using two methods, one more experimentally rigorous than the other. The methodology for collecting the data, its analysis and then the results each provided will be compared and contrasted. The first method involves a simple comparison of the intensity versus the scattering angle for an amorphous specimen and a semicrystalline specimen. The ratio of the area for each specimen was used to calculate a relative percent crystallinity for ITX. The second analysis method, which is more rigorous in that it includes several normalization and corrections to the data, includes the complete Hermans and Weidinger analysis of the data as described by Alexander [124].

3.3.4.1   Data File Collection

The actual WAXS data was collected as described previously in section 3.2.3. After the specimens were collected, the data was in the form of unsmoothed (x, y) pairs signifying intensity versus scattering angle. The data were used either unsmoothed, or smoothed using the Fourier transform smoothing routine that is incorporated as part of the Seimens Polycrystalline Software Package. Smoothing the data was found to aid in the efficiency of the data analysis procedure. Utilizing unsmoothed data in the area

comparison (semicrystalline area-amorphous area) steps involved in the procedure made it difficult to visually determine a "good" fit when the data were overlaid.

After smoothing, the data were reformatted into a PC ASCII file, and then transferred into Excel® 4.0 through the Apple File Exchange utility. After separating the data into individual columns using the parse function, the data was in a usable format for Excel and Cricket Graph which were used for the integration and plotting/fitting functions respectively. An example Excel data file is included in this dissertation as Appendix 1.

3.3.4.2   Analysis Method of Hermans and Weidinger

The normalization procedures used in the determination of crystallinity by the method of Hermans and Weidinger are more elaborate than the simple technique of ratioing the peak areas generated by separate semicrystalline and amorphous specimens, and include several steps. Before elaborating on the normalization procedures that were applied to the data, a brief description of the method of Hermans and Weidinger itself will be given. The method includes the following steps [124]:

Method of Hermans and Weidinger

1. The diffraction patterns of a series of semicrystalline polymer specimens are collected over a limited angular range. The specimens must have varying levels of crystallinity, and are normalized to equal x-ray optical density (μt) and equal intensity of the direct x-ray beam.

2. A reasonable demarcation line is drawn between the crystalline and amorphous scattering.

3. Suitable integral intensities proportional to the crystalline and amorphous fractions are selected and measured to give I_c and I_a respectively.

4. The regression line that gives the statistically optimum linear dependence of I_c on I_a is calculated.

5. Finally, inspection of the linearity of I_c versus I_a confirms that the method utilized for measuring them is in agreement with theory. The regression line may then be used to determine the crystalline fraction of any other specimens of the same material from their I_c and I_a values by reference to the established regression line.

The method neglects corrections for certain intensity factors, including the polarization factor, and the correction for incoherent scattering since the technique relies on proportionality between the experimentally measured I_c and I_a and the crystalline and amorphous fractions respectively. For this reason, it is not required that the complete integral intensity be measured, and therefore consistent regions were chosen between 2θ values of 8 and 36 degrees for all integrations.

As was mentioned earlier, the method does include normalizations to equal x-ray optical density (μt) and equal intensity of the direct x-ray beam for all specimens. The details of these corrections will now be discussed.

3.3.4.3   Data Normalization Routines

The WAXS data collected for evaluation of the crystalline index in ITX was evaluated by two techniques, the first with no corrections or normalizations to the raw data, and the second method incorporating normalizations for equal x-ray beam intensity and optical density for all specimens. Direct comparison of the peak areas of semicrystalline and amorphous samples provided an estimate of crystallinity in ITX, however, since the method uses areas proportional to the crystalline and amorphous fractions it was thought that the values obtained were only an index of the crystalline

content. This theory was supported when the unnormalized peak areas were used in the Hermans and Weidinger analysis, and the results were non-linear as described in step 5. After re-calibration and alignment of the diffractometer, new data files were collected. The normalizations were then applied to these new files as follows.

3.3.4.3.1   Normalization for Equal X-Ray Beam Intensity

The first normalization applied to the WAXS data in order to improve the consistency of the data was the normalization for equal x-ray beam intensity. It was noted that the intensity of the diffractometer was not constant, and could in fact drift over the course of a day. For this reason, and that it typically takes several days to collect a series of data files, the beam intensity was noted at the start and end of each run. The two values, I_{before} and I_{after} were averaged, and then the average values were normalized to the highest intensity noted. This value is noted henceforth as I_{Normal} in the data files, and all intensity values were normalized as appropriate. The actual value of the variation observed worked out to be $\pm 0.01\%$ of ~14,000 counts in intensity, or $\pm$ 110 counts variation in x-ray beam intensity on any given day for this data series. This correction served to adjust the data to constant direct beam intensity as suggested by Alexander [124].

3.3.4.3.2   Normalization for Equal X-Ray Optical Density

The next correction undertaken on the raw WAXS data was the normalization for effective scattering mass, or optical density, D. Optical density is defined in Equation 3.4 as:

$$D = \mu\, t \qquad\qquad (3.4)$$

where:

$$\mu t = - \log_e I/I_o \qquad (3.5)$$

μ is an absorption coefficient, t is the film thickness, and I and I_o are the beam intensities measured with the specimen in the holder, and measured through the empty fixture respectively. The I and I_o values used to determine D for each specimen are experimentally by scanning from -1.0 to 1.0 degrees, and integrating the intensity versus angle peaks between - 0.9 and 0.9 degrees in the Seimens software routine. Initially, only one I and Io value were determined for each specimen, however this eventually proved inadequate. The intensity of the data is very dependent on this correction when the specimen sized is relatively small, as was ITX. In order to reduce the variability of the data, it was necessary to take 5-6 intensity measurements with and without the specimen in the instrument. The integrated values for each I and I_o value were then averaged, and D recalculated.

The optical density correction was found to be the most crucial normalization factor in that its effect on the final integrated area calculated for each ITX specimen was substantive. An additional observation on this correction was that the I and I_o values measured were also a function of the instrument fixture. Different values of I and I_o were obtained if they were measured with the empty specimen holder in place in the fixture, or with the fixture alone. The numbers used in this evaluation were collected without the empty fixture in place for the I_o value . This resulted in I/I_o numbers ranging from 0.64 to 0.69 for the ITX specimens, where with the empty specimen holder in place the fractions were closer to 0.8-0.9. This *could* result in a significant systematic error if all the I and I_o measurements were not collected in a similar manner, and therefore it is worth noting in this procedure.

3.3.4.3.3   Normalization for Air Scatter

Once the optical density of the ITX is measured for each specimen, the raw intensity data can now finally be normalized for air scatter using the following expression noted in Equation 3.6 [122].

$$ I_N = I / \big(D \exp \left(- D \sec \theta \right) \big) \qquad (3.6) $$

where the expression contained a term for the fluctuations of the primary beam intensity that was discussed and included in the calculations earlier in section 3.3.4.3.1.   This correction to each data point is included in the calculations and is designated as "Normalized Intensity" in column E of the sample data file.   With this calculation, the normalizations to the raw data files before integration are now complete.

3.3.4.4   Data Integration Method

The WAXS data presented here were numerically integrated using two methods, the first Simpson's Rule which was discussed previously in section 3.3.1.2. Unfortunately, the data evaluated did not appear consistent when integrated with this method.   Apparently the scatter in the data contributed to unreliable results.   The integrated areas obtained were not consistent with visual inspection of the data, i. e. the area under the peak did not consistently increase with increasing annealing time, even though it appeared reasonable.   Instead of Simpson's Rule, the trapezoid rule was used for numerical integration of the WAXS files as stated in Equation 3.7 [125].

$$\int_a^b f(x) \approx \frac{b-a}{2n} \left[f(x_0) + 2f(x_1) + 2f(x_2) + \ldots + 2f(x_{n-1}) + f(x_n) \right] \qquad (3.7)$$

where f is a continuous function on [a, b], and the partitions are regular [125].

Numerical integration using the trapezoid rule peak area integration results that were consistent within the same order of magnitude, unlike the Simpson's Rule results.

Before the actual integration step, a linear baseline was drawn between ~ 8 and 34 degrees for all data files. The line fit to these points was considered the baseline, and was subtracted from the normalized data, with the result tabulated in column H and illustrated in Figure 3.9. After this step, all the data files were "shifted" to a similar position on the y-axis as shown in the plot in Figure 3.10. The files were then integrated, and the rest of the Hermans and Weidinger analysis completed as outlined in section 3.3.4.2.

3.3.4 Determination of the Theoretical Heat of Fusion

The final step in the series of analyses completed using the WAXS results was the determination of the theoretical heat of fusion of ITX. This procedure involves combining the results from the Hermans and Weidinger analysis just described with DSC data. The specimens used in the crystalline content experiments above were evaluated by DSC to determine the heat of fusion for each specimen.

The series of ITX specimens were scanned in the Perkin-Elmer DSC-7 using a heating rate of 20 °C/min. between 50-400 °C. The melting endotherms were then integrated using the Perkin-Elmer software package. The heat of fusion data were then plotted against the corresponding percent crystallinity values obtained for each specimen, and the value for the theoretical heat of fusion extrapolated.
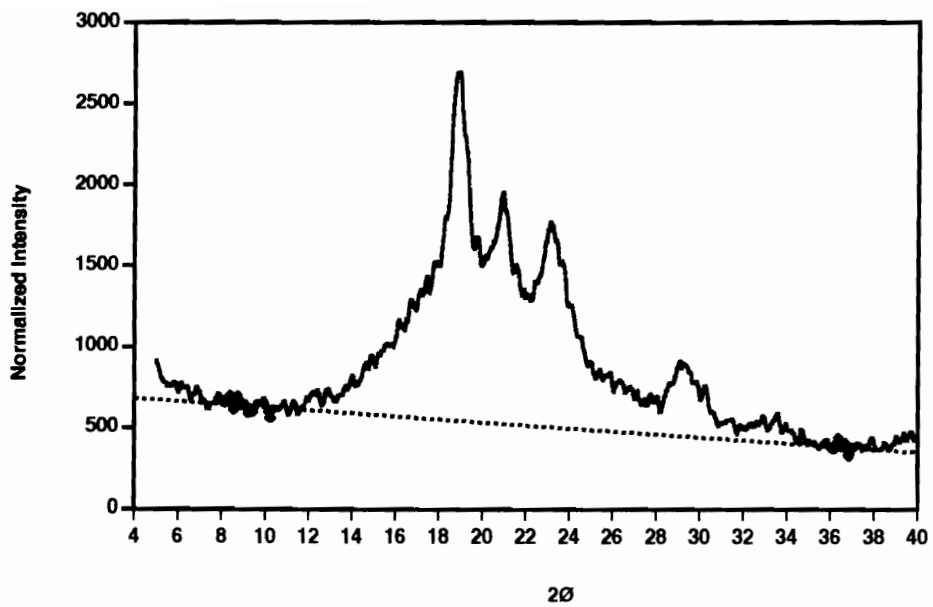
Figure 3.9   ITX (annealed at 300 °C/5 min.) WAXS baseline determination and subtraction example file.
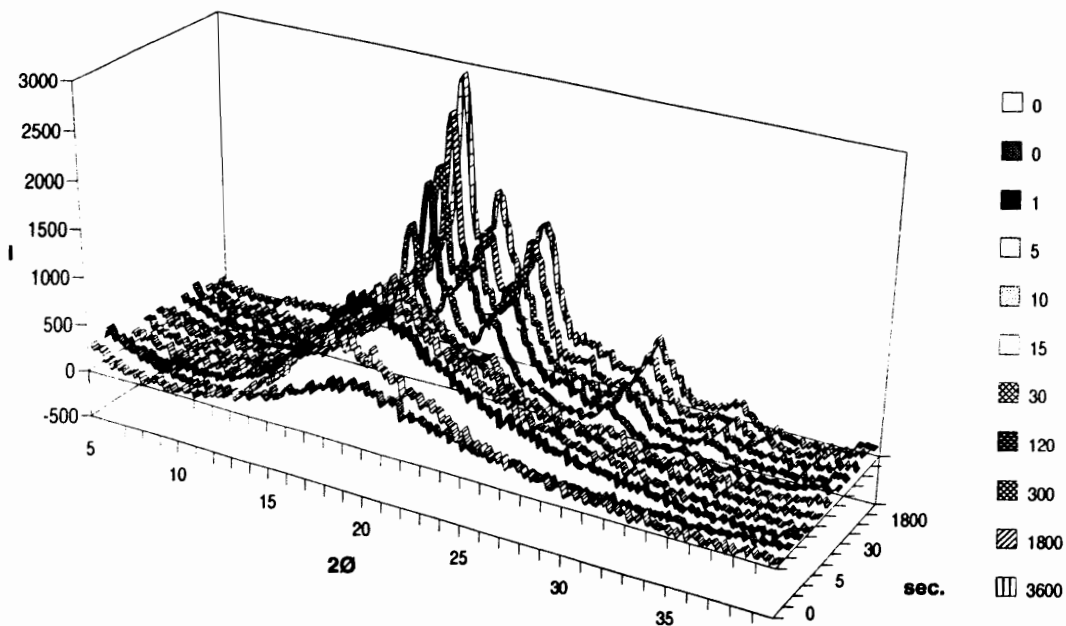
Figure 3.10   ITX WAXS composite plot of normalized intensity versus 2θ showing how the baseline correction scaled the data series. Specimens are plotted as a function of annealing time (sec.) at 300 °C.

CHAPTER 4

CRYSTALLIZATION and MORPHOLOGICAL STUDIES of ITX

4.1   Introduction

A fundamental understanding of the processing-property relationships for ICI's Intermediate Temperature Semicrystalline (ITX) polymer, both neat and as a composite matrix material, is essential since the properties of semicrystalline thermoplastics are strongly influenced by processing history. Processing history is particularly important for high performance polymers such as ITX which melt at relatively high temperatures where degradation may commence. The research presented in Chapter 4 focuses on evaluating the crystallization behavior of ITX.

After a brief introduction to ITX, the initial portion of this chapter (section 4.3) concentrates on discovering how manipulating the polymer melting temperature and melt residence time during processing influences the crystallization behavior that evolves in neat ITX specimens. Next, isothermal crystallization studies are presented which were

completed to determine if any variations existed in crystallization kinetics, nucleation density, the type of crystalline morphology, and the level of crystallinity which developed as a function of melt temperature and time. These results are discussed in section 4.4. The crystalline morphology of ITX was evaluated as well, both for the neat resin, and for the case of ITX crystallized in the presence of a few carbon fibers as a function of thermal treatment. The results of the morphological studies are presented in section 4.5. Finally, section 4.6 discusses the determination of the absolute crystalline content for ITX, and section 4.7 summarizes the trends observed over the course of the project.

4.2   Material Description

The ITX evaluated in this research was supplied by ICI Fiberite Advanced Composites as a semicrystalline, white powder. Information is not available for publication on the chemical composition of ITX as is discussed in section 3.1. ITX is somewhat similar in behavior to PEEK (poly(ether ether ketone)), but was engineered for higher temperature applications. The material displays a glass transition temperature (T_g) at approximately 180 °C, and a melting point (T_m) about 360 °C in contrast to PEEK whose T_g and T_m are circa 140 and 340 °C respectively [12, 28, 29]. The higher T_g and T_m characteristic of ITX expands its potential application temperature window upwards, making it a candidate for such applications as the High Speed Civil Transport (HSCT) composite commercial aircraft. At the same time, the higher thermal properties also make the material more difficult to prepare and characterize using conventional equipment. In addition, moving the glass transition and melting temperatures upward by manipulating the chemistry also narrows the window between T_m and the onset of degradation.   In   fact,   PEEK   has   been   noted   to   begin   to   degrade

even within the normal thermal processing range suggested for the material [11]. Therefore, before beginning fundamental crystallization studies with this material, its thermal stability will be briefly examined, as well as the potential melt sensitivity of ITX.

4.3   Thermal Stability Studies

In addition to thermal stability, i. e. weight loss as a function of temperature, another related aspect was examined as part of the initial portion of this study, the potential melt sensitivity of ITX. Many crystallizable polymers are known to show melt sensitivity, i. e. the crystallization behavior and nucleation density, N, of the polymer are influenced by the melt treatment temperature, T_f, that the polymer is exposed to prior to crystallization [105-108, 127-131].   Since the majority of crystalline polymers are heterogeneously nucleated, that is polymer crystals initiate predominately from impurities or from the surface of incompletely melted crystalline "ordered" material left in the melt, variations in thermal history can have a profound effect on the crystallization behavior of the material. This behavior is especially relevant with stiffer or more polar polymers as was discussed recently by Khanna et al. [127-130]. As the material is taken nearer to its equilibrium melting temperature, or held for longer times in the melt at lower temperatures, it becomes more completely disordered. The more disorder, the lower the population of unmelted material or "nucleation density". If nucleation density is lowered, greater supercooling and/or longer times are subsequently required for the material to crystallize. If ITX is melt sensitive, then care must be taken to ensure that all specimens see the same thermal history during the characterization process. Inconsistency in the experimental melt treatments could result in variations in the observed melting

temperature, crystallization temperature, crystallization rate and ultimate crystalline content data generated, thus rendering the data and any interpretation suspect.

4.3.1   Initial Thermal Stability as a Function of Melt History

As noted earlier ITX, like PEEK, is a high performance semicrystalline thermoplastic material designed for applications in advanced composites where high thermal stability, good chemical and solvent resistance and superior mechanical properties are required.   When examined by TG-DTA, ITX shows excellent thermal stability through a wide temperature range as represented by minimal weight loss below 500 °C as seen in Figure 4.1.   ITX "as received" powder was scanned from room temperature upwards at 2 °C/min. in both air and nitrogen environments.   The five percent weight loss temperatures observed at this heating rate were 520 °C and 524 °C respectively, confirming the high temperature stability claims for this material under these conditions.

4.3.1.1   Effect of Cooling Rate on ITX Crystallization Behavior

The effect of varying the cooling rate during dynamic crystallization of ITX was initially screened by heating and cooling specimens utilizing the Seiko DSC system. Two ITX powder specimens were repeatedly heated at 10°C/min. to 385 °C, and then subsequently cooled four times each to determine if changes in the cooling rate would affect the observed DSC results.   The results, melting (Tm), crystallization (Tc), and glass transition (Tg) temperatures, are summarized in the plots shown in Figures 4.2a and b.
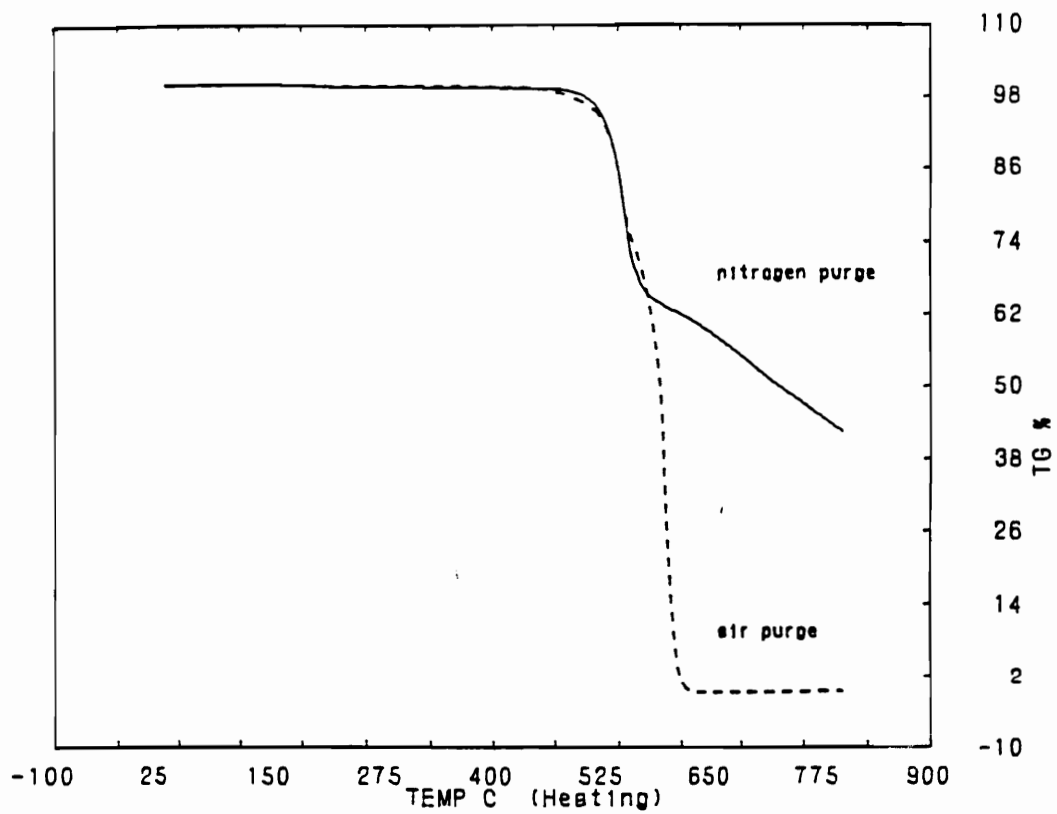
Figure 4.1   TG-DTA thermal stability results for ITX as a function of temperature evaluated in air and nitrogen environments heating at 2 °/min. The five percent weight loss temperatures are 520 and 524 °C respectively under these conditions.

**Observed ITX Thermal Transition
Temperatures as a function of
Cooling Rate**
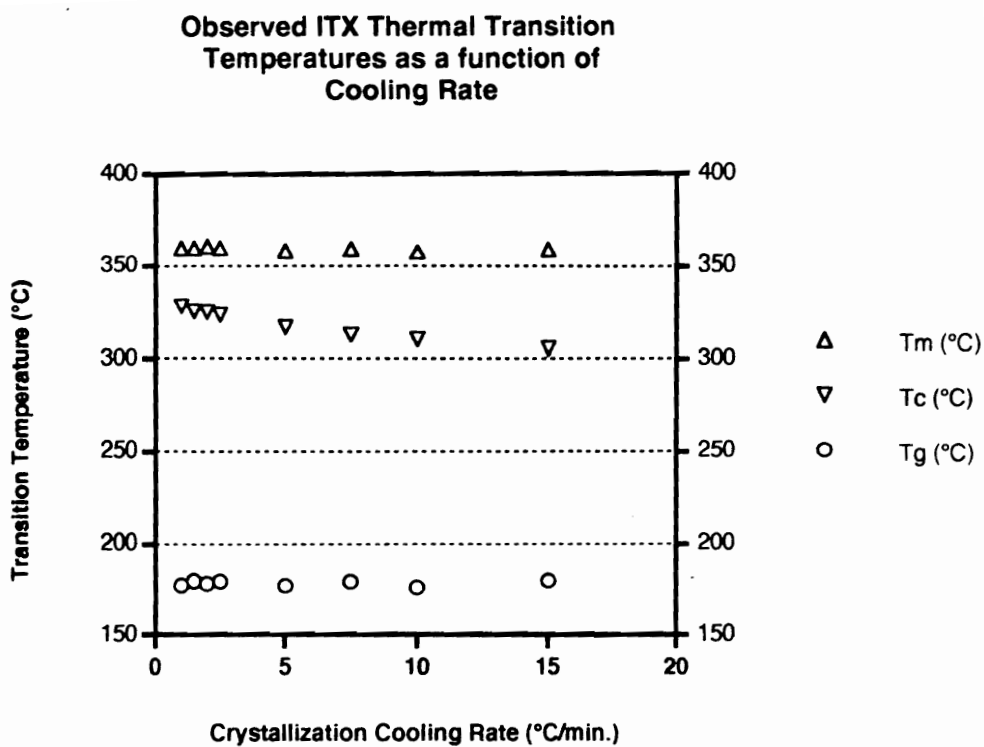
Figure 4.2a   Variation in the observed thermal transitions for ITX as a function of crystallization cooling rate (cooled between 1 and 15 °C/min.) after heating to 385 °C at 10 °C/min.

Observed ITX Thermal Transition
Values as a function of Cooling Rate
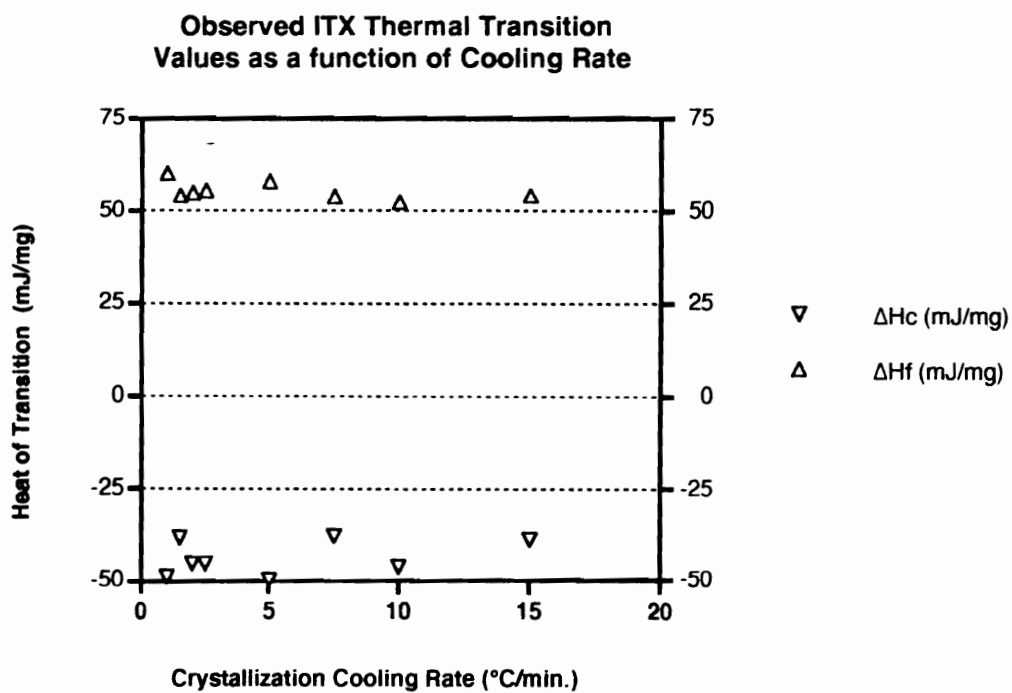
Figure 4.2b   Variation in the observed heats of fusion and crystallization for ITX as a function of crystallization cooling rate (cooled between 1 and 15 °C/min.) after heating to 385 °C.

The plot in Figure 4.2a is a composite of the DSC thermal transitions observed for ITX as a function of cooling rate. The melting and glass transition temperatures measured at 10 °C/min. after cooling at 1.0, 1.5, 2.0, 2.5, 5.0, 7.5, 10, and 15 °C/min. were essentially constant. Only the crystallization temperature (Tc) decreased as a function of cooling rate. As the cooling rate increases, the material typically supercools by an increasing amount before the onset of crystallization.

The data collected in Figure 4.2b represent the heats of fusion (ΔH_f) and crystallization (ΔH_c) for the ITX specimens described in the previous paragraph. Both data sets show some scatter, which reflects the difficulty in consistently integrating the area under the measured endo- and exotherms, but otherwise the values for each are again essentially constant. This trend suggests that variations in the cooling rate within the range examined do not significantly affect the level of crystallinity generated during cooling.

Several possible reasons for the scatter in the heat of fusion and crystallization data values collected above including the following. The scatter in the ΔH_c data may be partially due to the non-linear baselines observed at higher cooling rates with the Seiko DSC 210 instrument which make it difficult to consistently choose a reasonable low temperature integration limit. As the cooling rate increases, the baseline typically curves concave upwards on the low temperature side of the crystallization peak. This curvature is most pronounced when the instrument reaches the lower temperature limit of controlled cooling. Since this "out-of-control limit temperature" shifts upwards in temperature as the cooling rate increases, data collection is restricted to low cooling rates for this particular instrument-polymer combination.

In summary, two observations were made during the course of this series of experiments:

1) After melting at 385 °C, the melting (T_m) and glass transition (T_g) temperatures measured for ITX are not significantly affected by variations in the dynamic crystallization cooling rate beyond the consistent shift expected due to increasing cooling rate. The crystallization temperature <u>does</u> appear to decrease slightly more than T_m and T_g dectease.

2) ITX dynamic crystallization is essentially fast enough that the area under the crystallization peak appears insensitive to variations in cooling rates ranging between 1 and 15 °C/min.

Together, the data from this initial screening test completed with a fixed melting procedure suggest that the crystallization behavior of ITX is not significantly affected by variations in the crystallization cooling rate between 1 and 15 °C/min. as evaluated. Cooling rate does not appear to be a significant variable if dynamic crystallization is completed utilizing cooling rates of 15 °C/min. or slower. [The effects of faster cooling rates were not evaluated, ~ 15°C/min. cooling was the maximum rate possible over the ITX crystallization range with the Seiko system.]

4.3.1.2 Initial Melt Temperature Effects on Crystallization Behavior

The next step in the initial evaluation of the heat history sensitivity of ITX was completed by taking a single powder specimen and subjecting it to repeated heating and cooling cycles in the DSC. Each heating cycle ended at a successively higher final melting temperature. The melting temperatures ranged between 376 °C to 416 °C in 5 °C increments. It was hoped that either of two following behaviors would be observed: 1) successive scans would essentially duplicate one another suggesting the material was not melt sensitive, or 2) initial scans might be similar, and later scans would begin to deviate from previous scan shapes indicating that the higher melt temperatures might be more detrimental to the material than lower melt treatment temperatures. DSC curves

showing the melting and crystallization behavior of ITX subjected to the experiment described above are shown in Figures 4.3a and b respectively. Heat flow is plotted as a function of temperature with peaks facing concave down indicating endothermic transitions, and peaks turned concave up indicating exothermic transitions. Figure 4.3a illustrates the melting behavior of ITX "as received" powder as it is heated at 10 °C/min. Each successive melting cycle was programmed to end 5 °C hotter, i. e. 376, then 381 °C etc. The 5 °C increments in heating provided the thermal history for the subsequent crystallization experiment seen in Figure 4.3b. Figure 4.3b shows the cooling curves for each heat-cool cycle. The DSC thermogram baselines are progressively offset for clarity in both figures.

Instead of replicating each other, the ITX melting and crystallization peaks change in character with increasing melt temperature. Variations in peak shape are observed immediately, and none of the melting or crystallization peaks exactly duplicate a previous scan. This nonreproducible behavior suggests that ITX is melt sensitive under the thermal conditions utilized. As the polymer sees higher melt treatment temperatures, the measured melting and crystallization temperatures, T_c and T_m respectively, decrease. This trend is illustrated graphically in Figure 4.4. The observed changes in the peak shape suggest that the heats of melting and crystallization, ΔH_f and ΔH_c, are also decreasing, signaling that the final level of crystallinity in ITX is affected by higher melt treatment temperatures as well. However, when the peaks are integrated, the results are not conclusive. Both ΔH_f and ΔH_c remain essentially constant, only edging slightly outside the standard deviation (one σ) of the data collected, therefore indicating that degradation is not as likely. Overall, these data suggest that the level of crystallinity which develops in ITX is not significantly changed under these experimental conditions, even though the peak crystallization temperature does decrease.
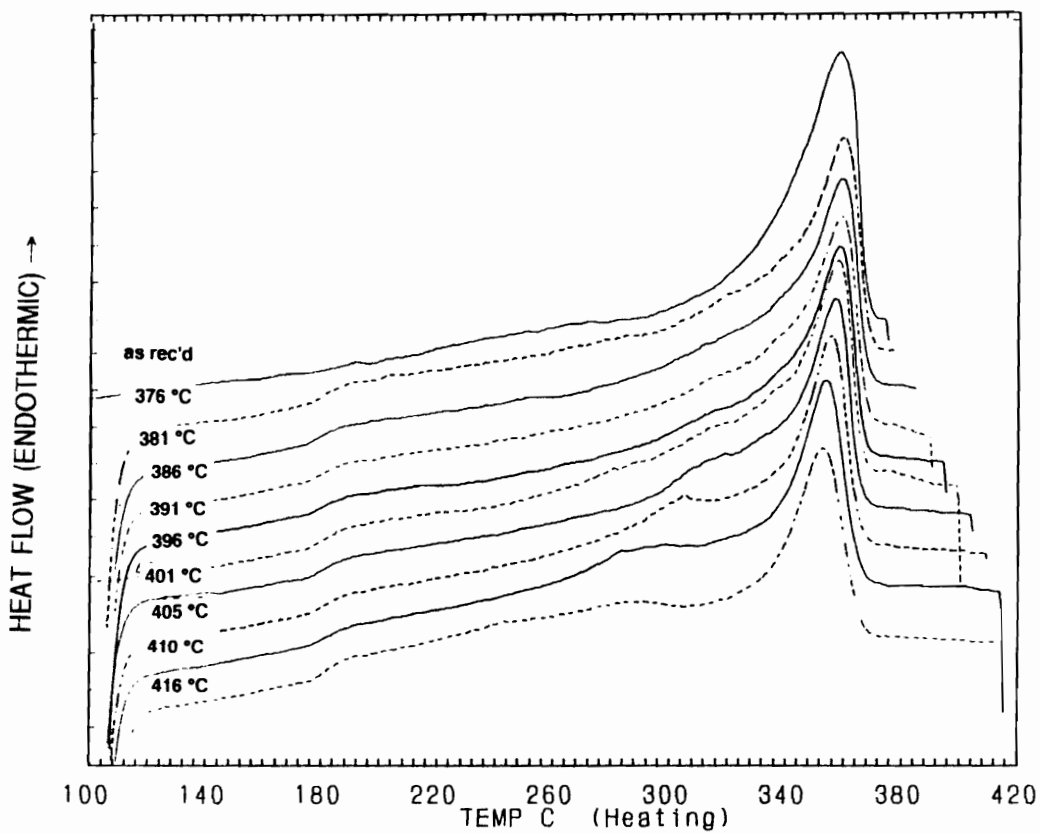
Figure 4.3a   Variation in the melting behavior of ITX with increasing melt treatment temperature, T_f, between 376 and 416 °C.
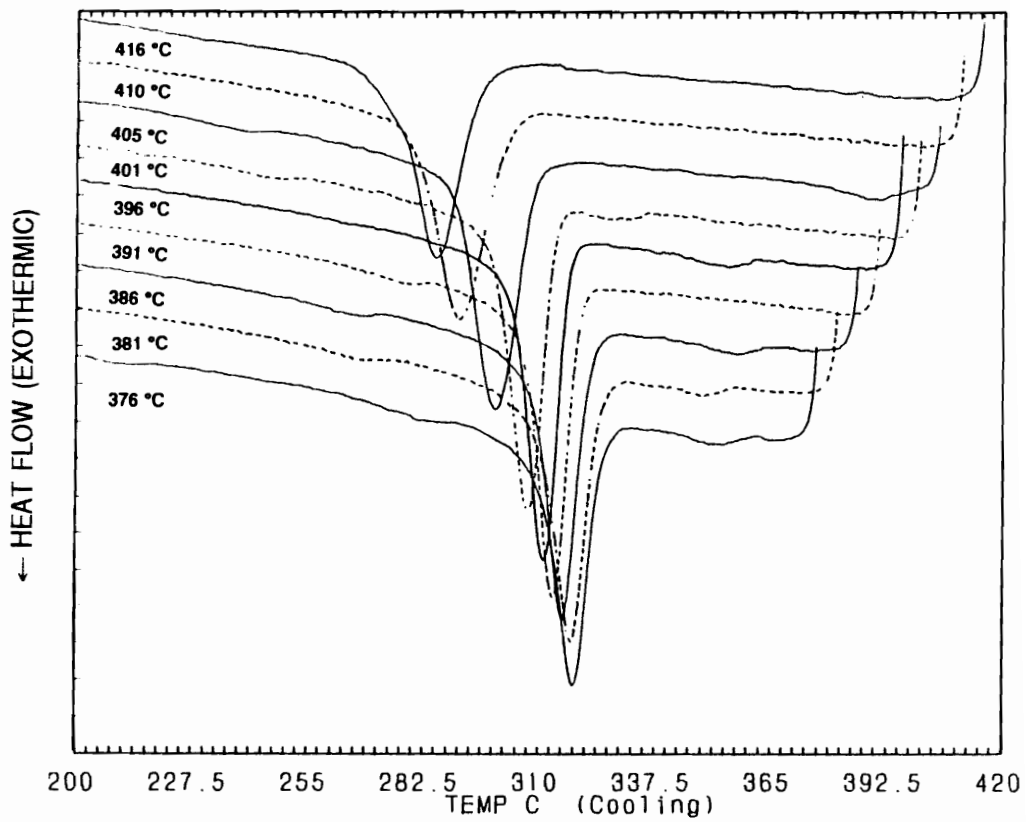
Figure 4.3b   Changing crystallization behavior of ITX with increasing melt treatment temperature.
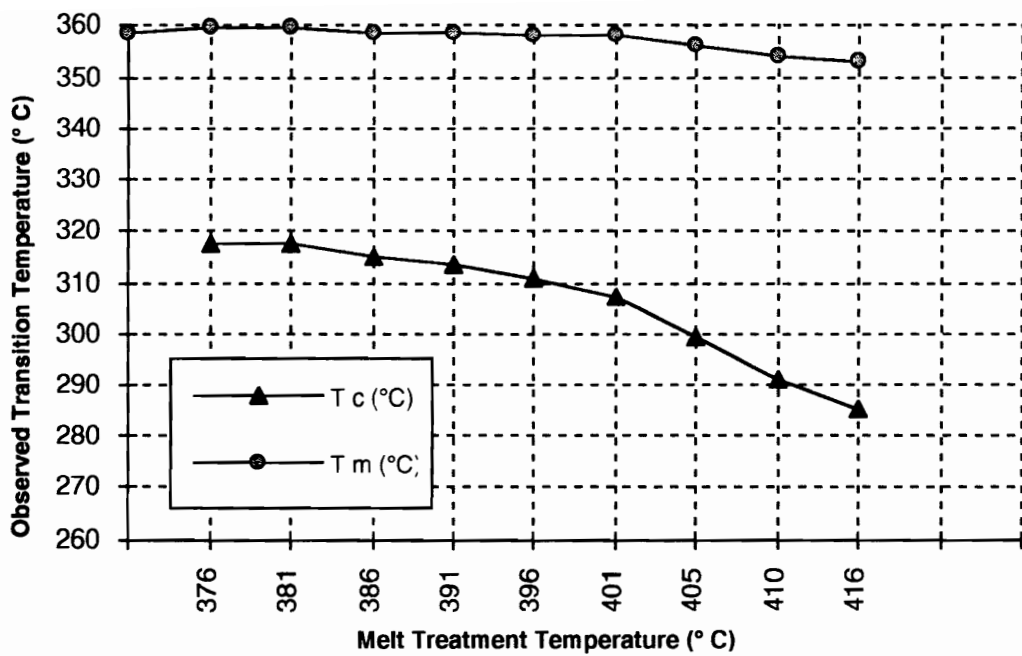
Figure 4.4   Decrease in observed melting and crystallization temperatures for ITX with increasing melt treatment temperature. Note that the trend is more pronounced for the crystallization peak.

Two possible interpretations for these types of changes in peak intensity and position in a DSC curve are: 1) the polymer may be beginning to degrade, or 2) the nucleation density of the specimen is decreasing with the increasing heat treatment as some of the residual crystal nuclei that initiate the crystallization process are melting. Additional melting leaves a smaller population of ordered "seed" material in the melt to start recrystallization. Greater supercooling would then be required to promote nucleation. This is consistent with the observed drop in T_C with increased treatment times. However, since this experiment convoluted both time and temperature by reheating the same specimen, additional work was needed so that definitive conclusions could be drawn as to whether time in the melt or melt temperature was the more significant factor.

4.3.1.3   *Effect of Initial Melt Time on Crystallization Behavior*

In order to separate the effects of residence time in the melt, as opposed to melt treatment temperature, an additional set of experiments was performed. The crystallization behavior of the material was monitored as a function of increasingly longer treatment times at a moderate but fixed melt temperature. The DSC melting and crystallization data for ITX held at successively longer melt treatment times at 398°C is shown in Figures 4.5a and b respectively. A *single* ITX specimen was heated (10 °C/min.) to the selected hold temperature, and then cycled (heat-cool) to accumulate 5, 15, 30 and finally 60 minutes total time in the melt. The material was cooled at 5 °C/min. to 100 °C before reheating. Both the melting (Figure 4.5a) and crystallization (Figure 4.5b) peaks show changes in their thermal profiles as the total time in the melt increases. Focusing on the crystallization peaks shown in Figure 4.5b, it is obvious that
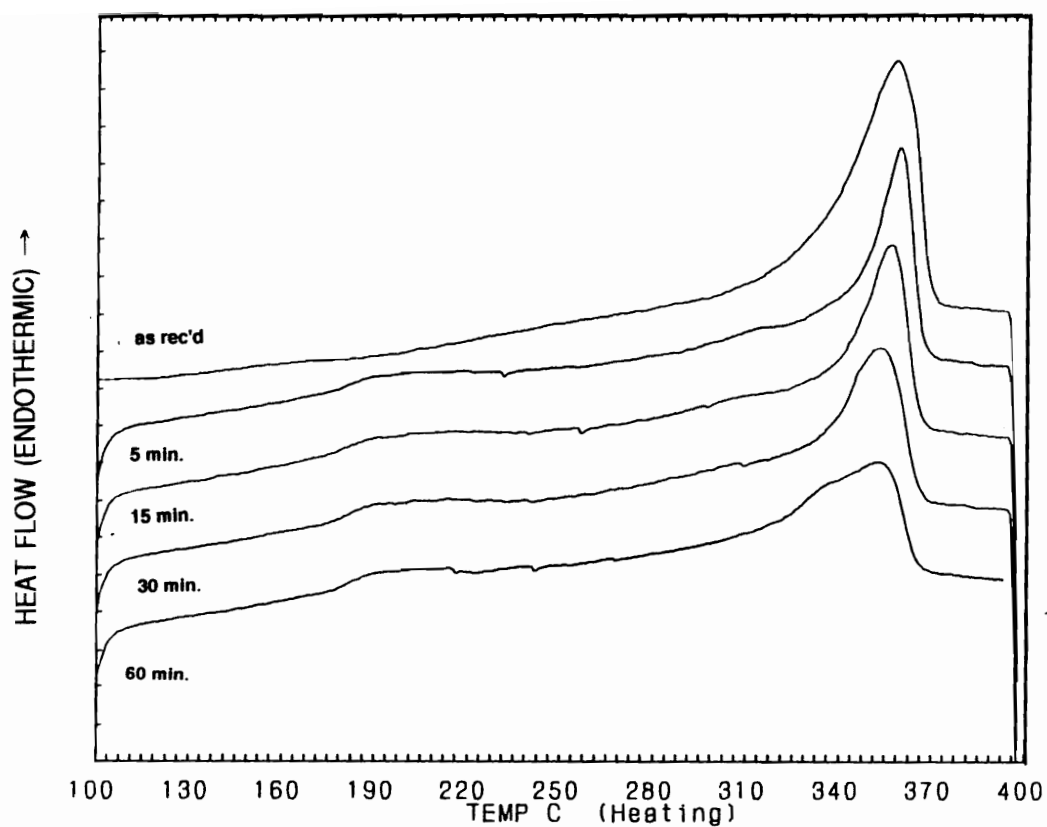
Figure 4.5a   Variation in the melting behavior of ITX with increased residence time in the melt at 398 °C: 5 min., 15 min., 30 min., and 60 min. The cooling rate between cycles was 5 °C/min.
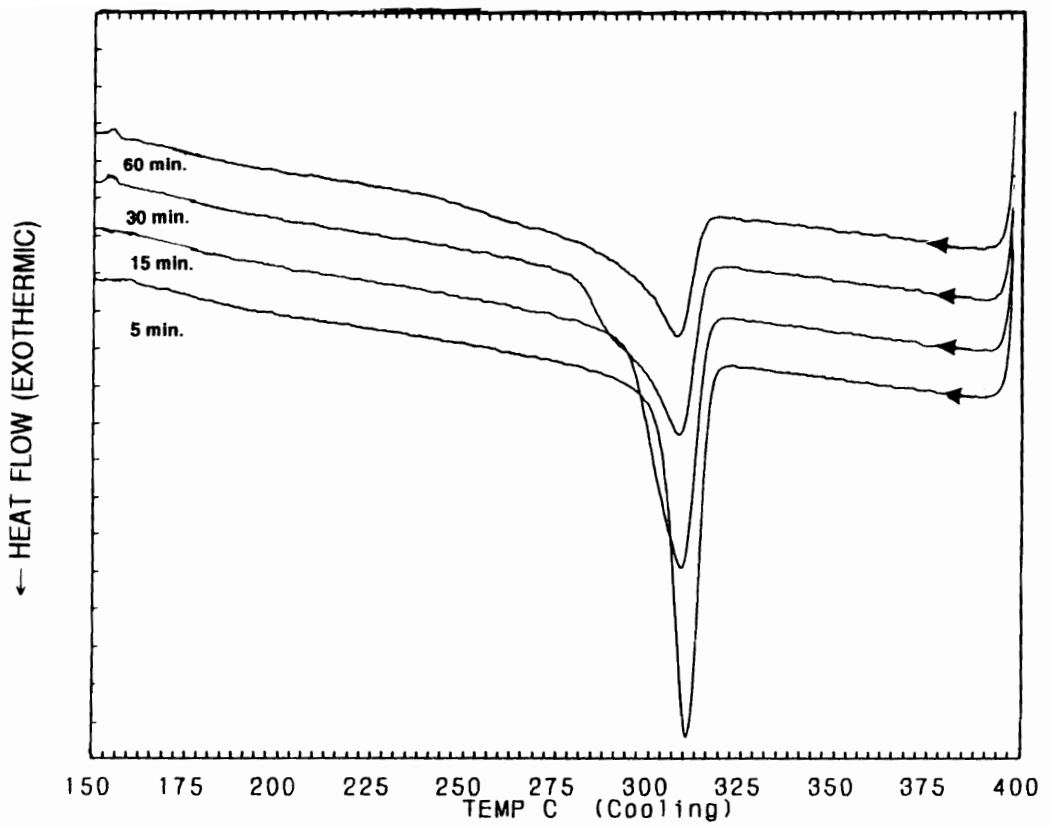
Figure 4.5b   Changing crystallization behavior of ITX with increased residence time in the melt at 398 °C: 5 min., 15 min., 30 min., and 60 min. Cooling rate between cycles was 5 °C/min.

as the polymer sees longer melt times at 398 °C, the crystallization temperature, T_c decreases noticeably. In addition, it takes longer to complete the crystallization process as suggested by the successively lower temperatures where the heat flow curve returns to the baseline and the breadth of the crystallization peak. The peaks also appear to be visibly shallower with increasing melt pretreatment. These observations are confirmed when the peaks are integrated, both the heats of fusion and crystallization show a slight decrease, especially at the longest times evaluated. This data is summarized graphically in Figure 4.6.

4.3.1.4   Melt Sensitivity as a Function of Melt Temperature

The variations in the crystallization behavior of ITX noted previously are consistent with a decrease in the nucleation density within the molten polymer, i. e. melt sensitivity, as a function of hold time in the melt. However, the initial work convoluted the effects of both time and temperature within the same specimen. To clarify if melt treatment temperature was also a significant processing variable, a third series of experiments was completed to determine if T_f must be controlled in order to obtain consistent fundamental crystallization data.

The experiment was designed so that each single ITX specimen was held at a selected melt temperature for a hold time, 15 minutes, that earlier tests indicated would not significantly reduce the relative crystalline content which would subsequently develop. In this way, the experiment simulates processing ITX at a series of increasing treatment temperatures, with all other variables held constant. Each specimen of ITX powder was subjected to the following thermal history:
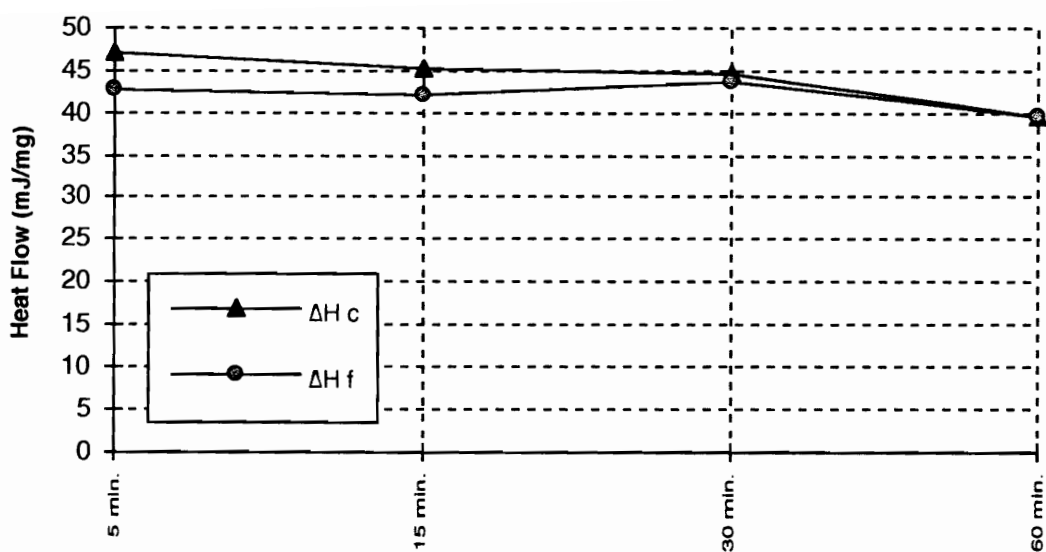
Figure 4.6   Observed melting and crystallization enthalpy for ITX held in the melt at 398 °C for 5, 15, 30 and 60 minutes before crystallization. Note the change appears more prominent at the 60 minute hold time.

1) Heat @ 10 °C/min. to a given Tf between 383-448 °C,
2) Hold for 15 minutes @ Tf,
3) Cool @ 5°C/min. to 100 °C, and
4) Heat @ 10 °C/min. to determine the heat of melting, ΔH_f and the crystallization onset temperature, T_C.

The results are presented in Figure 4.7. The heat of melting, which is proportional to the relative crystalline content of the specimen, and the observed crystallization temperature values measured after melting ITX polymer at a series of melt treatment temperatures are shown. While small changes in Tc and ΔH_f are noted consistently for all heat treatments, specimens exposed to temperatures above ~405 °C show the most marked reduction in the relative level of crystallinity which develops on cooling when compared to those treated to less severe melting conditions. However, the drop in ΔH_f does not continue as dramatically above circa 415 °C. Instead, the measured values for ΔH_f and T_C nearly stabilize, suggesting indirectly, but not conclusively, that polymer degradation may not be a major cause of the decrease in the heat of crystallization measured under these specific conditions as was observed by Jonas et al in their work with PEEK [11].

4.3.1.5   Summary of Initial Results

Overall, the "time in the melt" experiments suggest that the crystallization behavior of ITX, like other stiff-chained polymers, is affected by thermal treatments even at moderate times such as those that might be typical for composite processing [20, 131]. The decrease in the observed crystallization temperatures is consistent with a decrease in the nucleation density of the polymer as suggested earlier. A greater degree of supercooling is needed to initiate crystallization, and the overall crystalline content is only slightly diminished. These observations imply that all specimens must be

Heat of Fusion vs Melt Treatment Temperature

Observed Crystallization Temperature vs Melt Treatment Temperature
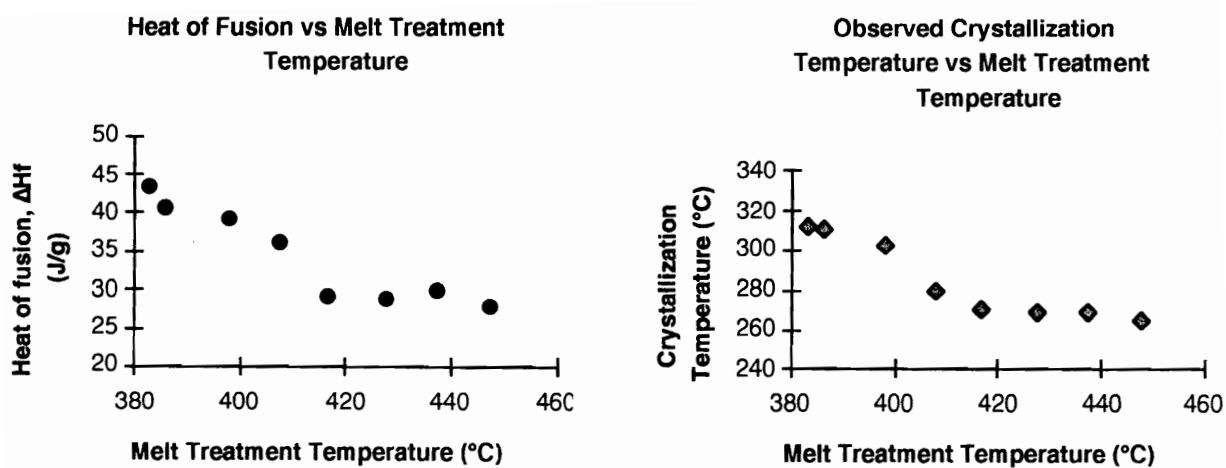
Figure 4.7   Heats of fusion and crystallization temperatures determined as a function of thermal history for ITX powder specimens held in the melt for 15 minutes at a specific temperature; followed by crystallization during 5 °C/min. cooling.

treated to similar melt treatment times and temperatures if data for ITX crystallization studies are to be compared .

4.3.2   Melt Sensitivity as a Function of Melt Time & Temperature

Clearly, examining the melt sensitivity of ITX has revealed that the crystallization and melting behavior of the material is affected by either the residence time in the melt, or the melt treatment temperature that the polymer sees before crystallization as reflected by the changes in the ΔH_f and T_C values observed as has been seen for PEEK [11]. The problem however, is that extending this argument from the previously presented melting observations to crystallization behavior is only indirectly supported. The ΔH_C values that would correspond to the data sets shown in Figure 4.7 are not included here due to difficulties integrating the data. The Seiko DSC 210 cooling system was unable to attain either a reproducible melting temperature when heating against the required constant liquid nitrogen flow, nor could it maintain a linear cooling rate at 5 °C/min. sufficiently far below T_C to establish a reasonable baseline for peak integration. For these reasons, additional work was needed to:

1) confirm the validity of previous results that suggest ITX crystallinity is a function of melt history,

2) to establish if similar trends would develop under more realistic (faster) heating and cooling rates, and

3) investigate the crystallization behavior of ITX as a function of both time and temperature in the melt.

A systematic crystallization study was completed using the Perkin-Elmer DSC-7 Thermal Analysis system to establish the behavior of ITX as a function of time and temperature [f(t, T_f)] in the melt under a nitrogen purge. The DSC-7 was able to

reproducibly melt the specimens heating against an ice bath, and provide controlled cooling over the entire temperature range of interest. <u>Powder specimens were subjected to a thermal history designed to replicate that used in actual ICI recommended ITX-carbon fiber composite preparation profile as follows</u>:

1) heat @ 36 °C/min. to a Tf between 380-410 °C,
2) hold for between 1-30 minutes @ Tf, and
3) cool @ 36°C/min. to 100 °C.

The extent of crystallinity generated was monitored via the heat of crystallization, ΔH_C. Seventy-seven distinctly different thermal treatments were summarized for each of the four variables studied: crystallization onset (T_{co}) and peak (T_{cp}) temperatures, crystallization peak breadth and heat of crystallization. Restated, each intersection point between time and temperature for the variable of interest on the three-dimensional plot represents a separate experiment, unlike previous work with PEEK where fewer melt temperatures and times were used to interpolate crystallization behavior [11]. The data reported were from single specimens. The reproducibility of the temperature and heat of crystallization values noted was evaluated by running replicate specimens under the same conditions, and by performing multiple analyses on the same file. Typical variations in the temperature values were ±0.01 °C and ±0.20 °C when the files were either reanalyzed or the experiments repeated, respectively. The heat of crystallization values varied by ±0.2 to ±0.5 J/g when the data were evaluated repeatedly, or a new specimen tested as described above.

Two crystallization temperatures were monitored for ITX over the course of this study, the crystallization peak onset and peak maximum temperatures, T_{co} and T_{cp} respectively as noted earlier. This was done to more fully characterized the crystallization behavior of the material. The first temperature, T_{co}, was taken as the

temperature defined by the intersection of extrapolated lines determined by: 1) a tangent to the leading-side of the peak, and 2) the baseline. This temperature describes the beginning of crystallization, and approximates the point where the heat flow curve deviates from the baseline. The other characteristic temperature, T_{cp}, was taken as the temperature of the minimum (exothermic heat flow negative) for the heat flow curve during crystallization.

A third temperature was also extrapolated at the *end* of the crystallization peak, in the same fashion as T_{co}, and designated T_{ce}. Taken together, the extrapolated onset and end temperatures define an index of the "peak breadth" characteristic of the crystallization process at a given temperature. Results for peak breadth were noted in minutes, not temperature, to follow changes in the amount of time necessary to crystallize the material as a function of thermal history.

The results from these experiments are presented in Figures 4.8a-d. Figure 4.8a shows the T_{co} temperature as f(t, T_f), Figure 4.8b is a similar plot showing the T_{cp} temperature, Figure 4.8c is a plot of the breadth of the crystallization peak over the same experimental range, and finally Figure 4.8d shows the heat of crystallization, ΔH_c, which develops as a function of the thermal history the material sees before recrystallization. All four plots show the variable of interest three-dimensionally, i. e. with the property shown as a function of both the melt time and temperature the material sees before crystallization. Note that the time axis is non-linear in all cases, meaning that the property changes with respect to time are <u>more</u> pronounced at short times than the curve shape initially implies.

In general, all four of the three-dimensional plots in Figures 4.8a-d share remarkably similar responses. In each case, there is a considerable systematic change in the property measured as the time and melt temperature the polymer encounters
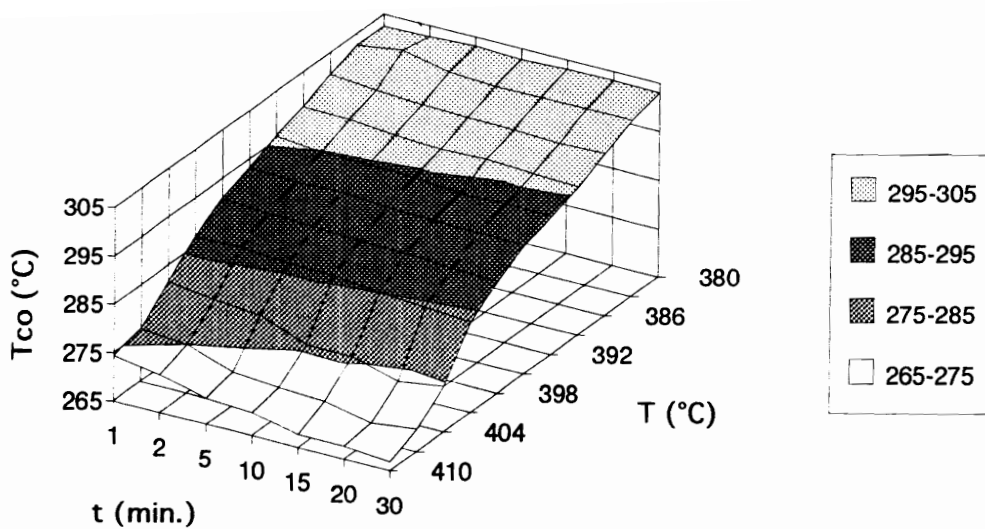
Figure 4.8a   Crystallization onset temperature (T_{co}) for ITX determined as a function of time (1-30 min.) and temperature (380-410 °C) in the melt when cooled at 36 °C/min. in nitrogen.
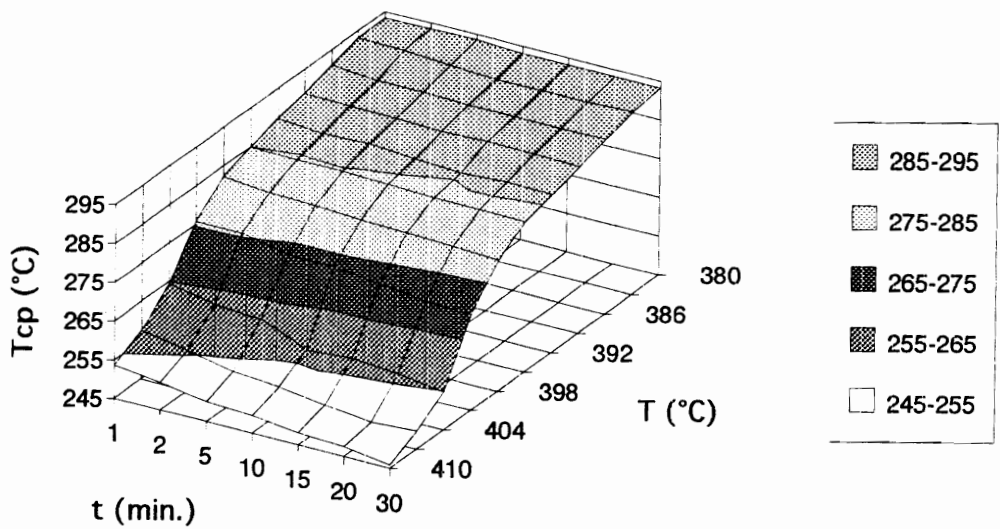
Figure 4.8b   Peak crystallization temperature (T_{cp}) for ITX determined as a function of time (1-30 min.) and temperature (380-410 °C) in the melt when cooled at 36 °C/min. in nitrogen.
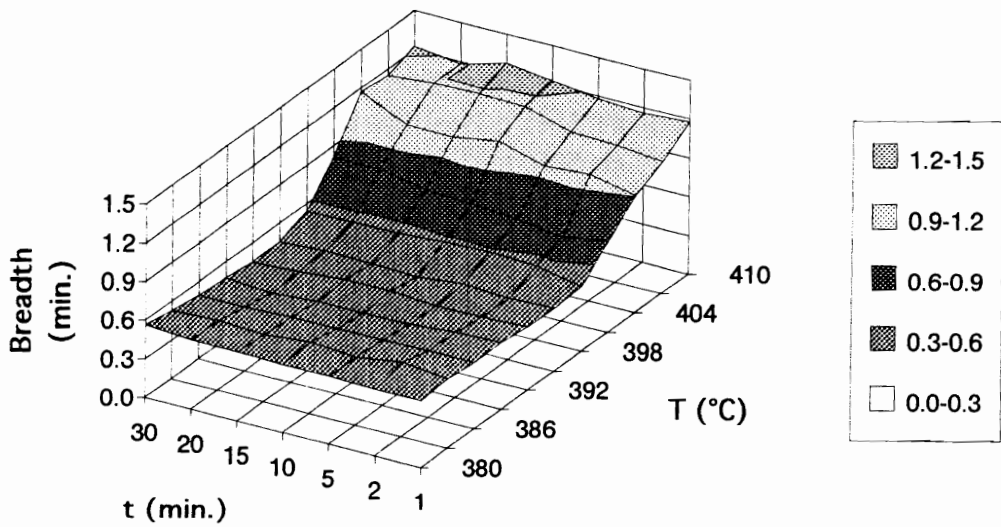
Figure 4.8c   Peak breadth (onset to end) in minutes for ITX determined as a function of time (1-30 min.) and temperature (380-410 °C) in the melt when cooled at 36 °C/min. in nitrogen.
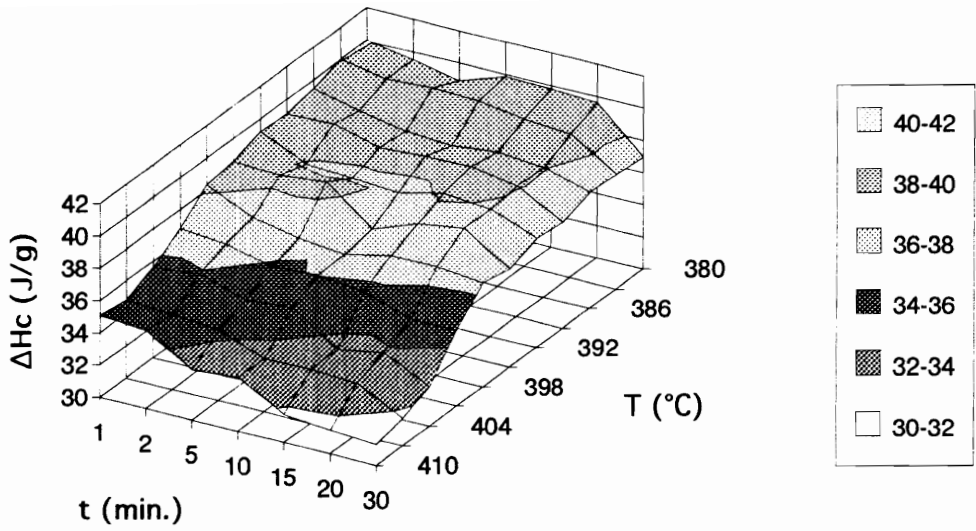
Figure 4.8d — Heat of crystallization for ITX determined as a function of time (1-30 min.) and temperature (380-410 °C) in the melt when cooled at 36 °C/min. in nitrogen. NB: z-axis range = 30 - 42 J/g.

increases in severity. As the melt treatment temperature increases, even short times in the melt are sufficient to shift the crystallization onset and peak temperatures lower, diminish the ultimate crystallinity generated within the crystallized specimen, and increase the time frame over which the process occurs. Finally, when the effects of both time and temperature are combined, the response to both variables is additive, and in the same detrimental direction. Overall, increasing the melt time and temperature that ITX endures before crystallization influences the crystallization profile as defined by four factors: crystallization onset and peak temperatures, crystallization peak breadth and heat of crystallization. The effect of melt time and temperature on each factor will now be discussed individually.

4.3.2.1 ITX Crystallization Onset and Peak Temperature as a Function of Melt Time and Temperature

In both crystallization temperature data sets the general trend is the same, as either time or melt treatment temperature increases, the onset and peak temperatures observed shift downwards in magnitude. The plots in Figures 4.8a and b summarize the effects of increasing time and temperature in the melt on the crystallization behavior of ITX. The onset of crystallization temperature, T_{co}, decreases approximately 36 °C over the range tested, from 303 to 267 °C for specimens treated to 380 °C/1 min. and 410 °C/30 min. thermal histories respectively. The temperature of the crystallization peak maximum, T_{cp}, displays a similar trend. T_{cp} drops from 293 to 246 °C, a decrease of 47 degrees, for tests carried out at the 380 °C/1 min. and 410 °C/30 min. thermal history extremes. [The temperature decrease for T_{cp} is greater than that of T_{co} because it also carries information on the time it takes to complete crystallization, as well as the temperature shift associated with the onset of crystallization. This point will be

addressed in greater detail in the next section.]

The observed shift in the crystallization temperature of ITX as a function of thermal history is significant because the crystallization temperature influences the morphology of the material which is generated. Microstructural fluctuations in spherulite size, lamella thickness and spherulite organization can have a profound effect on the properties of semicrystalline polymers, and crystallization temperature can in turn influence each of these variables [10, 22, 132]. The Thomson-Gibbs expression shown in Equation 4.1 relates one property, the observed melting temperature of a semicrystalline material, to lamellar thickness, ℓ, which is itself a function of supercooling, ΔT ($\Delta T = T_m°-T_c$) according to the following relationship:

$$T_m = T_m ° \left(1 - 2 \, \sigma_e/(\Delta H_f) \, \ell \right) \qquad (4.1)$$

where: $T_m°$ is the equilibrium melting point (when $x \gg \ell$),
T_m is the observed melting temperature,
σ_e is the fold surface interfacial free energy, and
ΔH_f is the heat of fusion per unit volume of crystal [104, 133, 134].

The data in Figures 4.8a and b show that more severe processing conditions shift the observed crystallization temperature downwards, which increases the supercooling at T_c. Since lamellar thickness is inversely related to supercooling, the microstructure of the spherulites formed as Tc drops will be affected correspondingly, i. e. ℓ will decrease as T_c decreases. Consequently, Equation 4.1 states that the observed melting temperature of the material generated will also decrease, and this is what is observed. Processing ITX at "higher" temperatures or for "longer" times will affect its thermal characteristics. The experimentally determined melting temperature of "severely" processed material will be lower, the peak broader, and therefore its useful temperature range diminished relative to that of material that sees less rigorous thermal processing.

In fact, the melting peak broadens such that it is difficult to integrate the experimentally determined heat of fusion values consistently. For this reason, only the heat of crystallization data is reported in this portion of the study.

Spherulite lamellar thickness is not the only microstructural variable which can affect the properties of a high performance semicrystalline polymer or polymer composite. Schultz has also shown that the mechanical properties of PEEK are a function of average spherulite size, a variable which is also affected by the crystallization temperature and the molecular weight of the polymer [132]. In work with isotactic polypropylene, he has also correlated crystalline microstructure to tensile strength, impact strength and fracture mode of spherulitic semicrystalline materials [10].

In summary, the lamellar thickness, as monitored by observed melting temperature, is apparently affected by the crystallization temperature used to generate ITX's crystalline microstructure. Now, what if instead of remaining constant, the crystallization temperature becomes a variable within a crystallizing structure due to temperature gradients during processing? Then the crystalline microstructure and mechanical properties of the semicrystalline material can become exceedingly complex and unpredictable using the simple models that generally assume constant melt and crystallization conditions throughout a process. The implication is that if thermal gradients during processing expose different regions of a complex part to different melt temperatures, the final part may exhibit a range of spherulitic microstructures and thermal properties.

4.3.2.2 Crystallization Peak Breadth as a Function of Melt Time and Temperature

Examination of the next three-dimensional plot, crystallization peak breadth as a

function of thermal history in Figure 4.8c, shows that peak breadth [defined by extrapolated onset and end points on a DSC crystallization curve] is also influenced by thermal history. The plot shows that with increasing temperature and time in the melt, the overall crystallization process takes longer. Broader DSC peaks are generated, increasing in duration from 0.5 to 1.2 min., which indicates that ITX crystallization can take more than twice the time for completion when the material is melted under more rigorous conditions before processing. The time difference between the high vs. low temperature and long vs. short time melt treatments is not the only significant point. Since the crystallization process occurs over an increasingly longer time range, it is therefore also occurring over a correspondingly wider temperature range (~20 versus 40 °C) under dynamic cooling conditions. In fact, as the cooling rate increases, the variations in crystallization temperatures that any region can experience are compounded. As the temperature range is magnified, so will the variations in crystalline microstructure that any one part will contain.

4.3.2.3   Heat of Crystallization as a Function of Melt Time and Temperature

The next factor considered in this melt time-temperature three-dimensional format is heat of crystallization for ITX as a function of thermal history. As mentioned earlier, Figure 4.8d summarizes the crystallization results from seventy-seven distinctly different thermal treatments, and again the variable under consideration, ΔH_c, is affected by thermal history. The area under the crystallization peak for the most stringent conditions (410 °C/30 min.), and therefore the relative crystallinity which develops on cooling, is reduced by approximately 20 % with respect to ΔH_c observed for the mildest melt treatment (380 °C/1 min.) examined. This decrease in crystallinity further

complicates ITX's morphology, not only can the microstructure differ as a function of crystallization temperature, but the level of crystallinity can vary as well leading to the development of a more complex crystalline structure.

4.3.2.4   ITX Crystalline Content as a Function of Melt Time and Temperature

When the heat of crystallization data just presented in Figure 4.8d is evaluated utilizing the theoretical heat of fusion determined for ITX as explained in Equation 4.2, the plot of crystalline content as a function of thermal history shown in Figure 4.8e is generated.

$$\% \text{ crystallinity} = \left(\Delta H_c / \Delta H_{f\ 100\% \text{ crystalline material}} \right) \times 100 \qquad (4.2)$$

A theoretical value for the heat of fusion of 180 J/g was utilized in these calculations. [This value was determined using the method that will discussed later in section 4.6.]

The three-dimensional data set presented in Figure 4.8e illustrates how the crystalline content varies in ITX as a function of thermal history. Since the values are proportional to the heat of crystallization data just presented, it is reasonable that the same trends are observed. ITX percent crystallinity varies as a function of thermal history, ranging from a maximum of ~22% crystallinity for the least severe pre-crystallization treatment to ~17% crystallinity for material melted for 30 minutes at 410°C.

4.3.3   DSC Melt Sensitivity Studies in Air

A similar, though not quite as extensive, melt sensitivity study was completed in air utilizing the Perkin-Elmer DSC-7 and individual powder ITX specimens as a $f(t, T_f)$
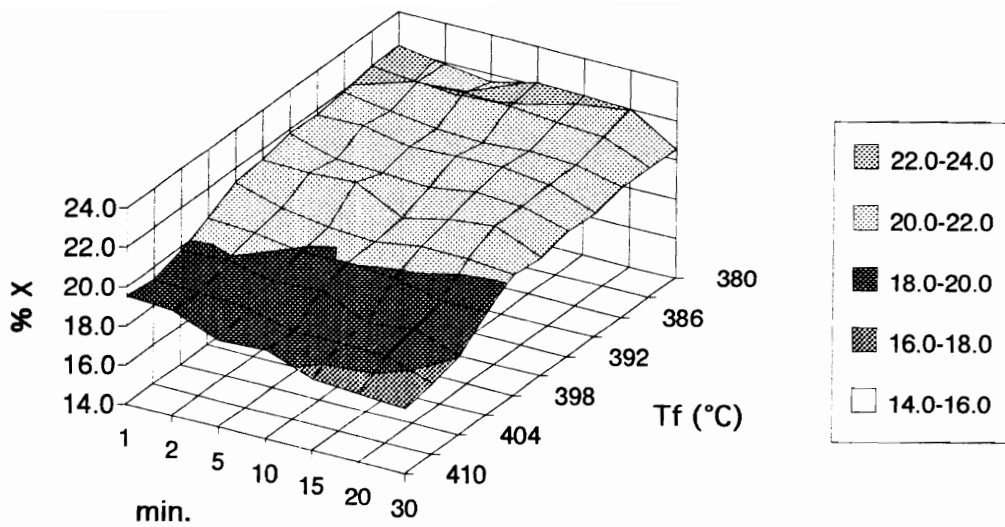
Figure 4.8e   Crystalline content for ITX determined as a function of time (1-30 min.) and temperature (380-410 °C) in the melt when cooled at 36 °C/min. under nitrogen purge. NB: y-axis range shown = 14-24 %.

The specimens were purged with air instead of nitrogen during the thermal treatment time, and crystallization process. The more extensive ITX crystallization behavior study in nitrogen was designed to mimic the actual consolidation of a composite part in a nitrogen purged autoclave. To determine if similar crystallization behavior changes occur in ITX when crystallized after high temperature melt treatment in an air environment, a reduced set of experiments was completed using the same dynamic (36°C/min. heating & cooling) profile described in section 4.3.2. However, only nine specimens were evaluated. These specimens were chosen at the minimum, median and maximum melting temperatures typical for composite consolidation, i. e. 386, 395 and 404 °C. Each melt temperature was evaluated three times utilizing melt times of 1, 15 and 30 minutes.

The air DSC data are presented in the same format as for the data obtained under nitrogen purge. Three-dimensional plots showing the crystallization onset, T_{co}, and peak, T_{cp}, temperatures as a $f(t, T_f)$ in air are shown in Figures 4.9a and b respectively. Figure 4.9c is a plot of peak breadth as $f(t, T_f)$. Finally, Figures 4.9d and e are the plots of the heat of crystallization and ITX percent crystallinity as a function of thermal history respectively.

The crystallization onset and peak temperatures for ITX melted in air show similar trends as do those for material melted in nitrogen. The temperatures measured for each decrease 30 and 40 °C respectively between the least severe (386°C/1 min.) and most severe (404°C/30 min.) melt conditions employed for this part of the study. These decreases in the observed crystallization temperatures correspond directly to those observed for ITX which was thermally treated in nitrogen. There, T_{co} again decreased by ~30 °C, and T_{cp} dropped by ~40 °C respectively over the same temperature range utilized, 386 to 404 °C. Essentially, ITX crystallizes over the same
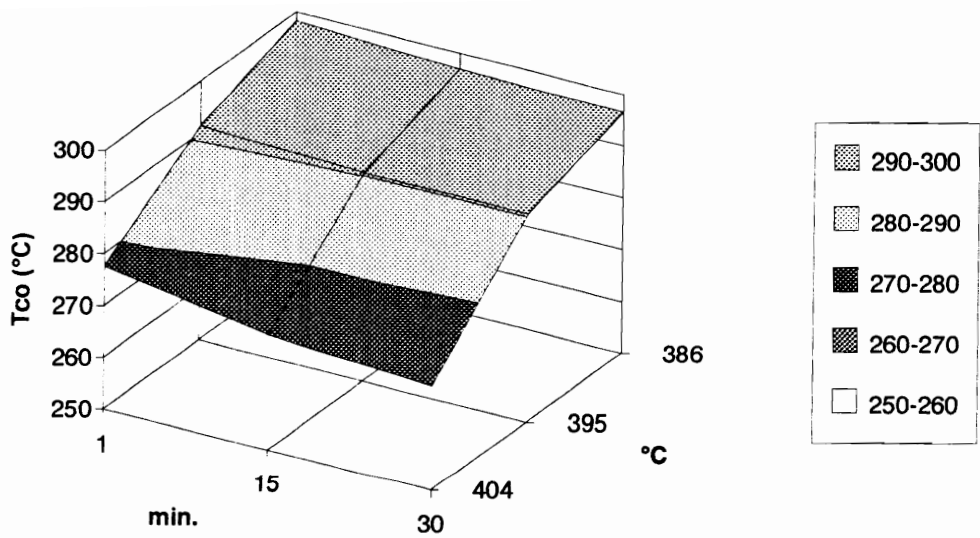
Figure 4.9a   Crystallization onset (T_{CO}) temperature for ITX determined as a function of time (1-30 min.) and temperature (386-404 °C) in the melt when cooled at 36 °C/min. under air purge.
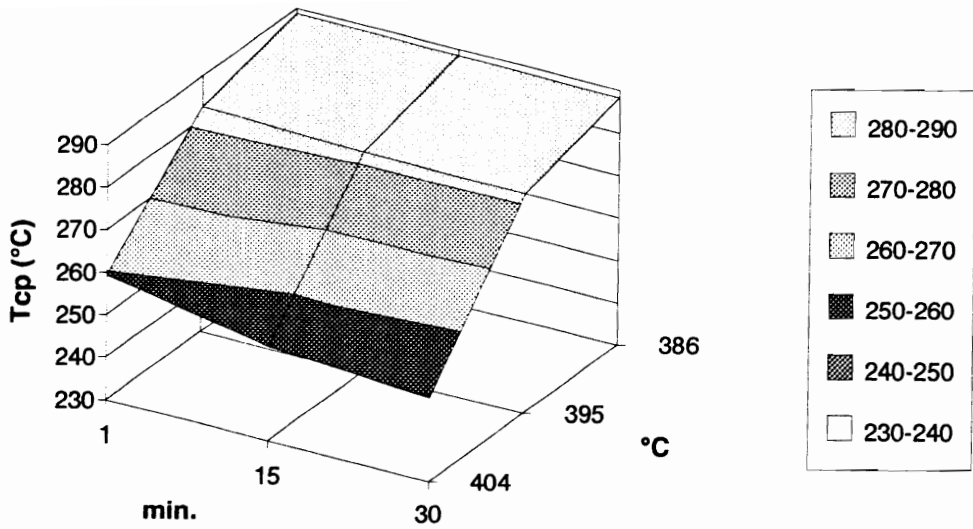
Figure 4.9b   Peak crystallization (T_{cp}) temperature for ITX determined as a function of time (1-30 min.) and temperature (386-404 °C) in the melt when cooled at 36 °C/min. in air.
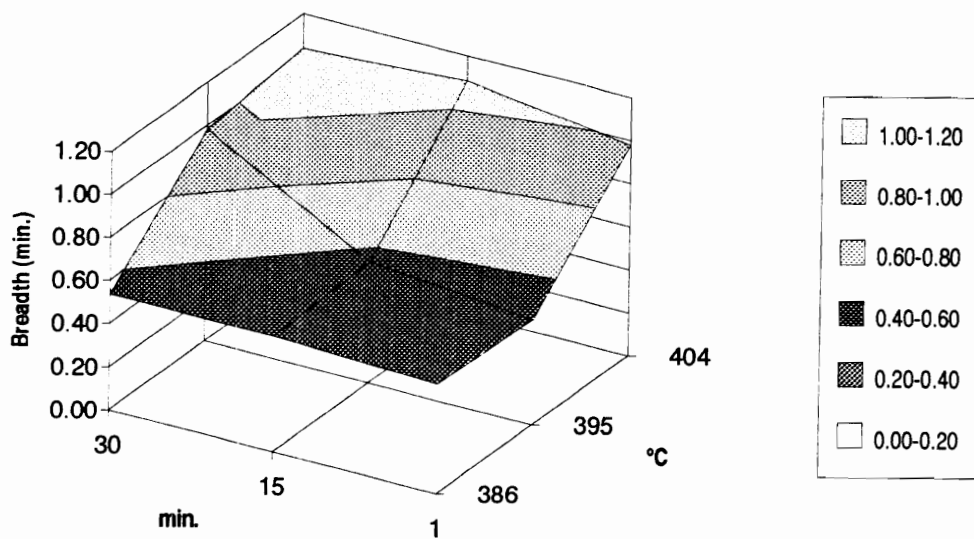
Figure 4.9c   Peak breadth (onset to end) in minutes for ITX determined as a function of time (1-30 min.) and temperature (386-404 °C) in the melt when cooled at 36 °C/min. under air purge.
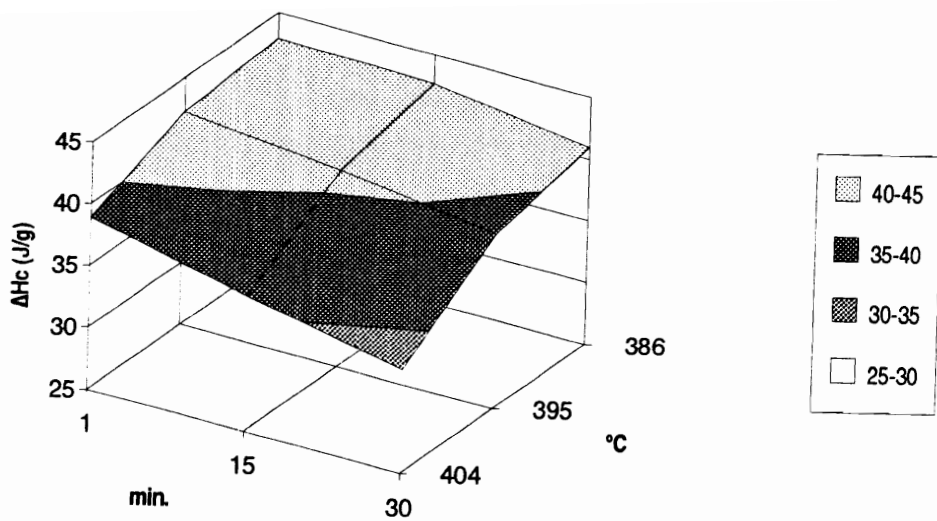
Figure 4.9d   Heat of crystallization for ITX determined as a function of time (1-30 min.) and temperature (386-404 °C) in the melt when cooled at 36 °C/min. in air. NB: y-axis range shown = 25-45 J/g.
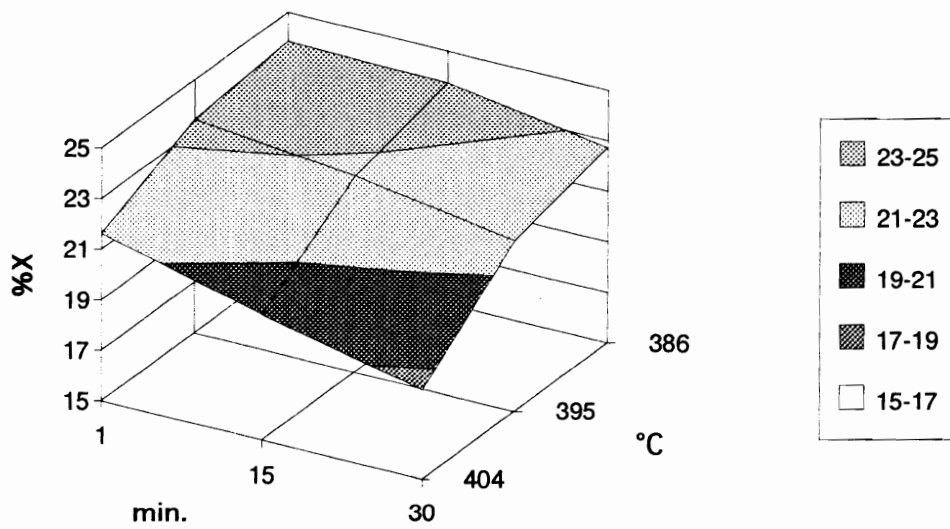
Figure 4.9e   Crystalline content for ITX determined as a function of time (1-30 min.)
and temperature (386-404 °C) in the melt when cooled at 36 °C/min. in
air. NB: y-axis range shown = 15-25 %.

temperature range whether it is thermally treated in an air or nitrogen environment under these conditions. This data suggests that for this material, processing heat history is more significant than processing atmosphere under the conditions considered.

The crystallization peak breadth, which relates to the time necessary to complete the crystallization process, again shows that it takes longer to completely crystallize ITX when the initial thermal history increases in duration and intensity. Peak breadth increases from 0.5 min. to 1.0 min. as the thermal treatment in air increases from 386 °C/1 min. to 404°C/30 min. These numbers are almost exactly replicated by the DSC data collected in nitrogen. There, the peak breadth increases from 0.5 to 1.2 min. over the same 386 to 404 °C temperature and 1 to 30 min. melt-time cycle. Here, as with the crystallization temperature results just presented, the experimental data show no significant difference in the time required to crystalline ITX evaluated in an air or a nitrogen environment.

The final variables under consideration are the heat of crystallization and crystalline content generated by ITX as a $f(t, T_f)$ in an air environment. The data for each are shown in Figures 4.9d and e respectively. These are the first parameters where the data show any differences as a function of processing environment. Even then, the differences are relatively small. The heat of crystallization decreases by 10 J/g when treated at 386 °C/1 min. and 404°C/30 min. respectively in air versus a change of 7 J/g when ITX is melted in nitrogen using the same thermal profile, for a difference of 3 J/g.

When evaluated using the theoretical heat of fusion as noted previously in section 4.3.2.4, Equation 4.2, the air data show a 5% decrease in absolute crystallinity generated as a $f(t, T_f)$ between the two extremes in treatment just as do the nitrogen data. Again, there appear to be no significant differences in the crystallization behavior

of ITX as a function of processing environment. The crystalline content generated when ITX is melted in air and nitrogen are essentially identical.

4.3.4 Summary of Crystallization Behavior as a Function of Thermal History

In summary, the observed changes in the crystallization behavior of ITX as $f(t, T_f)$ are apparently all detrimental, e. g. the level of crystallinity generated decreases, the processing time increases because the material must be cooled more extensively before crystallization occurs, and the crystallization process takes longer. More specifically, over the melt temperature-time conditions evaluated, the crystallization behavior of ITX displays the following trends.

1) The area under the crystallization peak, and therefore the relative crystallinity which develops on cooling, is reduced by approximately 20 % with respect to ΔH_c observed for the mildest melt treatment examined (380 °C/1 min.). This correlates with a drop in absolute crystallinity of ~5%.

2) Crystallization takes place within a lower temperature window, i. e. an ~40-50 °C downward temperature shift is noted for T_{co} and T_{cp} crystallization temperatures as the melt treatment conditions increase to melt temperatures and times of 410°C and 30 minutes respectively.

3) The overall crystallization process takes longer, i. e. when defined by DSC peak breadth, ITX crystallization takes more than twice as long after a severe (410 °C/30 min.) versus a mild (380 °C/ 1 min.) melt treatment. Peak breadth increases from 0.5 to 1.2 min. As a consequence, crystallization gradually occurs over a wider temperature range (~20 versus 40 °C) as the melt conditions become more severe .

4) ITX specimens display similar trends when evaluated in air instead of nitrogen. The absolute crystalline content again drops by 5% over the ICI recommended processing window, and similar types and order of magnitude changes occur in crystallization temperatures, and peak breadth characteristics.

The variations in processing conditions presented here, even though within the manufacturers recommended range for the material, are sufficient to affect crystallization behavior as was observed. The corresponding changes in crystalline content are likely to affect the physical properties and the solvent resistance of the semicrystalline matrix material that ultimately results as well.

Unfortunately, even though the trends in the data are clear, the fact remains that direct comparisons between these results and other published crystallization studies are impossible since the conditions utilized to collect this data are specific to this material and its recommended processing profile. In order to generate a more universally applicable crystallization study of ITX, the polymer must also be evaluated using recognized DSC kinetics methodology. Avrami isothermal crystallization studies are one classical means of quantifying just how extensively the crystallization behavior of ITX is affected by its processing thermal history. The next section of Chapter 4 will discuss a series of classical Avrami studies that were completed within the thermal processing window suggested by the manufacturer for ITX. In this way, the data will relate both to actual processing conditions, and to the more classical studies in the literature.

4.4   Kinetics of Isothermal Crystallization

4.4.1   Avrami Crystallization Analysis

The isothermal quiescent crystallization behavior of ITX was characterized using DSC and the well known Avrami isothermal crystallization kinetics method [106-108]. The Avrami analysis follows the normalized crystalline content within a material, at a

fixed temperature, as a function of time. As was described earlier, powder specimens were subjected to either a high (404°C) or low (373 °C) temperature 15 minute melt treatment before cooling to the isothermal crystallization temperature. A hold time of 15 minutes was chosen to mimic a typical time that this thermoplastic might see at the maximum temperature during composite processing. At the end of the hold period, the samples were quenched to T_C, the crystallization temperature, by calling for the fastest DSC cooling rate, 320°C/min.

After collection, the DSC data were transferred to a Mac IIci for integration via Simpson's Rule since the DSC-4 TADS software is incapable of evaluating data collected in the isothermal program mode [125]. Partial integrals were calculated and normalized to the total area under the crystallization peak versus time as noted in section 3.3.1.1 and 3.3.1.2. From the partial area data, the extent of conversion as a function of time was then calculated. The extent of conversion or crystallization data (weight fraction amorphous material as a function of time) were then analyzed using the standard linear form of the Avrami expression:

$$\ln\,[-\ln\,(1-X_C\,(t))\,] = \ln\,K + n\,\ln\,t \qquad (4.3)$$

where: X_C (t) or X = the normalized crystalline fraction as f (t)
K = the bulk crystallization rate constant,
n = the Avrami dimensionality exponent, and
t = time.

Using the expression in this form (Equation 4.3) allows graphical determination of the ln K (intercept) and n (slope) variables. The bulk crystallization constant, K, contains information on the temperature dependent nucleation density and growth rate for the material, and n often carries information on the dimensionality of the crystal growth

under those conditions.

The series of analyses described above were carried out for two melt treatment temperature extremes chosen to simulate the ITX composite processing window extremes, 386 and 404 °C. Lower (373 °C) temperature data sets were also collected to verify these results. The data were analyzed, and the results for the bulk conversion rate constant, ln K, as a function of crystallization temperature and thermal history were evaluated.

4.4.2 Bulk Conversion Rate Constant as a Function of Crystallization Temperature

Due to standard DSC instrument limitations, very fast (lower T_C) and very slow (higher T_C) crystallization data are experimentally inaccessible. That is, very rapid crystallization occurs at the lower temperature limit due to the high nucleation densities encountered, and the data are lost in the initial quench phase machine drift as seen in the example in Figure 4.10a. Higher temperature crystallization is slower, so data collection is limited by the longer residence times needed at higher temperatures. Two factors are important. First, long times at higher temperatures may induce possible chemical reactions (crosslinking) or degradation in the polymer. Secondly, longer data collection times also spread out the data over a broader time frame, decreasing the signal to noise ratio, and masking some of the signal in baseline drift (Figure 4.10b). The peak shapes shown in Figures 4.10a-b illustrate why isothermal crystallization could only be monitored by DSC for experiments between 270-290 °C and 304-319 °C for the high and low melt treatment temperatures respectively. All data collected were from curves intermediate to the extreme cases just described.

Figures 4.11a-b are typical example sets of Avrami data showing the progression
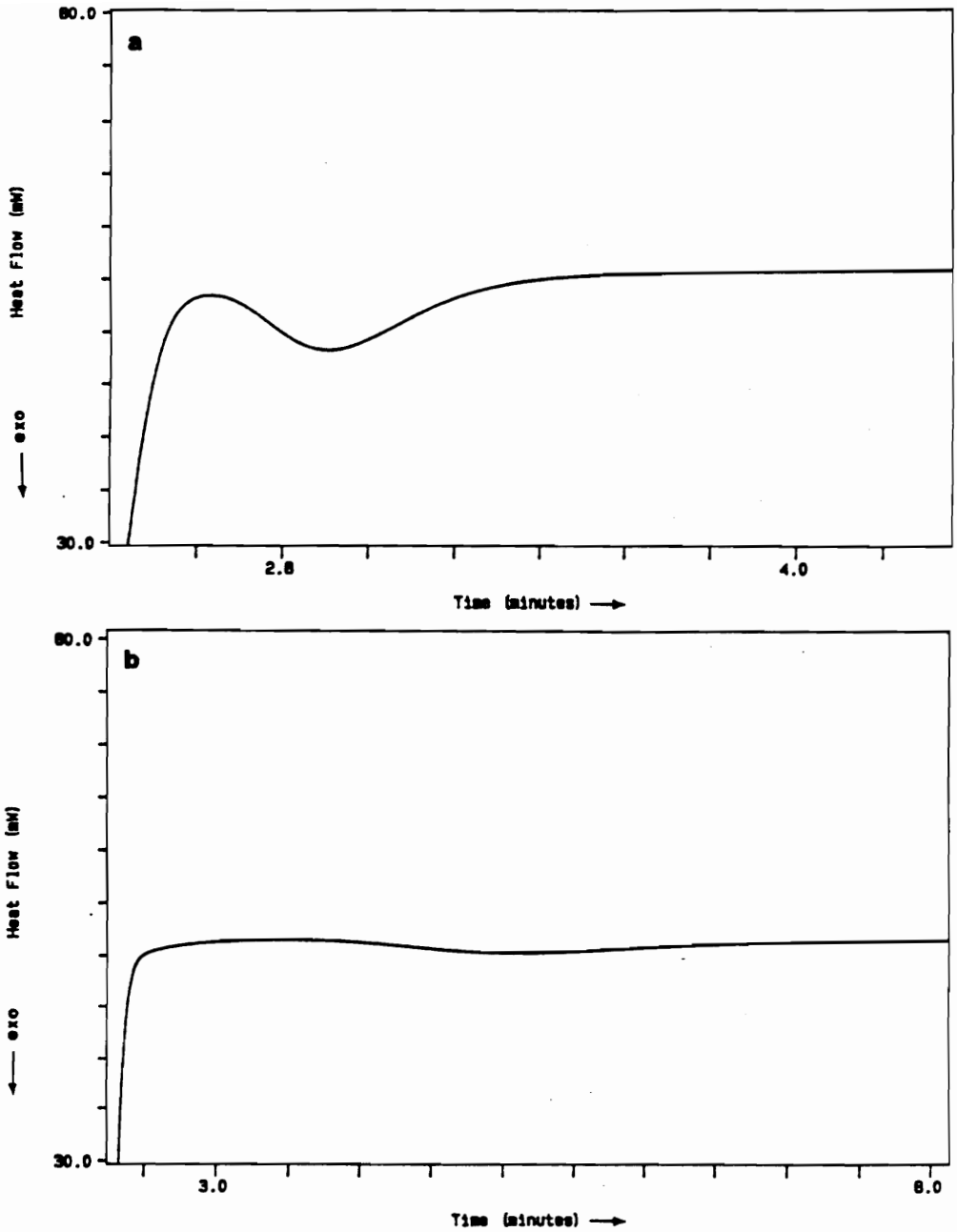
Figure 4.10a-b   DSC data showing the limiting cases for data collection: a) "low" Tc data where the initial data is lost in the equilibration process, and the b) "high" Tc case where the data is spread over a wider time range.
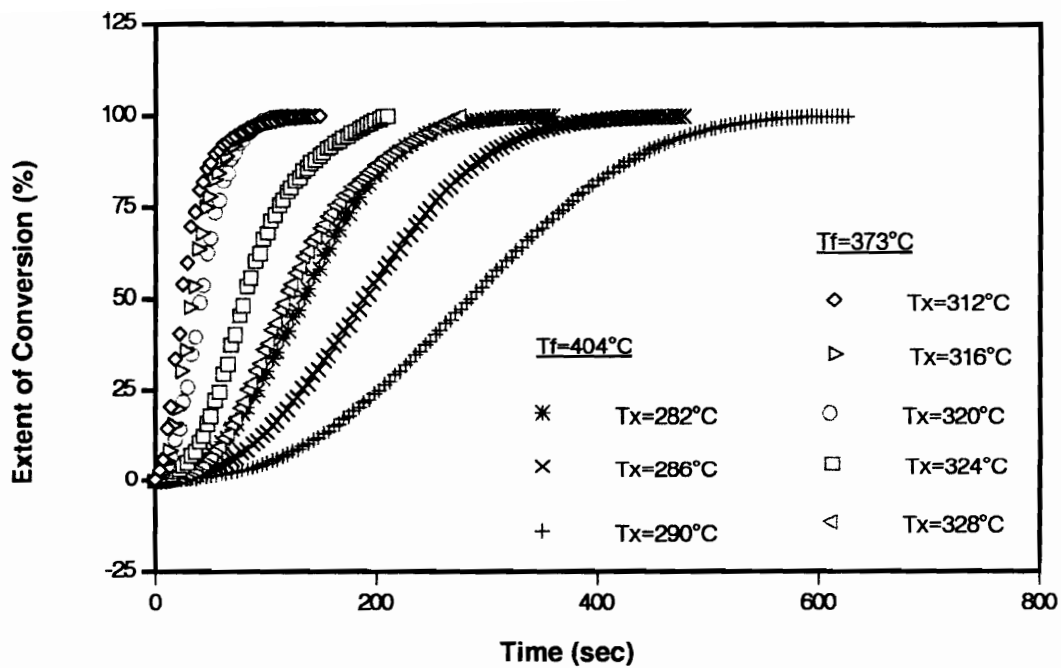
Figure 4.11a   Conversion as a function of time for several crystallization temperatures after a 15 min. melt pretreatment at 373 or 404 °C.
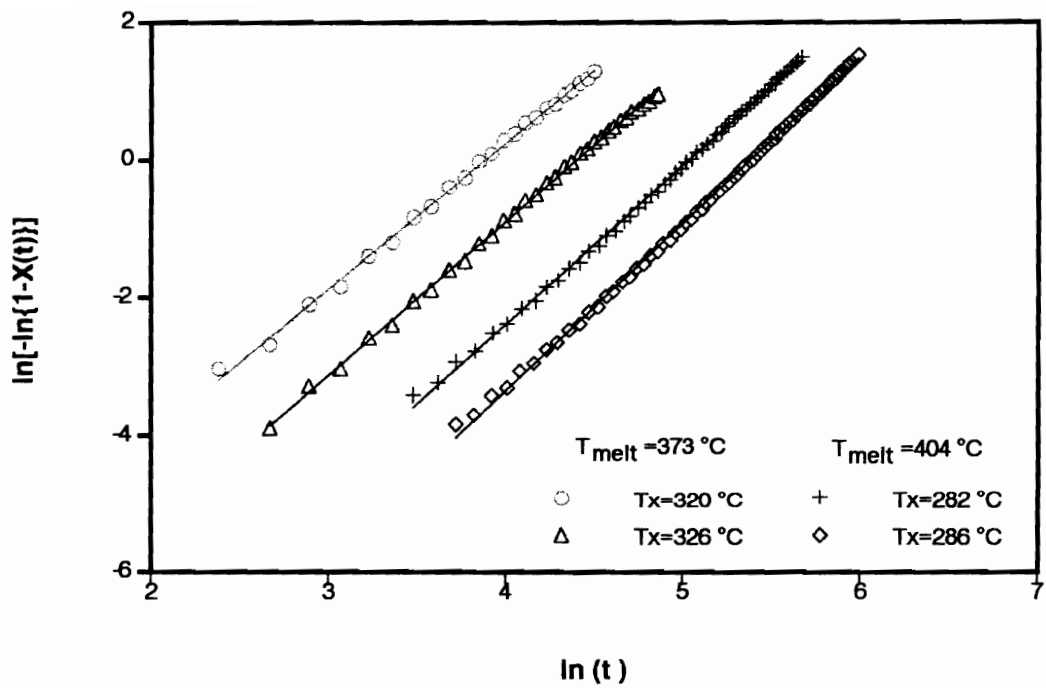
Figure 4.11b   Avrami plots for several crystallization temperatures after a 15 min. melt pretreatment at 373 or 404°C.

of analyses incorporated within this procedure. Figure 4.11a shows typical crystalline conversion versus time plots for ITX as a function of melt temperature. Conversion time decreases as T_C decreases as expected for constant treatment temperatures, but material melted at the higher melt treatment temperature takes longer to crystallize, <u>even at lower temperatures</u>. Figure 4.11b contains typical Avrami plots for ITX melted at the lowest and highest melt treatment temperatures evaluated. The lnK values are calculated from the intercept and n from the slope of a line fit to the data. Here too the ln K values behave unexpectedly, the rate constants for material melted at higher temperatures are lower that for material that sees a less severe melt treatment.

In general, the crystallization kinetics of ITX melted at 404 °C are very different from that of the polymer melted at lower temperatures as might be expected from the earlier results. Figure 4.12 summarizes the values for the bulk conversion constant, lnK, as a function of crystallization temperature for ITX specimens which saw either the high or low temperature melt treatment. Two differences in the crystallization behavior as a function of melt treatment temperature are illustrated in this plot. First, the specimens melted at the higher temperature subsequently crystallized at lower temperatures than did the lower melt treated specimens. These lower T_C values observed for the 404 °C specimens are consistent with the earlier data suggesting that nucleation density greatly decreases with higher melt temperatures. Hence, greater supercooling is required to promote crystallization within the same time scale as seen previously.

The second significant difference in behavior between the two data sets is that the specimens which crystallized at the *lower* temperatures were those that were quenched from the *higher* melt treatment temperatures. They have smaller bulk crystallization rate constants than did the other specimens which crystallized at higher T_C's after quenching from the lower melt treatment temperature as noted earlier. This is
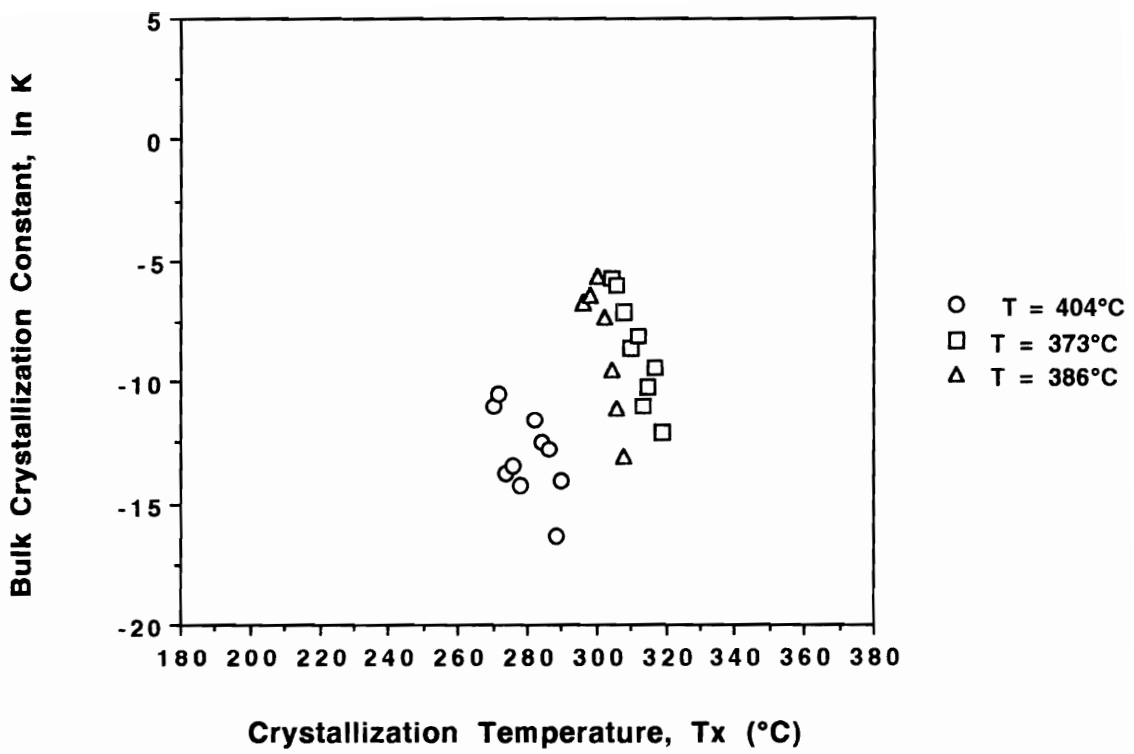
Figure 4.12   Bulk crystalline conversion constant, ln K, as a function of melt treatment temperature and crystallization temperature. Note that instead of the conversion rate increasing as expected for the material crystallized at lower temperatures, it decreased with higher temperature melt treatment.

the exact opposite of what is expected on the basis of supercooling arguments alone. Bulk crystallization rate constants often follow a somewhat bell shaped curve; increasing to a maximum moving upwards from the T_g, and then decreasing again as the equilibrium melting temperature is approached. The ITX crystallization data all fall to the right of the maximum, within the "nucleation control" regime of crystallization, where conversion rate should increase as T_C decreases.

If N is drastically reduced as suspected, it is reasonable that its reduction should be echoed in the K values measured for the two different melt treatments as shown in the following expression for ln K. For the case of heterogeneous nucleation, assuming three-dimensional growth, the nucleation density, N, is directly related to K as follows [106]:

$$\ln K = \ln N + 3 \ln G + \ln (^{4\pi}/_3) \qquad (3)$$

where G is the linear crystalline growth rate at a temperature. The trend suggested above is observed in Figure 4.12, the ln K values for the specimens melted at 404 °C are orders of magnitude lower than the 373 °C data, even though G typically increases with increasing supercooling in a manner similar to that described for ln K.

In summary, the behavior exhibited by the ln K data again supports the observation that higher melt temperatures and/or longer melt times either reduce the nucleation density, or initiate degradation in ITX. This physical or chemical change is a function of thermal history, and is reflected in the crystallization kinetics of the material. The next step is to monitor the semicrystalline morphology of ITX as a function of melt treatment time and temperature to determine if the microstructure of the material is affected by processing as well. Before moving on to the morphological studies, the reproducibility of the ln K data just presented will be discussed.

4.4.3 Analysis Reproducibility

The application of the Avrami method to the crystallization of semicrystalline polymers is well established. As described in the literature review, several researchers have examined the variation in the Avrami data collected utilizing this analysis method, and have suggested numerous corrections and limitations to the method [109-115]. In this section, the selection of a data set for analysis, and the integration method utilized will be examined in more detail.

In order to verify the validity of the trends in crystallization behavior for ITX as a function of thermal history, the reproducibility of the data will be evaluated by examining the effect varying each <u>analysis</u> parameter has on the ln K term. The experimental evaluation variables that will be examined include:

1) crystallization peak integration start & stop limits,
2) integration baseline choice , and
3) whether the full or partial conversion as f(t) data set is fit for the Avrami analysis.

A series of analyses were completed to evaluate the effect the three variables, integration limits, baseline choice and conversion limits have on the Avrami bulk conversion rate constant. The discussion here summarizes the results for one typical ITX isothermal crystallization data set (T_f = 386 °C/T_c = 298 °C) which was examined by systematically varying these variables. The crystallization peak integration baseline and limits utilized in this discussion will be denoted as tangent, 3° polynomial, linear baseline (short "tail" or time), and linear (long "tail" or time). Their significance is as follows:

- the term "tangent" is used to describe a linear peak integration baseline which was established by drawing a tangent to the DSC crystallization curve at the end of crystallization, after the heat flow signal restabilized,

- the notation "3° polynomial" is used when start and stop limits for the integration are chosen visually, and a 3-rd order polynomial was fit to those limits to establish an integration baseline,

- the "linear (short tail)" description is given to the crystallization data sets which were integrated using a standard, linear baseline between chosen start and stop limits, and where the chosen end of crystallization was taken at as short a time or "tail" on the curve as possible, and finally

- the nomenclature "linear (long tail)" describes the case where integration limits were chosen at a longer time to determine how sensitive the analysis was to the integration end limit.

The plots in Figures 4.13 a, b and c illustrate the evaluation limit and baseline choices that were just described, and applied to the data for ITX crystallized isothermally at 298 °C after melting at 386 °C for 15 minutes. Figure 4.13a shows the millivolt DSC signal as a function of time as well as the tangent baseline evaluation method which is one option on Mettler DSC instrumentation [135]. The tangent was drawn by visually choosing where the signal stabilized, in this case at ~2.2 minutes into crystallization, and drawn across the data. Figure 4.13b is a similar plot for the same data set, however, here the start and stop limits are chosen by inspection, and the baseline choice is the polynomial fit to the data described earlier. This method was chosen to approximate the curved sigmoidal integration baselines offered on several commercial systems. Finally, Figure 4.13c illustrates the linear baseline integration method typically offered by Perkin-Elmer, TA Instruments, and Seiko Instruments and others. Here the start and stop limits are again chosen by inspection, but two separate end limits were taken to determine if the Avrami data were more consistent when the end point was taken at a longer or shorter time after the crystallization peak stabilizes. The two peak end times evaluated were 2.04 and 2.58 minutes into crystallization respectively, with the start of the integration taken at 0.60 minutes for both data files.

The plots in Figures 4.13 a-c were used to determine the start and stop limits for the numerical integrations used in evaluating the crystallization behavior of ITX as described earlier in Chapter 3. After the limits were chosen, the data were integrated, and partial areas calculated as a function of time. Next the partial area data was utilized to calculate the conversion as a function of time. Finally, the conversion data was used to complete the Avrami analysis plot of $\ln[-\ln(1-X(t))]$ versus $\ln(t)$, where $\ln K$ is calculated as the intercept of the line fit to the data.

An example data set showing the next step in the process is shown in Figure 4.14 where the Avrami plot for ITX crystallized at 298 °C, and integrated with a 3-rd order polynomial baseline. This figure also illustrates the final variable under consideration in this discussion, the selection of the data set range selection utilized in the Avrami analysis, i. e. % conversion range "start and stop". When the Avrami analysis is completed, only a portion of the conversion data is incorporated into the final step. Often the short and long time data show more scatter than do the data within e. g. the 15-50 % conversion range. As crystallization progresses, the curve may deviate from linearity as impingement occurs. The two data sets shown are designated as the "full" data set (+) and the "partial" (·) data sets. The purpose of this portion of the analysis is to determine whether, and how, the Avrami results are affected by this screening. The main focus of this analysis is the $\ln K$ term, however, some Avrami dimensionality or "n" data is also included to illustrate the variation in this term as well.

The bulk conversion rate constant ($\ln K$) data generated by examining the Avrami integration and analysis procedure are summarized in Figure 4.15. The $\ln K$ results ($\ln$ scale) are shown as a function of analysis method on the y-axis, and as a function of the data set size used for the Avrami plot. Table 4.1 compiles this data, including the Avrami dimensionality or "n" term, and the standard deviations calculated for the results.
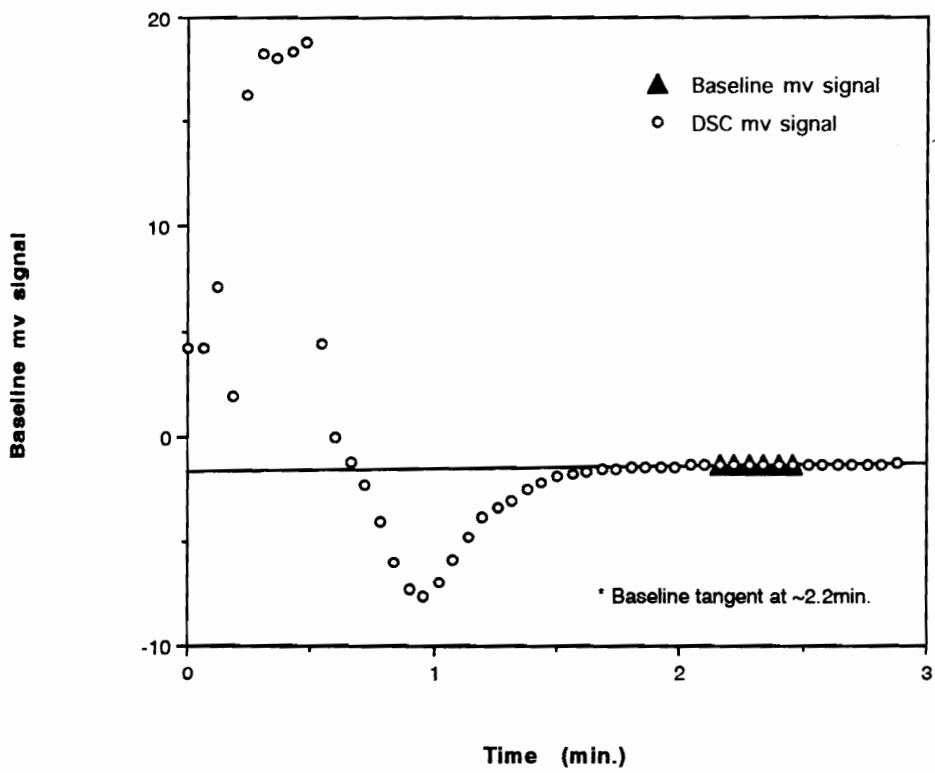
Figure 4.13a   Millivolt DSC signal as a function of time for the tangent baseline crystallization peak integration method.
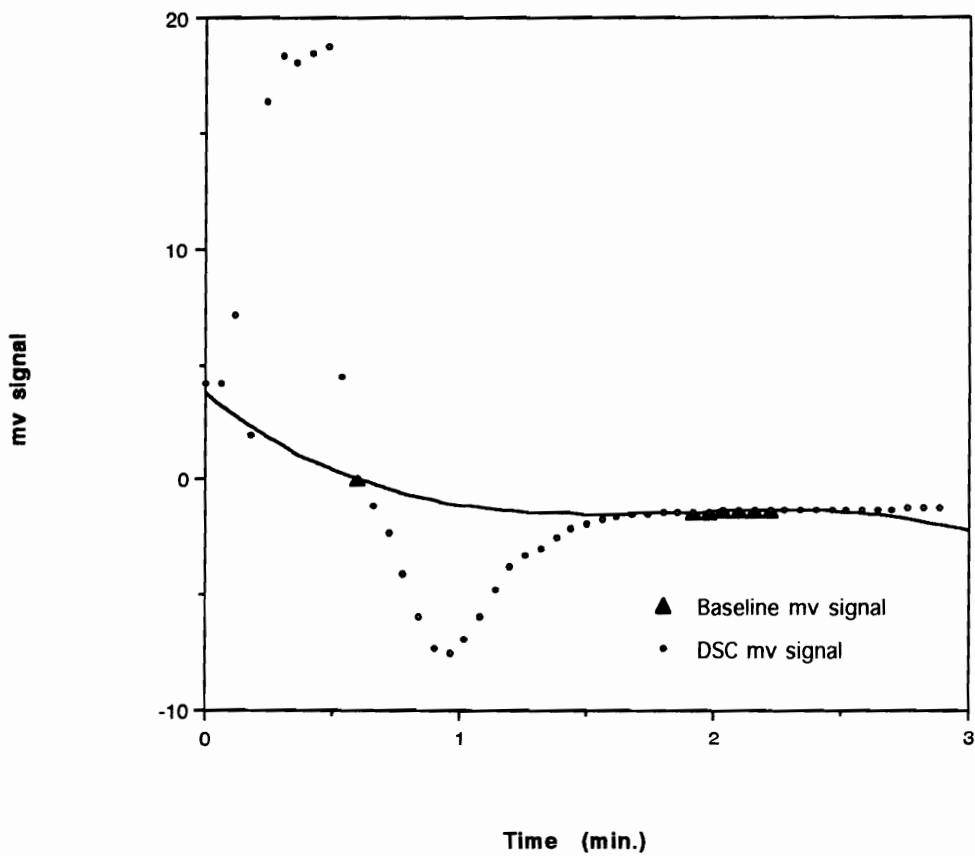
Figure 4.13b   Case number two where the start and stop integration limits are chosen by inspection, and the baseline is a 3 ° polynomial fit to the data.
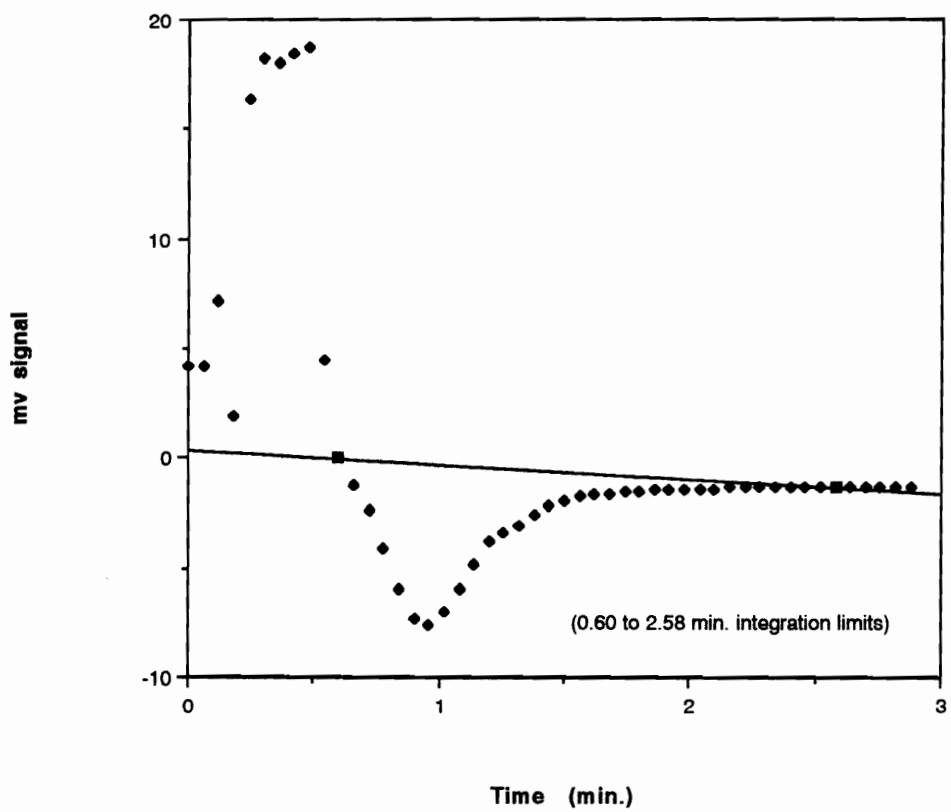
Figure 4.13c   Linear baseline integration method: start and stop limits are chosen by inspection, and two separate end limits (2.04 and 2.58 minutes into crystallization respectively). Longer time limit case illustrated.
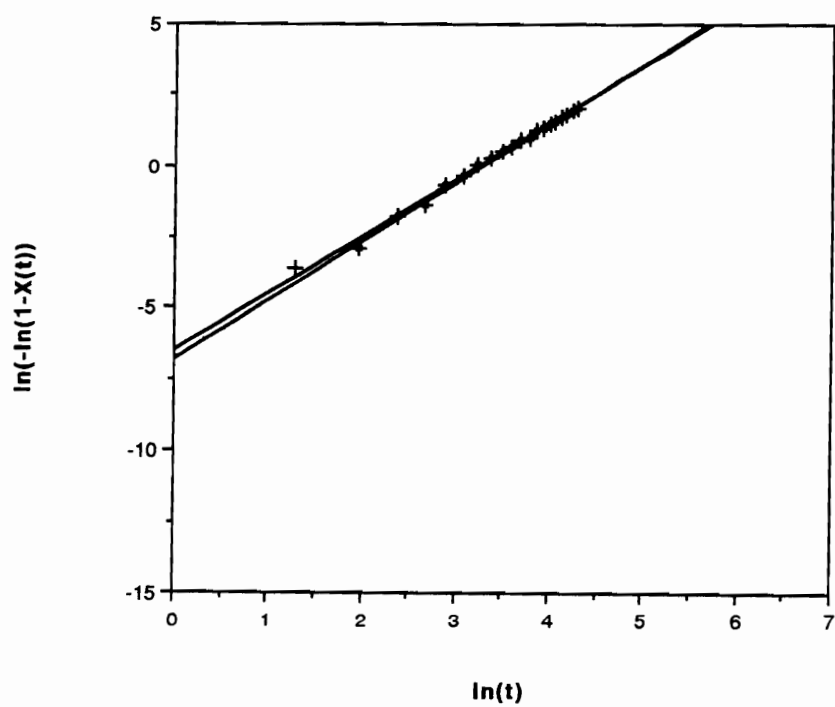
Figure 4.14   Avrami plot for ITX crystallized at 298 °C after melting at 386 °C for 15 min.   The data set was then integrated with a 3-rd order polynomial baseline.
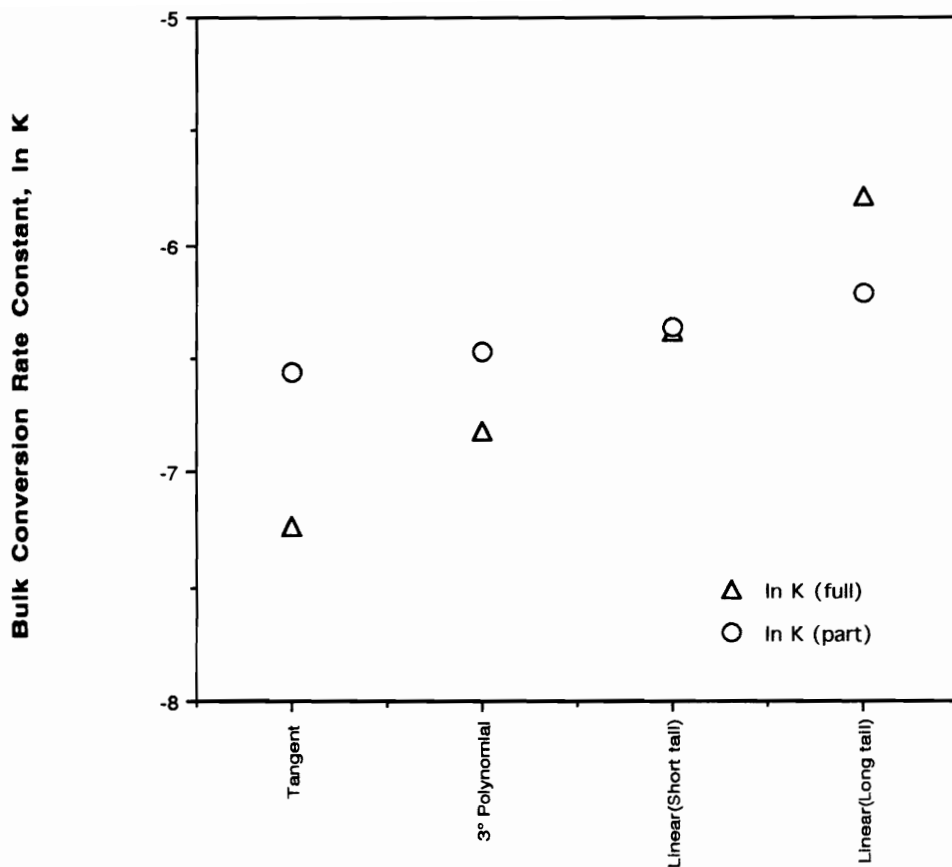
Figure 4.15   The bulk conversion rate constant (ln K) data generated by
                      examining the Avrami integration and analysis procedures.

Table 4.1 Variation in the Avrami bulk conversion rate constant (ln K) and dimensionality exponent (n) as a function of analysis parameters. The specimen used for this analysis was melted at 386 °C for 15 min. prior to crystallization at 298 °C.

Analysis Method	n (all data)	n (partial set)	ln K (all data)	ln K (partial set)
3° Polynomial	2.09	2.00	-6.82	-6.47
Tangent	2.14	1.98	-7.23	-6.55
Linear(Short tail)	1.88	1.89	-6.38	-6.36
Linear(Long tail)	1.62	1.78	-5.78	-6.21
Mean	1.88	1.88	-6.46	-6.38
Standard Deviation	0.26	0.10	0.73	0.17

The most prominent feature of the ln K data shown in Figure 4.15 is that the standard deviation of the results is the greatest (ln K = -6.55 ± 0.62) when the full conversion range (~ 0-100%) is used for the Avrami plot, and much smaller (ln K = -6.40 ± 0.15) when the data are limited to the linear region of the ln[- ln (1-X (t))] versus ln (t) plot for each analysis. In addition, the different integration choices contribute to the scatter in the ln K values determined. The two most extreme values result when the data are integrated with a tangential baseline (low value), or with a linear baseline long-time endpoint (high value). The case where a linear baseline, and shorter time limits are chosen results in almost identical ln K results for both the full and partial data sets.

If only the "partial" data set examples are considered now, another important feature of the data can be observed. There appears to be little statistical difference in the ln K results as a function of integration method if the data incorporated in the final step of the Avrami analysis are restricted to the linear portion of the curve. Only the "tangent" case data is slightly greater than one standard deviation away from the calculated mean of the results. It appears that the choice of baseline and integration limits are less critical to the reproducibility of the final ln K and n results than the selection of which data to incorporate in the Avrami plot.

4.5   Morphological Studies

The purpose of this section of Chapter 4 is to examine the semicrystalline morphology of ITX as a function of processing variables, i. e. melt time and temperature. If the nucleation density (N) within the ITX melt is affected by thermal history as suspected, the effects should be reflected in the semicrystalline morphologies which result from the two extreme melt treatments. Melting ITX at a lower temperature should leave a high N, resulting in a fine crystalline texture, whereas a lower N should remain

after a high temperature melt, generating a coarser crystalline microstructure. These studies are discussed in section 4.5.1.

An additional variable, the effect of adding a few carbon fibers to the ITX melt was also investigated. Carbon fibers are known to act as nucleating sites for some polymers, leading to the generation of transcrystalline growth along the fiber surface [see Section 2.3.3]. A series of experiments were completed to determine if incorporating fibers into ITX would give similar results, and this work will be presented in section 4.5.2.

Also included in section 4.5 are additional studies which utilize a combination of optical microscopy and differential scanning calorimetry to determine the linear growth rate, (G), of ITX as well as the nucleation density, (N), of the material as a function of thermal history. These topics are addressed in sections 4.5.3-5.

4.5.1 ITX Semicrystalline Morphology

A series of experiments were performed using polarized optical microscopy (POM) to observe the ITX crystallization process as a function of melt treatment temperature and time, and record the final morphology which resulted. Powder specimens were prepared for the morphological studies by scattering a thin layer of powder on a glass slide, and then covering the powder with a second slide. After a quick pre-melt treatment (room temperature to 360 °C @ 50 °C/min. up and down) the samples were ramped up to either of the melt treatment temperatures noted earlier, 373 or 404 °C, under a nitrogen purge at 20 °C/min. in a hot -stage. After a 15 minute hold at T_f, the polymer was cooled at 5 °C/min., and the crystallization behavior monitored.

The optical micrographs in Figure 4.16a and b show two patently different
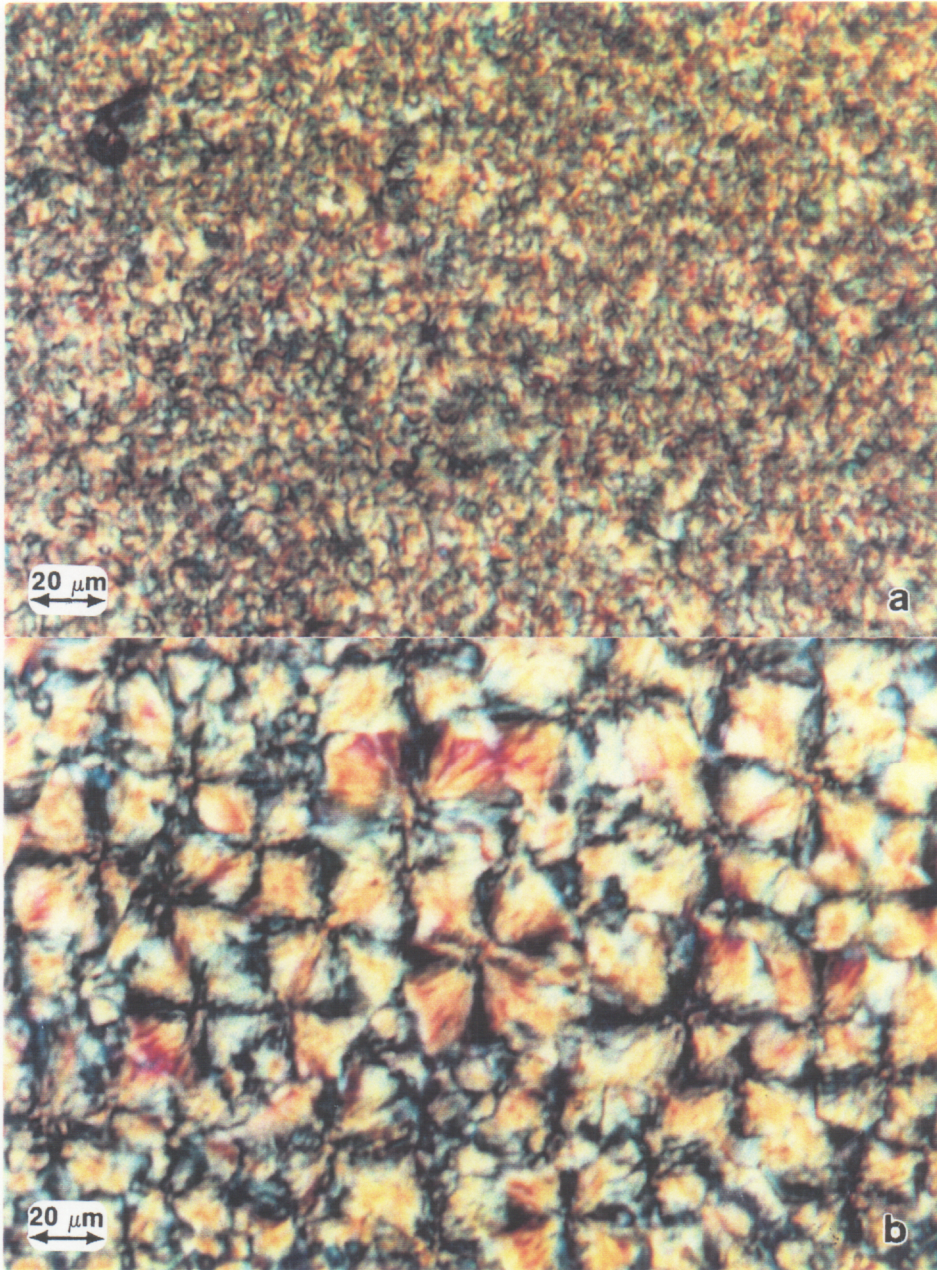
Figure 4.16a & b   Different crystalline morphologies observed for ITX as a function of thermal history. The finer crystalline texture shown (a) is the result of a melt treatment temperature of 386 °C for 15 minutes, followed by cooling at 5 °C/minute. The larger spherulitic structure shown (b) developed after melting ITX at 404 °C for the same amount of time before subsequent cooling.

morphologies for ITX, yet the magnification (156X) is the same for both. The upper micrograph showing a very fine, indistinct texture, was generated by melting the powder at 373 °C prior to crystallization. The lower photograph contains large, distinctly visible individual spherulites that are the product of a higher 404 °C melt temperature followed by an identical cooling history. These trends in spherulitic characteristics were observed consistently throughout this work, both for isothermal and dynamic cooling crystallization experiments. Melting ITX at a higher temperature resulted in a courser, more distinct spherulitic structure, while lower melt temperatures generated a finer texture.

This difference in crystallization behavior extends to rapid cooling experiments which mimic actual processing conditions as well. When ITX was cooled at approximately 30 -40 °C/min. in the hot stage during crystallization, a difference in semicrystalline morphology was clearly noted again for the two melt treatments. The specimen melted at the 373 °C temperature limit shows a finer texture than does the specimen where the material was melted at 404 °C before cooling. This is an important observation in that it suggests that these differences could develop under the actual consolidation conditions summarized in Figure 3.2.

These micrographs clearly show that any deviations in melt history prior to crystallization substantially affects the nucleation density and observed final morphology for ITX. The fine spherulitic texture is the result of innumerable nucleation sites initiating at approximately the same time. Subsequent growth is rapid, such that it takes only 1-2 minutes to completely fill the viewing region with superstructure. At the opposite extreme, the specimens melted at 404 °C before cooling nucleated slowly, often taking 7-8 minutes or longer, to completely fill in the amorphous melt region with spherulitic structures. In addition, the nucleation density was less for the 404 °C melt specimens than for the material melted at lower temperatures. This will be discussed further in the

section 4.5.4. One final difference was noted between the two observed microstructures that was of practical importance to the linear growth rate determination experiments. The nucleation density was lower, and individual spherulites were sufficiently well separated during crystallization to allow experimental measurement of the linear growth rate, G, for the material melted at higher temperatures, but not at the lower temperature boundary.

4.5.2   ITX Morphology in the Presence of Carbon Fibers

It is known that the presence of foreign matter can affect the nucleation behavior of semicrystalline materials, and is in fact the basis for the introduction of nucleating agents into polymers to enhance their crystallization behavior [98]. Another frequently observed behavior in semicrystalline materials is the phenomenon of surface nucleation and transcrystalline growth associated with semicrystalline composites prepared with thermoplastic matrix materials and reinforcing fibers [2, 4, 6, 7, 20, 22, 38, 71, 75, 85-95]. Of concern is whether the reinforcing fibers, in this case Hercules® IM-8 carbon fibers, can heterogeneously nucleate crystallization in ITX. If the surface nucleation density is high, a transcrystalline morphology can result, which may affect subsequent composite mechanical properties [71, 75, 91]. Transcrystallinity, the columnar lamellar growth habit, with crystalline growth initiating on a surface and continuing normal to the surface, is the result of restricted growth in the orthogonal direction from the fiber surface. This growth behavior has been observed in a number of polymer-carbon fiber systems including PEEK and PPS [38, 75, 85, 86, 88]. As was discussed in Chapter 2, the effect of transcrystallinity on the mechanical properties of composites is still a controversial subject in the literature.

ICl Fiberite prepares composite pre-preg pairing ITX with IM-8 carbon fibers, and therefore this system was selected for the majority of the work presented here, however other carbon fibers were initially evaluated as well. A series of specimens were prepared as follows.

Materials:
- ITX powder

- AS4 carbon fibers
- IM-8 carbon fibers

Optical Microscope Thermal Profile:

1) place fibers & ITX powder on glass slide
2) heat @ 50°/min. to 350°C (20 cc/min. N2 purge)
3) cool @ 50°/min. to RT
4) re-heat @ 50°/min. to Thold
   - T hold = 386 or 404°C
   - time = 15 minutes
5) cool @ 5°C/min. to follow crystallization

The first three steps in the thermal profile are included to introduce an initial thermal history to the polymer powder such as might be included during thermal melt pre-pregging operations. The slower cooling rate at the end of the experiment was necessary in order to observe crystallization over a reasonable time frame.

Several general trends regarding the nucleation behavior of ITX crystals emerged over the course of this evaluation. First, whether in the presence of carbon fibers, or with neat ITX resin alone, morphological texture consistently changes with melt treatment temperature. Higher melt treatment temperatures generate a distinctly larger spherulitic texture, while lower melt temperatures result in a fine texture as seen in Figure 4.17 a and b respectively. Secondly, the nucleation mode changes for ITX specimens crystallized with IM-8 carbon fibers. When ITX is melted at lower (386°C) temperatures, bulk nucleation of crystals occurs within the molten material, and growth
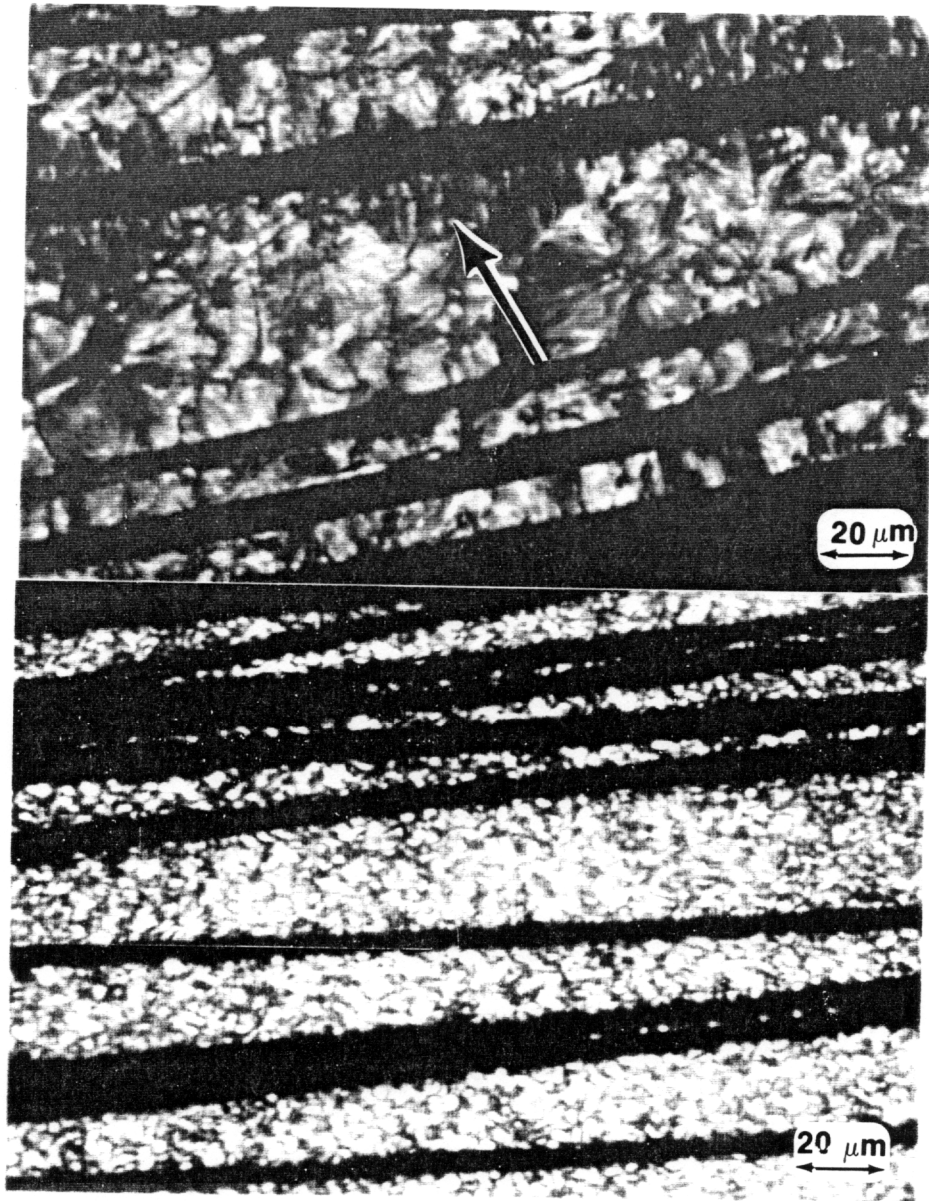
Figure 4.17 a & b   Crystalline morphologies observed for ITX as a function of thermal history when crystallized in the presence of IM-8 carbon fibers after melt treatments of 386 or 404 °C followed by 5°C/min. cooling rates.

continues in an identical manner to that observed with the neat resin. Bulk and fiber surface nucleation density initiate concurrently. The situation is different however when the polymer is melted at the higher (404°C) temperature. ITX appears to initiate nucleation off the surface of IM-8 carbon fibers first, and in some cases, develop transcrystalline regions. Transcrystallinity is not consistently present however. These trends are not repeated with the AS4 carbon fibers, there instead nucleation density appears indifferent to the presence of the fibers.

4.5.3   Linear Growth Rate Determination

The linear growth rate for ITX spherulites was determined using polarized optical microscopy (POM) for a series of crystallization temperatures. The specimens were prepared as described earlier, with the exception that each specimen was melted twice. The powder specimens were heated at 50 °C/min. to 360 °C, and immediately cooled back to room temperature at the same rate. This "first melt" served two purposes. It simulated a first melt that a powder specimen might see during a composite thermal prepregging process, and it gave all specimens a similar initial thermal history. After the specimens returned to room temperature, they were reheated to the high melt treatment temperature used in this study, 404°C. [The lower melt treatment temperature (373 °C) noted in the morphological studies section was not used in this series of studies; the nucleation density remaining after a lower temperature melt treatment was too high to follow nucleation and growth over a sufficiently long time frame for the evaluation of the growth rate.] Each specimen was held for 15 minutes at the treatment temperature, and then quench cooled (~90 °C/min.) to an isothermal crystallization temperature. Crystallization was monitored through crossed polarizers to follow the nucleation and

subsequent growth of the ITX spherulites. ITX spherulitic growth was photographed using a 35 mm camera, and the photomicrographs were used for the growth rate determinations. Figure 4.18 contains a series of optical micrographs that illustrate spherulitic growth as a function of time at 300 °C.

The data were analyzed graphically to determine the growth rate in μm/sec for each isothermal temperature evaluated. A micrometer was used to measure either the radius or the diameter of a set of developing spherulites for each crystallization temperature photograph. The measured spherulite dimensions were averaged at each time, and converted to microns from inches using the calibration factor described earlier. The time readings for the experiment were normalized to the time when the controller reached the programmed isothermal temperature. The data were plotted as the average spherulite radius versus normalized time. The slope of the line fit to the data gives the linear growth rate for each isothermal crystallization temperature as shown in Figure 4.19.

This process was completed for a series of crystallization temperatures, and the growth rate values measured for ITX melted at 404 °C for 15 minutes before crystallization are summarized in Figure 4.20a. The data show the expected trend, growth rate increases with decreasing crystallization temperatures. In addition, the linear growth rate was also determined for ITX as a function of melt time and temperature. This analysis was completed due to the ambiguity in the literature on PEEK were G has reported to be both independent and dependent on melt conditions by Kumar and Deslandes respectively [12, 20]. The results of G as f(t, Tf = 404°C) are summarized in Figure 4.20b where linear growth rate is shown for ITX melted at 404°C for a series of times (1, 2, 5, 10, 15, 20, and 30 minutes). G was also evaluated for lower melt temperatures, however incomplete data sets frequently resulted. The trend
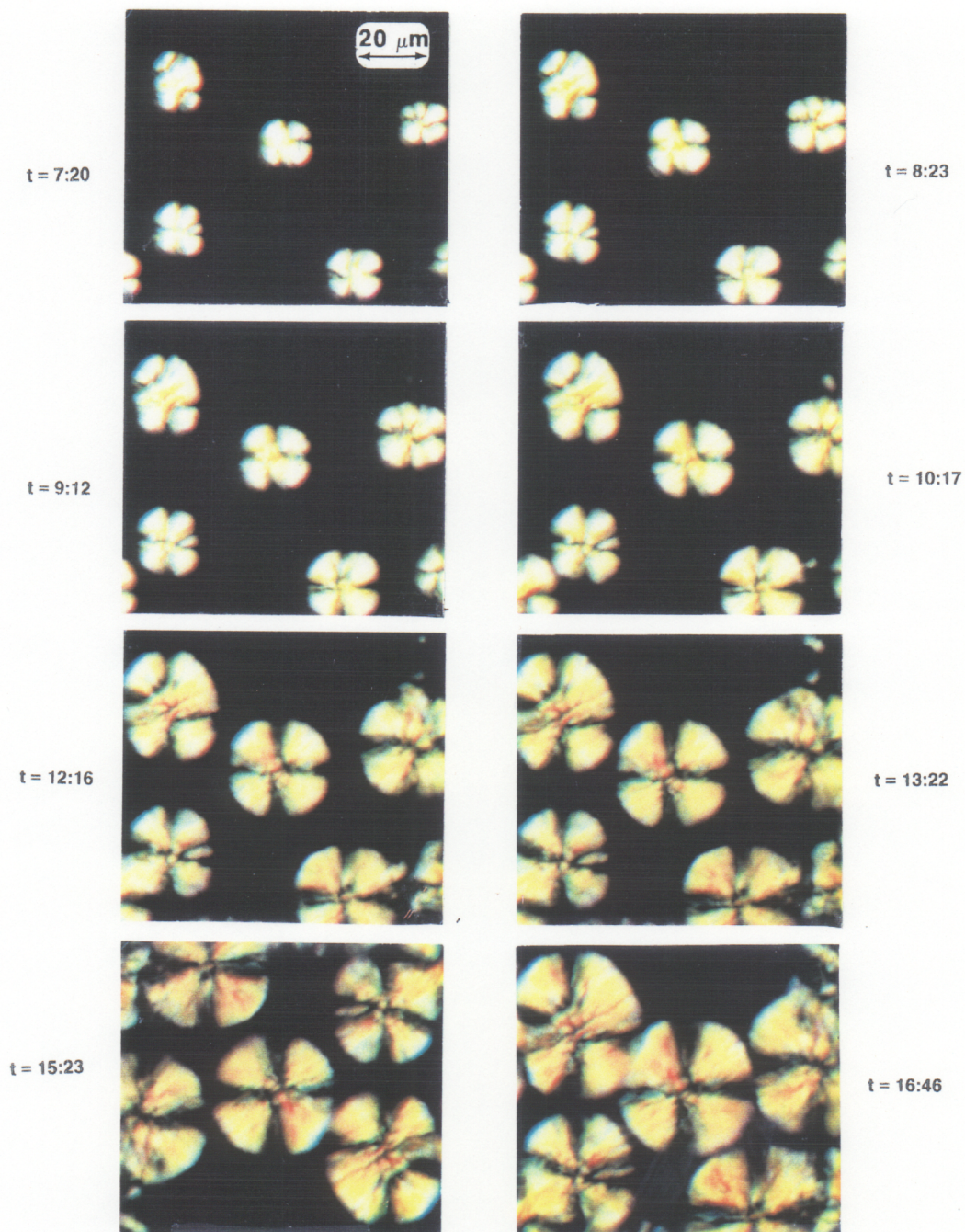
Figure 4.18   Example photomicrographs showing the crystallization process for ITX after melting at 404 °C. Times noted are in minutes at 300 °C.
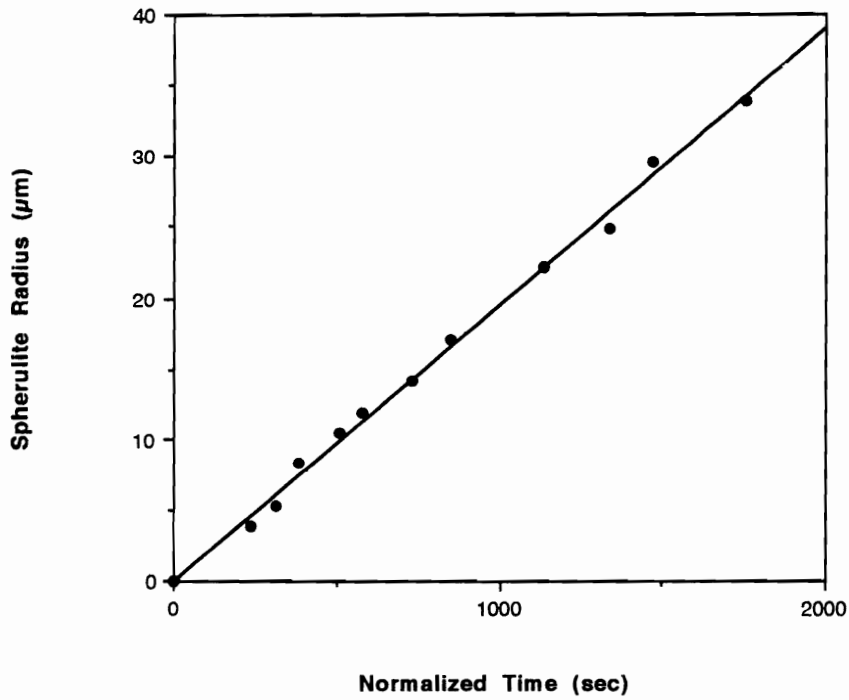
Figure 4.19 Sample ITX linear growth rate data illustrating the graphical analysis process utilized to obtain linear growth rate data. Specimen shown was melted at 404 °C for 15 min. before crystallization at 282 °C.
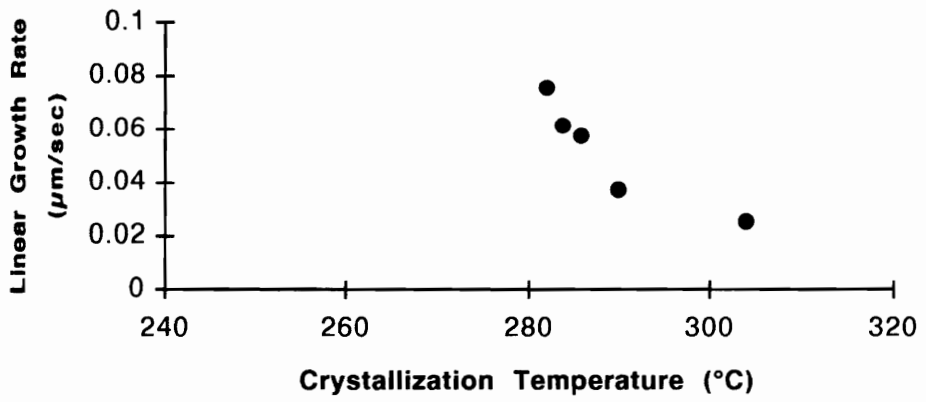
Figure 4.20a   Linear growth rate determination data for ITX powder melted at 404 °C for 15 minutes prior to isothermal crystallization at 300 °C.
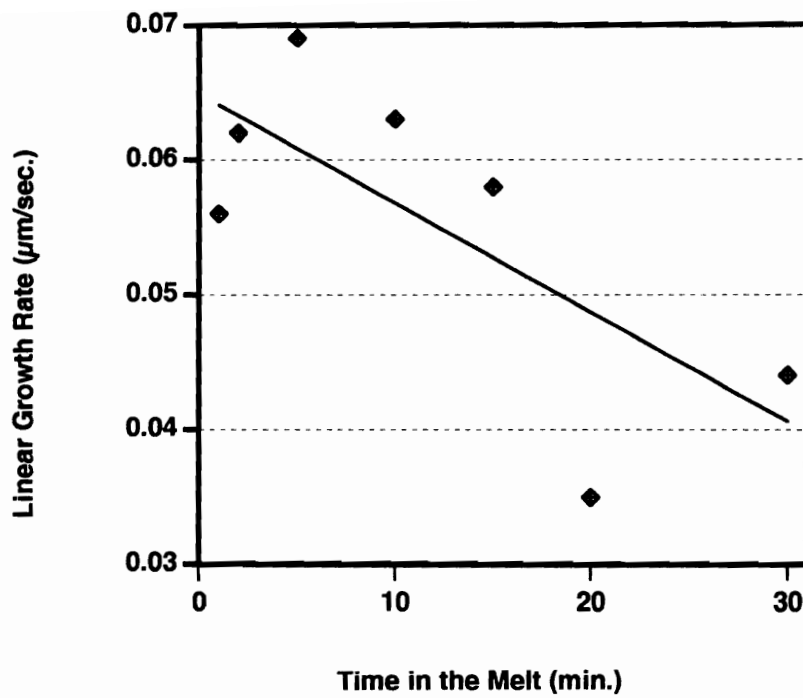
Figure 4.20b   Linear growth rate determination data for ITX powder melted at 404 °C for 1, 2, 5, 10, 15, 20 and 30 minutes prior to isothermal crystallization at 300 °C.

seen in Figure 4.20b suggests that G decreases by approximately 1/3, from ~0.06 to ~0.04 μm/sec, after ITX is held in the melt for ~30 minutes. The decrease in growth rate versus melt time is the same, down by 1/3, is the same as that noted for PEEK by Deslandes in Chapter 2 [20]. A change in the growth rate as a function of thermal history suggests that some degradation is occurring in ITX when it is melted under the more severe conditions. Thermal history may generate some level of degradation or cross-linking, which would be reflected in a decrease in the growth rate of the material as was observed.

Growth rate determinations were not possible for ITX melted at the lower melt treatment temperatures using this procedure. The data sets generated were incomplete either due to very high nucleation densities or very rapid rates precluding the analysis. The number of nucleating sites at the start of crystallization was so high that it was not possible to visually follow the growth of any individual spherulites following these methods. In addition, crystallization occurred almost instantaneously for the lower melt temperature treatment specimens, leaving insufficient time for a series of photographs.

The very obvious difference in nucleation density observed near the start of crystallization for a specimen melted at 373 °C is in marked contrast to that for ITX melted at 404 °C/15 minutes prior to isothermal crystallization as is illustrated in Figure 4.21. The initial nucleation density is much higher for ITX melted at the lower temperature than when melted at 404 °C as was predicted earlier. These micrographs suggest that the initial nucleation density in ITX is strongly affected by its thermal history. They also support the Avrami ln K values and the morphological differences already noted for the material as a function of thermal history.

The next step is to quantify any differences in the nucleation density of ITX as a function of thermal history. This calculation will be completed utilizing the G values
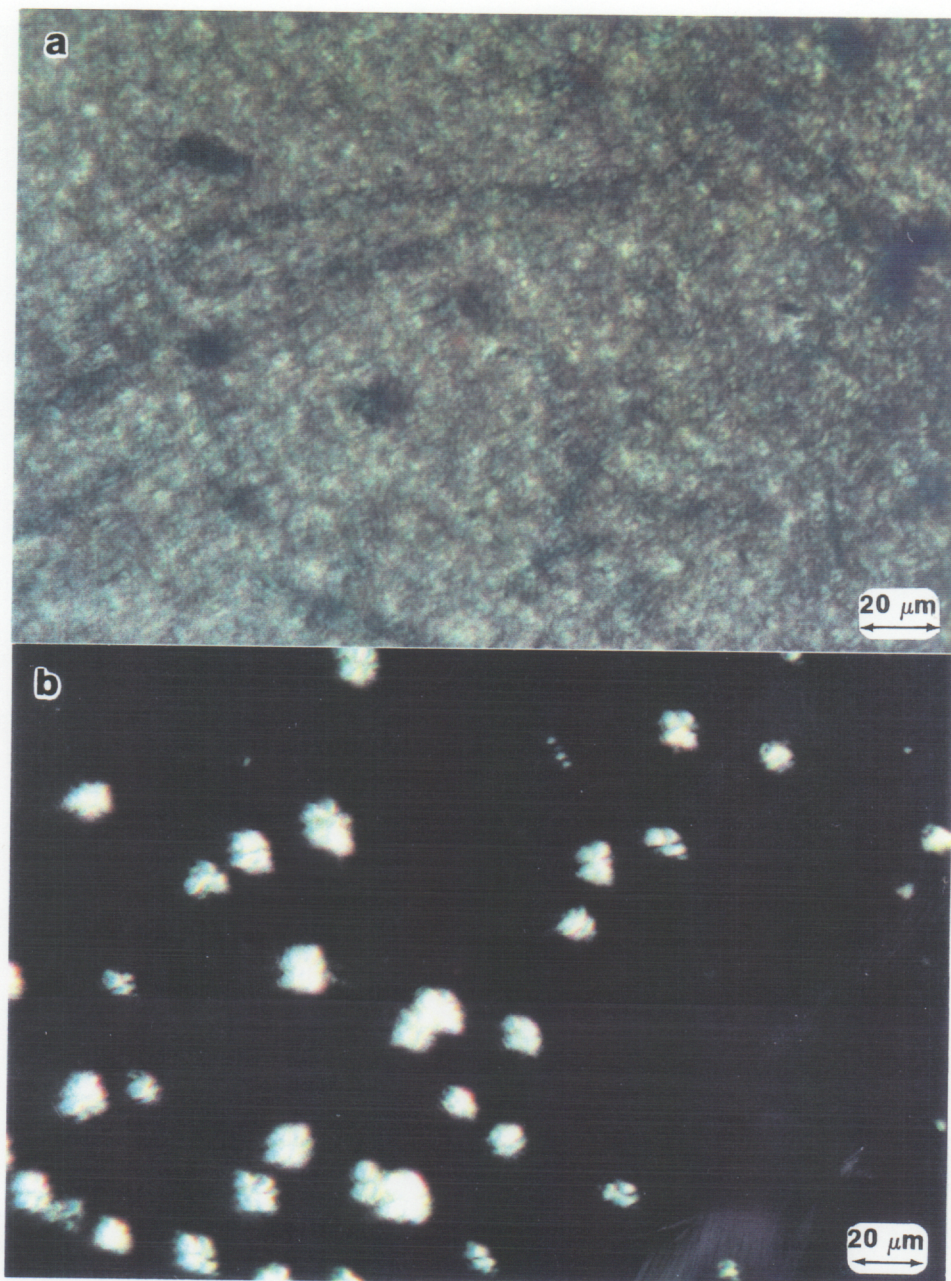
Figure 4.21   Different nucleation densities observed near the start of crystallization for ITX specimens pretreated to either a) 373 °C or b) 404 °C melt temperatures. The bright regions in the dark background indicate the nucleation sites.

determined assuming that G was independent of thermal history, and "checked" by contrasting the results to those obtained using the smaller G evaluated as f(t, Tf).

4.5.4   Nucleation Density Determination

Once the linear growth rate is known as a function of temperature, and *if three-dimensional growth is assumed*, it is possible to quantitatively estimate the nucleation density of the polymer (N), and determine if melt treatment is affecting the number of initial nucleating sites.   [Three-dimensional growth was assumed as an Avrami dimensionality exponent, n, of 2.8±0.2 was determined for ITX melted at 404 °C prior to crystallization between 270-290 °C.] This estimation for N is possible using the Avrami expression noted earlier.   For the case of heterogeneous nucleation with three dimensional-growth, the nucleation density, N, is related to G and K as expressed in Equation 4.3.   G was obtained experimentally for each individual crystallization temperature. Both the Avrami bulk conversion constant, K, and the growth rate data are available for the specimens crystallized between 282-290 °C, and are listed in Table 4.2 below.

The nucleation densities calculated for ITX crystallized between 282-290 °C are of the same order of magnitude, and increase with decreasing T_C as expected.   N ranges from 5.3×10^9 to 3.6×10^9 cm^{-3} for crystallization temperatures of 282 to 290 °C, respectively.   Using the G value for 304 °C to calculate the nucleation density for ITX melted at 373 °C gives in a nucleation density four orders of magnitude higher (4.9×10^{13} cm^{-3}) for specimens melted at the lower melt treatment temperature.

This result is consistent with all the experimental results thus far.   Visual observation of the nucleation process shows a higher nucleation density at low melt temperatures, and this difference is reflected in the different crystalline morphologies

Table 4.2   ITX nucleation densities calculated for several crystallization temperatures after melt treatment at 404 °C assuming uniform three dimensional growth.
* Growth rate value determined for 404°C/30 min. melt treatment before crystallization.

Melt Treatment Temperature T_f (°C)	Crystallization Temperature T_C (°C)	Nucleation Density at T_C (#/cc)	G at T_C (cm/sec)	K at T_C (sec^{-3})
404	282	5.3E+09	7.5E-06	9.4E-06
404	284	4.1E+09	6.1E-06	3.9E-06
404	286	3.6E+09	5.7E-06	2.8E-06
404	290	3.6E+09	3.7E-06	7.6E-07
373	304	4.9E+13	2.5E-06	3.2E-03
386	300	1.3E+13	4.0E-06*	3.5E-03

which develop for ITX melted at the two temperature extremes. Also, the low N values seen at higher melt temperatures are consistent with the variation in the DSC crystallization curves that initiated the investigation into the potential heat sensitivity of the ITX polymer. It is clear that the nucleation density is greatly affected by the thermal history the polymer sees during processing.

The last row in Table 4.2 contains the nucleation density results obtained utilizing a G value of approximately 0.04 μm/sec. as determined after holding the ITX in the melt for 30 minutes before crystallization at 300 °C. When this G value is substituted into equation 4.3, and the appropriate K value for 300 °C included, the result for N is 1.3 x 10^{13} cm^{-3}, approximately the same as evaluated with a slightly larger G. Only a small difference is seen in the calculated nucleation density for ITX when G decreases due to thermal history. The small decrease in magnitude in G apparently is not at all as significant as the difference in nucleation density between the two temperature extremes already discussed. This observation again supports the theory that the effect of degradation on the crystallization behavior is relatively minimal under the conditions evaluated.

4.5.5 Nucleation Density Regeneration

Until this point, indirect experimental evidence supported the hypothesis that melt sensitivity was the preferred explanation over polymer degradation as the source of the variations in the crystallization behavior in ITX as a function of temperature. Now, with the observation that growth rate also varies with thermal history, there is experimental evidence that indicates that some level of degradation also plays a minor role. To determine whether a drop in nucleation density, i. e. melt sensitivity, or degradation was the primary factor controlling crystallinity development, a series of experiments were

designed to attempt to thermally "regenerate" crystalline nuclei and subsequent crystallinity in specimens that had seen a rigorous thermal history. ITX specimens were subjected to the most severe melt pretreatment conditions tested previously (410 °C/30 min.), the crystallinity evaluated, and then this same specimen was put through the heat-cool process repeated for a series of lower "second" melt treatment temperatures between 360-385 °C. This process is illustrated in Figure 4.22, and the regeneration procedure utilized is as follows:

Step 1) Heat ITX powder to 410 °C @ 36 °C/min. and then hold for 30 min.,
Step 2) Cool @ 36 °C/min. to 100 °C,
Step 3) Reheat at the same rate to a second T_f [taken at 5 °C or smaller intervals between 360-385 °C], hold for 15 min.,
Step 4) Cool again to evaluate ΔH_c .

The final crystallization data summarized in Figure 4.23 indicates that when ITX is melted for the second time at lower temperatures in step 3, crystalline nuclei which formed during cooling in step 2 are incompletely melted. Partial melting of crystallites leaves a "higher" nucleation density behind during the final recrystallization step, and allows the material to recrystallize once again at lower supercooling relative to step 2. In addition to crystallizing at a higher temperature, the step 4 crystallization peak is also sharper and narrower than the high melt-temperature peak, and the area under the curve is larger. As can also be seen in Figure 4.23, melting ITX above ~370 °C diminishes the trend described above. The second crystallization peak begins to broaden again, the crystallization peak area decreases, and T_c onset and peak move downwards in temperature. This reversal in behavior suggests that melting is more complete and therefore the nucleation density diminished once more. These observations correlate well with the crystallization behavior noted initially for ITX, as melt temperature increased, T_c onset, peak and ΔH_c all decreased.
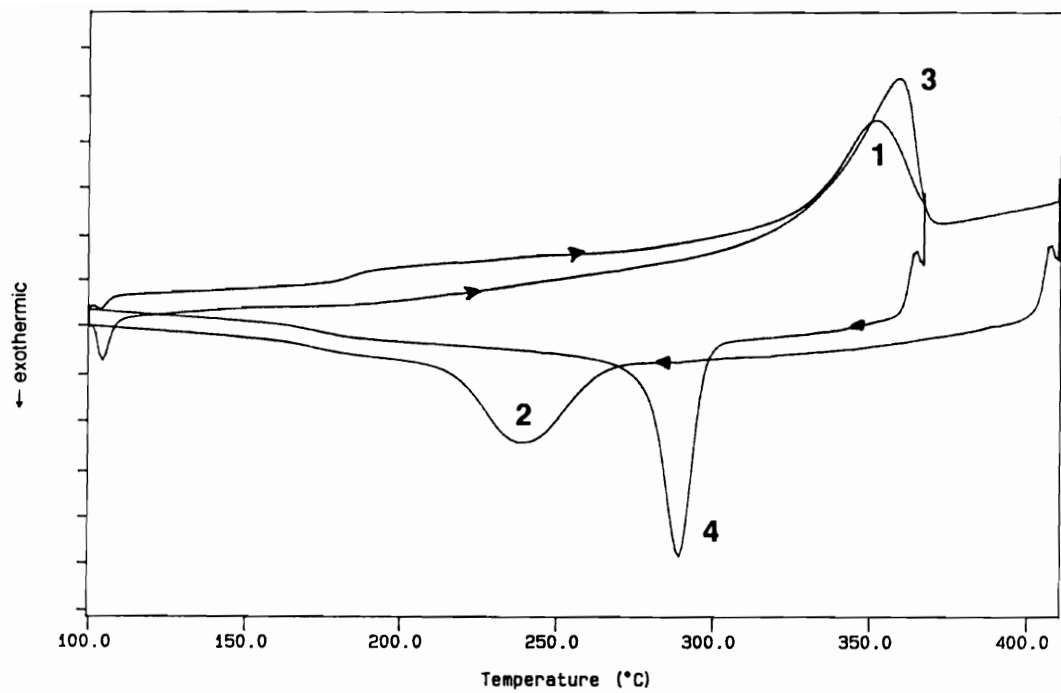
Figure 4.22   DSC thermal profile illustrating the nucleation density regeneration procedure utilized for the ITX specimens. [The upper line in the overlapping melt region corresponds to the first melt, the lower to the second melt.]
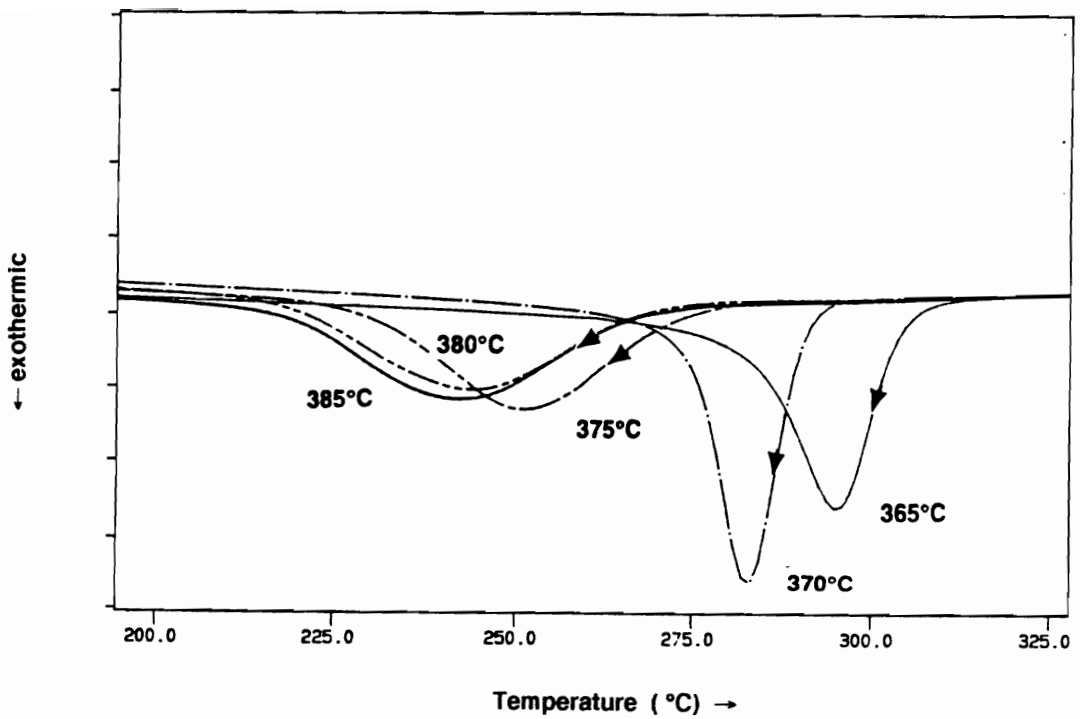
Figure 4.23   DSC data summary showing crystallization peak area as a function of the secondary melt treatment temperature. Note that as T_f increases from 365 to 385 °C melt temperatures that the crystallization peaks broaden, and move to lower T_c temperatures.

The crystallization data for the series of "second" or "lower" melt treatment temperature cycles is summarized in Figure 4.24. The area is normalized to the maximum peak area generated by melting ITX at the lowest temperature, for the shortest time evaluated earlier, i. e. $\Delta H_C \cong 41.0 \pm 0.5$ J/g (380 °C/1 min.). After normalization, the ΔH_C peak area is plotted versus the "step 3" or "second" melt treatment temperature. The data were treated in this way to show how the regeneration effect varies as melt treatment temperatures progress through the ITX melting temperature region of ~360-361 °C up to 385 °C. Melting ITX powder at 410 °C for 30 min. results in a fractional crystallization peak area of ~0.75 relative to the maximum peak area possible (solid diamonds). After cooling and then remelting the material as described before to "regenerate" crystalline nuclei, the "after treatment" peak areas (open squares) vary from ~ 0.65 to 1.00 and then back down to 0.75 of the maximum peak area possible.

This behavior can be explained by dividing the data into three different regions as follows. In the first region, ITX specimens received second melt treatments below 365 °C, and were only partially melted. For these specimens, partial melting literally means that there was less material available to observe recrystallizing by DSC subsequently in step 4. The ΔH_C values obtained in this region were therefore less than, or approximately equal to, those obtained for the 410 °C/30 min. treatment.

The second response region in Figure 4.24 is bounded by ~365-372 °C. This middle region is characterized by ΔH_C values that are approximately equal to 90% or greater of the maximum values observed for ITX as described above. The material is melting, but apparently sufficient order is retained in the melt to rapidly initiate crystal growth. The nucleation density remains high, and the near maximum level of crystallinity reforms on cooling.
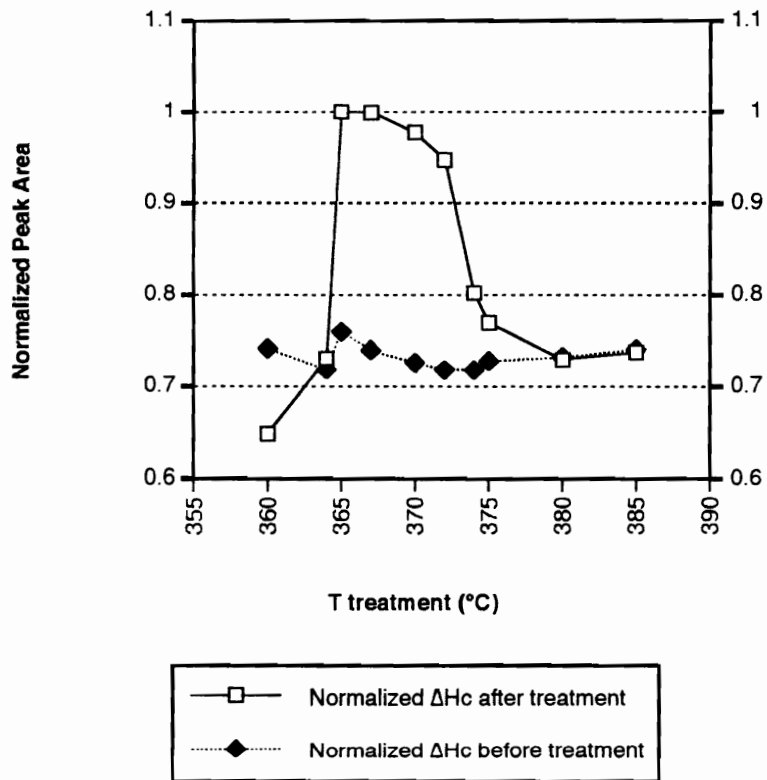
Figure 4.24   Heat of crystallization data showing how thermal treatment is reflected
               in the increased area under the crystallization peak for ITX subjected to
               a lower temperature second melt temperature before recrystallization.

The final type of crystallization behavior observed during this experiment is noted when ITX is remelted above ~374 °C. This last case is characterized once again by diminishing levels of crystallinity regenerating during cooling in step 4 of the thermal treatment. The data generated in this region correlates with the trends observed in the melt time-temperature studies discussed earlier. As melting becomes more complete, less order is retained in the melt, and the nucleation density of the material decreases invoking the now familiar crystallization response; ΔH_c and Tc decrease with higher Tf's, and peak breadth increases.

4.6 ITX Crystalline Content Determination

4.6.1 Introduction

Wide angle X-Ray scattering (WAXS) was employed in order to quantitatively estimate the absolute level of crystallinity in ITX. Quantification of crystalline content was accomplished using the method of Hermans and Weidinger for determining percent crystallinity in a semicrystalline material [117-124]. The x-ray data collection and initial analysis were performed using the Seimens Polycrystalline Software Package. After smoothing the files using the Seimens routines, the data were analyzed using two different methods. In the first method, the Seimens integration package was used to integrate and manipulate the data in order to ratio peak areas and approximate the crystalline fraction as a function of the total peak area. No corrections or normalization routines were applied to the data. The second analysis method utilized was more rigorous. The data were transferred from the Seimens system, and integrated, then analyzed using the method of Hermans and Weidinger for determining percent

crystallinity. Corrections were made for beam intensity, optical density, and all data were normalized following the procedures summarized by Alexander [124]. The analysis procedures involved in both methods will now be presented, along with a comparison of the results for the two data sets.

4.6.2 WAXS Crystallinity Estimation

The physical and mechanical properties of polymers are dependent on the degree or level of crystallinity each contains. Quantification of the percent crystallinity of a semicrystalline polymer is typically determined by one of several different physical measurements such as x-ray diffraction, density, infrared absorption or nuclear magnetic resonance. It is generally accepted that these numerical values for the amorphous and crystalline content of a polymer vary from technique to technique, and cannot be defined unambiguously [124].

With respect to WAXS analyses, the ambiguity arises from the original two-phase concept of polymer structure. This model of polymer structure divides semicrystalline morphology into two distinct regions, one perfectly crystalline and the second amorphous. Research has shown that instead of such distinct divisions, polymer crystalline microstructure contains defects and imperfections resulting in diffuse scattering that contributes to amorphous background scattering. The end result is that crystalline structure is generating, and adding to, the WAXS signal attributed to amorphous material. This renders suspect the simple method commonly used to estimate the percent crystallinity by separating the diffraction pattern into shape (crystalline) and diffuse (amorphous) components [124]. In this section, the percent crystallinity will be determined for ITX using the simple method just described. Then, in

section 4.6.3, the more rigorous percent crystallinity analysis method of Hermans and Weidinger will be completed, and the results compared to the estimation technique.

Basically, in the percent crystallinity estimation method, the WAXS data are separated into crystalline and amorphous components, and the areas under the curves compared [136]. Data collection and the initial analysis were performed using the Seimens Polycrystalline Software Package. After smoothing the data files using the Seimens routines, the data were then analyzed. First, the Seimens integration package was used to manipulate the data and subtract a baseline from the amorphous data, and this curve is used as a "template" for the shape of the amorphous scattering as shown in Figure 4.25. The same baseline removal procedure is completed for the semicrystalline scattering pattern.

Next, the contribution from the amorphous material to the total scattering intensity is estimated, and removed from the total intensity area. This is done by "sketching in" an area similar to the template shape, whose magnitude fits under the scattering curve. Then this estimated area is subtracted as a "baseline" from the total scattering intensity. Figure 4.26 is an example total scattering intensity file for a semicrystalline ITX specimen. The x ' s noted along the curve illustrate how the amorphous peak area is estimated by subtracting the baseline curve created by the x ' s. Figure 4.27 shows the remaining crystalline contribution to the scattering intensity after removal of the "amorphous baseline" curve from the total scattering intensity. The final step in the analysis is to ratio the peak areas [% X = (crystalline / total scattering intensity area) * 100] thereby approximating the crystalline fraction as a function of the total peak area. No corrections or normalization routines were applied to the data before this analysis other than the amplitude correction completed by subtracting the baselines.

This procedure was applied to a series of five semicrystalline ITX specimens, and
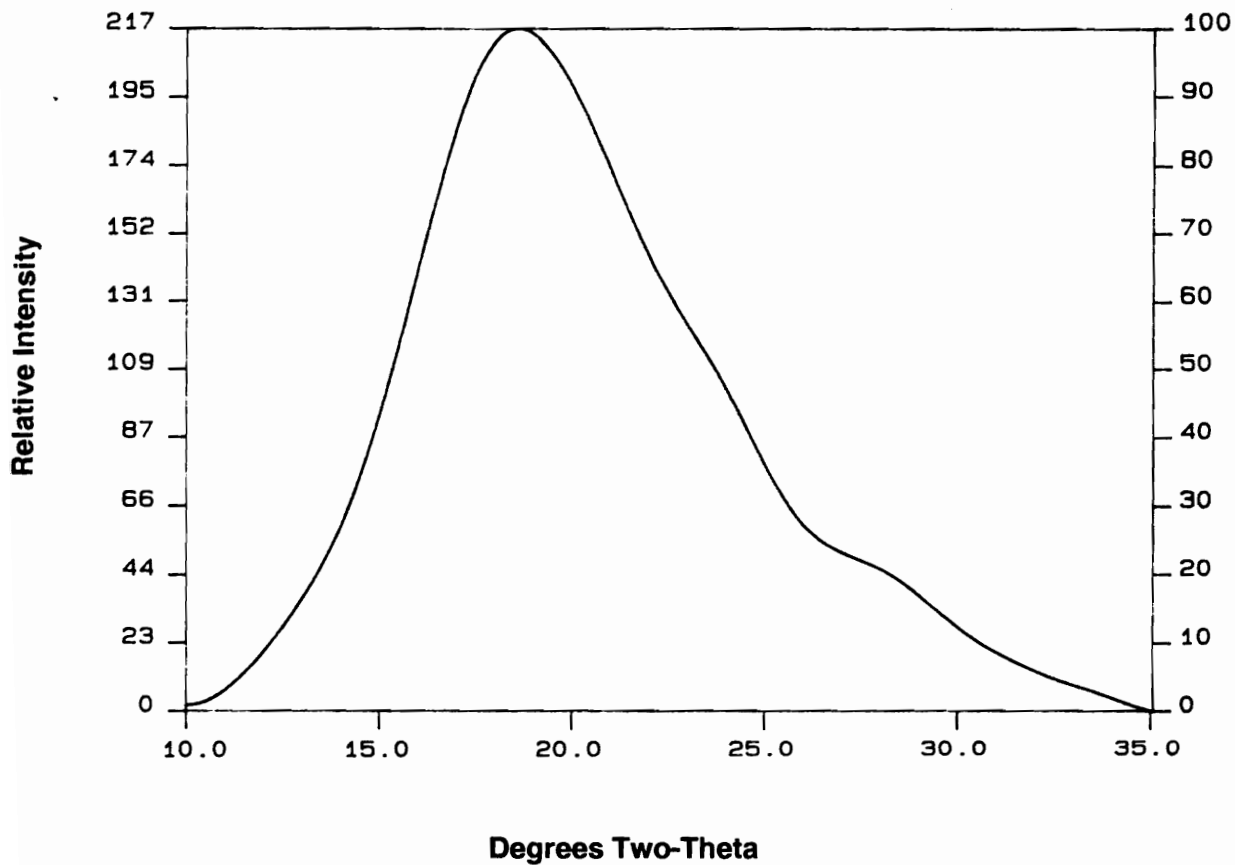
Figure 4.25   Amorphous WAXS data after subtraction of a baseline. This curve is used as a "template" for the shape of the amorphous scattering data.
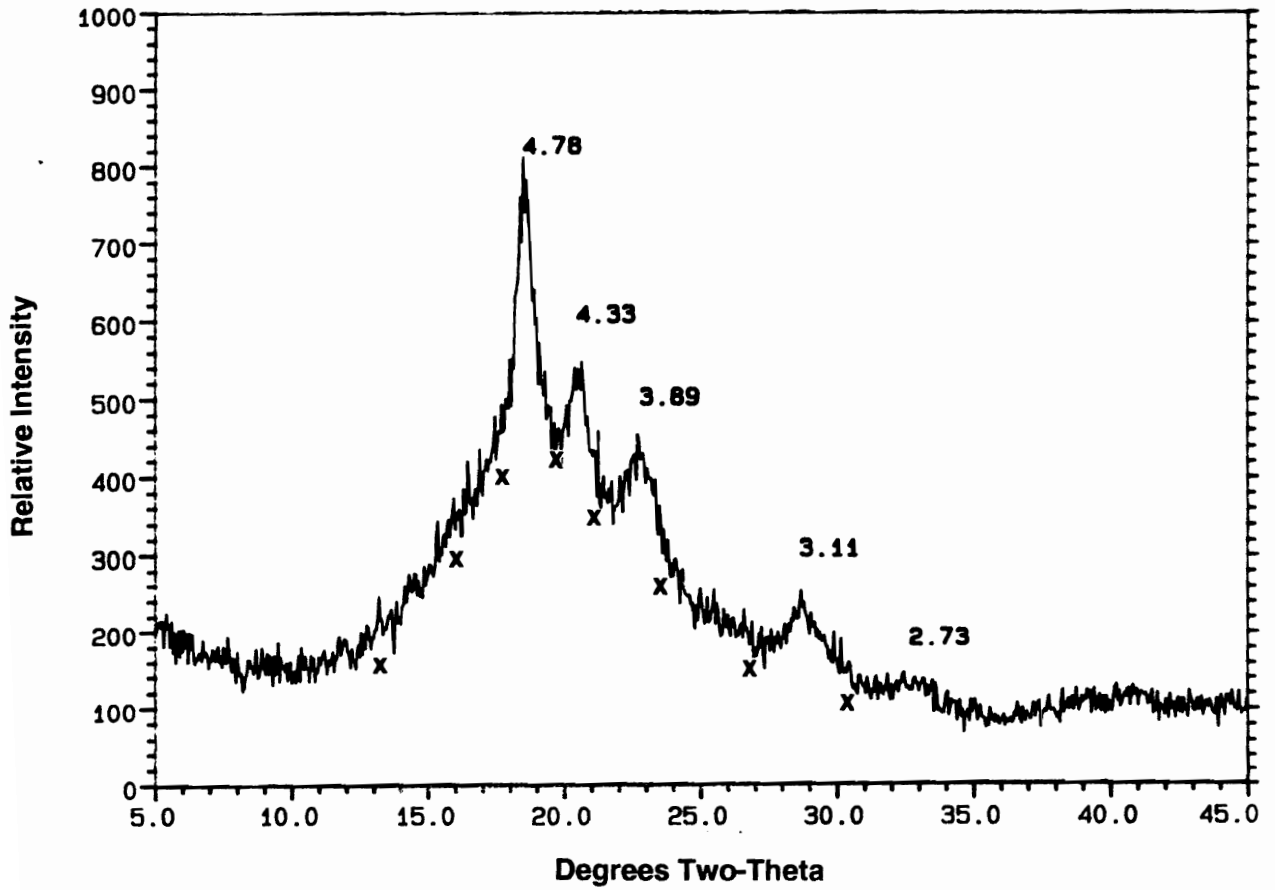
Figure 4.26   Example total scattering intensity file for a semicrystalline ITX specimen. The x's noted along the curve illustrate how the amorphous peak area is estimated by subtracting a "baseline curve" created by these points.
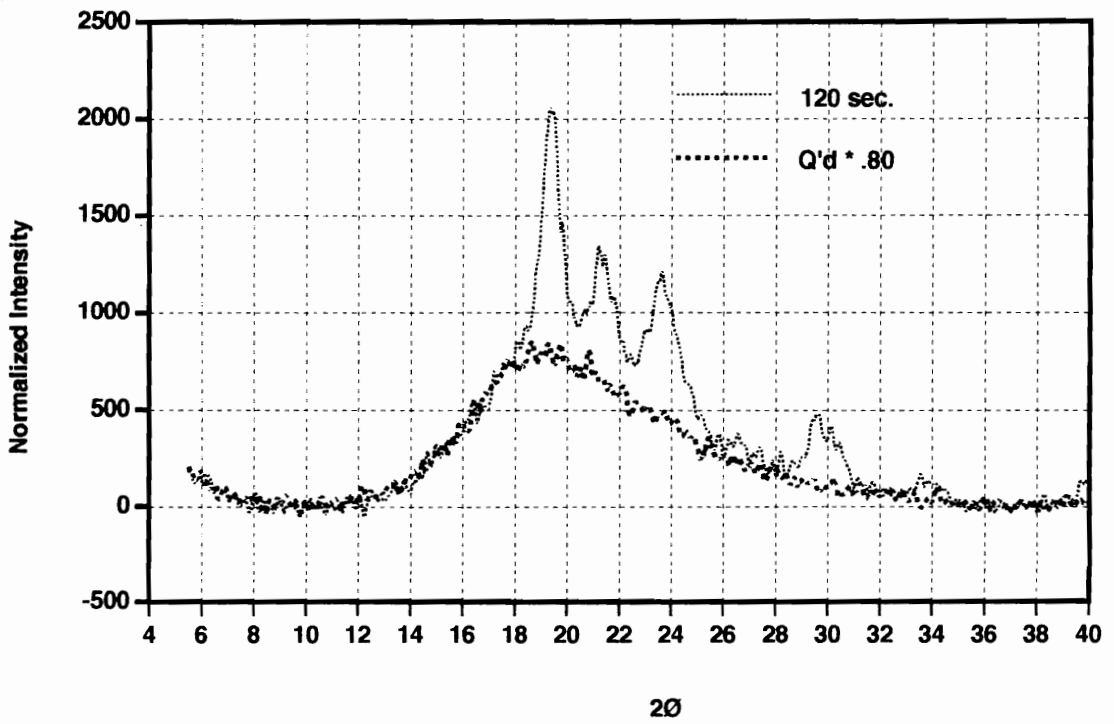
Figure 4.27   ITX crystalline contribution to the scattering intensity after removal of the "amorphous baseline" curve from the total scattering intensity.

the results for the estimation of the percent crystallinity present in each are given in Table 4.3. This method estimates the percent crystallinity in ITX as ~20 and 35 % for the semicrystalline films and the as-received powder respectively. Now the percent crystallinity in ITX will be estimated using the Hermans and Weidinger method.

4.6.3 Hermans and Weidinger WAXS Analysis

The second analysis procedure utilized in the determination of the degree of crystallinity in semicrystalline ITX was the common method of Hermans and Weidinger [117-123]. This analysis method was more rigorous than the estimation method just described, and the normalization and corrections incorporated within the procedure are detailed more completely in Chapter 3. To summarize, the analysis incorporates the following steps:

Method of Hermans and Weidinger

1. The diffraction patterns of a series of semicrystalline polymer specimens are collected over a selected angular range. The specimens must have varying levels of crystallinity, and are normalized to equal x-ray optical density [optical density: $\mu t = - \log_e (I / I_0)$ where μ = an absorption coefficient, t = thickness] and equal intensity of the direct x-ray beam.

2. A demarcation line is estimated and drawn between the crystalline and amorphous scattering.

3. Suitable intensities <u>proportional</u> to the crystalline and amorphous fractions are selected and integrated to give I_c and I_a, the crystalline and amorphous fractions respectively.

4. The regression line that gives the statistically optimum linear dependence of I_c on I_a is calculated.

5. Finally, inspection of the linearity of I_c versus I_a confirms that the method utilized for measuring them is in agreement with theory, whereupon the

Table 4.3 Percent crystallinity evaluation for ITX utilizing the WAXS "estimation" method.

WAXS % Crystallinity Data	Percent Crystallinity	Mean	Standard Deviation
Amorphous ITX film			
#1	0.0	0.0	0.0
Semi-x'tal ITX specimen A			
#1	18.6	18.9	0.4
#2	19.2		
Semi-x'tal ITX specimen B			
#1	20.5	20.5	0.0
ITX Powder			
#1	35.4	34.7	1.0
#2	34.0		

regression line may be used to determine the crystalline fraction of any other unoriented specimens of the same material from their I_c and I_a values by reference to the established regression line.

After collection following the parameters discussed in the experimental section, the data were smoothed using the Seimens routines. Next, the WAXS intensity versus scattering angle data were transferred from the Seimens system to a Mac IIci for integration. The data were then analyzed, making corrections for variations in incident beam intensity, and x-ray optical density.

After normalization for the incident beam intensity and optical density, the data were plotted, and a baseline was subtracted to set the data to a similar starting amplitude as shown in Figure 3.11. The end result for the data series is shown in Figure 3.12. Once the data were normalized, the total scattering area was integrated for the semicrystalline and amorphous specimens, and a similar subtraction routine was established to evaluate the crystalline contribution to the total scattering area .

The crystalline contribution to the total scattering intensity was evaluated as suggested in the Hermans and Weidinger method step 2. A demarcation line was instituted by subtracting a "scaled multiple" of the amorphous scattering peak from each semicrystalline specimen to generate I_c and I_a respectively. Figure 4.28 illustrates this procedure. Both data files, the semicrystalline data file under consideration, and the "multiple " of the amorphous file were plotted as an over-lay plot. The amorphous data file was multiplied by a factor in 0.025 increments (e. g. Am *0.975, 0.950, 0.925 etc.) in order to scale the amorphous halo so that it exactly fit under the semicrystalline scattering curve. [For this data set, a difference of one 0.025 increment translates into a change of ± 2.5% crystallinity determined for the specimen.] When the size of the amorphous halo visually appeared to fit well under the curve, the multiplier factor was retained. The value determined, [area * factor = amorphous contribution, or (I_a)], is
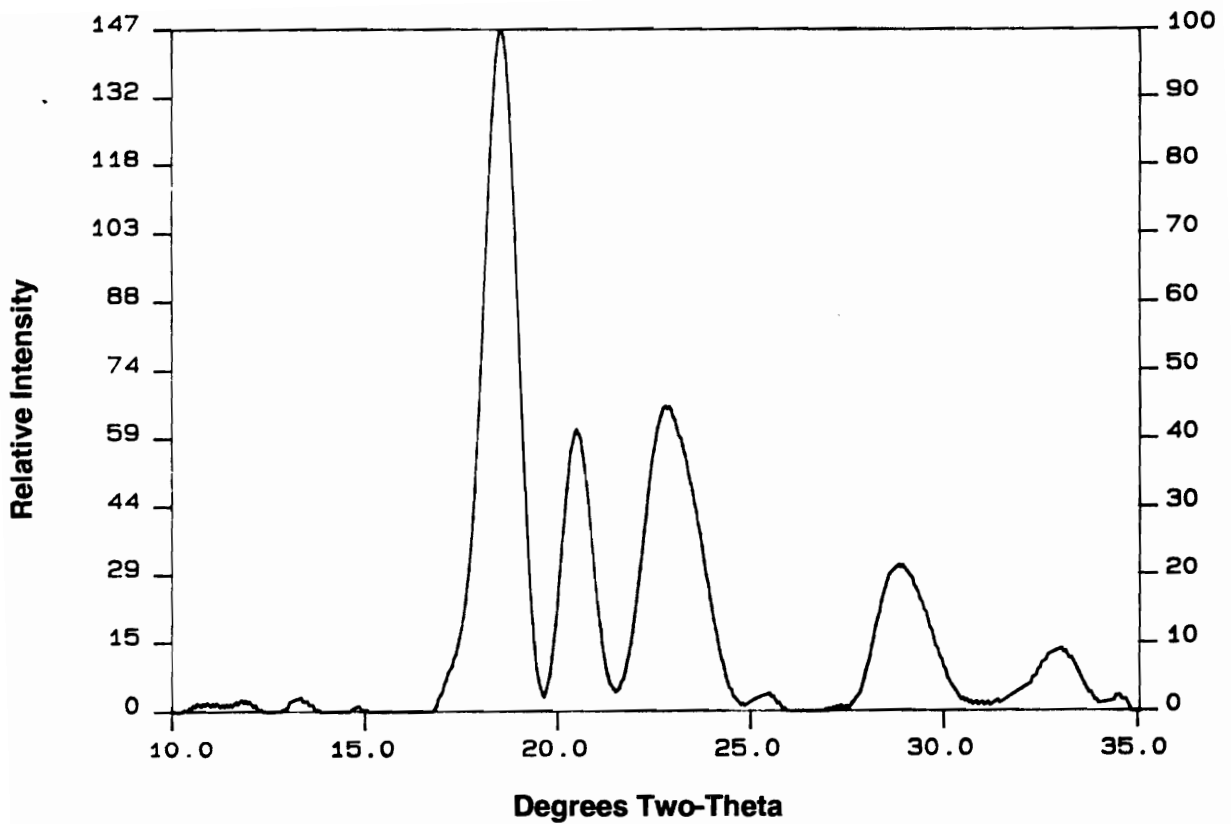
Figure 4.28   The crystalline contribution to the total scattering intensity evaluated by subtracting a "multiple" of the amorphous scattering peak file from each semicrystalline specimen to generate the value I_C which is proportional to the crystalline scattering contribution.

proportional to the amorphous fraction in the semicrystalline specimen. Once the amorphous area was known, the crystalline contribution was evaluated as:

total peak area - amorphous peak area (I_a) = crystalline area (I_c)　　　(4.4)

which is proportional to the crystalline content of the specimen. The results for I_c and I_a were collected for the series of ITX specimens, and are tabulated in Table 4.4.

After the results for I_c and I_a were collected, the data was plotted in the classical Hermans and Weidinger format as shown in Figure 4.29. In this treatment, the values of the crystalline and amorphous integrated areas, denoted as o_{cr} and o_{am} respectively, are plotted as suggested in step 4 of the method description. A straight line was fit to the data. The equation of the line was then used to solve a set of linear equations and determine the areas of a 100 % amorphous or 100 % crystalline specimen denoted as **A** or **C** (A = 9320 and C = 24820) [122].

The plot in Figure 4.29 was generated in this manner, but also by restricting the data to the amorphous and longer crystallization time data. These data were excluded from consideration based on the amorphous integration values measured for each specimen. It appears that the data collected for the short crystallization times are unreasonable in that the quenched data curve used is <u>smaller</u> than the amorphous halos observed for the short crystallization time data.. The curves for the 1, 5, 10, 15, and 30 second data appear to be larger in magnitude than do the rest of the data, and therefore the correction is meaningless. These data were reanalyzed 4 separate times, (i. e. re-scanned and analyzed) and no improvement was observed. It is possible that the correction for optical density is not accurate here as the films used in the analysis were very thin, and the optical density of the material was therefore low. In this situation, D is

Table 4.4 The experimental results for I_c and I_a were collected for the series of ITX specimens. Area results are reported in relative units.

ITX Processing Conditions (time @ 300 °C)	Integrated Area via Trapezoid Rule	Amorphous Area (Ia)	Crystalline Area (Ic)
Quenched	9344	9344	
1 sec.	11331	9344	1987
5 sec.	11132	9344	1788
10 sec.	11111	9344	1767
15 sec.	8209	6541	1668
30 sec.	9621	6541	3080
2 min.	11407	7709	3698
5 min.	12084	7475	4609
30 min.	13383	7335	6048
60 min.	16283	7008	9275
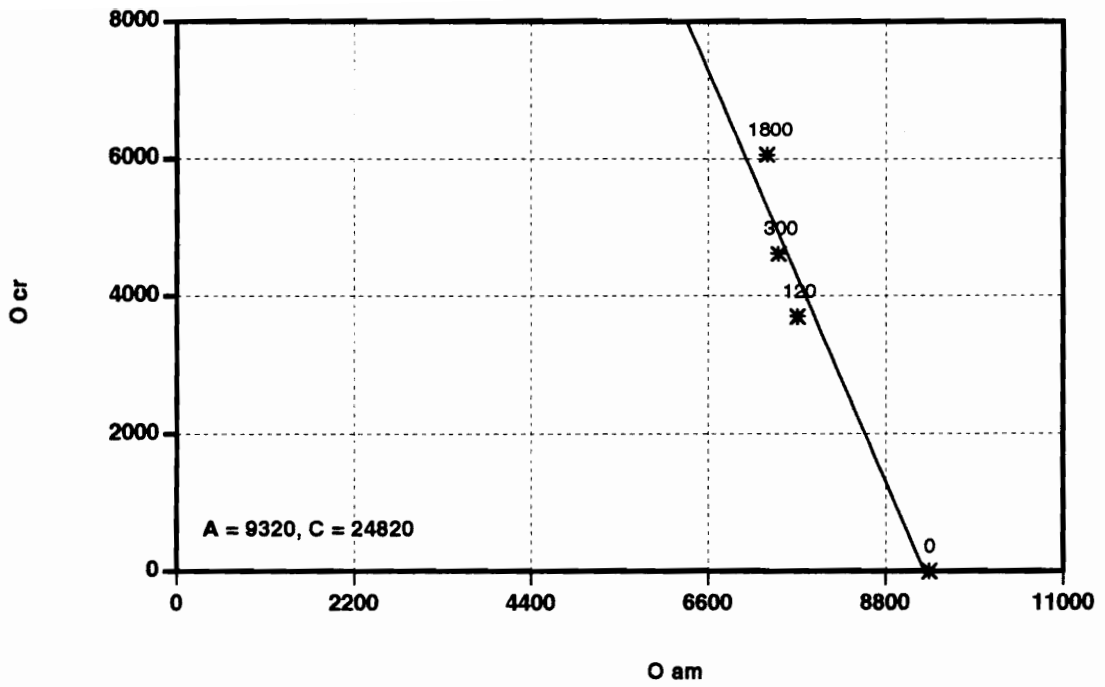
Figure 4.29   The values for the crystalline and amorphous integrated areas (denoted as o_{cr} and o_{am} respectively).

correspondingly difficult to reproducibly determine as fluctuations in beam intensity are magnified through the optical density correction. The low optical density of the amorphous specimens may account for the scaling differences noted for several of the shorter annealing time specimens.

Taking the results of the linear regression fit to the data in Figure 4.29 allowed the determination of A and C, the 100 % amorphous or crystalline areas as noted earlier. The percent crystallinity index for the series of ITX specimens was then solved, and the results are summarized in Table 4.5 along with the percent crystallinity determined using the ratio of the integrated areas. The values of the percent crystallinity are much larger calculated via the area ratio method on the normalized data, than for the Hermans and Weidinger analysis. The Hermans and Weidinger method in fact is in surprisingly good agreement with the data calculated using the "crystallinity estimation" method discussed previously. The optical density, D of the material is relevant to any consideration of the validity of the agreement between the estimation method results and those generated using the Hermans and Weidinger approach.

Even though the data for the estimation method were not normalized or corrected for incident intensity, they are still in good agreement with that from more rigorous analysis. This may be as a result of the quantity of material analyzed. The data for the estimation method was collected using several layers of material, up to ~ 40 mils in thickness, in order to achieve an absorption coefficient of ~ 0.64. While this is similar to the D values for the Hermans and Weidinger method at 0.64 to 0.68, only 1-2 layers of material were utilized in the second method. The x-ray optical density correction may play a pivotal role in the reproducibility of the data generated using this analysis method, one that was correctly accounted for with the larger specimens.

Table 4.5 The percent crystallinity index calculated for the series of ITX specimens using the Hermans and Weidinger analysis. Also included are the percent crystallinity determined using the ratio of the integrated areas.

Annealing Time at 300 °C	WAXS % X Data (area ratio method)	WAXS % X Data (Hermans & Weidinger)
0 sec	0.0	0.0
1 sec	17.5	0.0
5 sec	16.1	0.0
10 sec	15.9	0.0
15 sec	20.3	29.8
30 sec	32.0	29.8
120 sec	32.4	17.3
300 sec	38.1	19.8
1800 sec	45.2	21.3
3600 sec	57.0	24.8

4.6.4 Theoretical Heat of Fusion Determination

The final step in the series of analyses completed using the WAXS results just described was the determination of the theoretical heat of fusion for ITX. Once the crystalline content is determined in a series of semicrystalline specimens utilizing the method of Hermans and Weidinger, it is possible to estimate the theoretical heat of fusion for a 100% crystalline ITX specimen by combining the WAXS data, and some simple DSC heat of fusion results. This analysis will once again be completed twice, once with the estimation method data, and also with the Hermans and Weidinger percent crystallinity results.

The series of ITX specimens were scanned in the Perkin-Elmer DSC-7 using a heating rate of 20 °C/min. between 50-400 °C. The melting endotherms were then integrated using the Perkin-Elmer software package. The heat of fusion data obtained were then plotted against the corresponding percent crystallinity values obtained for each specimen by WAXS, and the value for the theoretical heat of fusion extrapolated. The correlation between the heat of fusion values determined by DSC and the WAXS percent crystallinity values are seen in Figures 4.30 and 4.31 and Tables 4.6 and 4.7 for the Hermans and Weidinger and estimation method respectively. A linear regression fit of the data resulted in a calculated enthalpy of melting value of 188 and 180 J/g for a 100 % crystalline specimen of ITX, which is amazing agreement between the two studies. The experimentally determined theoretical heat of fusion value for ITX is higher, but of the same order of magnitude as than that reported for PEEK at 130 J/g [33].
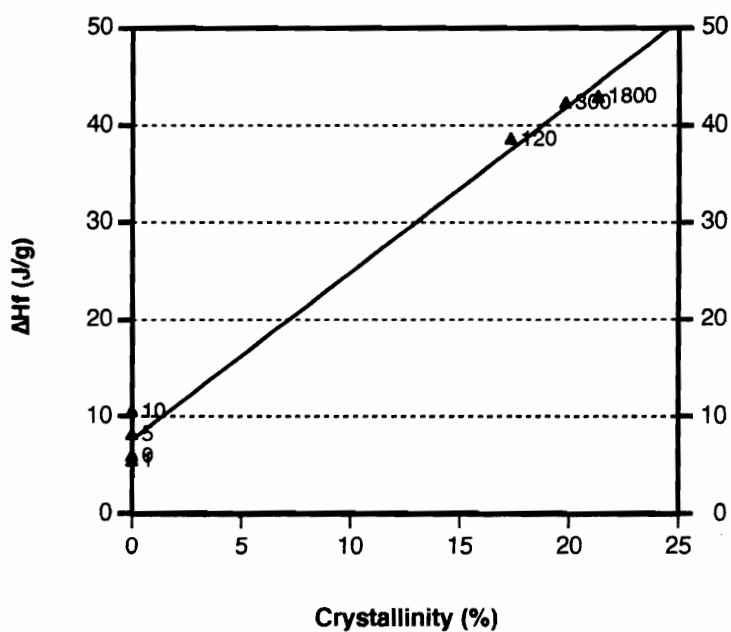
Figure 4.30   The experimental correlation between the heat of fusion values
determined by DSC and the WAXS percent crystallinity values for ITX.
A linear regression fit of the data resulted in an enthalpy of melting
value of 180 J/g for a 100 % crystalline specimen.
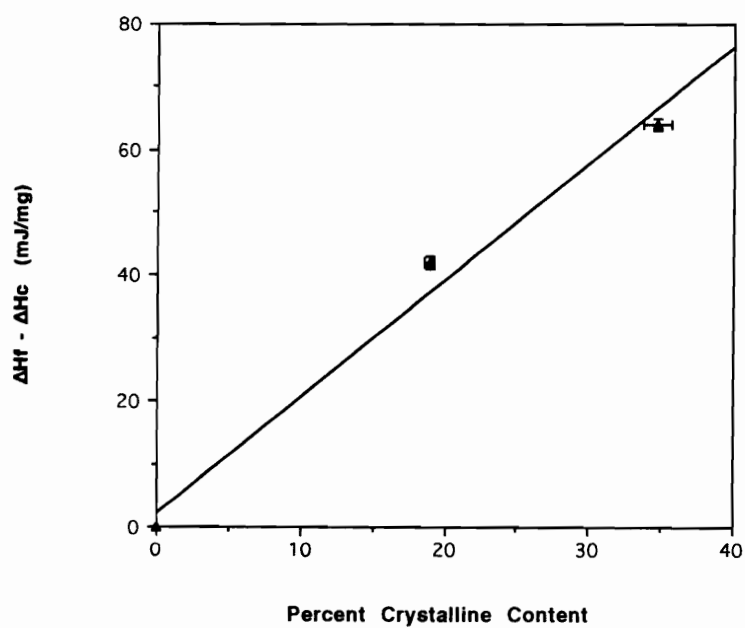
Figure 4.31   The experimental correlation between the heat of fusion values
                determined by DSC and the WAXS percent crystallinity values for ITX
                estimated utilizing unnormalized WAXS peak areas results in a
                theoretical heat of fusion of 188 J/g.

Table 4.6 Correlation between the heat of fusion values determined by DSC and the WAXS percent crystallinity values are seen in Figures 4.30 for the Hermans and Weidinger method .

DSC Heat of Fusion Data	ΔHft (J/g)	ΔHc (J/g)	ΔHf-ΔHc (J/g)
0 sec	35.1	29.1	6.0
1 sec	38.4	32.9	5.5
5 sec	41.0	32.7	8.2
10 sec	37.0	26.4	10.6
15 sec	35.4	14.2	21.2
30 sec			
120 sec	38.7	0.0	38.7
300 sec	42.4	0.0	42.4
1800 sec	43.0	0.0	43.0
3600 sec			
ΔHf Calculations			
H&W	180.4 J/g		

Table 4.7 Correlation between the heat of fusion values determined by DSC and the WAXS percent crystallinity values seen in Figure 4.31 for the estimation method.

DSC Heat of Fusion Data	ΔHf (mJ/mg)	ΔHc (mJ/mg)	$\Delta Hf-\Delta Hc$ (mJ/mg)	Mean (mJ/mg)	Standard Deviation (mJ/mg)
Amorphous ITX film					
#1	43.3	28.9	14.4	14	1
#2	39.8	28.0	11.8	13.5	1.5
#3	42.3	28.0	14.3		
Semi-x'tal ITX specimen #1					
#1	42.4		42.4	42	1
#2	40.6		40.6	41.7	0.9
#3	42.0		42.0		
Semi-x'tal ITX specimen #2					
#1	48.0	5.3	42.7	39	4
#2	40.6	5.4	35.2	39.4	3.8
#3	40.8	0.5	40.3		
ITX Powder					
#1	64.1		64.1	64	1
#2	63.9		63.9	64.4	0.7
#3	65.2		65.2		
ΔHf calculation: 187.8 J/g					

The theoretical heat of fusion values determined using the normalized and unnormalized ITX WAXS data are very similar at 180 and 188 J/g respectively. Apparently, a simple ratio of the crystalline peak area to that of the total area gives a reasonable estimation for the crystallinity index of ITX when optical density variations are not the primary cause of scatter in the data.

4.7   Summary

A summary of the ITX project results presented in this chapter will be presented here, organized in the same order as the chapter. Initial melt and thermal stability results will be presented, followed by a summary of the crystallization behavior of ITX collected under the actual processing conditions used in composite consolidation. Then the isothermal kinetics studies will be reviewed, and the morphological studies will be included. Finally, the crystalline content determination of ITX by WAXS and the theoretical heat of fusion analyses will be summarized.

4.7.1   Initial ITX Crystallization Behavior

ITX, like PEEK, displays excellent thermal stability through a wide temperature range when examined by TG-DTA. The five percent weight loss temperatures observed at this heating rate were 520 °C and 524 °C in nitrogen and air environments respectively. Initial "time in the melt" experiments which convoluted both melt time and temperature suggested that the crystallization behavior of ITX, like other stiff-chained polymers, was however affected by thermal treatments <u>even at moderate times</u> typical of composite processing. A decrease in the observed crystallization temperature was

observed, which was consistent with a decrease in the nucleation density of the polymer, and required that all specimens be treated to similar melt treatment times and temperatures for ITX crystallization studies.

4.7.2 ITX Crystallization Behavior as a Function of Melt Time and Melt Temperature

The initial examination of the melt sensitivity of ITX revealed that the crystallization and melting behavior of the material was affected by either the residence time in the melt, or the melt treatment temperature that the polymer saw before crystallization. A series of crystallization studies were then completed using the processing conditions recommended for consolidation of ITX composites, and the effects of both melt time and temperature were considered separately. Changes in the crystallization behavior of ITX as $f(t, T_f)$ were observed as either the melt temperature or duration were increased. The level of crystallinity generated decreased, and the processing time increased as the crystallization rate decreased. More specifically, over the melt temperature-time conditions evaluated, the crystallization behavior of ITX displayed the following trends.

1) When melted under the most severe (410 °C/30 min.) conditions, the area under the crystallization peak, and therefore the relative crystallinity which develops on cooling, is reduced by approximately 20 % with respect to ΔH_C observed for the mildest (380 °C/1 min.) melt treatment examined. This correlates with a drop in absolute crystallinity of ~5% in both air and nitrogen environments.

2) When evaluated under both air and nitrogen, the crystallization window gradually shifts downward by 40-50 °C for both T_{co} and T_{cp} crystallization temperatures, as the melt treatment conditions increase to 410 °C and 30 min. in the melt.

3) Irrespective of the purge gas, the overall crystallization process takes longer

when the material is treated more harshly. Peak breadth increases from 0.5 to 1.2 min. as melt temperature and time increase from 380 °C/1 min. to 410 °C/30 min. Therefore, crystallization gradually spans a wider temperature range (~20-40 °C) as melt treatment increases in duration.

These changes in crystallization behavior resulted from variations in processing conditions that were <u>within</u> the manufacturers recommended range for the material. The corresponding decrease in crystalline content are sufficient that they could affect the physical properties and the solvent resistance of the semicrystalline matrix material that ultimately results as well.

4.7.3 Isothermal Crystallization Studies

In order to compare the crystallization behavior of ITX with other polymers, the material was also evaluated by DSC utilizing the classical Avrami isothermal crystallization methodology. The next section summarizes the results of these studies, work that was also completed within the thermal processing window suggested by the manufacturer for ITX.

In general, the crystallization kinetics observed for ITX melted at 404 °C were very different from those of the polymer melted at lower temperatures. Two major differences were noted. First, the ITX specimens that were melted at higher temperatures crystallized at *lower* temperatures than those that were quenched from the *lower* melt treatment temperatures, which is consistent with the earlier data suggesting that nucleation density greatly decreases with higher melt temperatures. The second significant difference in crystallization behavior between the data generated with ITX melted at high versus low temperatures is that the specimens which crystallized at the *lower* temperatures have *smaller* bulk crystallization rate constants than did the other specimens which crystallized at higher T_C's following quenching from the lower melt

treatment temperature. In addition to differences just noted in kinetics, the nucleation densities calculated for ITX melted at higher melt temperatures versus the lower temperature limit also showed a dramatic difference. Calculated the nucleation densities for ITX melted a lower (373 °C) temperature results in a nucleation density <u>four orders of magnitude higher</u> than that for specimens melted at the higher melt treatment temperature limit (404 °C).

The linear growth rate, G, was also seen to decrease slightly as a function of thermal history as well. Holding ITX in the melt for 30 min. at the 404 °C melt temperature limit resulted in a decrease in G of approximately 1/3 with respect to milder melt treatments. The small decrease in magnitude in G is not as influential on the calculation of N as is the melt temperature utilized prior to crystallization. But, the change in the growth rate as a function of thermal history does suggest that some degradation is occurring in ITX when it is melted under the more severe conditions. Thermal history may generate some degradation or cross-linking, which is reflected in a decrease in the growth rate of the material.

To determine whether a drop in nucleation density, i. e. melt sensitivity, was in fact the primary factor controlling crystallinity development, a series of experiments attempted to <u>thermally "regenerate"</u> crystalline nuclei and subsequent crystallinity in specimens that had seen a rigorous thermal history. ITX specimens subjected to the most severe melt pretreatment conditions tested previously (410 °C/30 min.), were put through the heat-cool process again for a series of lower "second" melt treatment temperatures between 360-385 °C. It was seen that if ITX was remelted at a lower temperature (365-374 °C) it was possible to regenerate crystalline nuclei, and subsequently develop the same level of crystallinity as seen for the case of the least severe melt conditions. The ability to "regenerate" nuclei and crystallinity in previously

melted material suggests that unlike previous work on PEEK, <u>degradation does not appear to play a key role</u> in controlling the crystallization behavior of ITX within the processing range examined. Fluctuations in nucleation density induced by thermal history are far more influential in determining crystalline content and morphology for this material.

4.7.4 ITX Morphological Studies

The semicrystalline morphology of ITX, and its variation with thermal history, were examined by optical microscopy. Two patently different morphologies are generated for ITX melted at the extremes of the processing range recommended by ICI. A very fine, indistinct texture, was generated by melting ITX powder at the low temperature (373 °C) limit prior to crystallization, and growth was rapid, such that it required only 1-2 minutes to completely fill the viewing region with superstructure. At the opposite extreme, specimens melted at 404 °C before cooling nucleated slowly and less readily, and often required 7-8 minutes or longer to completely fill in the amorphous melt region with spherulitic structures. The higher melted specimens contained large, distinctly visible individual spherulites instead of a finer texture. These trends in spherulitic characteristics were observed consistently throughout this work, both for isothermal and dynamic cooling crystallization experiments, and under rapid cooling experiments which mimic actual processing parameters as well. Melting ITX at a higher temperature and/or for longer times resulted in a courser, more distinct spherulitic structure, while lower melt temperatures generated a finer texture.

Even in the presence of carbon fibers, ITX's morphological texture consistently changed with melt treatment temperature as was just described for the neat resin. In

addition, the nucleation mode changed for ITX specimens crystallized with IM-8 carbon fibers. When ITX was melted at lower (386°C) temperatures, bulk nucleation of crystals occurred within the molten material, and growth continued in an identical manner to that observed with the neat resin. Bulk and fiber surface nucleation initiated concurrently. The situation was different however when the polymer was melted at the higher (404°C) temperature. ITX appears to initiate nucleation off the surface of IM-8 carbon fibers first, and in some cases, develops transcrystalline regions. Transcrystallinity was not consistently present however. These trends were not repeated with the AS4 carbon fibers, there nucleation density concentration appeared indifferent to the presence of the fibers.

4.7.5   ITX Crystalline Content and Heat of Fusion Determination

Wide angle X-Ray scattering (WAXS) was employed in order to quantitatively estimate the absolute level of crystallinity in ITX using two methods for determining percent crystallinity in a semicrystalline material. First, a simple percent crystallinity "estimation method" was employed where WAXS intensity versus scattering angle curves were separated into crystalline and amorphous components, and the areas under the curves compared. The percent crystallinity in ITX was estimated as ranging between ~20-35 % for the semicrystalline films and the as-received powder respectively. When the percent crystallinity was calculated utilizing the method of Hermans and Weidinger, the level of crystallinity for a series of specimens annealed at 300 °C for times of 1-1800 sec. ranged from 17 to 25 %. The data for short annealing times was inconsistent, and could not be evaluated, but the scans for longer annealing times were analyzed.

Utilizing the results from the Hermans and Weidinger analysis, it was possible to

estimate the theoretical heat of fusion for a 100% crystalline ITX specimen. Enthalpies of melting were calculated for both the estimation and Hermans and Weidinger method data sets. Values of 188 and 180 J/g for a 100 % crystalline specimen of ITX were determined respectively.

To conclude, while the existence of some polymer degradation has been suggested by the observation of diminishing growth rates as a function of thermal history, it appears that ITX's crystallization behavior is substantially affected by its melt sensitivity, i. e. the susceptibility of the crystalline nuclei of the material in the melt to decrease as thermal history becomes more strenuous. Conversely, manipulating thermal history can also apparently "regenerate" crystalline nuclei within the recommended processing constraints such that ITX's melt sensitivity is effectively reversible in contrast to earlier work with PEEK [11, 20]. ITX's decreased nucleation density is primarily responsible for the variations observed in ITX's crystallization temperature, bulk conversion rate and morphology as a function of time and temperature in the melt during processing.

CHAPTER 5

THE INFLUENCE of DEFORMATION (SHEAR STRAIN) DURING BOND FORMATION on ADHESIVE BOND STRENGTH

5.1   Introduction

5.1.1   Purpose and Justification for this Research

After their initial preparation by extrusion or blowing, commercial polymer films may be reheated above their glass transition temperature, stretched, and then quickly quenched to induce and retain molecular orientation.   The intent is to enhance the physical properties of the film in the draw direction by preferentially ordering the polymer chains [137, 138, 139].   The modulus of elasticity and ultimate strength of the film are increased by molecular orientation since preferential alignment along the loading direction allows the covalent bonds along the chain to carry loads applied parallel to the deformation direction.   However, this improvement in mechanical properties is typically anisotropic.   Film mechanical properties in the perpendicular or transverse direction are

generally inferior to those for the machine or draw direction since the orientation process leaves mainly weaker intermolecular Van der Waals forces to carry any applied stress in that direction [139].

While the deliberate manipulation of polymer processing conditions to enhance film properties through orientation is well known, little work has been done to determine if molecular orientation can induce a similar effect on the polymer "film" within an adhesive bond. In fact, instead of drawing or shearing a bondline, authors emphasize the need to support members during setting or curing in order to avoid movement. This requirement for stabilization is often cited as one of the disadvantages for using adhesives [140]. If a thermoplastic adhesive is sheared during bonding, potentially high shear strains can develop leading to molecular orientation within the adhesive. The characteristic relaxation behavior as a function of temperature for the adhesive will then determine if the polymer chains have adequate mobility to relax before the material solidifies. When relaxation times are short, little preferential orientation will be retained as the polymer cools within a bondline. Conversely, longer inherent relaxation times may leave some ordering behind. The resultant molecular anisotropy could ultimately affect bond performance, just as residual thermal stresses left behind during thermoset cure can affect bond strength [140].

The goal of this research is to determine if shearing a viscous polymeric adhesive during bond formation imparts sufficient molecular orientation within the bondline such that bond performance is influenced. Secondly, if orientation is generated, what effect does it have on the mechanical performance of adhesively bonded systems? The approach taken to address these questions included a research plan with the following objectives:

1. identification of an adhesive-adherend system that could be sheared to impart orientation during processing, yet still fail cohesively <u>within</u> the adhesive when tested to see any effects of the shearing,

2. development of a bond preparation technique to generate bonds with molecular orientation parallel or perpendicular to the testing direction,

3. determination of the mechanical properties of oriented bonds versus control or unsheared bonds, and

4. finally, correlation of the mechanical properties with the level of molecular orientation present within the bondline.

Selection of the adhesive-adherend pairs utilized in this study, and development of the sheared-bond preparation technique required an initial evaluation of the suitability of several adhesively bonded systems. After this process, the work focused on the behavior of two commercial semi-crystalline hot-melt adhesives, Dow DAF® 821 and Du Pont Surlyn® 1601, bonded to aluminum in a lap-shear configuration.

5.1.2. Organization of this Chapter

The discussion of this research will be organized in the following manner. The literature review in section 5.2 will present background information on adhesives, adhesion, polymer structure-property relationships, molecular orientation and its influence on polymeric materials. Section 5.3 will provide information on the materials, and section 5.4 the experimental techniques and methodology utilized in completing this project.

After introducing the research parameters, the experimental results will then follow in the next three sections. Section 5.5 will focus primarily on the mechanical property evaluations of the two commercial hot-melt adhesives. Section 5.6 will present

the corresponding results for the adhesive molecular orientation determinations on these materials, and finally section 5.7 will discuss the post-failure bond analysis conducted to determine bond failure mode. A summary with conclusions will complete Chapter 5 in section 5.8. Recommendations for future work will be included in Chapter 6.

5.2   Literature Review

5.2.1   Adhesion Theory

The Adhesives Research Committee recognized the need to understand the basis of adhesion in their first report issued in 1922 stating that "there is still no generally acceptable explanation of the action by which glues etc. cause surfaces to stick together" [141]. Since that time, several different theories have been proposed to explain the interaction, or "mechanism of adhesion" between two different materials across an interface, however, adhesion science still remains controversial in that no universal theory of adhesion exists [142, 143]. Initially, particular adhesion theories were promoted as universal explanations for the observed phenomenon. It is only in comparatively recent years that it has been freely acceptable to consider which theories are appropriate for each particular example of adhesion under scrutiny, and then evaluate the contributions each theory might make to an overall understanding of the observed behavior [141].

Adhesion has been defined in several ways, for example "as a non-magnetic attraction between substances that makes it necessary to do work to separate them following contact and cure" [144]. More specifically, the ASTM definition of adhesion states that "adhesion is the state in which two surfaces are held together by interfacial

forces which may consist of valence forces or interlocking action, or both. The second definition implies that there are both mechanical and chemical contributions to the adhesion process between adhesive and adherend, however, the major theories proposed to explain adhesion primarily promote one factor over the other [142, 145]. The simple mechanical theory of adhesion is as an example of interlocking action favored over valence forces. On the other hand, valence force contributions to adhesion cover a wider range of interactions including both primary and secondary chemical bridges arising from chemical reactions between adhesive and adherend and residual electrical forces surrounding molecules respectively, and are promoted in the adsorption and electrostatic theories of adhesion among others.

Over the years, several different theories have been proposed to explain adhesion. Depending on the reference, these theories are divided into between four [141, 145, 146] and six [144] proposed mechanisms that explain probable contributions to adhesive bonding. One common property of each of these theories; mechanical interlocking, diffusion, adsorption, electrostatic forces, and chemical and acid-base reactions is that they do not always work. For some adhesive phenomena, these theories provide qualitatively satisfactory explanations for observed behavior, while in others respects they either fail totally, or even lead to conflicting results [146]. Since the composition and preparation of any adhesive joint is a complex incorporation of various adhesion effects, it is extremely difficult to definitively confirm or reject any of the individual theories summarized in following section at this time.

5.2.1.1 Mechanical Theory of Adhesion

The mechanical theory or mechanical interlocking theory of adhesion is the oldest theory proposed to explain adhesion [146]. This theory suggests that a hooking mechanism provides adhesion between irregularities and microcracks on the substrate surface and the adhesive through this sequence:

1) a low-viscosity liquid adhesive flows into and fills surface pores and cracks, surrounding any projections on the adherend surface before solidification as shown in Figure 5.1a ,

2) the adhesive cures or hardens in place, and

3) the solid adhesive is held in place by a mechanical hooking mechanism which anchors it to the adherend as shown in Figure 5.1b.

High strengths have been obtained with this type of adhesive bonds, even when the intrinsic interaction between the adhesive and substrate is low [145].

Theories promoting adhesion through mechanical interlocking have both intuitive appeal and direct experimental support as seen in studies by Packham and Venables on polyethylene bonded with treated aluminum and on the influence of etching aluminum and titanium surfaces respectively [147, 148]. Packham studied the behavior of polyethylene sintered onto the surface of aluminum previously anodized in acid electrolytes to generate dense barrier layer of oxide with a range of surface morphologies. Measurements of bond strength showed a direct correlation with the size (120-330Å) and relative number of the hexagonal surface oxide cells available for interaction with the adhesive. Venables et al. also investigated surface roughness and its influence on mechanical interlocking contributions to bond strength with titanium and aluminum substrates. They found that the existence of an oxide surface layer was not
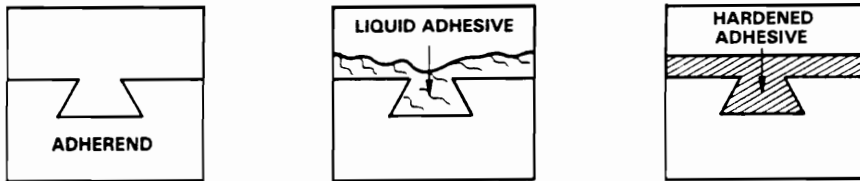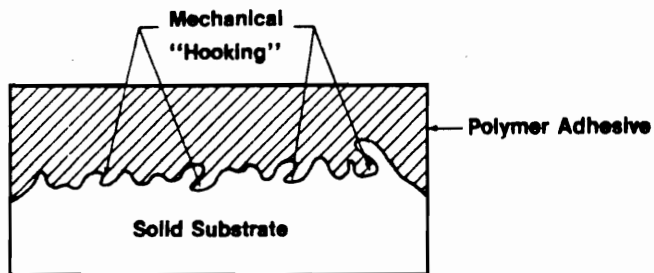
Figure 5.1a)   Illustration of the filling and solidification mechanism proposed to explain adhesion, and b) schematic representation of mechanical hooking mechanism [144].

sufficient to promote bond strength, but that the oxide must be both extremely rough and porous on a microscopic scale. When these conditions were not met, then separation of the adhesive from the substrate occurred at the interface at relatively low levels of stress. In addition, they also determined that when exposed to a hostile environment, bond strengths can deteriorate due to a change in the chemistry and morphology of the oxide layer on the substrate. If the oxide is converted to the weaker hydroxide, it is less tightly bound to the underlying metal, and therefore forms a weaker bond.

Even with experimental results confirming that mechanical interlocking positively influences bond strength, two observations in particular prevent this theory from universal acceptance as a explanation for adhesion. The first contradictory observation refuting the theory that adhesion arises solely from mechanical interlocking is the fact that strong adhesive bonds can be prepared between surfaces as smooth as optical glass flats. The second example comes from work by Maxwell bonding wood with varying degrees of roughness [149]. Instead of increasing, bond strength eventually decreases with increasing surface roughness as failure initiates at the rough wood surface .

In summary, even though mechanical interlocking is not the universal explanation for adhesion between surfaces, experimental evidence currently supports the theory that mechanical interlocking does make a significant contribution to bond strength where conditions allow the interpenetration of the adhesive into the rough surface of the substrate [141]. When the rough surface of the more rigid component is sufficiently strong to resist fracture, more energy will be needed to deform and fracture an adhesively bonded system when mechanical interlocking is present. Adhesion applications where this phenomenon is particularly relevant include polymer-to-textile

bonding, and when bonding other porous materials such as wood, paper and treated metal oxide surfaces in aluminum and titanium structural bonds [144].

5.2.1.2   Diffusion Mechanisms in Adhesion

The classical work supporting the concept that interdiffusion between the adhesive and substrate is an important factor in some adhesively bonded systems was completed by Voyutskii and Vasenin [150-152]. The diffusion theory of adhesion relates predominately to high polymer bonding, and suggests that if two polymers are in close contact at temperatures above their glass transition temperatures, the long chain molecules, or least portions of the flexible chains will interdiffuse [141]. This interdiffusion produces a boundary layer in which the different polymer chains have intermingled, resulting in entanglement and generating an actual physical bond [144].

The boundary layer which is produced has been shown by microscopy studies to be composed of a composition gradient which varies gradually from one phase to the other over a zone ranging from 10 to 1000 Å thick as illustrated in Figure 5.2 [153]. Of course, the extent of interdiffusion depends upon the affinity of the polymeric adhesive and substrate molecules for each other. However, even thin diffusion boundary layers of only 10 to 20 Å thick have been seen to increase bond strength significantly [144].

Much of the evidence supporting the diffusion theory of adhesion between a polymeric adhesive and substrate is indirect and deductive [141]. However, the theory is supported by the fact that molecular size, viscosity, polymer type, temperature, curing time, pressure and solubility all affect the quality of the bond [141, 146]. A diffusion bond is characterized by the disappearance of a clear boundary between the two phases and by the development of the gradual transition zone instead of one interface.
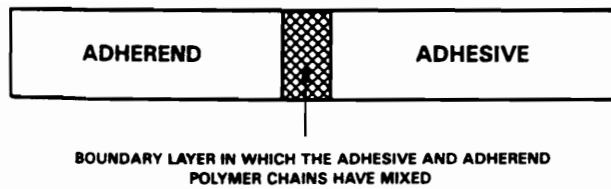
Figure 5.2   Schematic representation of the boundary layer generated via diffusion mechanisms in adhesion [144].

In summary, the diffusion theory of adhesion is limited to the adhesion of polymeric adhesives and substrates where chain mobility is sufficient for generation of an interdiffused region. Examples where diffusion theory is applicable include solvent welding of two polymer pieces in the presence of a solvent and contact bonding between two adhesive layers. This theory does not apply to a system where materials and bonding conditions do not allow diffusion of the adhesive into a substrate such as metal or glass.

5.2.1.3   Adsorption Theory

If an adhesive cannot diffuse into a high density substrate, and yet adhesion occurs, an additional rationale is necessary to explain the phenomenon. The adsorption theory of adhesion suggests that adhesive bonds are formed as a result of secondary molecular or van der Waals forces [141, 144-146]. Included in the designation "secondary forces" are London dispersion forces (temporary molecular dipoles inducing dipoles in surrounding molecules), dipole-dipole interactions such as hydrogen bonding and dipole-induced dipole attractions generated between molecules with permanent dipoles and surrounding molecules, ionic attractions and covalent bonds. These forces are on the order of 0.1 to 40 kJ/mol.

The adsorption theory of adhesion is the most generally accepted theory of adhesion, since all adhesive bonds display some level of secondary force interactions [144]. In fact, these are the same forces which provide cohesive strength within a material, an may also be available to provide adhesive strength between two materials across the interface of a joint [144]. However, for secondary forces to be present across an interface, and significant, the two materials must be in intimate contact as these

forces are only effective over distances on the order of a few angstroms. For this reason, the adhesive must spread completely over the surface of the adherend, wetting the surface evenly.

The degree to which a liquid adhesive wets a solid adherend is typically measured by the contact angle, θ, it forms with the substrate as shown in Figure 5.3. When an adhesive forms a contact angle of zero, the liquid adhesive spreads easily over the adherend. This type of behavior occurs when the molecular attraction between the adhesive molecules and the substrate is greater than are the intermolecular interactions within the adhesive itself.

Direct evidence for the positive influence of adsorption on adhesion arises within the practice of adding small amounts (0.001-0.1 mole fraction) of functional groups into an adhesive to enhance adhesive bond strength [154]. Functional groups within an adhesive show considerable specificity with respect to adherends. One example is carboxyl groups, which are copolymerized with acrylic, methacrylic or maleic acids, and known to promote adhesion to metals.

5.2.1.4   Electrostatic Theory of Adhesion

Initial work with pressure-sensitive tapes by Derjaguin et al. led to the development of the next explanation for adhesion under consideration [155]. The electrostatic theory of adhesion suggests that the adhesion forces which arise between adherend and adhesive layers are strengthened by electrical attractions across their interface. The proposed mechanism notes that in systems when the electrons within the adhesive and adherend occupy different energy levels, a transfer of electrons between the two surfaces can cause the buildup of an electric double layer at the adhesive-
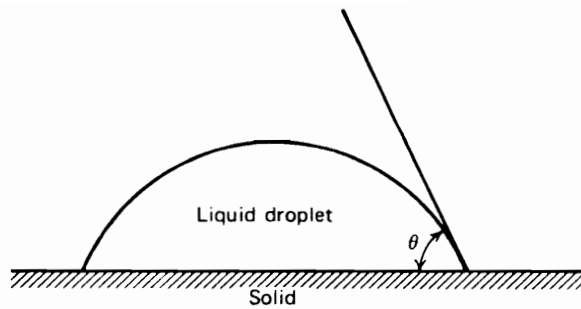
Figure 5.3 Illustration of the contact angle, θ, which a liquid adhesive makes when wetting a substrate surface [156].

adherend boundary. Because of the electron transfer, each component at the interface will be oppositely charged, and the bond will be strengthened by the electrical attraction generated across the interface.

This theory was developed to explain the observed behavior of pressure sensitive tapes where the separation of the adherends and breaking the bond was accompanied by the drawing apart of the two components. At this time, the electrostatic theory contributions to adhesion are considered as an additional strengthening factor in adhesion rather than an initial bonding cause [144]. The practical significance of the attractive forces generated are still being debated [146].

5.2.1.5   *Chemical and Acid-Base Reaction Theories of Adhesion*

The final theories of adhesion, the chemical and acid-base reaction theories are related to the adsorption theory of adhesion, and in fact are not considered separate theories but are included within the adsorption theory in some references [141, 145]. These two theories are similar to the adsorption theory in that they also suggest that there are interactions between the adhesive and substrate, the difference lies in the extent of interaction. The chemical and acid-base reaction theories of adhesion suggest that actual chemical reactions occur between the adherend and adhesive to form chemical bonds [144]. The reactions can generate ionic, covalent or metallic bonds between the two surfaces with bond strengths ranging from 50 to 1100 kJ/mol.

The acid-base theory of adhesion is based on the Lewis acid (electron donor-acceptor) concept, with the polymeric adhesive evaluated for acidity or basicity [144]. Two main approaches have been used for this determination. Anderson, Fowkes and Hielscher classified polymers according to their behavior within a "sandwich" prepared

from a metal and a semiconductor. Polymers are divided into three types: type 1, 2 or 3 depending on the type of charge they develop at the interface, e. g. type 1 polymers act as a Lewis base by accumulating positive charges near the semiconductor surface. The second classification system was suggested by Fowkes and Maruchi using the concept of contact angles [144]. They divided the thermodynamic work of adhesion, W_A, into two components, one due to dispersion forces and the other due to acid-base reactions. Selected liquids are used to determine each of the first two components, and the acid-base contribution is evaluated by subtraction.

The acid-base theory implies that selection of appropriate acid-base reactions between the adhesive and the adherend can help control adhesion within that system.

5.2.2 Classes of Adhesives

Adhesive bonding is a process where materials are united with the aid of a substance capable of holding the materials together, i.e. the adhesive [143, 157]. After joining, adhesives transfer the stresses from one member to another in a manner that distributes them more uniformly than do conventional mechanical fasteners. The initial choice of adhesive depends on the load level required; will the adhesive be acting as a joint sealant, or will it be loaded as in a structural joint where it must transmit stresses while maintaining its own structural integrity? A choice of an adhesive is typically made from among five main groups of adhesives:

- Structural
- Hot melt
- Pressure sensitive
- Water based
- Ultraviolet and electron beam cured

Adhesives are also classified by application between structural adhesives and other non-structural applications such as sealants. [143]. A structural adhesive is defined as a material which can transfer loads between adherends in service environments to which the entire system is exposed. Most structural adhesives are thermosets, however some thermoplastics such as cyanoacrylates, thermoplastic polyimides and anaerobics are used.

Structural adhesives are further classified as chemically reactive, evaporation or diffusion, hot-melt, delayed-tack, film, pressure-sensitive, or electrically and thermally conductive adhesives by the Society of Manufacturing Engineers [158]. The discussion will now center on hot-melt adhesives and their characteristics which are summarized in Table 5.1 as the focus of this research project was on two commercial hot-melt adhesives.

5.2.3 Characteristics of Hot-Melt Adhesives

The second group of adhesives listed previously, hot-melt adhesives, often have "loose" dual classification both as hot-melt and structural adhesives [158]. These adhesives are 100 % solid thermoplastics. They are solid up to their melting point, where they melt and are typically applied to the substrate. On cooling, the material rapidly solidifies, and the bond is formed. Hot-melts are classified as structural adhesives, but most will not withstand elevated temperature loading without creep. High performance materials such as polyamides and polyesters will however withstand limited loads when used below their melting temperatures. Several advantages and limitations of hot-melt adhesives are included in Table 5.2.

Table 5.1 Characteristics of Hot-Melt Adhesives [158].

Hot melt
100% solid thermoplastics
Melt sharply to a low-viscosity liquid, which is applied to surface
Rapid setting, no cure
Melt viscosity is an important property.
Nonpressure sensitive and pressure sensitive
Compounded with additives for tack and wettability

Table 5.2 Advantages and Limitations of Hot-Melt Adhesives [158].

Hot melt
100% solids, no solvents Can bond impervious surfaces Rapid bond formation Good gap-filling capability Rigid to flexible bonds Good barrier properties

Thermoplastics have limited
    elevated-temperature
    resistance.
Poor creep resistance
Little penetration due to fast
    viscosity increase upon
    cooling
Limited toughness at usable
    viscosities

Technically, all thermoplastic materials could be classified as hot-melt adhesives, but the primary materials used industrially include: ethylene and vinyl acetate copolymers (EVA), polyvinyl acetates (PVA), polyethylene (PE), amorphous polypropylene (PP), thermoplastic elastomers such as those composed of block copolymers of styrene and elastomeric segments or ether and amide segments , polyamides, and polyesters [158]. In general, hot-melt adhesives are solid at temperatures below 79° C (175°F), can be melted and resolidified repeatedly, and solidify from a low viscosity at application. Typical application temperatures for hot-melt adhesives range from 149 to 188 °C (300 to 550 °F) [159, 160].

5.2.4 Structure-Property Relationships in Adhesives

Just as in other interdisciplinary branches of materials science, adhesion science also attempts to account for the properties of materials, or more specifically adhesively bonded systems, in terms of the microstructure of the component parts of an adhesive joint. Several aspects of microstructure are considered relevant in determining the performance of a bonded system including the morphology, cross-link density if present, and phase of the adhesive as well as the topography and nature of the surface layers of the substrate [161]. In addition, modifications to the basic microstructure characteristic of the adhesive can result due to interaction with the substrate as in the case of PPS on copper [162], or by variations in the preparation or curing of the initial bond [140], therefore adhesive microstructure cannot be studied in isolation. Instead, it is generally suggested that adhesion or "the ability to hold materials together" is not an intrinsic property of any one adhesive, but rather the response of an adhesively bonded system consisting of substrate(s), the adhesive, the interfaces, and the interaction among these

parts to some deformation [161, 163-166].

One method for scrutinizing the interactions between the different components of an adhesively bonded joint that contribute to bond toughness was summarized by Packham [161]. In this treatment the energy required to break an adhesive bond in a particular manner is described as the sum of the various energy-absorbing processes involved in the fracture process. The fracture energy per unit area (**P**) of a hypothetical joint can be written as:

$$P = W + \Psi_{v/e} + \Psi_{plast} + \Psi_{substrate} + \cdots \qquad (5.1)$$

where the terms are defined as follows. The first term in the expression, **W,** is the energy required to create new surfaces through bond fracture. The magnitude of W arises from either W_a or W_c, the work of adhesion or cohesion for adhesive or cohesive failure respectively, or from a mixture of the two mechanisms for the case of mixed-mode failure. The three Ψ terms, $\Psi_{v/e}$, $\Psi_{plastic}$, and $\Psi_{substrate}$ refer to other energy loss mechanisms, viscoelastic energy losses, plastic deformation, and substrate energy absorption respectively which may occur during fracture and are typically orders of magnitude larger than the surface energy contribution term **W**.

The influence of the bulk mechanical properties of the adhesive on joint behavior are approximated in the Ψ terms, each energy dissipation term contributing to the overall fracture energy required to break the bond. Viscoelastic energy losses ($\Psi_{v/e}$) may occur as the adhesive is stressed and relaxes, i. e., the more effective the energy dissipation, the greater the bond strength. The deformation rate and temperature at failure will be reflected in the magnitude of the viscoelastic energy losses, and result in a temperature and rate dependence of P. The magnitude of the second term, plastic work ($\Psi_{plastic}$),

may also be significant with ductile adhesives. Plastic work is also rate and temperature dependent. The final energy dissipation term accounts for work absorbed by the substrate during fracture. The substrate term (Ψ substrate) will be relevant when permanent deformation of the substrate occurs during fracture.

In addition to the energy dissipation mechanisms noted above, the nature of the interface between the adhesive and substrate also significantly influences bond strength. This effect arises since the "strength of the interface" dictates the load the joint will bear, and thus the extent to which the bulk materials, adhesive, and substrate are stressed [161]. The load in turn influences the magnitude of the energy dissipated either viscoelastically or plastically. The "stronger" the interface, the more influential the microstructure of the adhesive will be on bond fracture. The substrate surface can also influence bond strength, both by affecting the microstructure of the adjacent adhesive as noted previously, or through changes in topography.

5.2.5   Structure-Property Relationships in Hot-Melt Adhesives

The previous section focused on the bulk properties of adhesive materials and discussed methods for evaluating the contributions each component within the adhesively bonded system makes to adhesive bond strength. Now the emphasis of the discussion will shift down an order in magnitude to the microstructure within the polymeric adhesive and how variations in microstructure affect adhesive bond strength. The following sections will present information on the composition of hot-melt adhesives, processing effects on microstructure, and how microstructure affects adhesion.

5.2.5.1   Hot-Melt Adhesive Components and Properties

It was noted earlier that hot-melt adhesives are 100% solids, i. e. they contain no solvents, however they are not 100% polymeric in composition. Instead hot-melts contain additional components that influence processing and performance of the material, as pure thermoplastics generally have limited adhesive properties [158]. The components in a hot-melt adhesive can be divided into two categories, the polymer and diluents. Typical diluents are additives whose purpose is to increase tack and wettability. They include waxes, plasticizers, tackifiers, stabilizers, extenders and pigments. The functions these diluents provide include:

- Lowering viscosity for ease of application,
- Enhancing wettability,
- Enhancing adhesive strength, and
- Increasing rigidity (extenders) or flexibility (plasticizers).

The second material category, the polymer, is generally a high molecular weight material whose purpose is to provide strength and high viscosity to the adhesive. The need for a high viscosity must be balanced with ease of processing, hence the addition of diluents which lower viscosity, and consequently, overall adhesive strength.

The end use characteristics of the adhesive including crystallinity, melt index, softening temperature and mechanical properties are all a function of the polymer-diluent package designed for an application. This balance between components for strength and components for processing generally results in limited toughness, low heat resistance, and poor creep resistance for hot-melt adhesives [158]. The application conditions, including the amount of adhesive and the pressure applied to the bondline can also affect final use properties of a hot-melt adhesive joint.

5.2.5.2   *Processing Effects on Adhesive Morphology and Adhesion*

Just as processing variables influence polymer morphology and crystallinity within an adhesive, the resulting microstructure in turn affects the mechanical properties of the adhesive, and ultimately of the adhesively bonded system through the adhesives contribution to the fracture energy of the joint [161]. Physical cross-links are generated within an adhesive material when polymer chain segments are restrained either by incorporation within a crystal lattice, in blocks as in thermoplastic elastomers, or within an ion-rich aggregate or cluster via the pendent ionic groups characteristic of an ionomer [167-169].

These physical cross-links, both crystalline and ionomeric, impede the movement the associated polymer chains, increasing the elastic modulus and yield strength of the material. In addition, reduced chain mobility results in increased relaxation times and consequently slower creep and stress relaxation behavior in semicrystalline adhesive materials, as well as increased viscosity and a higher glass transition temperature in some ionomeric polymers [161, 168-170]. Unlike thermosets however, these physical chain associations are temporary, they disperse and reform as a function of temperature and are therefore susceptible to processing history [161]. The dynamic properties of ionomeric materials are also a function of temperature, displaying a rubbery plateau in the modulus-temperature curves illustrated in Figure 5.4, that are not present in the parent polymer [168].

The presence of crystallinity affects the viscoelastic response of a material, and this effect is monitored through one of the terms in Equation 1, $\Psi_{v/e}$. This contribution can be so significant to adhesion that the rate and temperature dependence of adhesion
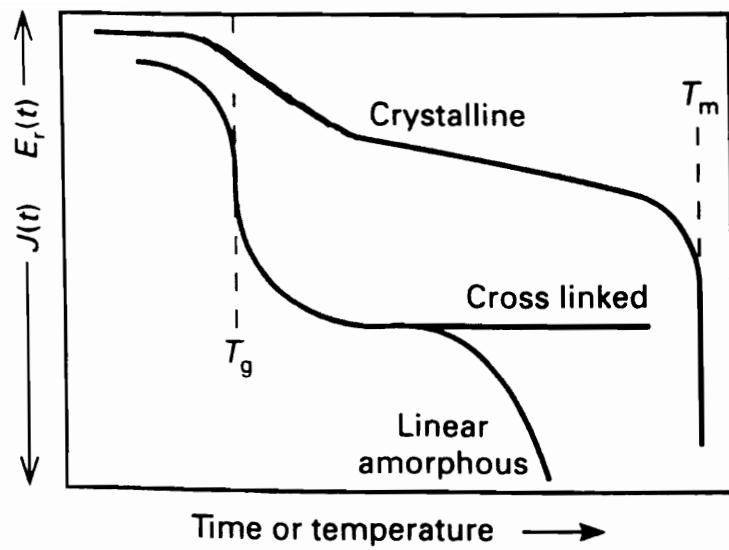
Figure 5.4 The dynamic mechanical behavior of a linear amorphous, cross-linked amorphous and semicrystalline material as a function of temperature [168].

correlates directly with the peaks for the loss tangent (tan δ) or the loss modulus (E'') [161].

The effect of crystallinity changes are complex, and are sensitive to the rate of testing and temperature. Quenching and annealing are known to affect adhesive performance [161]. As crystallinity decreases, tensile properties are affected, i. e. tensile strength at break peaks then decreases, and both tensile yield strength and elongation at break decrease for ethylene-vinyl acetate (EVA) hot- melt adhesives as a function of acetate content (increasing acetate content decreases crystallinity and glass transition temperature) [171]. Peel strength is often affected as well by increasing crystalline content by reducing the ductility of the adhesive material, and subsequently reducing the plastic energy term, $\Psi_{plastic}$, in Equation 5.1.

The cooling rate utilized in bond preparation has also been observed to effect adhesion [172]. Rapid cooling of polyolefin and polyester hot-melt adhesives provides enhanced adhesion, particularly for polyethylene coatings on oxidized copper or steel where peel strengths increased on quenching. It was noted that quenching only lowered the level of crystallinity present moderately, and smaller spherulites were produced. When slow cooling methods are applied, adhesive ductility is increased. This result is reflected in the Ψ term, and higher peel strengths.

Overall, the effect of processing variables on crystalline microstructure and on adhesion is complex, and must be considered within the context of adhesive-adherend system. Factors such as the adhesive and adherend chemistry, mechanical properties, the level and morphology of crystallinity generated within the adhesive, and the presence of other components which influence crystallization such as plasticizers, ionic groups, or tackifiers can modify the microstructure and hence the response of an adhesive to loading. The intention of this project is to add yet another variable to this complicated

group. The goal now is to systematically affect the morphology present within an adhesive by imparting preferential order, i. e. molecular orientation, within the adhesive layer and study its effect on adhesive bond strength.

5.2.6 Molecular Orientation Effects

Many commercially prepared films are reheated above their glass transition temperature, stretched, and then quickly quenched to induce molecular orientation and enhance the physical properties of the material in the draw direction. The modulus of elasticity and ultimate strength of the material are increased by orientation since it allows the covalent bonds along the chain axis to carry loads applied parallel to the stretching direction. Conversely, the properties in the perpendicular direction are usually inferior since uniaxial orientation leaves mainly weaker intermolecular Van der Waals forces to carry any loading.

Changes in molecular orientation are also known to affect other polymer characteristics including gas permeability, electrical properties, density, abrasion resistance, density and optical properties [137, 139]. Since the positive effects of molecular orientation on mechanical properties are well known, and commercially important, it is surprising that little work has been done to determine if molecular orientation has a similar effect on adhesive bond strength. If a thermoplastic adhesive is sheared during bonding, potentially high shear strains can develop leading to molecular orientation within the adhesive. If the molecular orientation is retained within the adhesive during cooling, preferential ordering may remain that could ultimately affect bond properties [140].

5.2.6.1. Development of Molecular Orientation

One of the most influential factors concerning the level of molecular orientation which is retained by a polymer is whether the material is semi-crystalline or amorphous. Greater levels of orientation can be retained in a semicrystalline polymer due to the action of the crystalline physical crosslinks reducing chain mobility [161, 170, 173]. When stretched, semicrystalline materials can produce both orientation as shown in Figure 5.5, and regions of three-dimensional order, i. e. crystallites [173]. Since the presence of crystallinity affects both the processing and the properties of a polymer, the microstructural features present in a semicrystalline polymer are relevant, and will be discussed next.

Quiescently crystallized semicrystalline polymers contain different structural components than do amorphous, or unordered polymers. The basic units present in a crystalline polymer are platelet-like single crystallites, or lamellae which are on the order of 100-200 Å thick. They frequently have a folded chain growth habit, depending on preparation conditions. If a polymer is crystallized from the bulk, initial crystallization occurs as a single crystal. Eventually, intermediate sheaflike structures known as hedrites form, and then finally as the lamellae branch outward, sphere-shaped crystalline structures, or spherulites form which contain lamellar structures.

The regions between lamellae contain amorphous material, and if present, low molecular weight materials and impurities, some of which are excluded from the more ordered crystalline structure during crystallization. The individual lamellae, which are not as ordered as in single crystals, are connected together by tie molecules, molecules which may lie partially in several lamellae. X-ray and electron diffraction analyses of spherulitic structures show that the chain or c-axis of the molecule as it is
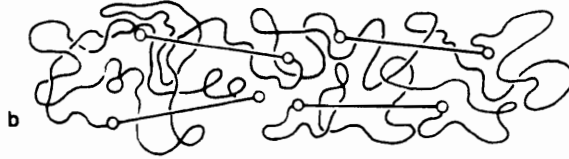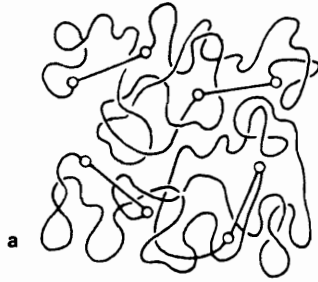
Figure 5.5 When stretched or sheared, molecular orientation can result in a polymeric material: a) unoriented, b) oriented case [174].

designated by convention, is oriented perpendicular to the flat surfaces of the lamellae. The type of spherulitic structure described here is illustrated in Figure 5.6 [161].

The thermal history a semicrystalline adhesive sees may affect the morphology as well. Large spherulites tend to develop at elevated temperatures, and low cooling rates. Smaller structures are more characteristic of lower precrystallization melt temperatures, and faster cooling rates. In addition, the degree of perfection of the crystal, the number of ties chains and the fineness of the structure which develops are all a function of the thermal profile the adhesive material sees while crystallizing.

5.2.6.2. *Effect of Orientation on Adhesive Bond Strength*

Perfect spherulitic textures are not universally seen in melt processed polymers, instead high nucleation densities and polymer flow during crystallization can result in a fine spherulitic texture, or row nucleated structures [103, 161]. In addition, shear induced orientation can be retained in a semicrystalline polymer due to the action of the crystalline physical cross-links reducing chain mobility [161, 170, 173].

Orientation within an adhesive has been the focus of studies by Schreiber et al., but at a molecular monolayer level [175]. Their research examined the alignment of model adhesive compounds at the surface of an adherend. Ordering was found to exist outward from the adherend for several molecular layers. The effect of chain orientation on polymer fractures has also been addressed [176-178]. Kambour has suggested that if an applied stress is parallel to the orientation direction, then craze initiation and growth, and subsequent craze breakdown and crack extension, are inhibited and occur at higher stress levels compared to the isotropic material [176]. Conversely, if the applied stress is perpendicular to the orientation direction, the same processes will occur more readily.
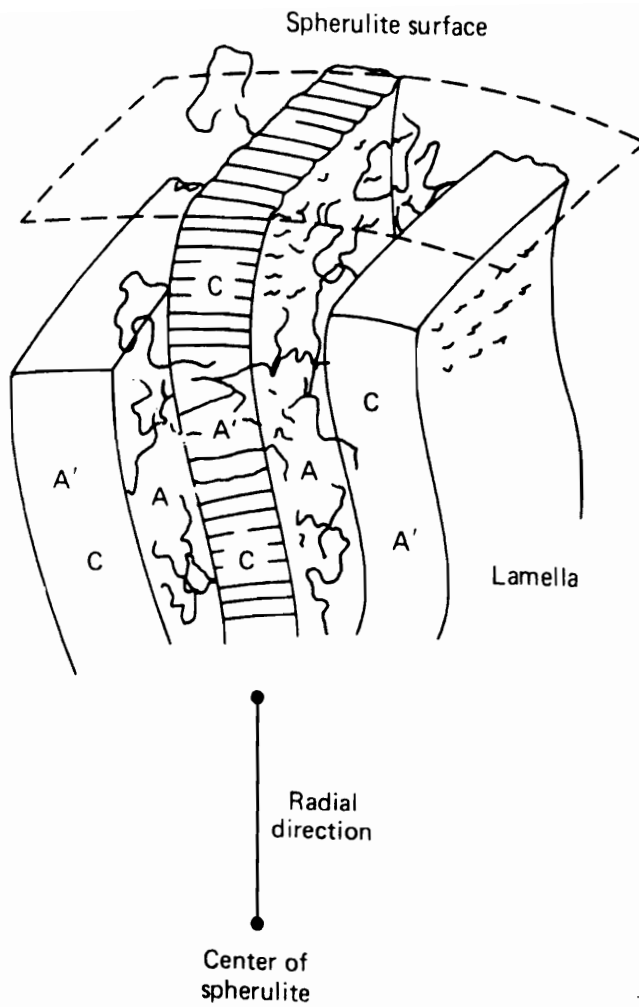
Figure 5.6   Possible structure of a spherulite [161].

The explanation offered is that orientation parallel to the stress direction, and therefore normal to the craze growth direction, has already caused the alignment of molecular chains and hence pre-empted the crazing process. Sternstein and Rosenthal suggested a flaw spectrum model to explain orientation effects, i. e. the orientation of the polymer chains changes the direction of the adventitious elliptical flaws which provide the stress concentration necessary for craze initiation, and thus the stress pattern is altered [177]. Farrar and Kramer have investigated the microstructure and micromechanics of crazes formed in oriented polystyrene [178]. They found that crazes formed by an applied stress parallel to the orientation direction are smaller, possess a higher fibril volume fraction, and have a slower stress concentration near the tip than crazes formed by a stress applied perpendicular to the orientation direction such that the parallel crazes are stronger.

The goal of this research is to take advantage of some of processing induced effects just noted, including shear, to induce molecular orientation within the adhesive layer and subsequently determine its effect on adhesive bond strength. It is anticipated that molecular orientation can affect adhesive bond strength, and in fact may potentially be a processing related mechanism for influencing adhesive bond strength in a controlled manner.

5.3   Material Descriptions

Section 5.3 will discuss the adhesive and adherend materials that were evaluated over the course of this research project. Preliminary work was completed using various thermoplastics that were readily available in the laboratory. Once it was established that a discernible difference existed in bond strengths between control and sheared bonds,

the emphasis of the study shifted to commercial adhesive and adherend materials as is described in the next two sections.

5.3.1 Adhesives

A variety of adhesive-adherend material systems were screened initially for this project. To be considered "suitable" for incorporation within the study an adhesive-adherend pair had to meet two criterion. First, the adhesive-adherend pair had to be deformable under bond preparation conditions since shear was used to induce molecular orientation in the adhesive, and yet it had to retain sufficient bond integrity to form a lap shear bond. If the adhesive viscosity was too high, manual shearing was not possible; if too low, the uncured bond fell apart. The second system requirement was that the bonds must fail predominately in a cohesive mode, i. e. within the adhesive. Since the purpose of the study was to track the influence of orientation within the adhesive on bond properties, adhesive failure at the interface did not supply useful information for this study.

Several adhesive-adherend pairs were evaluated, and judged unsuitable, for further study at this time. The materials, and the reasons for their disqualification or inclusion in the study are summarized in Table 5.3.

The materials evaluated as adhesives noted in Table 5.3 include: Phillips high density polyethylene (HDPE), poly(vinyl chloride) (PVC) polymer powder, Eastobond® hot melt adhesive, Dow Adhesive Films (DAF®) 821 and 899, Surlyn ® 1601 and Nucrel ® 0903. The first three materials listed, HDPE, PVC, and the Eastobond® hot melt adhesive were taken from the laboratory stock of miscellaneous polymer samples for preliminary work. Only the information stated was available on these materials, further

Table 5.3 Adhesive-adherend pairs initially evaluated for suitability in the adhesive orientation versus bond strength study.

Adhesive	Adherend	Comments
Phillips HDPE	aluminum	gradient in strength with orientation
Eastobond ® hot melt adhesive	aluminum	adhesive peeled off adherend
PVC [poly (vinyl chloride) polymer powder]	PC [polycarbonate strips]	excellent adhesion, all adherend failure
DAF ® 821	aluminum	gradient in strength with orientation
DAF ® 899	aluminum	gradient in strength with orientation
Surlyn ® 1601	aluminum	gradient in strength with orientation
Nucrel ® 0903	aluminum	gradient in strength with orientation

information on composition was not pursued when data collected with these specimens was not consistent, or unattainable as noted in Table 5.3.

The primary adhesives used in this study were two commercial semicrystalline copolymers, DAF® 821 and Surlyn ® 1601. The Dow material is a copolymer of ethylene and acrylic acid, with the acrylic acid present at approximately 20.5 weight percent. The melting point (T_m) as determined by DSC is 85 °C. The Du Pont adhesive is an ionomeric copolymer of ethylene and methacrylic acid, with the acid comprising 10 mole percent of the final composition. The methacrylic acid was 50% neutralized with sodium in this formulation. The melting point of the Du Pont material is 105°C. The chemical composition and microstructure of these two polymers is summarized in Figure 5.7. The materials for this work were donated by The Dow Chemical Company and E. I. Du Pont & Nemours.

Additional preliminary work was also completed utilizing two other Dow and Du Pont materials as well, DAF 899 and Nucrel 0903 respectively. The DAF 899 is similar in composition to the DAF 821 however, the material only contains 6.5 % acrylic acid by weight as opposed to the DAF 821 which contains 20.5 % acid groups. The 821 film was chosen for further work over the 899 material. The Nucrel material is also a copolymer like the Surlyn, however it only contains 9% acid groups, and is not neutralized [179].

5.3.2. Adherends

The adherends utilized in this work initially included both polymeric and metallic materials. The polymeric adherends were prepared from GE Lexan® polycarbonate strips cut to dimensions of 1.0" x 3.0" x 0.0625". In all cases, preliminary

Du Pont Surlyn ® 1601

$$-\left[CH_2-\underset{\underset{O^-Na^+}{\overset{\overset{CH_3}{|}}{C}}=O}{\overset{\overset{CH_3}{|}}{\underset{|}{C}}}\right]_n\left[CH_2-CH_2\right]-$$
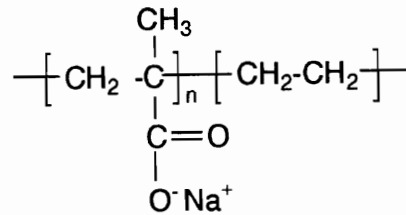
- copolymer of ethylene and methacrylic acid
- n = 10 mole %
- ionomeric material, 50 % neutralized (Na^+)
- $T_m \cong 105\,^\circ C$

Dow DAF ® 821

$$-\left[CH_2-\underset{\underset{OH}{\overset{\overset{}{|}}{C}}=O}{CH}\right]_n\left[CH_2-CH_2\right]-$$
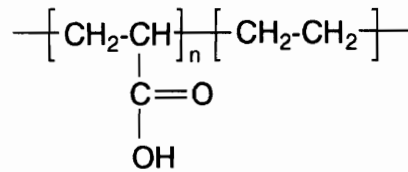
- copolymer of ethylene and acrylic acid
- n = 20.5 weight %
- $T_m \cong 85\,^\circ C$

Figure 5.7 Chemical composition and microstructure of the two primary adhesives utilized in this study: DAF 821 and Surlyn 1601.

studies involving the polymeric adherend-adhesive pair resulted in the PC yielding, shear-banding and fracturing before the PVC failed within the lap shear bondline. Even though these specimens were prepared from thinner PC coupons than recommended for a polymeric lap shear bond, which might account for the adherend failure, another disqualifying characteristic also existed. The PVC was too viscous to shear manually under the preparation conditions evaluated and this system was therefore judged unsuitable for further evaluation. The focus of further work shifted to bonds prepared from aluminum.

Aluminum was chosen as an adherend for further work, because on inspection, prepared lap shear bonds did not show any apparent bending in the adherend, instead all energy dissipation at break appeared to be within the bondline. While some of the initial work was completed with aluminum 6061 T6 coupons cut from large sheets, the majority of the adhesive bonds were prepared with purchased coupons. The aluminum coupons were purchased from Q-Panel of Cleveland, Ohio as pre-cut lap shear bond coupons of dimensions 4.0" x 1.0" x 0.065" as is recommended in ASTM D1002-72 for testing shear properties of adhesion by tension loading. The metal designation for these coupons was 2024 T3 Bare. Alloy 2024 is a high strength alloy that was introduced in the 1930's for tension loading applications in the aircraft industry.

The Aluminum Association has established guidelines for aluminum nomenclature [180]. The notation 2XXX indicates that the major alloying element in 2024 T3 Bare is copper at 4.4%. Also present in this commercial alloy are: 0.6% manganese, and 1.5% magnesium with aluminum comprising the remainder. The 6XXX notation for the 6061 T6 Bare material indicates that it has magnesium (1.0%) and silicon (0.6%)as major alloying elements, along with manganese (0.28%) and chromium (0.20%) with the aluminum. The mechanical properties of these two materials are listed

in Table 5.4.

The "T" and subsequent numeric designation gives information on the tempering each alloy received. The "T" notation indicates that the metal was thermally treated, with or without strain hardening. A "T3" alloy is solution heat treated, cold worked and then naturally aged at room temperature. The "T6" nomenclature indicates that the material was also solution heat treated, but then artificially aged at higher than room temperature [180].

5.4   Experimental Methodology

5.4.1   Mechanical Property Evaluation

A variety of adhesive-adherend material systems were screened initially for this project as described earlier, and this screening was accomplished on the basis of mechanical properties. To be considered "suitable" for incorporation within the study an adhesive-adherend system had to meet two criterion. First, the adhesive-adherend pair had to be manually deformable under bond preparation conditions since shear was used to induce molecular orientation in the adhesive, and yet the adhesive had to retain sufficient bond integrity to form a lap shear bond. If the adhesive viscosity was too high, manual shearing was not possible; if too low, the unset bond fell apart. The second system requirement was that the adhesive bonds must fail predominately in a cohesive mode, i. e. within the adhesive. Since the purpose of the study was to track the influence of orientation within the adhesive on bond properties, adhesive failure at the interface did not supply useful information for this study.

Table 5.4 Typical mechanical properties of the two commercial aluminum alloys utilized in this work [180].

Property	2024 T3 Bare	6061 T6 Bare
Ultimate Tensile Strength (ksi)	70.1	45.0
Tensile Yield Strength (ksi)	50.0	39.9
Shear Strength (ksi)	40.6	29.7
Fatigue Limit (ksi)	20.3	13.8

Single lap shear bonds were used to evaluate the tensile strength of both the sheared and unsheared adhesives. This bond geometry was chosen for two reasons. First, lap shear bonds mimic actual joint configurations where deformation could occur during bond preparation [181]. Secondly, the bonds were readily prepared using the shearing technique developed to induce molecular orientation within the bond region before testing.

Since lap shear bonds were the test method of choice for this study, it is important to recognize some of the limitations of the technique. Any test of an adhesively bonded joint is an evaluation of an adhesively bonded system consisting of adhesive, adherend and interphase regions [163]. Small changes to any portion of the system could affect the overall performance of the adhesive bond. In addition, the strain state of a loaded lap shear bond is not pure shear, but instead is more complex. [This point will be discussed in further detail in section 5.4.1.3.1.] In order to single out the effects of shear induced molecular orientation on the performance of adhesively bonded structures, great care was taken to prepare the bonds as consistently as possible, however, the scatter in the data was still evident.

5.4.1.1 Adhesive Bond Preparation

The aluminum coupons utilized in these studies were purchased pre-cut to the dimensions specified in the ASTM method noted previously for preparation of lap shear bonds. No chemical surface treatments were applied to any of the adherends in this work, however, two pre-bonding preparation steps were found to help reduce inconsistent bond failure, solvent prewashing and grit blasting the surface of the bond overlap region.

5.4.1.1.1 Adherend Surface Preparation

Since adherend surface contamination is known to affect bond strength, the bonds were all prepared in a similar manner. All as-received aluminum coupons were washed in 1, 1, 1-trichloroethane to remove any surface oil or contamination, and then air dried while resting in a rack. Initially, no other surface preparations were made before bonding, but in an effort to reduce the level of scatter in the data, additional surface modification steps were added.

The solvent washing procedure eventually involved rinsing the coupons several times. The coupons were initially washed in 1, 1, 1-trichloroethane and then air dried while resting in a rack. After they were dried, they were again rinsed in methanol, and air dried in the hood. No other surface preparations were made before bonding the preliminary samples. Inconsistent results again, however, led to the incorporation of an additional surface preparations step before bonding, i. e. grit blasting.

The surface of the aluminum coupons within the lap shear bond overlap region was grit blasted using the Empire Abrasive Equipment Corporation Blast Finisher Model MH 36485 in the Chemical Engineering Department. The grit used was A. F. S. Testing Sand 50-70. Samples prepared in this manner were washed a second time in methanol after blasting to remove any leftover grit. The bonds were then prepared using the specially modified method for generating molecular orientation within the adhesive bondline. A description of this method will follow in section 5.4.1.3.1.

5.4.1.1.2 Adhesive Preparation

Both adhesives were ultimately applied as films between the overlapping

aluminum coupons to prepare the lap shear bonds, however different levels of preparation were required before each of them was ready to bond. The DAF® 821 adhesive film material was used in the "as received" film form. Rectangular pieces were cut with a razor blade to approximately 1" x 1 1/2". Two layers of material at ~3.5 mils each were placed in the lap shear bond region before heating to 265 °F (130°C).

In contrast to the DAF 821, the Du Pont material originated in pellet form, and therefore films had to be prepared before bonding. The films were compression molded in air at 375 °F (~191°C), and then cut to size before bonding at 380 °F (193°C). A similar total film thickness was applied to the bondline for both materials, and both adhesives were vacuum dried overnight, and then stored in a dessicator between cutting and when the bonds were prepared.

5.4.1.1.3   Bonding Conditions

Bonding conditions were customized to the adhesive-adherend pair under investigation. Initially, the temperature where the adhesive melting endotherm returned to the DSC baseline, plus ~45 °C, was chosen to prepare the bonds. These values correspond to ~102.2 and 147.4 °C respectively for the Dow and Du Pont materials for bond preparation temperatures of 150 and 193 °C. Repeated bond preparations however resulted in choosing temperatures of 130 and 193 °C respectively to prepare the most consistent DAF 821 and Surlyn 1601 bonds. These temperatures were sufficiently high that there was sufficient "cooling time" after removal from the press that the bonds could be manually sheared, but the adhesive did not appear to darken in color indicating degradation.

The actual heating and pressure cycles used for the two adhesives are as follows:

Dow DAF 821:

- T_m = 130 °C (265 °F)
- 5 minute preheat, and
- 2 minutes at a pressure of ~40 psi.

Du Pont Surlyn 1601:

- T_m = 193 °C (380 °F)
- 7 minute preheat, and
- 2 minutes at a pressure of ~50 psi.

The bonds were removed from the press hot, and manually sheared, either parallel (//) or perpendicular (⊥) to the bond testing direction within approximately 2 minutes from removal. The bonds were then cooled to ambient temperature by resting them on a room temperature metal surface. Figure 5.8 shows the shearing process used to prepare the oriented bonds.

Ideally, a randomly oriented adhesive would develop without shearing, and preferential molecular orientation would be generated as is illustrated in Figure 5.9 when the bonds were sheared either parallel or perpendicular to the testing direction. By offsetting the coupons before setting them in the press and allowing extra adhesive on all sides, bonds could be prepared that were sheared approximately 1/8" in either the parallel or perpendicular direction to the bond length. Control bonds (C) were prepared with each batch of sheared bonds, however, they were handled such that they were not shifted in either direction while the hot-melt adhesive was curing. Care was taken to ensure that the bonds remained flat, checking them both during shearing, and by inspecting them before mechanical testing. All lap shear bonds were measured as well before testing, and any noticeably sideways-skewed or wedge-shaped bonds whose

a)

//
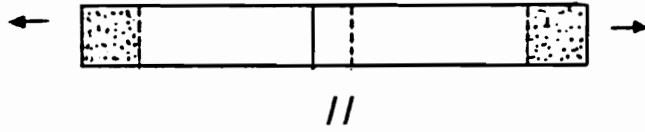
b)

⊥
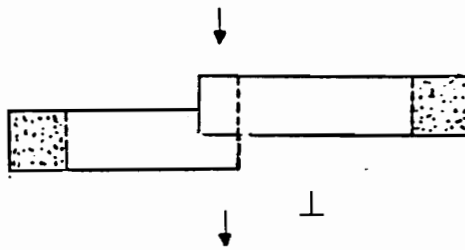
Figure 5.8 Schematic illustrating the shearing process used to prepare oriented bonds. a) parallel bonds-initial overlap of ~5/8" sheared to ~1/2", and b) perpendicular bonds-initial overlap of ~7/8" sheared to ~1".
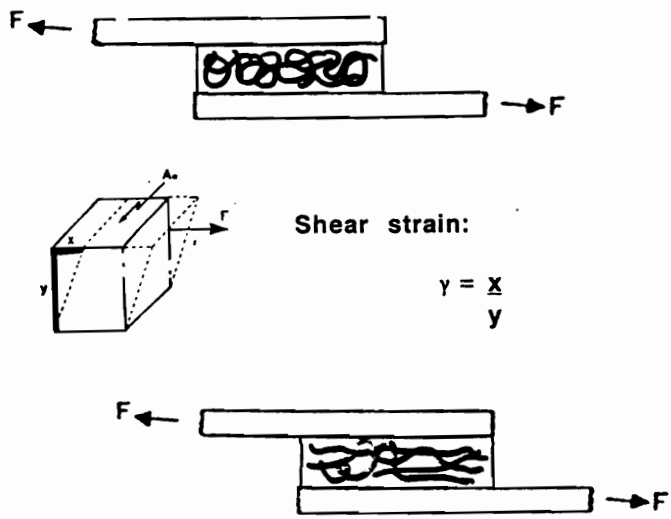
Figure 5.9 Schematic illustrating the shearing process used to generate oriented chain morphology from a random orientation.

thickness varied along the bondline were discarded. As the bonds were exposed to the open air while awaiting shearing, the "cooling time" prior to shearing varied, and was noted for each specimen. Finally, all bonds were trimmed before testing to remove any excess adhesive material from the sides of the bond. Any spew on the bond ends was also trimmed to generate a consistent geometry in the region of highest tensile and peel stress concentration at the bond line [182].

5.4.1.2   *Testing Conditions*

The majority of the lap shear bonds were tested on an Instron Model 4204 Universal Testing Machine using a crosshead speed of 0.05 "/min. The initial gauge length was 4.0 inches for all specimens. Peak loads at break were read off the digital system console, in pounds. Some of the preliminary data in this study were collected using an older universal testing machine, an Instron 1125. The data were collected under the same conditions, crosshead speed = 0.05 "/min. and gauge length = 4.0 inches, however, the data were reported only on the paper chart which traces the progress of each test. All load values were taken off the paper plot according to the scaling factors noted for each test.

5.4.1.3   Data Analysis Methods

The data collected for the lap shear tests in this study were entered into a standard "template" spreadsheet file for organization and evaluation. A sample data file is shown in Table 5.5. Further discussion on the methods used to evaluate the data are in the next several sections 5.4.1.3.1-4.

Table 5.5 Sample lap shear bond batch data file showing measured variables and calculation methods utilized in the data evaluation.

901219-56	DAF 821 (20.5% acid) bonded to Aluminum		
ADHEREND PRE-TREATMENT			
1,1,1-trichloroethane	-	-	-
12/7/90 sand blast lap region	Yes	Yes	Yes
12/19/90 methanol wash	Yes	Yes	Yes
BONDING CONDITIONS			
12/19/90			
bonding temperature	255 ° F		
pressure	1200# on 24 sq. in. = ~ 50 psi		
time	2 min./5 min.		
ADHEREND DIMENSIONS			
Aluminum	**Bond #1**	**Bond #2**	**Bond #3**
	(parallel)	**(perpendicular)**	**(control)**
coupon #1	0.0620	0.0620	0.0625
coupon #2	0.0640	0.0635	0.0630
total adherend thickness (in.)	0.1260	0.1255	0.1255
	Bond #1	**Bond #2**	**Bond #3**
ADHESIVE BOND DIMENSIONS	**(parallel)**	**(perpendicular)**	**(control)**
3 layers @ 3.5 mil/layer			
bond thickness (in.)	0.1270	0.1275	0.1270
adhesive thickness (in.)	0.0010	0.0020	0.0015
shear strain (%)	125	62	-
side #1 (in.)	0.568	0.674	0.567
side #2 (in.)	0.568	0.674	0.567
average bond length (in.)	0.568	0.674	0.567
	Bond #1	**Bond #2**	**Bond #3**
MECHANICAL PROPERTIES	**(parallel)**	**(perpendicular)**	**(control)**
load at yield (lbs.)	626	802	904
load at break (lbs.)	582	738	873
shear stress at yield (psi)	1102	1190	1594
shear stress at break (psi)	1025	1095	1540
extension at yield (in.)	0.039	0.049	0.050
extension at break (in.)	0.039	0.050	0.051
strain at yield (%)	6.9	7.3	8.8
strain at break (%)	6.9	7.4	9.0
failure mode	cohesive	cohesive	cohesive
TESTING CONDITIONS			
cross-head speed (CHS): "/min.	0.05		
chart speed (CS):	10 " FS/10 min. = 1 "/min.		
full scale load (FSL):	20 % of FS (20,000#) = 2000#		
gauge length (GL): in.	4.0		

5.4.1.3.1   Average Shear Stress

The average shear stress at yield and/or break was calculated for all specimens in units of pounds/square inch. The dimensions of the bond were measured in all three directions using a Mitutoya micrometer before testing. The length on both sides of the bond were measured and averaged, as was the bond thickness. Bond width was taken as a constant at 1.00", the dimension of the aluminum coupon. Average shear stress was calculated as noted in Equation 5.2 [181]:

$$\tau = P/\, b\; l \qquad\qquad\qquad (5.2)$$

> where: P is load at break or yield,
> b is the joint width, and
> l is the average bond length.

The shear stress values calculated for each bond are noted on the spreadsheet under the "mechanical properties" section.

The expression in Equation 5.2 is the definition of adhesive shear strength which is used in the standard test described in ASTM D1002-72, and many designers analyzing stresses consider this simple equation to be sufficient even though it is known that the actual stresses are higher [182]. The stresses are higher than predicted here because this equation does not take into account the flexibility of the adhesive or adherend in the analysis or any bending in the system, but instead considers the adherends to be rigid, and that the adhesive deforms only in shear. If instead the adherends are elastic, the situation is more complex, and the adhesive distorts to a higher extent. The two cases for rigid and elastic adherends are shown in Figure 5.10, along with their corresponding bond shear stress diagrams.

a)
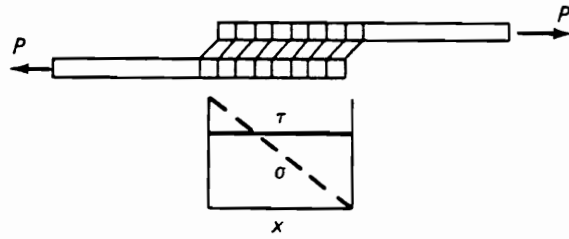
b)
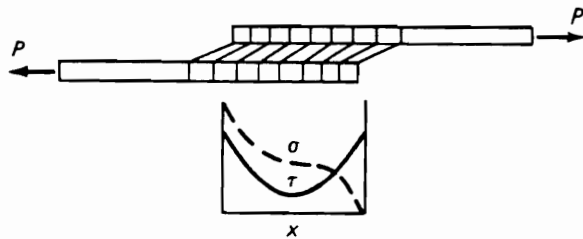
Figure 5.10 a & b Deformation profiles in single lap shear joints showing the adhesive shear stress, τ, and the adherend tensile stress, σ, for a) rigid and b) elastic adherends [182].

Several studies have been completed to more realistically model the stress state within a lap shear bond. Volkersen proposed a "shear lag" model to correct for the problem of differential shear. By assuming that an adhesive deforms only in shear, and the adherends only in tension, he developed a linear elastic algebraic solution for the shear stress distribution at any position along the length of a bond as shown in Figure 5.10b. This behavior contrasts with that of the rigid adherend model in Figure 5.10a in that the shear stress in the adhesive is at a maximum at each end.

While Volkersen's analysis incorporated contributions from the shear modulus of the adhesive, Young's modulus of the adherends, the size of the bonded region, and adhesive and adherend thickness it did not consider that the loading in lap shear bonds is not collinear [182]. Goland and Reissner took this into account, and introduced a bending moment factor, k, to evaluate the bending moment which is applied to the joint during testing in addition to the expected in-plane tension. The k term relates the bending moment on the adherend at the end of the bond overlap to the in-plane loading as shown in Figure 5.11a and b. The bending moment, or k value is 1.0 for a small load, but as loading increases, so does bond rotation, and k decreases. In addition, the Goland and Reissner analysis method considers the transverse (peel) stresses within the adhesive. Assuming that both shear and peel forces are uniform across the bond thickness, they found that peel stresses are at a maximum at the bond ends as in Figure 5.11c. Analyses on the lap shear bond stress state have also been completed by Renton and Vinson, Allman, and Adams and Peppiatt to evaluate the effects of adherend stress, variation in peel stress and variations in the stress state across the width of a bond respectively [182].

Bending moment $M_0 = Pt/2$

P

P

b)

Bending moment $M_0 = \dfrac{KPt}{2}$

$K < 1$

t

P

P
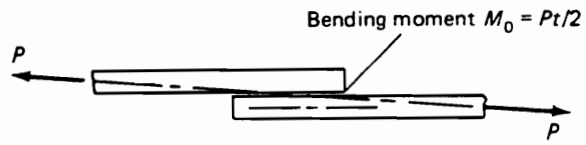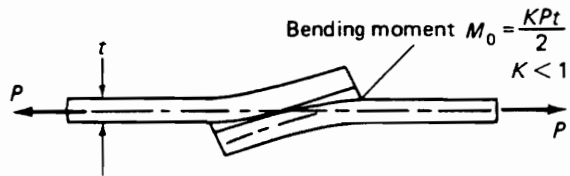
c)
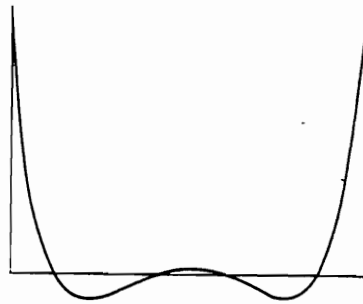
Figure 5.11a, b & c   The Goland and Reissner bending factor, k, for an a) undeformed lap shear joint, b) and deformed joint, and c) the associated transverse (peel) stresses [182].

5.4.1.3.2 Curve Integration

Initially, the strength data for the lap shear bonds was ranked only using the average shear stress values. However, in order to ensure that any trends generated this way were valid, some of the data were also evaluated by integrating the area under the stress-strain curves to determine a value proportional to the energy involved in fracturing the bond. The integrations were completed using a PC digitizing and analysis software package, Summa Graph and Summa Sketch II respectively.

Since most of the fracture peaks evaluated were relatively small, the plots were expanded on the photocopier to approximately fill the stage of the digitizer tablet. This was done to reduce the impact of any "operator" selection errors when choosing the points. The data were then digitized and scaled according to the calibration factors denoted by the graph paper and the chosen scaling on the instrument. Data files of (x, y) points were collected, and immediately integrated using the software program.

Similar trends were observed for data evaluated with both integration and shear stress at break ranking methods. If the average shear stress values suggested an increase or decrease in strength, the integrated area values reflected the same trends for all data examined by both methods. For simplicity, only the shear stress at break or yield values were reported for most of the joints evaluated over the course of this study.

5.4.1.3.3 Shear Strain

As a means for normalizing and comparing the deformation each adhesive joint received during preparation, the shear strain was calculated and tabulated on the batch spreadsheet for each sheared bond. Shear strain, (γ), is defined in Equation 5.3, and

illustrated in Figure 5.9 as:

$$\gamma = x/y \qquad (5.3)$$

where: x is the distance sheared, and
        y is the thickness of the sheared area.

The distance sheared, x is >> y. Typical shear strains ranging from 40 to 125 were generated during bond preparation within adhesive layers measuring from 0.001 to 0.003" in thickness.

5.4.1.3.4 Failure Mode

After fracture the failure surfaces of the lap shear bonds were examined by several methods. First, all bonds were inspected for apparent failure mode, and the results were noted on the batch spreadsheet. In addition, several of the bonds were examined in more detail by optical microscopy and by scanning electron microscopy. Photomicrographs obtained by each method are included later in this chapter. The final decision on the mode of failure was made after representative failure specimens were evaluated using Electron Spectroscopy for Chemical Analysis (ESCA) to verify the chemical composition of each surface. Additional details on these techniques follow in sections 5.4.2-5.4.4.

5.4.2 Optical Microscopy (Transmission/Reflection-OM)

Optical microscopy (OM) techniques were utilized for two purposes during the course of this study; first to examine the adhesive films for imperfections and voids prior to bonding, and secondly to evaluate the post-fracture surfaces of the lap shear bonds.

Reflection optical microscopy was completed using a Nikon Meausurescope optical microscope, model UM-2, along with an attached Polaroid camera. This system generated black & white photographs of the specimen under examination, and allowed examination of both the neat adhesive film, and the film after bonding to either a transparent polymeric adherend or an aluminum adherend.

The "as pressed" films were examined to determine whether the translucence of the film was a function of water or air droplets. Specimens of the film were cut and placed on the sample stage. Magnifications of 100X were used to examine the adhesive film surface.

Reflection optical microscopy was also suitable for examination of the fracture surfaces of the bonds after failure. The adherends, polymeric or aluminum, were placed on the sample stage. No sample preparation was required other than protecting the surfaces from contamination before examination by wrapping each pair in aluminum foil. Patterns generated during fracture were readily visible on the adhesive surface, and within the adhesive.

5.4.3 Scanning Electron Microscopy (SEM)

Scanning electron microscopy (SEM) was also used as an analytical technique to examine the fracture surfaces of the lap shear bonds after failure. A Cambridge model Stereoscan 200 SEM with an attached Polaroid camera was utilized to record the images.

Sample specimens were cut out from the actual aluminum adherends, either with metal cutters, or a Dremel® rotary cutter for examination. After cutting, the specimen was mounted on a standard aluminum viewing stem with double-faced adhesive tape

and silver paint. After drying overnight in a vacuum oven at room temperature, the specimens were sputtercoated with gold in an argon plasma for approximately 180 seconds.

5.4.4   Electron Spectroscopy for Chemical Analysis (ESCA)

Electron Spectroscopy for Chemical Analysis (ESCA), also know as X-ray Photoelectron Spectroscopy (XPS), was utilized to examine the surface chemistry of the failure surfaces of representative lap shear bonds prepared during this study. The instrument, a Perkin-Elmer PHI Model 5400 ESCA system, was equipped with a Mg Kα achromatic X-ray source (1253.6 eV) which operates at 15 keV and 400 watts with an emission current of 30 mA. The spectrometer was calibrated to the 4f $_{7/2}$ photopeak of gold, and 2p $_{3/2}$ peak from copper. During the analyses, the pressure inside the analysis chamber was maintained below 6.6 x 10^{-5} Pa (5 x 10^{-7} torr). Specimens ($\sim$ 1 cm x 1 cm) for the analysis were cut from the lap shear coupons with a Dremel ® rotary cutter. For analysis, the specimens were mounted on the spectrometer probe with double-sided tape. One specimen was prepared from each failure surface.

The objective of these experiments was to determine whether the chemical composition of the failure surfaces was characteristic of the adhesive or the adherend. From this information, and visual inspection of the bond surfaces, a failure mode would be chosen; adhesive, cohesive or mixed mode would be deduced.

To begin the analysis, a broad survey scan of binding energies between 0-1100 eV was collected for each specimen to identify the elements present. After identification of the peaks on the basis of characteristic binding energy, detail scans over narrower ranges were collected. Atomic concentration calculations and curve fitting were

completed on an Apollo 3500 computer using PHI software version 4.0. Quantitative data was generated using the expression [183]:

$$\text{Atomic fraction for element } C_X = \frac{n_x}{\sum\limits_i n_i} = \frac{I_x/S_x}{\sum\limits_i I_i/S_i} \qquad (5.3)$$

where I is the number of photoelectrons/second, n is the number of atoms of the element/cc of sample, and S is defined as the atomic sensitivity factor [183]. A table of atomic concentration (percent) of the identified elements was prepared for each surface. Finally, the atomic composition and concentration levels measured are then inspected to determine if they are characteristic of the adhesive, the adherend or both. If a clear difference in composition is observed, an assessment of the failure mode can be made. The ESCA data collected for this project, and its significance is discussed in section 5.7.2.

5.4.5 Fourier Transform Infrared Spectroscopy (FTIR) Linear Dichroism

The level of molecular orientation present in the adhesive films prepared for this research was determined utilizing the technique of Fourier Transform Infrared (FTIR) Linear Dichroism. The method is a special application of infrared spectroscopy which can provide a quantitative measure of the extent of preferential molecular orientation within a component or phase of a specimen [184, 185]. The data is collected by probing a polymeric chain with linearly polarized IR radiation as is described in section 5.2.6.5. The experimental details associated with collecting the linear dichroism data for this project are as follows.

By necessity, specimens were prepared for examination by IR dichroism in a different manner than the adhesive bonds were prepared. Neither the films within the bondline for the DAF 821 nor the Surlyn 1601 joints could be removed from the aluminum substrate without destroying or deforming the film. Since either case could modify the molecular orientation state measured for the specimen, a different technique was developed to shear the adhesive films between a non-stick surface. An EKCO Bakers' Secret® non-stick baking pan was cut up into several different size strips. Each size, 3" x 3" squares, 3" x 6" rectangles, and finally 1" x 4" strips were tried as a substrate to melt and shear the adhesive materials. The 1" x 4" geometry was judged the best choice as the other sizes generated joints that were too stiff to manually shear the bondline in a similar manner to that used in bond preparation.

The films were prepared at different temperatures, but similar pressures as was necessary for bonding. The films were melted at 465 °F (240 °C) and 300 °F (149 °C) for the Surlyn 1601 and DAF 821 adhesives respectively.

After holding the specimens for the same hold times as noted for the bonds, they were sheared and then immediately quench cooled in an ice bath. The specimens were quenched in an attempt to capture as high a level of molecular orientation as possible within the film. The levels then measured would reasonably correspond to a higher level or orientation than would be expected in a more slowly cooled aluminum bond. If no orientation is captured in this manner, it is unlikely that any could be expected in bonds sheared in the same manner and cooled more slowly either as more time would be allowed for chain relaxation. Several specimens were prepared using different shearing conditions.

Linear dichroism measurements were made with a Nicolet 510 Fourier Transform Infrared Spectrometer using a IGP Model 225 polarizer in absorbance mode. The machine was set-up to collect 32 scans for each of the background, sample and reference files. The reference files contained the background spectrum of the IGP polarizer used in the beam path to generate the linearly polarized radiation. The polarizer was mounted on a stage that could be rotated 90° to vary the polarization direction from parallel (//) to perpendicular (⊥) to the experimentally chosen reference direction.

After collecting a background file, reference files were collected of the // and ⊥ polarized radiation for subtraction from the sample files. These reference files consist of the background air absorbance, as well as that of the polarizer in each position. There is a difference in the absorbance measured in the two directions, especially in the smaller wavenumber regions, where the otherwise relatively straight baseline curves in opposing directions as a function of polarizer position. This is a particularly important correction to the data for this project as the most informative chromophore examined generates a double peak in the region of ∼ 720 cm^{-1} due to the in-plane and out-of-plane rocking of the methylene hydrogens within the ethylene portion of the copolymer [186].

When the background and reference files were complete, the sample data files were collected following the same procedure. After collection, the appropriate reference file was subtracted from its sample file, i. e. // from //, and the final corrected data files saved to disk. As a final step, the data files were scaled to each other and overlaid. The absorbance values for the peak at 720 cm^{-1} for each specimen were then tabulated as a function of the polarizer position. Other peak absorbances were also examined, but the results were the same as those noted for these peaks.

The final step in the analysis procedure involves calculating the Hermans' orientation function, f, for each specimen. This will quantify the level of orientation present in the adhesive film as a function of shearing. The absorbance data at 720 cm^{-1} was used to calculate the dichroic ratio, D, and ultimately the Herman's orientation function. The expressions used for these calculations are shown in Equations (5.4) and (5.5) respectively [184].

$$D = \frac{A\,/\!/}{A\perp} \qquad\qquad (5.4)$$

$$f(\Theta) = \frac{(D_0 + 2)\ (D - 1)}{(D_0 - 1)\ (D + 2)} \qquad\qquad (5.5)$$

where: A = absorbance of a chosen chromophore,
Θ = the average angle measured between the polymer chain and the reference axis,
$D_0 = 2 \cot^2 \alpha$ = zero for the chromophore of interest, methylene hydrogens, and
α = the angle between the polymer chain and the absorbing chromophore (transition moment).

The absorption at 720 cm^{-1} is characteristic of the in-plane rocking of the methylene hydrogens along the b-axis of the polyethylene unit cell [186]. Since shear induced crystallization was possible under the preparation conditions, this peak was selected to track any preferential orientation which developed within the crystalline portion of the material. The crystalline phase would be expected to retain a higher level of orientation than would the remaining amorphous fraction as the ordered crystalline material should relax more slowly than that in the less restricted amorphous phase.

A representative dichroism overlay spectra and analysis results file are included as Figure 5.12 and Table 5.6 respectively. The calculations for D and f were completed as described, and are presented in section 5.6.3.
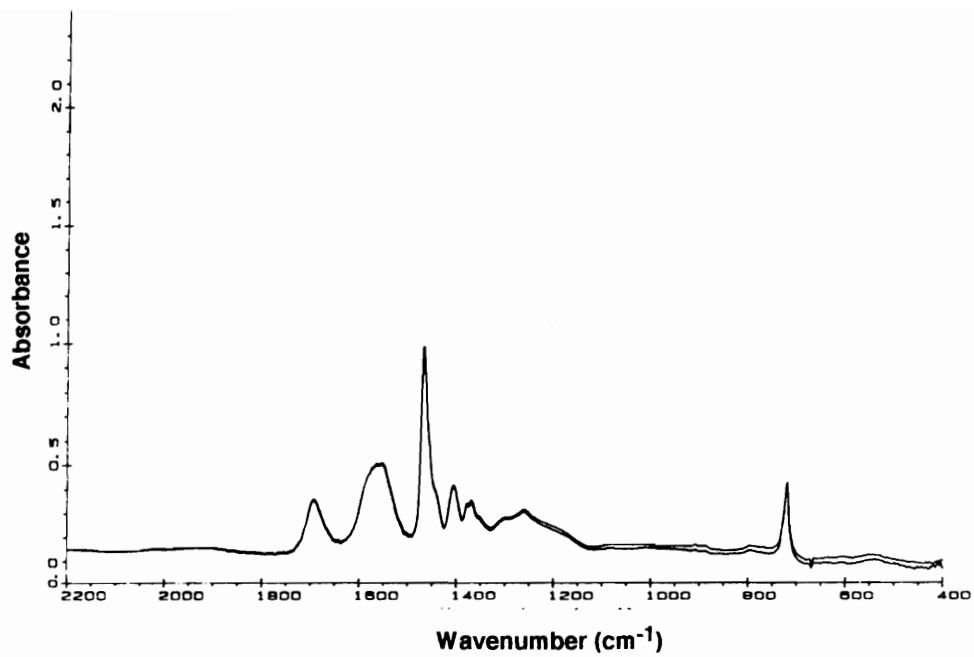
Figure 5.12   Representative FTIR linear dichroism data file collected for a Surlyn 1601 film sheared perpendicularly to the test direction after melting at 465 °F.

Table 5.6 Typical results summary for linear dichroism data, example shown in here is for the spectra in Figure 5.12.

910927-6C2	Perpendicular: Surlyn 1601 film, molded at 465 °F					
Wavenumber (cm-1)	Exp'tl Value (cm-1)	A //	A x	D	f	theta (degrees)
721	719.8	0.4231	0.4302	0.9835	0.0111	54.3
730						
1300						
1340						
1355						
1372						
1463						
1465	1467.2	0.9962	0.9906	1.0057	-0.0038	54.9
1470						

5.5   Mechanical Property Determination

5.5.1   Introduction

Since the purpose of this research was to determine if molecular orientation within an adhesive bondline affected ultimate joint strength, the preliminary portion of this project involved screening a variety of adhesive-adherend material systems. This evaluation process was accomplished on the basis of mechanical properties, and the goal of this initial work was two-fold, develop a methodology for generating orientation within the adhesive, and then identify the adhesive-adherend pair(s) for further study.

To be considered "suitable" for incorporation within the study an adhesive-adherend system had to meet two criterion. First, the adhesive-adherend pair had to be manually deformable under bond preparation conditions since shear was used to induce molecular orientation within the adhesive, and yet, the adhesive had to retain sufficient bond integrity to form a lap shear bond. If the adhesive viscosity was too high, manual shearing was not possible; if too low, the unset bond fell apart. The second system requirement was that the adhesive bonds must fail predominately in a cohesive mode as adhesive failure at the interface did not supply useful information regarding orientation effects within the thickness of the adhesive.

5.5.2   Shear (Molecular Orientation) Effects Study

The DAF® 821/899 and Surlyn ® 1601 materials were selected for additional evaluation for three reasons. First, bonds prepared with these materials survived the preparation process. Even after shearing, the adhesively bonded joints retained

sufficient integrity that they could be handled, measured and eventually broken on a universal testing machine. A second consideration was that initial mechanical property evaluations indicated significantly different behavior between control bonds and parallel or perpendicularly sheared bonds. Finally, lap shear bonds prepared from aluminum and either adhesive all displayed some level of cohesive failure when fractured. Some of the initial data used to draw these conclusions is summarized in Figure 5.13 .

The trends in fracture strength as a function of preparation method are the same for the initial data shown in Figure 5.13 for both the DAF 899 and 821 materials. The average shear stress at failure was ranked as follows: unsheared control bonds $>$ // $>$ $\perp$ bonds for each set. The DAF 821 adhesive was chosen for further evaluation over the 899 lower acid formulation as it was more readily sheared during bond preparation.

The preliminary data set which served as the basis for evaluating the suitability of the Du Pont 1601 adhesive for further study is shown in Figure 5.14. This plot summarizes the initial results of the average stress at break for several bond "sets" consisting of parallel, perpendicular and control bonds. The trends for the data are not as clear as with the DAF 821 and 899 data just presented. Instead, even though the unsheared control bonds again rank higher in strength than the sheared bonds, the parallel and perpendicularly sheared bond results are irregular. It appears that like the DAF 821 material, the Surlyn 1601 average stress at break is sensitive to shearing during bonding. For this reason, the Surlyn 1601 was selected for further evaluation in this project along with the DAF 821 adhesive.
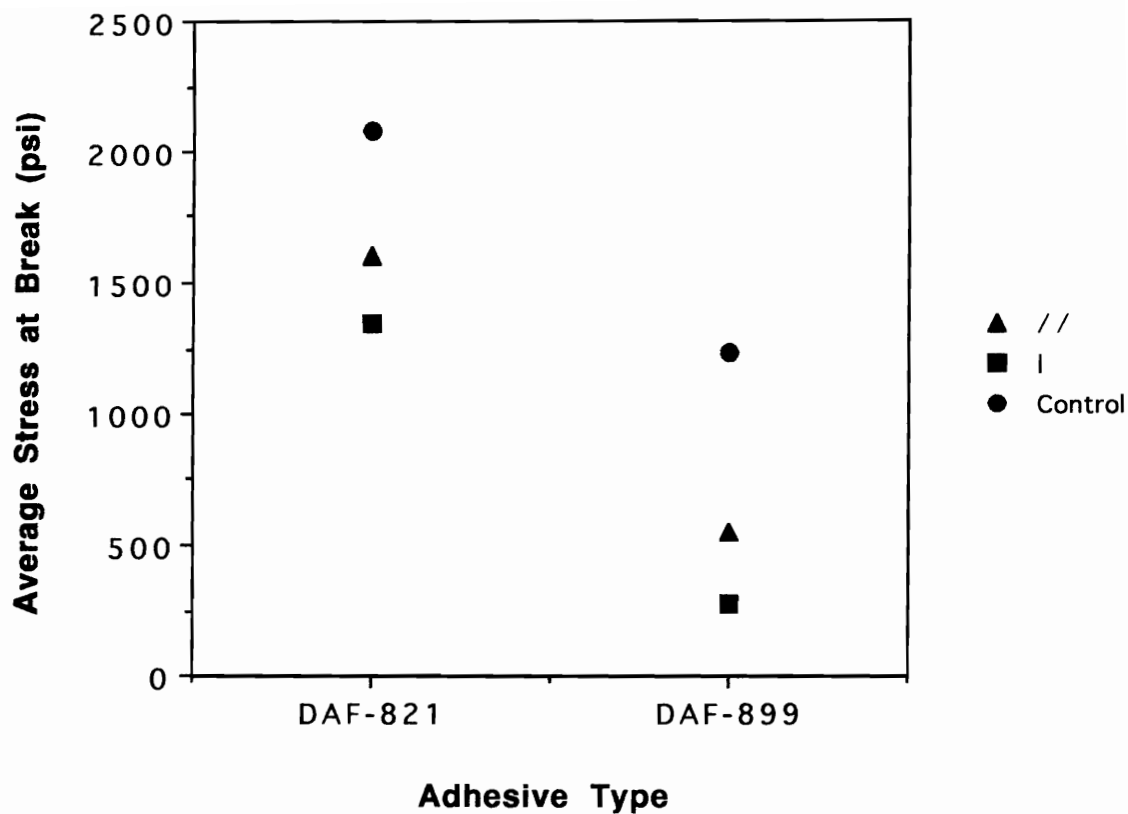
Figure 5.13   Initial tensile shear stress (TSS) data for both the DAF 899 and 821 adhesive materials. The average shear stress at failure was ranked as unsheared control bonds > // > ⊥ bonds for each set.
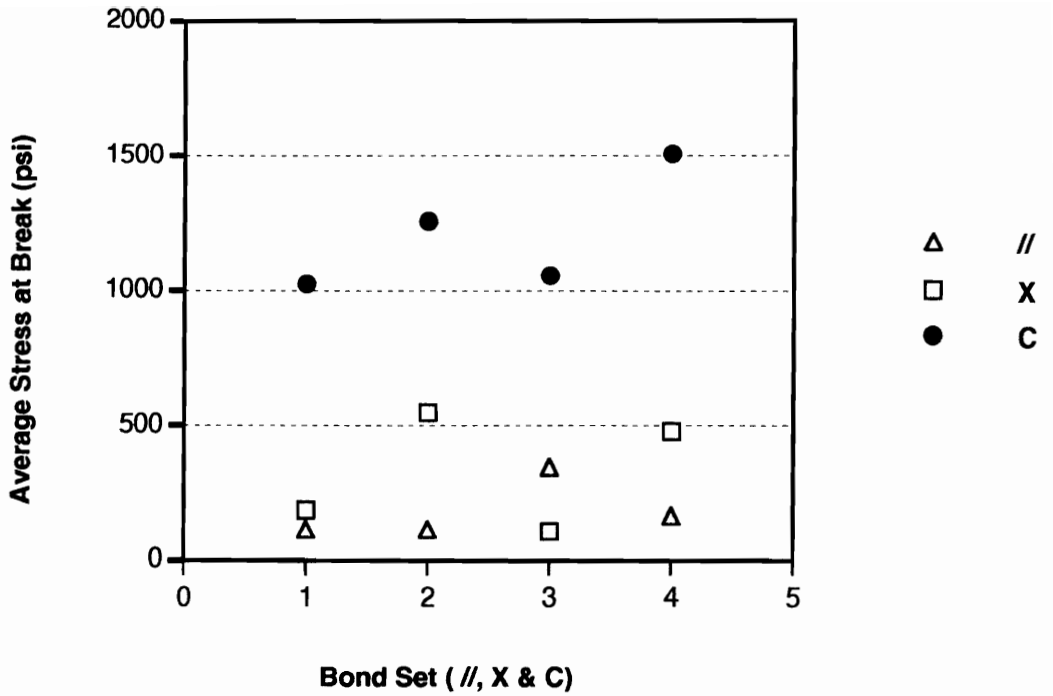
Figure 5.14 Preliminary data set utilized to evaluate the suitability of the Du Pont 1601 adhesive for further study. Initial results are of the average stress at break for several bond "sets" consisting of parallel, perpendicular and control bonds.

5.5.3 The Effect Shear Deformation During Cure on Adhesive Bond Strength

Even after carefully screening the adhesive-adherend systems utilized in this study, severe scatter problems in the measured data were commonplace. Variations of greater than ±100% of the calculated standard deviation for the average stress at break were observed. Several parameters were evaluated in an attempt to reduce the scatter, including normalizing for variations in: bondline thickness, bond preparation cooling rate, data reduction methods (bond toughness vs. peak tensile load comparisons), aging time before testing, lapsed cooling time before shearing, adhesive moisture content, and the presence of any non-uniformity's or initial flaws within the bonds. These parameters, and their effect on the observed value for lap shear bond strength, will now be examined one at a time.

5.5.3.1 Influence of Bondline Thickness on Lap Shear Bond Strength

The first experimental parameter that was examined in the attempt to identify and reduce the large variability in the observed average tensile shear stresses was the variation in adhesive thickness. It is known that in certain types of adhesive joints, bond line thickness can affect bond strength [181]. Other factors, e. g. local adhesive geometry, can also play a role in failure [182]. Gent et al. examined the two cases of thick and thin adhesive layers in shear tests [181]. They found that for the case of a thin adhesive the applied shear stress at break was related to adhesive thickness, however, for the thicker adhesive case the applied shear stress at break was instead a function of the crack length, and not adhesive thickness.

The average tensile shear stress (TSS) at break for a series of oriented and

control bonds prepared from Surlyn 1601 and aluminum were normalized for measured bond line thickness (±0.001"). This data is included in Figure 5.15. Inspection of just the control bond data from this figure, which is summarized in Table 5.7, shows that the scatter within the bonds is similar across the bond line thicknesses evaluated. The average TSS for all 20 bonds is 2034 ± 189 psi, for the five 0.001" thick bonds it is 2070 ± 173 psi, and for the five 0.0025" thick bonds the value is 2046 ± 202 psi. Overall, there appears to be no significant variation in the tensile shear strength measured for the bonds as a function of adhesive thickness. In fact, the standard deviation calculated for all bonds in this series is ~ ±10 % of the average stress at break. The standard deviation for the oriented bonds is on the same order of magnitude as for the control bonds, however it is not discussed in further detail here as they are so sparse.

5.5.3.2   *Influence of Cooling Rate on Lap Shear Bond Strength*

The second analysis parameter evaluated in the attempt to identify and reduce the large variability in the observed average tensile shear stresses was the cooling method used to prepare the adhesive bonds. The bond were prepared as described in section 5.4.1.1.3. After manual shearing, the bonds were placed on a room temperature bench top surface to cool. For this evaluation, additional bond sets were prepared, and the sheared or control bonds quenched. The bonds were quenched by placing them on the surface of a metal plate resting in an ice bath, and a second plate placed on top of them.

The average tensile shear stress was evaluated for bonds prepared from Surlyn 1601 and aluminum using both cooling methods. The data is plotted in Figure 5.16, and summarized in Table 5.8. The plot in Figure 5.16 is constructed with the slow cooled 3-
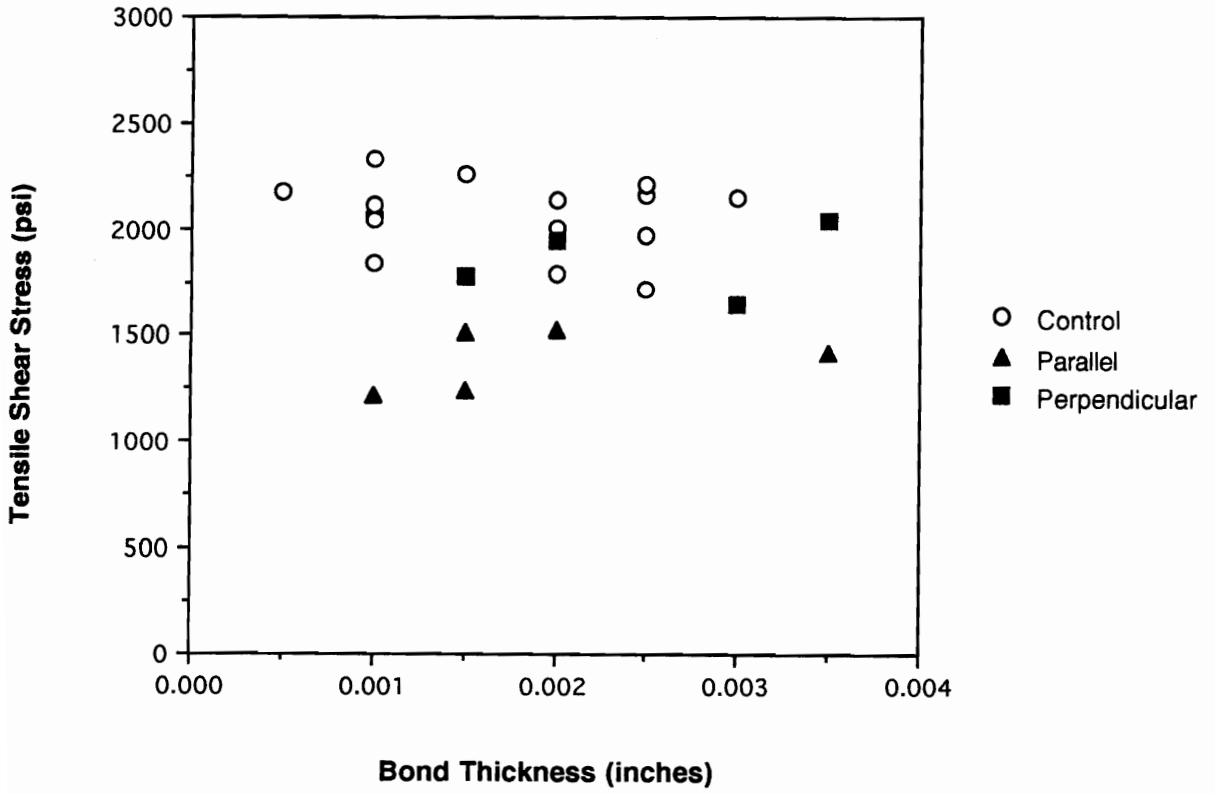
Figure 5.15   The average tensile shear stress (TSS) at break for a series of oriented and control bonds prepared from Surlyn 1601 and aluminum here normalized for measured bond line thickness (±0.001") for comparison.

Table 5.7 Control Surlyn 1601 bond data from Figure 5.15 showing that the scatter within the bonds is similar across the bond line thicknesses evaluated.

Tensile Shear Stress (psi) All Control Bonds	0.001" thick adhesive	0.0025" thick adhesive
2005		
2145	2326	2160
2326	2063	1973
2160	2045	1723
1650	1844	2212
1777	2118	2163
2063		
1973	Average:	Average:
2045	2079	2046
2153	Std. Dev.:	Std. Dev.:
2140	173	202
1844		
2255		
1723		
1794		
2212		
2118		
1949		
2177		
2163		
Average:		
2034		
Std. Dev.:		
189		
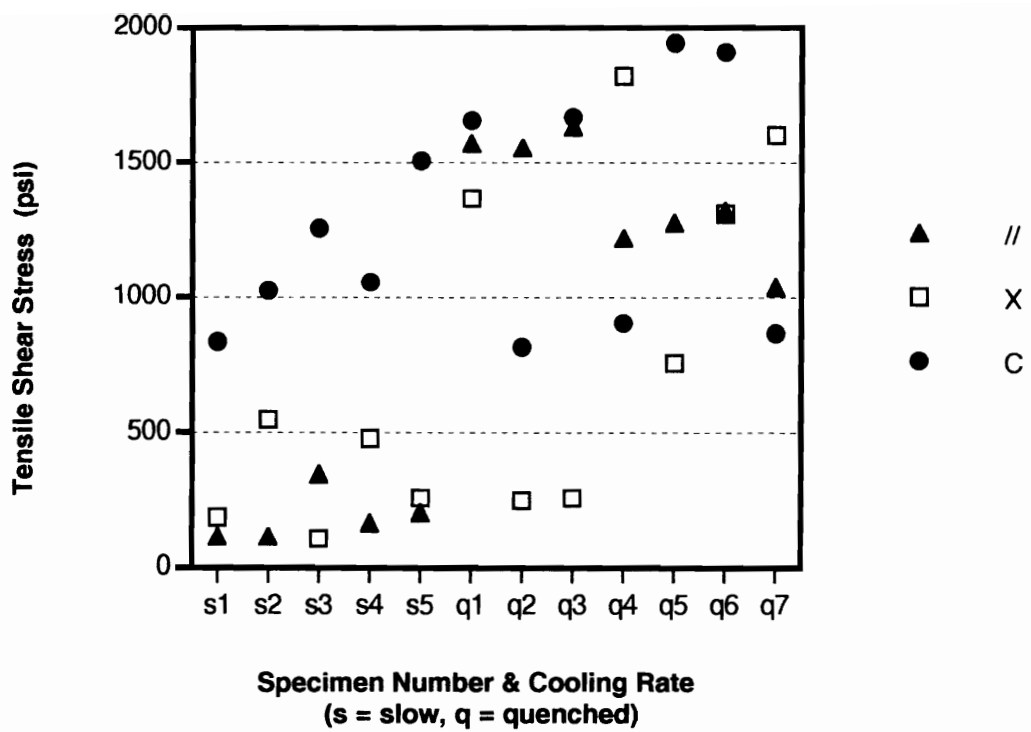
Figure 5.16   Average tensile shear stress evaluated for Surlyn 1601 and aluminum bonds prepared using both slow and quench cooling methods.

Table 5.8 Average tensile shear stress data summary for Surlyn 1601 and aluminum bonds prepared using both slow and quench cooling methods.

Slow Cooled Bonds			Quenched Bonds		
//	X	C	//	X	C
114	186	835	1571	1366	1657
115	546	1023	1554	246	816
344	106	1257	1633	256	1667
165	477	1056	1218	1820	904
202	257	1506	1276	756	1944
			1318	1310	1910
			1037	1601	866
Mean:					
188	314	1135	1372	1051	1395
Std. Dev.:					
95	189	256	219	636	511

specimen sets (//, ⊥, & C bonds prepared at the same time) on the left, and the quenched bonds on the right side of the plot denoted by "s" and "q" respectively.

There is a dramatic difference in the stress at break levels observed for the sheared bonds when they are prepared by quench versus slow cooling, along with a corresponding large increase in the scatter. Both the // and ⊥ oriented average bond strengths were affected. Measured TSS values increased from 188 ± 95 to 1372 ± 219 psi and from 314 ± 189 to 1051 ± 636 psi respectively. The average shear stress for the control bonds increased as well by ~ 20 %, but as the scatter is also large, this difference is not statistically significant. The deviation in the control bonds increased as well for the quenched bonds versus the slow cooled bonds with the observed strengths and standard deviations increasing from 1135 ± 256 to 1395 ± 591 psi.

The increase in bond strength noted for the quenched, oriented bonds as compared to that of the slow cooled specimens suggests that the quenched adhesive may retain a higher level of molecular orientation. If the adhesive cools and its viscosity increases sufficiently before the polymer chains have time to relax, additional orientation will remain within the bondline to influence mechanical properties. Another interpretation is that the crystalline spherulitic size may be affected by quenching. In Packham's work increased ductility associated with finer spherulitic texture resulted in higher observed peel strengths, which may be reflected in enhanced lap shear bond resistance to break at the bond ends where the peel forces are the highest [161].

The associated negative side-effect to quenching the lap shear bonds during preparation was the large increase in scatter observed in the data for both bond categories, sheared and unsheared. Even with spacers in place, it was difficult to quickly rest the bonds on cool metal plates, and place a second plate on top without jarring them. Shifting the unset bonds when the top plate was positioned skewed the

joints, which subsequently increased the variability in the mechanical property data. As a compromise measure, future bonds were placed on a metal surface to cool, instead of the wooden bench top, without using a cover plate.

5.5.3.3   Influence of Aging Time Before Evaluation on Lap Shear Bond Strength

The third experimental variable considered as a source for some of the inconsistency in the tensile data generated in this study was the bond aging time, i. e. the time lapse between bond preparation and evaluation. The average stress at break for bonds prepared from Surlyn 1601 is known to gradually increase over several weeks of aging due to secondary crystallization of the polyethylene component, therefore the Surlyn adhesive and aluminum coupons were chosen for this series of bonds [179].

Lap shear bonds were prepared as before, in sets of three sheared bonds plus one unsheared "control" bond. The bonds were prepared and then tested over the following intervals: 1) ~ 1 hour (denoted as "0 days"), 1, 2, 6 and 12 days. Sets of parallel and perpendicularly sheared bonds were prepared for each aging time noted. The tensile data at break for this study are summarized in Figure 5.17.

The variable plotted on the y-axis is not the tensile shear stress seen previously, but instead is the integrated area under the stress-strain curve for each specimen. As described earlier in the experimental methods, evaluating the bond data was accomplished in two ways: 1) by tabulating the load at break and calculating the average shear stress, and 2) by integrating the actual area under the stress-strain curve as a measure of the toughness of the bond. In all cases, any trends noted were the same for both data sets, toughness or stress at break.

The data showing the effects of aging Surlyn 1601 lap shear bonds before testing
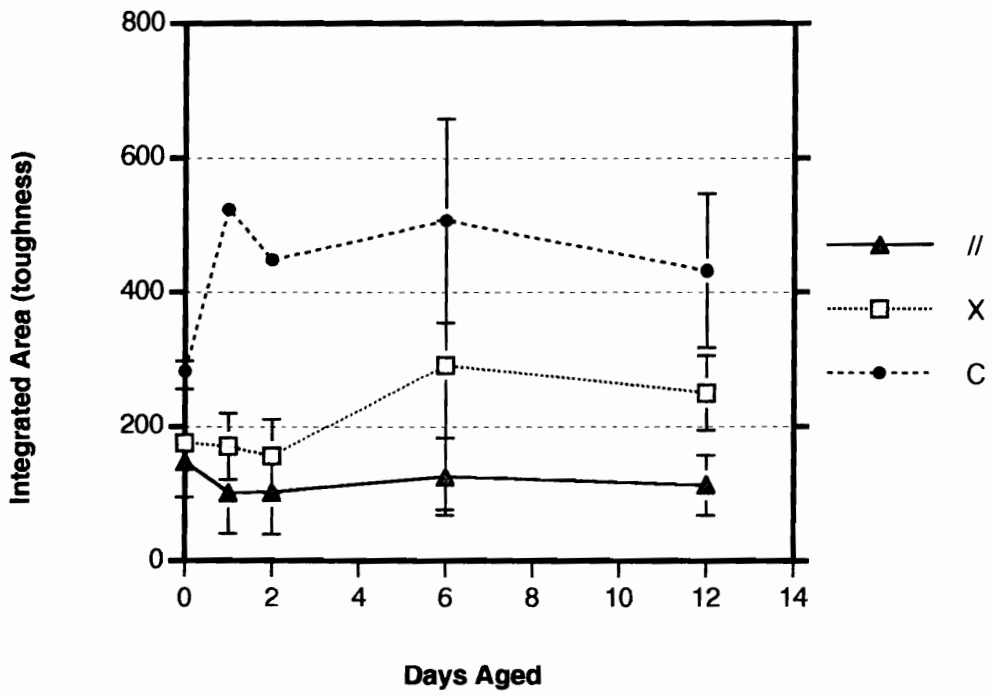
Figure 5.17   Bond toughness data for parallel and perpendicularly sheared Surlyn 1601 bonds as a function of aging time study before analysis.

are presented in Figure 5.17. The points shown and their corresponding standard deviations are calculated on the basis of three values. Only the control bonds show an initial slight increase in bond strength as a function of aging time before testing. The most significant change in strength occurs over the first 24 hours of aging. Afterwards, any fluctuations in measured strength are masked within the large standard deviation observed for the data. Based on these results it appears that there is no significant consequence of aging lap shear bonds before evaluating the mechanical properties in the context of this study. In addition, the majority of lap shear bonds for this work were evaluated within the two week period just evaluated.

5.5.3.4 Effect of Lag Time on Lap Shear Bond Strength

For this portion of the evaluation, lap shear bonds were prepared as before, in sets of two or three sheared bonds, with the balance of the four bonds in the set being unsheared "control" bonds. This was a practical decision based on the cooling behavior of the bonds, which is now the variable of interest. It is only possible to shear three bonds maximum during the time it takes them to cool utilizing the manual shearing method developed for this project. It can take up to ~180 seconds to shear a full set of three oriented bonds after they are removed from the press. Since the bonds wait in the open air, the semicrystalline adhesive has sufficient time to cool, crystallize, and the bond to set if not sheared immediately. The time that a bond waits between its removal from the press and the actual shearing is termed its "lag time", and is denoted in seconds.

The lag times for a series of oriented (// & ⊥) bonds were collected and applied as a normalization factor to plot tensile shear strength as a function of preparation

methodology. The lag time is a significant variable in this study due to the fact that each bond is manually prepared and sheared. It if takes longer to shear the first bond in a series, then the subsequent bonds will be sheared at longer lag times ... which directly corresponds to a lower shearing temperature. In the extreme case, when bonds are oriented at too low a temperature, they may fall apart during shearing. Until that temperature boundary is reached however, a potential gradient in molecular orientation may be generated and retained in the cooling adhesive as a function of time.

A series of lap shear bonds were prepared from both the DAF 821 and Surlyn 1601 adhesives and aluminum coupons as described previously. The lag time (±5 seconds) was measured as the lapsed time between when the hot bonds were removed from the press and when they were sheared. The data in this section will be presented in two ways, first as information on a series of bonds, and then the behavior of two example sets will be more closely examined.

Data collected from a series of //, ⊥ and control bonds prepared from DAF 821 adhesive (dried before bonding) is shown in Figure 5.18. Average shear stress at break is plotted as a function of the lag time before imparting orientation to the hot bond through shear deformation. The majority of the bonds were sheared within 30-90 seconds of the time when they were removed from the press with a few notable exceptions, namely the control bonds which will be discussed separately.

Both types of oriented DAF 821 bonds, parallel and perpendicular, were sheared on the average within ~±10 seconds of each other as is noted in more detail in Table 5.9. The mean lag times for each are 60 and 50 seconds respectively, however the standard deviation in lag time is larger for the // bonds as greater care is necessary to prepare them. The larger lag time is also reflected in a larger standard deviation within the TSS data for the // (1309 ± 264 psi) versus ⊥ (1647 ± 202) perpendicular bonds.
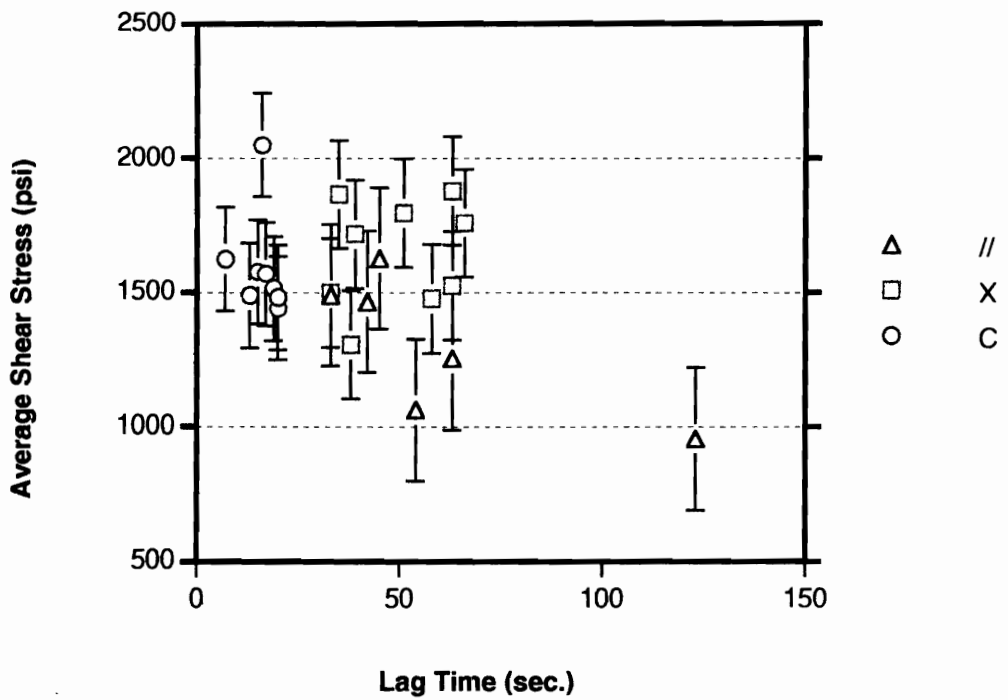
Figure 5.18   Data collected from a series of //, ⊥ and control bonds prepared from DAF 821 adhesive . Average shear stress at break is plotted as a function of the lag time before imparting orientation to the hot adhesive through shear deformation.

Table 5.9 Summary of tensile shear stress and lag time data collected for the //, ⊥ and control bonds prepared from DAF 821 adhesive in Figure 5.18.

Bond Type	Tensile Shear Stress (psi)	Lag Time (sec.)
Parallel (//) n = 6	1628	45
	1490	33
	1252	63
	1062	54
	1465	42
	955	123
// mean:	1309	60
std. dev.:	264	33
Perpendicular (X) n = 9	1867	35
	1498	33
	1717	39
	1305	38
	1879	63
	1476	58
	1796	51
	1759	66
	1525	63
X mean:	1647	50
std. dev.:	202	13
Control (C) n = 8	1569	17
	1442	20
	1577	15
	1489	13
	1626	7
	2051	16
	1514	19
	1482	20
C mean:	1594	16
std. dev.:	194	4

A third manner of viewing this data is seen in Figure 5.19 where the mean shear stress is shown versus the mean lag time helps clarify the differences between the data sets.

Overall, it takes longer to prepare the // bonds than the ⊥ bonds, and this difference is reflected in the data presented. The DAF 821 // bonds break at slightly lower average shear stresses than do either the control or ⊥ bonds suggesting that longer lag times before shearing may be significant, and detrimental. This cannot be stated unequivocally though, as numerous data sets collected over the course of the study as seen in Figures 5.20 and 5.21 show the trend reversing from batch to batch. The data in these two figures are plotted in a slightly different manner to emphasize the contrary trends that were observed. The notation on the x-axis indicated the order in which the bonds were sheared (direct correlation to lag time) with their ensuing stress at break on the y-axis. At this time it is not understood why this inconsistent behavior was so frequently observed. If increased levels of molecular orientation are retained, it is inconsistent that both increasing and decreasing strengths should be observed.

The control bonds prepared as part of this data set are all clustered within the first 30 seconds of the measured shear times. This is not because they are sheared, but instead the exact opposite is true. Since the control bonds are not oriented, but just simply removed from the hot plates and set aside to cool, it is possible to prepare them more quickly than the sheared bonds. Over the course of this project, control bonds were prepared by removing them either first or last from the hot plates without noticeably affecting their subsequent mechanical properties.
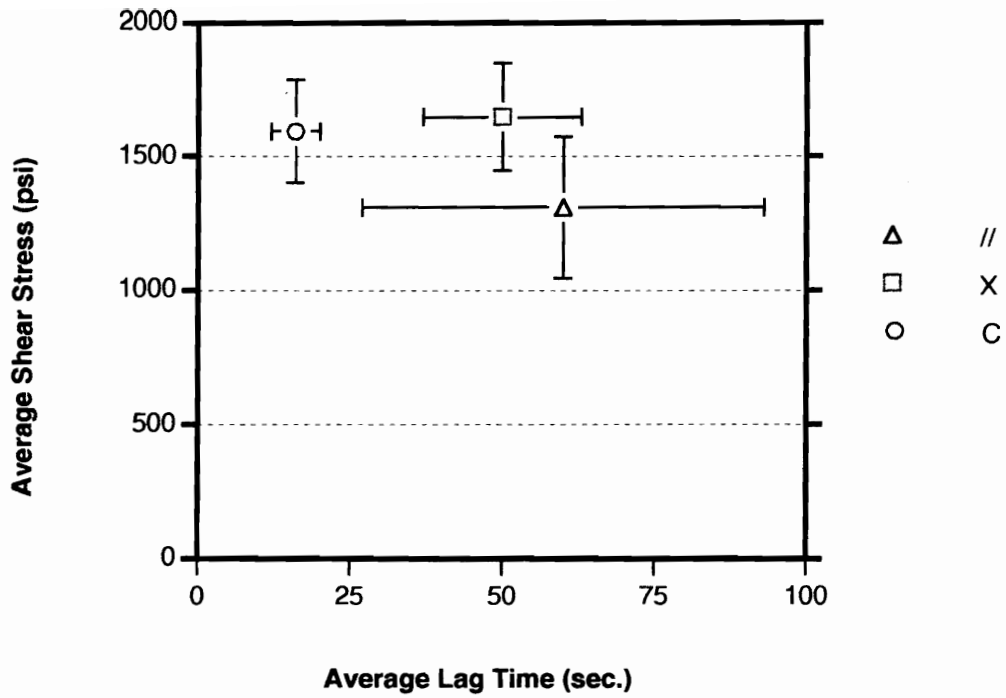
Figure 5.19   Mean shear stress versus the mean lag time for the DAF 821 bonds seen in Figure 5.18. Error bars denote the standard deviations in both lag time and average shear stress at break.
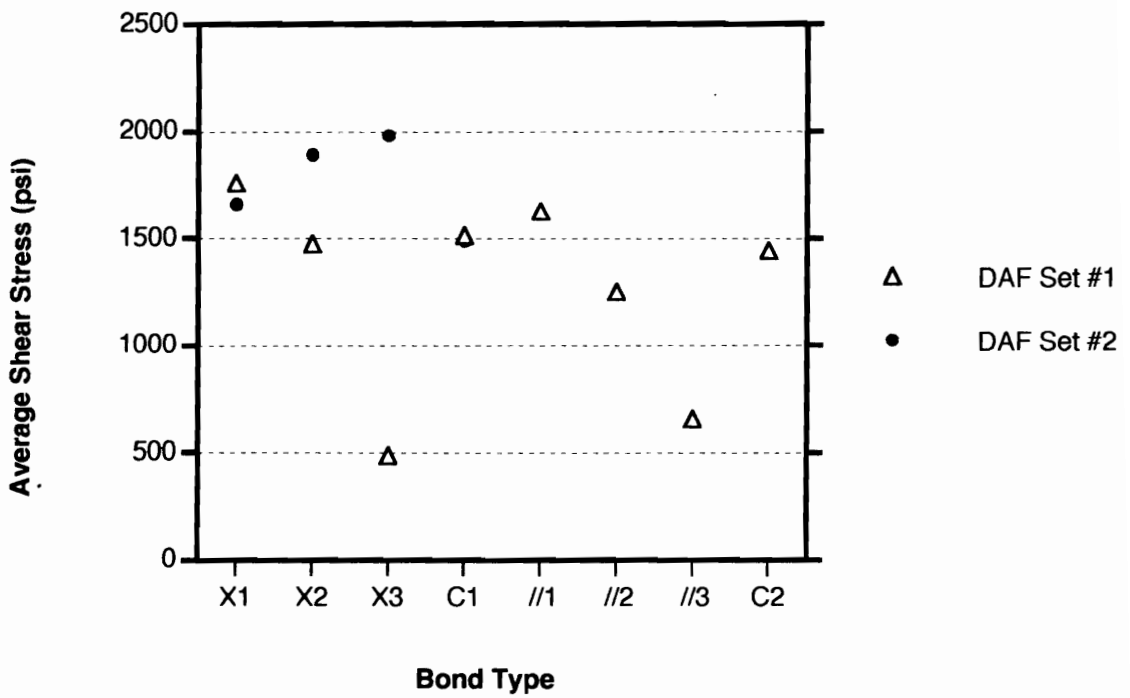
Figure 5.20   DAF 821 adhesive bond data, notation on the x-axis indicates the order in which the bonds were sheared. TSS is occasionally seen increasing and decreasing as a function of shearing time for ⊥ data.
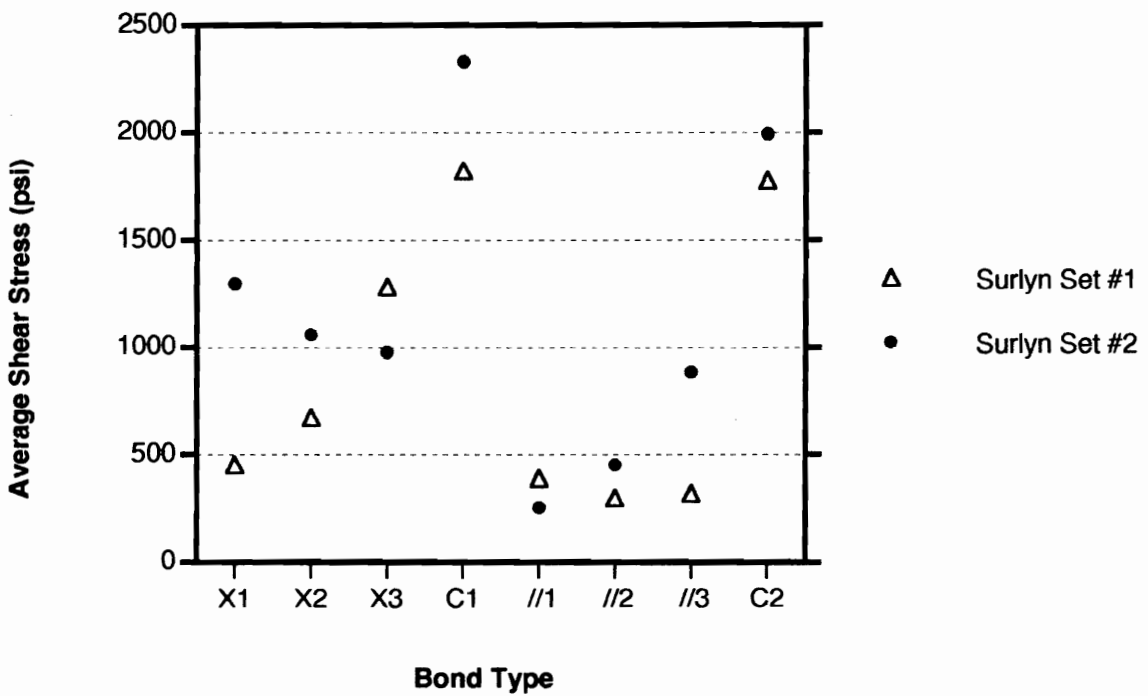
Figure 5.21   Surlyn 1601 adhesive bond data, notation on the x-axis indicates the order in which the bonds were sheared. TSS is occasionally seen increasing _and_ decreasing as a function of shearing time.

5.5.3.5 Influence of Moisture on Adhesive Performance

In addition to the parameters already considered; bond adhesive thickness, cooling rate, aging time, and lag time before bond orientation, the treatment the adhesive received before bonding was also examined. Adhesive bonds were generally prepared using dried adhesives. The adhesive films were prepared as described earlier, and then the cuts films were dried in a vacuum oven at ~170 °F (77 °C) for approximately 48 hours. After drying, the films were stored in a dessicator until they were used. Following this procedure reduced the number of sporadic, very low strength failures that initially plagued the study. Taking these precautions and care to prepare the bonds as consistently as possible resulted in much more consistent data. Standard deviations of ~ ±10 % of the measured bond strength, down from the initial ±100 % , where observed. Standard deviations of ~ ±10 % are more representative of the typical scatter that is seen in lap shear testing [187].

5.5.3.6 Effect of Bond Irregularities on Lap Shear Bond Strength

The final screening method each adhesive joint was subjected to before testing was a visual inspection. All bonds were examined before placing them in the grips of the testing machine. If the bond was skewed into a slight "v" shape instead of straight, or if any other flaws were immediately obvious flaws such as "wedges" from noticeable thickness variations in the adhesive were seen, a notation was added to the data before testing. It was noted that bonds that contained readily discernible flaws were also those whose strengths much lower than the typical scatter of ± 10% of the average. Those data were then excluded from further examination, and inclusion in the reported results.

5.5.3.7   Adhesive Bond Strength as a function of Molecular Orientation

After carefully scrutinizing the lap shear bond preparation procedures and evaluation processes utilized in this research including experimental parameters such as:

1) bond line thickness,
2) bond preparation cooling rate,
3) data reduction methods (bond toughness vs. peak tensile load comparisons),
4) aging time before testing,
5) lapsed cooling time (lag time) before shearing,
6) adhesive moisture content, and
7) the presence of any non-uniformities or initial flaws within the bonds

and taking extreme care to consistently prepare the bonds in the same manner, general trends finally emerged from the data indicating that shear induced molecular orientation was apparently affecting adhesive bond strength.

A final series of oriented lap shear bonds were prepared from the two commercial hot-melt adhesives, the DAF 821 and the Surlyn 1601 and aluminum coupons. The bonds were screened as appropriate through all of the steps just described, i. e. excluding flawed bonds etc. The data generated are shown as average tensile strength at break plotted versus the type of bond for each adhesive in Figures 5.22 and 5.23 for the DAF 821 and Surlyn 1601 respectively. The notation utilized on the plots is as follows: parallel sheared bonds (//), control bonds (C), and perpendicularly sheared bonds (X). Each data point is the mean of several specimens. The error bars included for each bond type are the standard deviations calculated for the corresponding group. Table 5.10 lists the data displayed graphically in Figures 5.22 and 5.23. The oriented lap
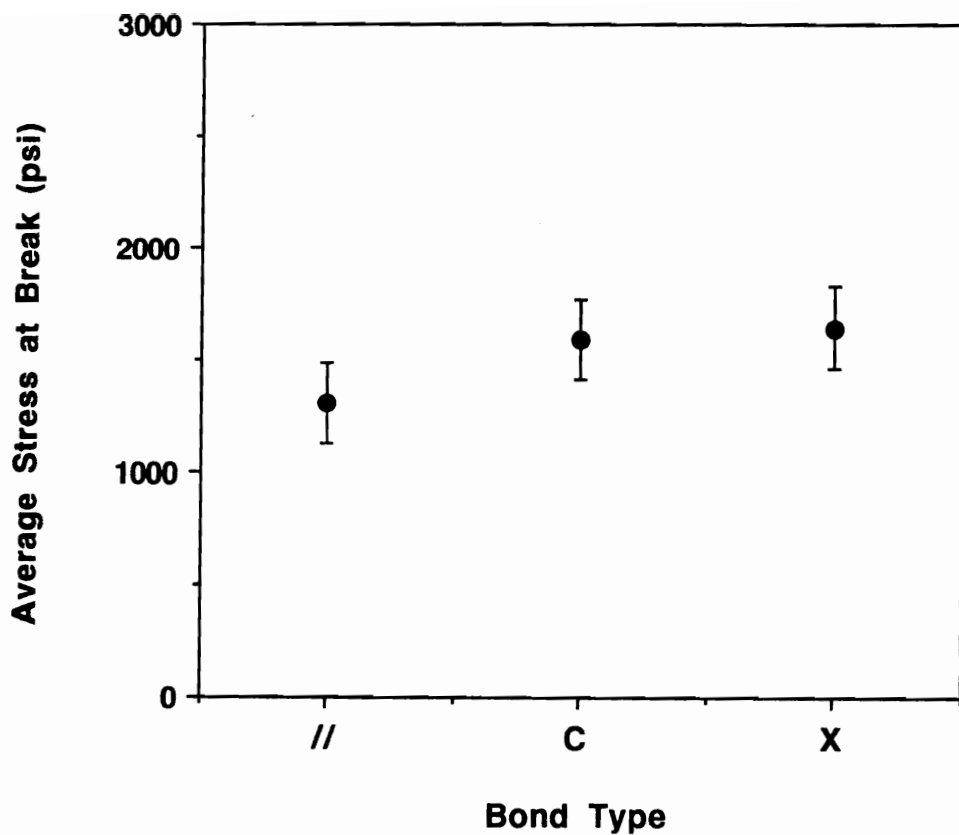
Figure 5.22   Average tensile strength at break versus type of bond for the DAF 821 adhesive. The notation is as follows: parallel sheared bonds (//), control bonds (C), and perpendicularly sheared bonds (X). Each data point is the mean of several specimens.
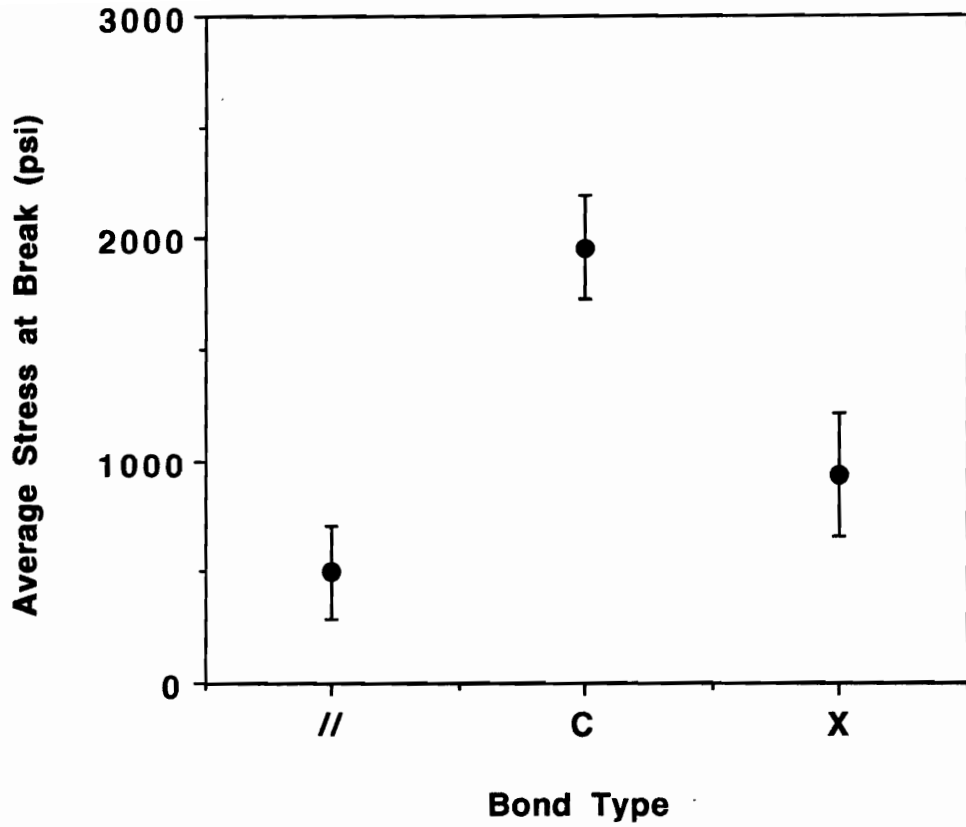
Figure 5.23   Average tensile strength at break versus type of bond for Surlyn 1601 adhesive. The notation is as follows: parallel sheared bonds (//), control bonds (C), and perpendicularly sheared bonds (X). Each data point is the mean of several specimens.

Table 5.10   Summary of the tensile shear stress data collected for //, ⊥ and control bonds prepared from both DAF 821 and Surlyn 1601 adhesives in Figures 5.22 and 5.23.

	Bond Type	Mean	Standard Deviation	Number of Specimens
DAF 821	//	1309	264	6
	⊥	1594	194	9
	C	1647	202	8
Surlyn 1601	//	498	208	12
	⊥	938	273	12
	C	1960	233	9

shear bond data still show a considerable amount of scatter, even with all of the precautions taken in preparing the bonds. Even with the scatter however, general trends in bond behavior as a function of the orientation process are observable.

The general trend observed in the data for both the DAF 821 and Surlyn 1601 adhesives is that the shearing process <u>does</u> result in differences in the observed bond strengths for these systems as compared with undeformed control systems. The observed differences in tensile shear stress at break could be a result of molecular orientation induced within the adhesive layer due to the high shear strains of $\gamma = 40\text{-}125$ generated during shearing. Instead of enhancing bond strength however, the process appears detrimental. The deleterious effects are more pronounced with the Surlyn 1601 bonds than with the DAF 821 specimens. There is little difference in the average tensile strength measured for the oriented versus the undeformed control DAF 821 bonds within the range defined by the standard deviation of the data. The Surlyn bonds however, do show a difference in strength between the control and the sheared bonds. Both parallel and perpendicularly sheared bonds are weaker than the control bonds. The parallel bonds are slightly weaker than the perpendicular bonds on the average, but it does not appear to be statistically significant.

Since there is a difference in strength at break as a function of deformation for the bonds, particularly for the Surlyn 1601 adhesive, the next step was to determine if that difference in behavior arises from molecular orientation generated during the shearing procedure, or if other factors were involved. This was accomplished by using linear dichroism to establish the existence, and quantify the level, of any molecular orientation within the adhesives.

5.6   Molecular Orientation Measurements

Fourier Transform Infrared Spectroscopy (FTIR) linear dichroism was used to quantify the level of orientation present in oriented, but unstressed films of each adhesive.   As was described in the experimental details in Section 5.4.5, separate sheared films were utilized in the orientation level evaluation, not the adhesive films from within the bond line as neither adhesive could be removed from the aluminum substrate without destroying or deforming the film.

5.6.1   FTIR Linear Dichroism Analysis

The FTIR linear dichroism measurements were completed in absorbance mode. The sheared film specimens were evaluated for molecular orientation by placing the polarizer in the beam path both parallel and perpendicular to the film shear reference direction, and collecting an absorbance spectrum.   After correcting the // and ⊥ data by subtracting the appropriate polarizer reference file, the absorption at 720 cm^{-1} was evaluated.   The measured values for each specimen were then tabulated as a function of the polarizer position, // or ⊥.   [Other peak absorbances were also examined initially as noted in the sample data presented earlier in section 5.4.5.   Their absorbance values were either proportional to the 720 cm^{-1} values giving the same results, or did not show any preferential absorbance as a function of polarizer alignment, so they were not considered further].

The doublet peak in the region of ~ 720 and 730 cm^{-1} was the focus of the linear dichroism evaluation for both adhesives.   This signal is characteristic of the in-plane and out-of-plane rocking of the methylene hydrogens within the ethylene chemistry present in

both adhesive polymer chains. A single peak absorption at 720 cm^{-1} is the result of in-plane rocking of the methylene hydrogens along the b-axis of the polyethylene unit cell [186]. The second peak at 730 cm^{-1} develops on crystallization as a result of the interaction of the methylene groups in the crystalline regions. For polyethylene, the 730 cm^{-1} peak arises from crystalline regions alone, and the 720 cm^{-1} band arises from both the crystalline and amorphous regions. Both bands are known to show dichroic properties, i. e. preferential absorption as a function of polarization direction in oriented samples. Since shear induced crystallization was possible under the preparation conditions, these peaks were selected to track any preferential orientation which developed within the crystalline portion of the material as well as the amorphous phase. The crystalline phase would be expected to retain a higher level of orientation than would the remaining amorphous fraction as the ordered crystalline material should relax more slowly than that in the less restricted amorphous phase.

The molecular orientation analysis procedure involves calculating the Hermans' orientation function, f, for each specimen to quantifiy the level of orientation present in the adhesive film as a function of shearing. The 720 cm^{-1} absorbance data just described was used to calculate the dichroic ratio, D, and ultimately the Herman's orientation function. The associated doublet peak at 730 cm^{-1} was not observed as expected, therefore all calculations were based on the 720 cm^{-1} band alone. The general expressions used for these calculations were described earlier. The expression in Equation 5.6 is in the form utilized for the calculations.

$$f(\Theta) = -2 \; \frac{(D-1)}{(D+2)} \tag{5.6}$$

where: Θ = the average angle measured between the polymer chain and the reference axis, and D is the experimentally determined dichroic ratio.

The value of Herman's orientation function, f (Θ), determined is representative of the average molecular orientation of the polymer chain with respect to the reference shear axis. Three extreme cases are defined; f(H) = 0, 1, or $-1/2$ which correspond to random, parallel or perpendicular molecular orientation states with respect to the reference axis [184].

5.6.2 Molecular Orientation Level Evaluation

The dichroic ratio was determined for DAF 821 and Surlyn 1601 adhesive films that were sheared parallel or perpendicular to the reference direction, as well as for unsheared control films. In all cases, a comparison of the parallel absorption to that measured perpendicular to the reference axis resulted in a dichroic ratio of approximately 1.0. The corresponding values of f (H or Θ) that were subsequently calculated from these D results all fall within the first category just described, i. e. the f(H) values were all approximately zero. A zero value indicates that the molecular orientation of the chromophore, and therefore of its corresponding polymer chain is random. No preferential molecular orientation was detected utilizing this technique. The results for these calculations are summarized in Table 5.11 for the two adhesives.

5.6.3 Summary: Correlation Between Molecular Orientation and Adhesive Bond Performance

These results, a value of one for D, and zero for f(H) indicate that there is no measurable preferential absorption of polarized ratio by the chromophore of interest, and thus no measurable levels of molecular orientation retained within the sheared

Table 5.11   FTIR linear dichroism results for //, ⊥ and control films prepared from both DAF 821 and Surlyn 1601 adhesives.

		Wavenumber (cm-1) *	A //	A x	D	fH
Surlyn 1601						
	//	720	0.639	0.663	1.036	-0.024
	⊥	720	0.988	0.977	1.011	-0.007
	Control	720	1.348	1.360	0.991	0.006
DAF 821						
	//	720	0.495	0.501	0.988	0.008
	⊥	720	0.378	0.384	0.986	0.009
	Control	720	1.451	1.458	0.995	0.003

* Peak Origin: b-axis, -CH2- hydrogen rocking, amorphous and crystalline regions

adhesive film. They also suggest that for the two commercial adhesives investigated, molecular relaxation was sufficiently rapid following shearing of the hot melt adhesive layer that it lead to an unoriented adhesive joint. Since the level of shear strain induced in the adhesive layers was rather extreme, $\gamma = 40\text{-}125$, molecular orientation should have developed readily. It appears however, that permanent molecular orientation is limited due to rapid relaxation in these two materials since no preferential orientation was found using this technique. The differences in the mechanical properties observed for the two adhesive systems cannot therefore be attributed to molecular orientation within the adhesive layer.

5.7 Post-Failure Bond Analysis

The linear dichroism experimental results suggest that molecular relaxation was sufficiently rapid following shearing of the hot-melt adhesive that an unoriented adhesive joint resulted. Since differences in the mechanical properties were observed for the two adhesives as a function of their preparation method, either other factors were controlling the failure of the bonds, or linear dichroism was unable to characterize these systems. The failure surfaces of the bonds were then examined for any clue to the observed differences in properties.

5.7.1 Adhesive Morphology

The morphology of the adhesive layer was next carefully examined to determine if any differences were present within the adhesive that could account for the variance in the average tensile shear stress that was determined. Over the course of the study, all

the adhesive bonds were visually inspected immediately after they were tested, and an initial characterization was made on the apparent type of failure present, e. g. adhesive, cohesive or mixed mode failure. A general, but not exclusive trend was observed. Bonds that were sheared appeared to fail in a cohesive or a cohesive/mixed mode, while unsheared control bonds failed more often in an apparent adhesive or adhesive/mixed mode. The failure surfaces of the two cases, sheared and unsheared frequently appeared different as well, and will be discussed further in the next two sections.

5.7.1.1 *Optical Microscopy of the Failure Surfaces*

Reflection optical microscopy (ROM) techniques were utilized to examine the post-fracture surfaces of the lap shear bonds. The technique permitted examination of the adhesive film while it was still bonded to the aluminum adherend, especially as in a case of cohesive failure. The adherends, polymeric or aluminum, were placed directly on the sample stage. No sample preparation was required other than protecting the surfaces from contamination before examination by wrapping each coupon pair in aluminum foil. Failure patterns generated during fracture were readily visible on the adhesive surface, and within the adhesive.

Figure 5.24a-d is a composite of four optical micrograph views of the failure surfaces of Surlyn 1601/aluminum adhesive bonds. Figures 5.24a and b are the fracture surfaces of unsheared control bonds, while c and d are parallel and perpendicular bonds respectively. The horizontal striations visible in all four pictures are the result of reflection off the texture of the aluminum surface under the adhesive. The vertical direction of the page corresponds to the testing direction used to fracture the lap shear bonds, and also to the shear direction utilized to prepare the parallel bond in c. The

perpendicular bond was sheared in the horizontal direction.

The control bonds have a very different morphology than that of the sheared bonds. The adhesive on the surface of the control bonds appears as a series of connected "flowers" or loops which are characteristic of a low-loading rate fracture [188]. The flower-like pattern in Figure 5.24a is typical, and is formed when a crack propagates outward from a defect within the center of the "flower". The surface of the dark circular or flower-shaped ridges which surround lighter color areas show ductile deformation, and the formation of fibrils where the adhesive was sheared during mechanical fracture. The failure mechanism which occurs when the critical shear stress is exceeded is illustrated in Figure 5.25 [174].

The sheared bonds do not show the same elaborate patterns, but instead the adhesive surface has ridges that correspond to the direction the bond was sheared before mechanical testing. The ridges are more prominent in the parallel than in the perpendicularly sheared bonds. The surface features of the failure surfaces of the adhesive were also examined by scanning electron microscopy.

5.7.1.2   Scanning Electron Microscopy (SEM) of the Failure Surfaces

Scanning electron microscopy (SEM) was also used as an analytical technique to examine the fracture surfaces of the lap shear bonds after failure. The SEM micrographs in Figures 5.26a-c show the fracture surfaces of three Surlyn 1601 adhesive bonds, a parallel sheared bond, a perpendicularly sheared bond, and an unsheared control bond respectively. The magnification is the same for all three micrographs at ~41X. The schematic illustrations beside each micrograph indicate the load direction applied to the bond at fracture.
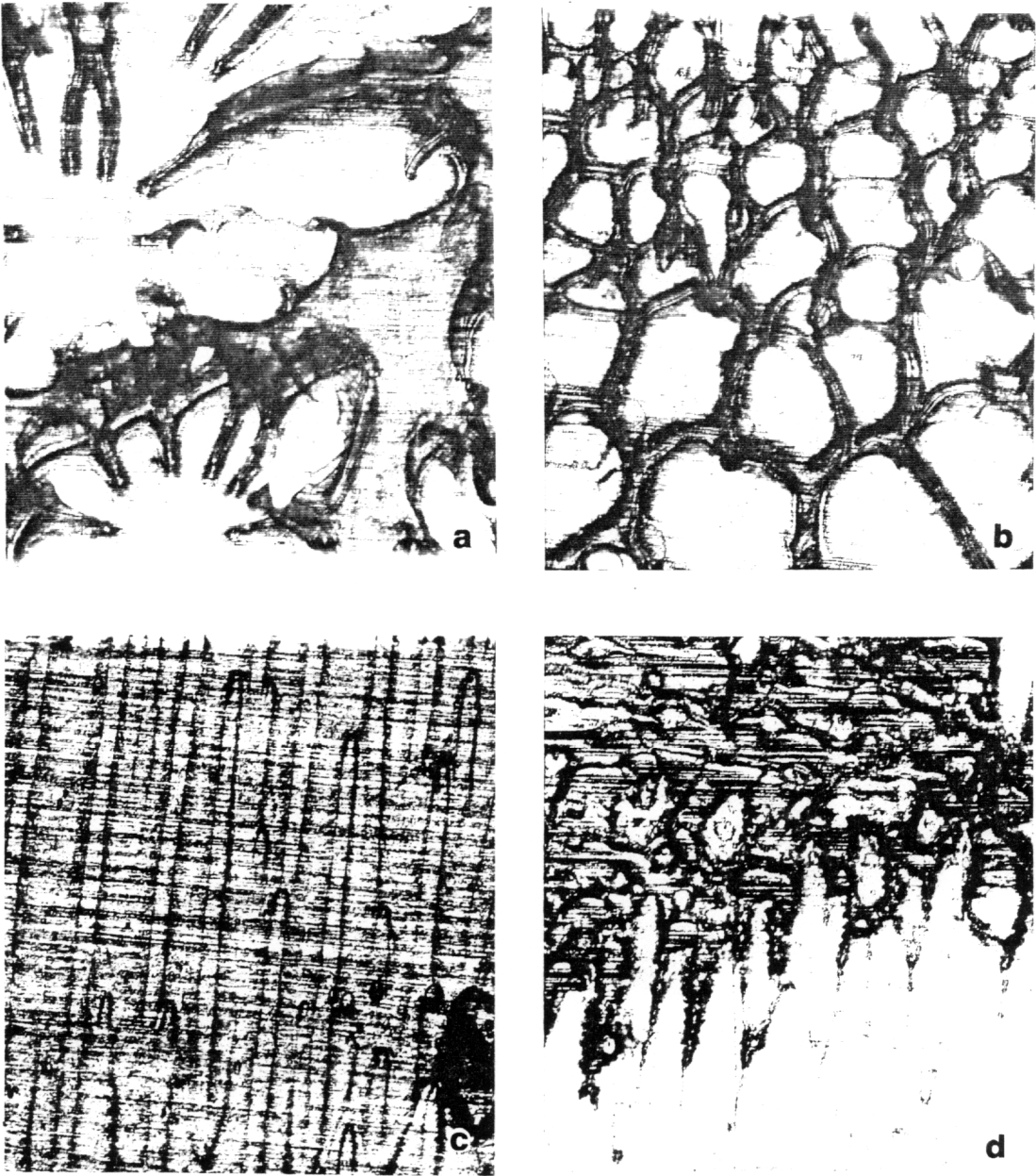
Figure 5.24   Four optical micrograph views of the failure surfaces of Surlyn 1601 and aluminum adhesive bonds. Figures 5.24a and b are the fracture surfaces of unsheared control bonds, while c and d are parallel and perpendicular bonds respectively. Magnification is 100X.
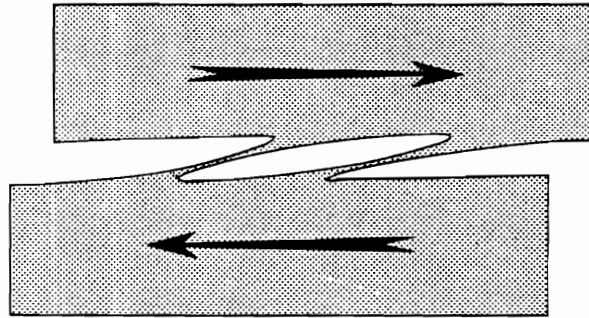
Figure 5.25   The shear failure mechanism which occurs when the critical shear stress is exceeded is in a polymeric material [174].
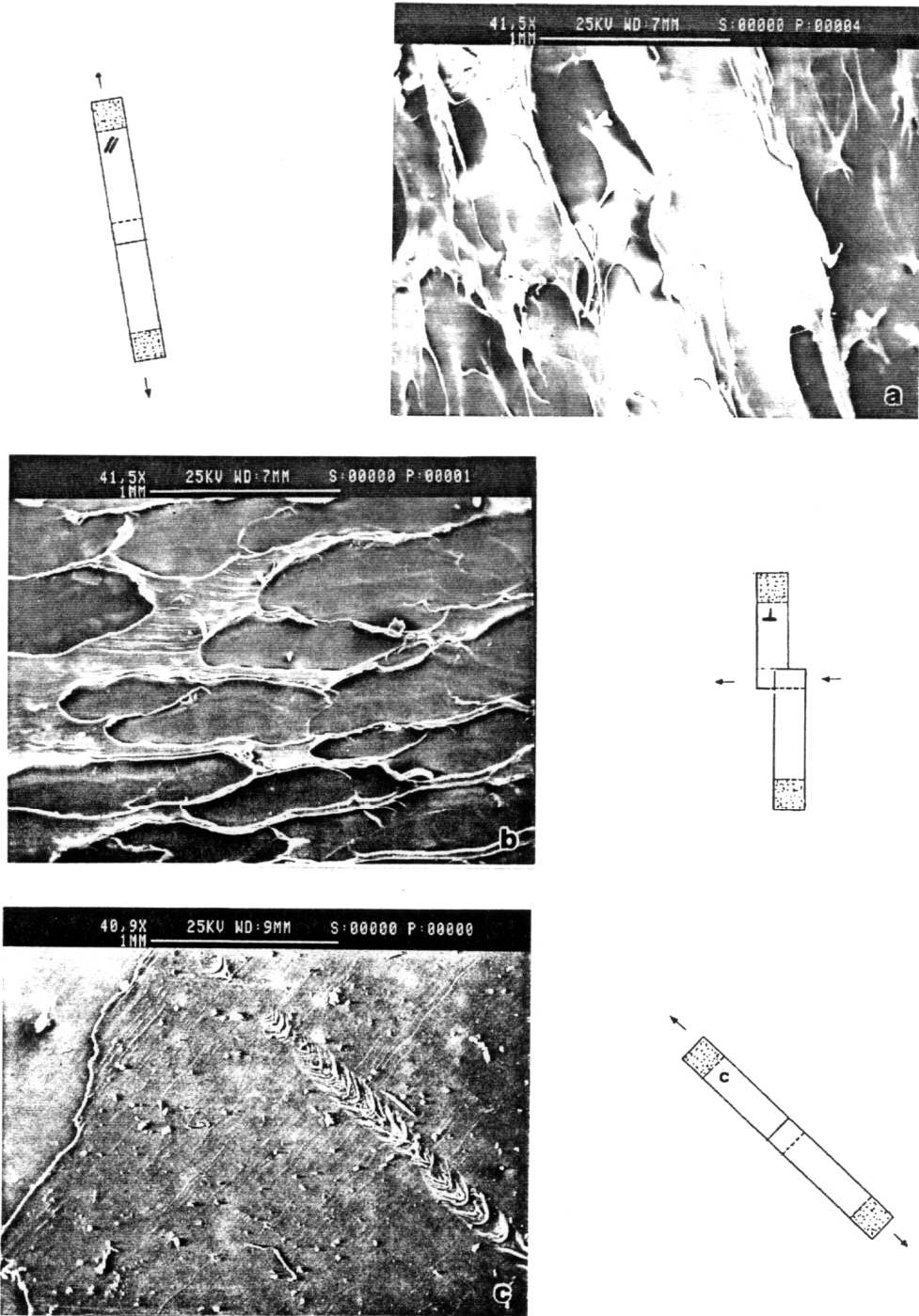
Figure 5.26 SEM micrographs of the fracture surfaces of three Surlyn 1601 adhesive bonds, a) parallel sheared bond, b) perpendicularly sheared bond, and c) an unsheared control bond respectively. The magnification is 41X. The illustrations beside each micrograph indicate the load direction applied to the bond at fracture.

Like those seen in the optical micrographs, the SEM adhesive fracture surfaces of the sheared versus the unsheared bonds are very different. The sheared bond fracture surfaces are composed of elliptical cavities as described by Kinlock, whose edges display fibrils [156]. The control bond adhesive surface is much smoother, but it contains a different type of feature, a U-shaped ramp, which is characteristic of tear fracture in polymeric materials and illustrated in Figure 5.27 [174].

The features described here, i. e. "smooth" surfaces on the control bonds and elliptical craters on the sheared bonds, were observed frequently, but not consistently on the fracture surfaces of the adhesive bonds. Numerous bonds featured patchy apparent mixed adhesive-cohesive failure modes. However, when these characteristic "smooth" and "cratered" surfaces were present, they regularly corresponded to apparent adhesive (control bonds) and cohesive failure (sheared bonds) of the bonds respectively.

5.7.2 Surface Analysis

Electron Spectroscopy for Chemical Analysis (ESCA) was utilized to sample the surface chemistry of the failure surfaces of representative DAF 821 and Surlyn 1601 lap shear bonds prepared during this study. One specimen was prepared from each type of failure surface, i. e. apparent adhesive or cohesive failure for each adhesive. The objective of these experiments was to determine whether the chemical composition of the failure surfaces was characteristic of the adhesive or the adherend. From this information, and visual inspection of the bond surfaces, a failure mode, adhesive, cohesive or mixed mode could be deduced. Initial visual examination of the fracture surfaces suggested that sheared bonds and undeformed control bonds failed in different modes in both adhesives, cohesive and adhesive-mixed mode failures predominated
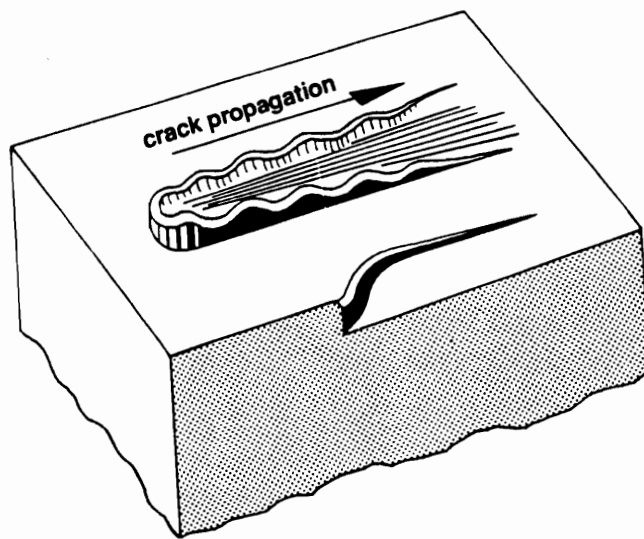
Figure 5.27   U-or V-shaped ramp generation mechanism, characteristic of tear fracture in polymeric materials [174].

respectively.

After identification of the ESCA peaks on the basis of characteristic binding energy, detail scans over narrower ranges were collected, and atomic concentration calculations and curve fitting were completed. A table of atomic concentration (percent) of the identified elements was prepared for each surface. This data is summarized in Table 5.12.

5.7.2.1   ESCA Analysis of DAF 821 Failure Surfaces

The objective of the ESCA experiments was to determine whether the chemical composition of the failure surfaces was characteristic of the adhesive or the adherend, and a failure mode assigned if possible to the two adhesives. Two DAF 821 adhesive failure surfaces, one apparent cohesive and one adhesive failure, plus an adhesive film specimen were evaluated, and the results included in Table 5.12.

The ESCA results for the DAF 821 adhesive fracture surfaces confirm the initial prediction that the control and sheared bonds fail predominately in an adhesive and cohesive mode respectively. Surface analysis of the control bond detected the presence of carbon, oxygen and aluminum (C, O, and Al), while the DAF 821 adhesive film specimen only contained C and O. The presence of the Al suggests that at least patchy adhesive mode failure is present in the unsheared control bonds.

The analysis of the parallel sheared DAF 821 bond specimen mimicked that of the DAF 821 adhesive film. ESCA detected only the presence of C and O on the apparent cohesive failure surface, which were in fact present at almost identical atomic concentrations to the adhesive film. The absence of any aluminum, with the visual determination that surface appeared covered with adhesive confirms that the sheared

Table 5.12 ESCA surface analysis results for DAF 821 and Surlyn 1601 adhesive bonds prepared with aluminum adherends.

Bond Description	Elements Present	Atomic Concentration (%)
DAF 821 unsheared-control bond apparent adhesive failure	C O Al	91.2 7.5 1.3
DAF 821 sheared-// bond apparent cohesive failure	C O	95.9 4.1
Surlyn 1601 unsheared-control bond apparent adhesive failure	C O Na F Al	72.8 19.8 1.1 1.1 5.2
Surlyn 1601 sheared-// bond apparent cohesive failure	C O Na	92.4 5.7 1.9
Aluminum Control (metal surface)	C O Al	53.5 37.0 9.5
Surlyn 1601 Control (adhesive film surface)	C O Na F	74.7 17.4 4.5 3.4
DAF 821 Control (adhesive film surface)	C O	94.6 5.4

DAF 821 bonds failed cohesively.

5.7.2.2   ESCA Analysis of Surlyn 1601 Failure Surfaces

The ESCA analysis of the Surlyn 1601 bond fracture surfaces was completed in a similar manner. Two Surlyn 1601 adhesive failure surfaces, one apparent cohesive and one adhesive failure, and a Surlyn adhesive film specimen were evaluated, and the results included in Table 5.12.

The ESCA results for the Surlyn 1601 adhesive fracture surfaces also confirm the initial predictions, i. e. the control and sheared bonds fail predominately in an adhesive and cohesive mode respectively. Surface analysis of a unsheared control bond detected the presence of carbon, oxygen, sodium, fluorine and aluminum (C, O, Na, F and Al), while the adhesive film specimen only contained the first four components; C, O, Na and F. The presence of the Al again implies that at least patchy adhesive mode failure is present in the unsheared control bonds. The detection of Na confirms that the ionomer formulation is sodium neutralized as indicated in the material description. The presence of the final element detected, fluorine is also reasonable on the adhesive film surface. The Surlyn 1601 adhesive films used in this study were all prepared from pellets pressed between platens coated with a PTFE mold release agent.

The analysis of the parallel sheared Surlyn 1601 bond specimen was similar to the results for the adhesive film, except fluorine was not detected. ESCA detected only the presence of C, O and Na on the apparent cohesive failure surface, which were the same components present on the Surlyn adhesive film. The absence of any aluminum, along with the visual determination that surface appeared covered with adhesive again confirms that the sheared Surlyn bonds failed cohesively.

5.8   Summary and Conclusions

In summary, after a series of adhesive-adherend systems were evaluated, two commercial semicrystalline hot-melt adhesives were chosen as candidate materials to evaluate the effects of shear induced molecular orientation on adhesive bond strength. After a procedure was developed to prepare oriented and unsheared control bonds, a series of mechanical property studies were completed with Dow DAF 821 and Du Pont Surlyn 1601 adhesives and aluminum coupons under various conditions. The results of this study will be summarized using the following format: 1) preliminary results that suggested molecular orientation may play a role in adhesive bond strength, 2) mechanical property determinations for two oriented bond systems, 3) FTIR molecular orientation level quantification study results, and finally, 4) correlation of observed adhesive bond performance with surface fracture analysis.

5.8.1   Preliminary Results

The DAF® 821/899 and Surlyn® 1601 adhesively bonded systems were selected for evaluation in this project to look at the effect of shear induced molecular orientation within an adhesive bond for several reasons. First, bonds prepared with these materials survived the preparation process. Then, even after shearing, the adhesively bonded joints retained sufficient integrity that they could be handled, measured and eventually broken on a universal testing machine. In addition, initial mechanical property evaluations indicated significantly different behavior between control bonds and parallel or perpendicularly sheared bonds. Tensile test evaluations showed that control bonds were typically stronger than bonds sheared parallel to the loading direction, but

occasional perpendicularly sheared bonds appeared unchanged or were in fact stronger than the control bonds.

On further testing, it was seen that lap shear bonds prepared from aluminum and either adhesive also displayed some level of cohesive or mixed-mode failure modes when fractured. Cohesive bond failure was necessary in order to address orientation effects within the adhesive layer as adhesive failure at the interface could be a function of surface treatment or contamination, and not due to shearing.

5.8.2 Mechanical Property Determinations

Variations of greater than ±100% of the calculated standard deviation for the average stress at break were observed in the initial lap shear bond data, and several parameters were evaluated in an attempt to reduce the scatter. These parameters, and their effect on the observed value for lap shear bond strength, will now be summarized.

First, bondline thickness variations were considered as the source of the scatter. The average tensile shear stress (TSS) at break for a series of oriented and control bonds prepared from Surlyn 1601 and aluminum were normalized for measured bond line thickness (±0.001"). Inspection of the control bond data shows that the scatter within the bonds was similar across the bond line thicknesses evaluated. Overall, there appeared to be no significant variation in the tensile shear strength measured for the bonds as a function of adhesive thickness.

Next, adhesive bond sets were prepared, and then either quenched or slow cooled. The average TSS for bonds prepared from Surlyn 1601 and aluminum showed a dramatic difference in the stress at break levels observed for the sheared bonds when they are prepared by quench versus slow cooling. Both the // and ⊥ oriented average

bond strengths were affected. The average shear stress for the control bonds increased as well by ~ 20 %, but since the scatter for all bonds was also large, this difference was not statistically significant.

The third experimental variable considered as a source of scatter was the bond aging time, i. e. the time lapse between bond preparation and evaluation, as Surlyn 1601 adhesives are known to gradually increase in strength over several weeks of aging due to secondary crystallization [179]. Lap shear bonds were prepared and then tested over several intervals. Only the control bonds showed an initial slight increase in bond strength as a function of aging time before testing, and that occurred over the first 24 hours of aging. Afterwards, any fluctuations in measured strength were masked within the large standard deviation observed for the data. Based on these results it appears that there was no significant consequence of aging lap shear bonds before evaluating the mechanical properties in the context of this study.

Since the bonds waited, cooling in the open air before shearing, the semicrystalline adhesive had sufficient time to cool, crystallize, and the adhesive to solidify if not sheared immediately. That wait time was termed "lag time", in seconds, and evaluated as an error source next. The lag times for a series of oriented (// & $\perp$) bonds were collected and applied as a normalization factor to plot tensile shear strength as a function of preparation methodology. Overall, it took longer to prepare the // bonds than the $\perp$ bonds, and this difference was reflected in the data presented. The DAF 821 // bonds broke at slightly lower average shear stresses than did either the control or $\perp$ bonds suggesting that longer lag times before shearing may be significant, and detrimental. This cannot be stated unequivocally though, as the trend was not universally observed.

Finally, drying the adhesive films in a vacuum oven before bonding was seen to

reduce, and maintain the typically observed scatter level within the lap shear bond data to ± 10 % when applied in combination with a visual inspection of the bond. All bonds were examined before placing them in the grips of the testing machine. If the bond was skewed into a slight "v" shape instead of straight, or if any other flaws were immediately obvious flaws such as "wedges", i. e. noticeable thickness variations in the adhesive were seen, a notation was added to the data before testing. It was noted that bonds that contained readily discernible flaws were also those whose strengths much lower than the typical scatter of ± 10% of the average. The data from flawed bonds were then excluded from further consideration.

Taking all these factors into consideration, a final series of oriented lap shear bonds were prepared from the two commercial hot-melt adhesives. The bonds were screened as appropriate through all of the steps just described. Average TSS at break for the two adhesives as a function of preparation method (//, ⊥ or control) showed that instead of enhancing bond strength, shearing the unset bonds during cure to generate preferential molecular orientation typically resulted in poorer mechanical properties for these systems. The effects were more pronounced with the Surlyn 1601 bonds than with the DAF 821 specimens. There was little difference in the average tensile strength measured for the oriented versus the undeformed control DAF 821 bonds within the range defined by the standard deviation of the data. The Surlyn bonds however, did show a difference in strength between the control and the sheared bonds, i. e. both parallel and perpendicularly sheared bonds are weaker than the control bonds. The parallel bonds are slightly weaker than the perpendicular bonds on the average, but it was not statistically significant.

To conclude, differences were detected in the mechanical properties of the sheared versus unsheared adhesively bonded systems that were compared utilizing lap

shear bonds. In order to determine if molecular orientation was in fact responsible for the detrimental effects observed, the technique of FTIR linear dichroism was applied to quantify the level of molecular orientation present within the adhesive layer.

5.8.3 Molecular Orientation Quantification

Since there were differences in strength at break observed as a function of deformation for the bonds, particularly for the Surlyn 1601 adhesive, the next step was to determine if that difference in behavior arises from molecular orientation. Linear dichroism was employed to test for the presence of molecular orientation within the adhesive films. The dichroic ratio, D, was determined for DAF 821 and Surlyn 1601 adhesive films that were sheared parallel or perpendicular to the reference direction, as well as for unsheared control films. In all cases, a dichroic ratio of approximately 1.0 was determined. The value of Herman's orientation function, which is representative of the average molecular orientation of the polymer chain with respect to the reference shear axis, was then calculated, and found to be zero. A zero value indicates that the molecular orientation of the chromophore, and therefore of its corresponding polymer chain is random. No preferential molecular orientation was detected within the adhesive films utilizing this technique. This result implies that the variations in the bond strengths measured cannot be attributed to gradients in the level of orientation induced within the adhesive layer as anticipated. Apparently, any molecular orientation induced in the polymer has sufficient time to relax within the time frame of adhesive crystallization/bond preparation.

5.8.4 Discussion of Observed Adhesive Bond Performance and Fracture Surface Characteristics

The molecular orientation level determination results indicated that the differences in the mechanical properties observed for the two adhesively bonded systems were not the result of molecular orientation within the adhesive layer. An examination of the fracture surfaces was completed next to help explain the observed variations in fracture behavior.

When observed using optical microscopy, the fracture surfaces of the sheared and unsheared bonds contain different features. The adhesive on the surface of the control bonds appears as a series of connected "flowers" or loops which are characteristic of a low-loading rate fracture [188]. The sheared bonds do not show the same elaborate patterns, but instead the adhesive surface has ridges that correspond to the direction the bond was sheared before mechanical testing. The ridges are more prominent in the parallel than in the perpendicularly sheared bonds. The surface features of the failure surfaces of the adhesive were also examined by scanning electron microscopy.

Like the optical micrographs, the adhesive fracture surfaces viewed by SEM show that the sheared versus the unsheared bond fracture surfaces are again very different. The sheared bond fracture surfaces are composed of elliptical cavities whose edges display fibrils. The control bond adhesive surface is much smoother, but it contains a different type of feature, a U-shaped ramp, which is characteristic of tear fracture in polymeric materials [174]. The features described here, i. e. "smooth" surfaces on the control bonds and elliptical craters on the sheared bonds, were observed frequently, but not universally on the fracture surfaces of the adhesive bonds. However,

when these characteristic "smooth" and "cratered" surfaces were present, they regularly corresponded to apparent adhesive (control bonds) and cohesive failure (sheared bonds) of the bonds respectively.

Next, ESCA was utilized to sample the surface chemistry of the failure surfaces of representative DAF 821 and Surlyn 1601 lap shear bonds. Initial visual examination of the fracture surfaces suggested that sheared bonds and undeformed control bonds failed in different modes in both adhesives, cohesive and adhesive-mixed mode failures predominated respectively. The ESCA results for the adhesive fracture surfaces confirm that the control and sheared bonds fail predominately in an adhesive and cohesive mode respectively. Aluminum is detectable on the surface of the apparent adhesive failure surfaces for both the DAF 821 and the Surlyn 1601 adhesive bonds, but not in areas of apparent cohesive failure.

Examination of the failure surface suggests that one possible explanation for the detrimental effect shearing induced in the lap shear bond mechanical properties is that shearing the viscous hot-melt adhesive to such high shear strains (γ= 40-125) may have generated voids in the adhesive layer, simply by straining the material further than it could flow (Figure 5.27). Then as the adhesive layer cooled and crystallized, the sheared material contracted, enhancing the already "open" voids. Subsequently, when the bond was tested this sheared or almost "perforated" layer becomes the "weak" layer that fails at loading. Failure in this manner could reasonably generate the crater and wall morphology frequently seen on the adhesive fracture surface.

CHAPTER 6

RECOMMENDATIONS

6.1   Introduction

The purpose of this chapter is to make suggestions for additional research on the two topics presented in this dissertation.   The format will be to treat each project separately, i. e. suggestions relating to the ITX crystallization project will be discussed in section 6.2, followed by suggestions for future work for the orientation effect on adhesion project in section 6.3.

6.2   Recommendations for Future Research-ITX Crystallization Project

Several areas remain unexplored in the basic characterization and examination of the crystallization behavior of ITX. Some of these oversights are deliberate, due to the restrictions on allowable analyses of ITX under the terms of the secrecy agreement

between Virginia Tech and ICI, and some of these suggestions for additional work have arisen over the course of writing up the project results.

One significant areas where this research project is lacking is that the complete microstructural chemical analysis and molecular weight of ITX utilized in this research is unknown. Characterization of the microstructure by nuclear magnetic resonance (NMR) would allow determination of the microstructure of ITX, and then ITX could be compared with literature values for materials with similar structures.

A second major area where additional information on the microstructure of ITX would have been relevant is in the thermal stability studies on the polymer. Knowledge of the molecular weight by gel permeation chromatography (GPC), and how it varies with thermal history along the lines of the research completed by Jonas et al. [11] could be crucial in confirming the conclusion that ITX is primarily thermally stable under the conditions examined. Even though the molecular weight characterization of PEEK-type compounds is non-trivial and involves: 1) sulfonation for 15 days in sulfuric acid followed by room temperature analysis in N-methyl-2-pyrrolidone (NMP), or 2) high-temperature analysis in 50/50 phenol/trichlorobenzene, the results could be illuminating. This type of analysis could monitor degradation in ITX via changes in the molecular weight of the material as a function of thermal history. An increase in the high molecular weight population would be expected in the case of degradation by cross-linking, and perhaps the generation of a low-molecular weight tail on the curve for the case of chain-scission. This dissertation suggests that ITX is not significantly degrading over the ICI suggested processing range between 386-404 °C based on the fact that on cooling, sufficient undegraded material exists such that ITX can regenerate abundant nuclei to recrystallize at relatively high levels of crystallinity. Examining the molecular weight of the specimens previously evaluated by DSC would confirm whether cross-linking or chain-scission were

occurring. If molecular weight were increasing, it could be contributing to the general slowdown in G, In K, and percent crystallinity that has been noted to occur as a function of increasingly severe thermal history before crystallization. At this point, the majority of these changes are attributed predominately to fluctuations in nucleation density.

A research area that was extensively studied, but may still be worth extending, includes the Avrami isothermal crystallization kinetics analyses completed. Now that it has been established that the nucleation density of ITX is a function of thermal history, repeating these experiments utilizing material that has seen multiple heat histories may be significant. If the Avrami analysis results for "rejuvenated" polymer, i. e. material that has been melted under severe conditions and then cooled and remelted, matched those of the less severely treated material, it would be strong support to the theory that degradation is not a significant factor under these conditions. In addition, completing the series of Avrami analyses begun here to determine In K systematically as a function of melt time, temperature and atmosphere could be of practical use in composite consolidation. A study of this nature could more accurately define a processing window that would generate consistent semicrystalline morphology and mechanical properties.

One additional research area that was investigated, but lead to indifferent results, was the SEM morphological examination of the crystalline structure of ITX as a function of melt time and temperature. A series of specimens, including both resin and ITX/IM-8 prepreg, were crystallized under various conditions and then examined after etching with the permanganic acid etchant recommended by Bassett, et at. for PEEK. The results were inconclusive. The etchant did not expose any significant spherulitic structures under the conditions utilized. Additional etching experiments could disclose how the morphological features revealed in the neat resin as a function of processing conditions are translated into an actual composite prepreg. The next step of course, would then be

to correlate the mechanical properties, especially tensile and interfacial shear strengths, to the observed structural features as well.

Finally, preparing a series of composite specimens utilizing the information on ITX crystallization as a function of thermal history would allow direct examination of the effect thermal history has on mechanical properties. Correlations might then be possible with the work on physical aging and environment completed by other VPI researchers [25].

6.3 Recommendations for Future Research-Molecular Orientation Effects on Adhesion Project

Initially, it appears that shearing adhesive bonds in order to impart molecular orientation within the bondline was either 1) ineffective, or 2) improperly completed. One possible explanation for the detrimental effect shearing induced in the lap shear bond mechanical properties was that the adhesive was sheared to too great a degree, and that voids were generated within the adhesive layer, and molecular orientation not retained. Molecular orientation, if induced and retained within the adhesive, may affect adhesive bond strength. However, this was not the case under the conditions evaluated. Several recommendations for further work to clarify whether ineffective bond preparation methods were utilized follow.

One experimental parameter that was difficult to control was the shearing process. If a jig design could be developed that allowed consistent shearing of the bond, and then rapid cooling, a large part of the project inconsistencies could be eliminated. With consistent shearing at lower levels, followed by quench cooling of the bond, it is more likely that any potential molecular orientation induced effects could be isolated.

Next, the adhesives utilized in this study were all commercial compositions which

typically have complex formulations. If a formulation was available containing only the base polymer, the molecular relaxation times might increase sufficiently to retain more preferential orientation. Then the effects of additional components could be addressed systematically by adding each component, and repeating the dichroism studies on the corresponding film. After identification of a system where orientation was generated, and retained, the mechanical properties could be evaluated again as in this research.

Finally, applying linear dichroism to determine the level of molecular orientation within the adhesive bondline may have been ineffective since the actual bond was not examined. The actual adhesive in the fractured bond was not examined as it was not possible to remove the film without deformation. The adhesive films that were tested for molecular orientation were prepared under similar conditions to the bonds, but a more reliable evaluation would include analysis of the bond itself. Reflection-absorption IR might be a reasonable technique for evaluating the adhesive film in situ. However, the technique typically demands scanning through the adhesive film, and then reflecting back again off from a polished aluminum surface beneath the specimen, so it may not be possible to utilize the same adhesive-adherend systems. Grit-blasting the aluminum surface was required with these adhesives to enhance adhesion, and the reflected signal off the rough surface may be too diffuse due to scattering. However, switching to an adhesive that could adhere well to a polished aluminum may present a viable alternative adhesively bonded system for evaluation using this technique. Examining the bond itself could more reasonably answer whether preferential molecular orientation exists in the adhesive, and whether it actually has any effect on adhesive bond strength.

APPENDIX I

	A	B	C	D	E	F	G	H	I	J	K	L
1		Raw Intensity	2θ (radians)	cos θ	Normalized Intensity (Y2)	D	Baseline Calculation (Y1)	Y2-Y1	Simpson's Rule	Partial Area (%)	Trapezoid Rule	Partial Area (%)
2	5.00	237	0.087	1.00	914	0.3816	672	242				
3	5.05	231	0.088	1.00	891		671	220				
4	5.10	225	0.089	1.00	868	Last-first	671	197				
5	5.15	220	0.090	1.00	848	21	670	178				
6	5.20	214	0.091	1.00	825		670	156				
7	5.25	209	0.092	1.00	806		669	137				
8	5.30	205	0.093	1.00	791	# terms	669	122				
9	5.35	203	0.093	1.00	783	580	668	115				
10	5.40	202	0.094	1.00	779		668	111				
11	5.45	202	0.095	1.00	779	Simpson's	667	112				
12	5.50	196	0.096	1.00	756	Total Area	667	89				
13	5.55	197	0.097	1.00	760	8624	667	93				
14	5.60	196	0.098	1.00	756		666	90				
15	5.65	200	0.099	1.00	771	Trapezoid	666	106				
16	5.70	197	0.099	1.00	760	Total Area	665	95				
17	5.75	201	0.100	1.00	775	12084	665	111				
18	5.80	204	0.101	1.00	787		664	123				
19	5.85	203	0.102	1.00	783	I norm.	664	119				
20	5.90	202	0.103	1.00	779	0.99555	663	116				
21	5.95	194	0.104	1.00	748		663	85				
22	6.00	186	0.105	1.00	717		662	55				
23	6.05	192	0.106	1.00	741		662	79				
24	6.10	192	0.106	1.00	741		661	79				
25	6.15	202	0.107	1.00	779		661	118				
26	6.20	193	0.108	1.00	744		661	84				
27	6.25	193	0.109	1.00	744		660	84				
28	6.30	194	0.110	1.00	748		660	89				
29	6.35	195	0.111	1.00	752		659	93				
30	6.40	196	0.112	1.00	756		659	97				
31	6.45	193	0.113	1.00	745		658	86				
32	6.50	185	0.113	1.00	714		658	56				
33	6.55	177	0.114	1.00	683		657	25				
34	6.60	171	0.115	1.00	660		657	3				
35	6.65	182	0.116	1.00	702		656	46				
36	6.70	182	0.117	1.00	702		656	46				
37	6.75	185	0.118	1.00	714		655	58				
38	6.80	190	0.119	1.00	733		655	78				
39	6.85	195	0.120	1.00	752		655	98				
40	6.90	194	0.120	1.00	748		654	94				
41	6.95	185	0.121	1.00	714		654	60				
42	7.00	187	0.122	1.00	721		653	68				
43	7.05	178	0.123	1.00	687		653	34				
44	7.10	171	0.124	1.00	660		652	7				
45	7.15	175	0.125	1.00	675		652	23				
46	7.20	173	0.126	1.00	667		651	16				
47	7.25	170	0.127	1.00	656		651	5				
48	7.30	160	0.127	1.00	617		650	-33				
49	7.35	159	0.128	1.00	613		650	-36				
50	7.40	162	0.129	1.00	625		649	-24				
51	7.45	160	0.130	1.00	617		649	-32				
52	7.50	168	0.131	1.00	648		649	0				
53	7.55	168	0.132	1.00	648		648	0				
54	7.60	168	0.133	1.00	648		648	1				
55	7.65	169	0.134	1.00	652		647	5				
56	7.70	172	0.134	1.00	664		647	17				
57	7.75	178	0.135	1.00	687		646	41				
58	7.80	177	0.136	1.00	683		646	37				
59	7.85	185	0.137	1.00	714		645	69				
60	7.90	182	0.138	1.00	702		645	57				
61	7.95	175	0.139	1.00	675		644	31				
62	8.00	173	0.140	1.00	668		644	24				
63	8.05	171	0.140	1.00	660		643	16				
64	8.10	173	0.141	1.00	668		643	25				
65	8.15	169	0.142	1.00	652		643	10				
66	8.20	173	0.143	1.00	668		642	25				
67	8.25	175	0.144	1.00	675		642	34				
68	8.30	172	0.145	1.00	664		641	23				
69	8.35	180	0.146	1.00	695		641	54				
70	8.40	182	0.147	1.00	702		640	62				
71	8.45	175	0.147	1.00	675		640	36				

	A	B	C	D	E	F	G	H	I	J	K	L
72	8.50	165	0.148	1.00	637		639	-3				
73	8.55	158	0.149	1.00	610		639	-29				
74	8.60	160	0.150	1.00	617		638	-21				
75	8.65	160	0.151	1.00	618		638	-20				
76	8.70	172	0.152	1.00	664		638	26				
77	8.75	181	0.153	1.00	699		637	62				
78	8.80	175	0.154	1.00	675		637	39				
79	8.85	168	0.154	1.00	648		636	12				
80	8.90	168	0.155	1.00	648		636	13				
81	8.95	165	0.156	1.00	637		635	2				
82	9.00	168	0.157	1.00	648		635	14	0	0.00	0.34	0.00
83	9.05	166	0.158	1.00	641		634	6	0	0.01	0.32	0.01
84	9.10	166	0.159	1.00	641		634	7	0	0.01	0.35	0.01
85	9.15	161	0.160	1.00	621		633	-12	-1	0.00	-0.60	0.00
86	9.20	153	0.161	1.00	591		633	-42	-1	-0.01	-2.12	-0.01
87	9.25	156	0.161	1.00	602		632	-30	-1	-0.03	-1.51	-0.03
88	9.30	156	0.162	1.00	602		632	-30	-1	-0.04	-1.49	-0.04
89	9.35	154	0.163	1.00	594		632	-37	-2	-0.06	-1.85	-0.05
90	9.40	155	0.164	1.00	598		631	-33	-1	-0.07	-1.64	-0.07
91	9.45	155	0.165	1.00	598		631	-32	-2	-0.08	-1.61	-0.08
92	9.50	162	0.166	1.00	625		630	-5	0	-0.08	-0.24	-0.08
93	9.55	168	0.167	1.00	649		630	19	1	-0.07	0.94	-0.08
94	9.60	170	0.168	1.00	656		629	27	1	-0.07	1.35	-0.06
95	9.65	172	0.168	1.00	664		629	35	2	-0.05	1.76	-0.05
96	9.70	168	0.169	1.00	649		628	20	0	-0.04	1.01	-0.04
97	9.75	168	0.170	1.00	649		628	21	1	-0.03	1.04	-0.03
98	9.80	166	0.171	1.00	641		627	13	0	-0.03	0.67	-0.03
99	9.85	169	0.172	1.00	652		627	26	1	-0.01	1.28	-0.02
100	9.90	175	0.173	1.00	676		626	49	1	0.00	2.46	0.00
101	9.95	177	0.174	1.00	683		626	57	3	0.03	2.87	0.03
102	10.00	171	0.175	1.00	660		626	35	1	0.04	1.73	0.04
103	10.05	168	0.175	1.00	649		625	24	1	0.06	1.18	0.05
104	10.10	163	0.176	1.00	629		625	5	0	0.06	0.24	0.05
105	10.15	154	0.177	1.00	595		624	-30	-1	0.04	-1.48	0.04
106	10.20	146	0.178	1.00	564		624	-60	-1	0.02	-3.00	0.02
107	10.25	145	0.179	1.00	560		623	-63	-3	-0.01	-3.17	-0.01
108	10.30	145	0.180	1.00	560		623	-63	-1	-0.03	-3.14	-0.04
109	10.35	152	0.181	1.00	587		622	-35	-2	-0.05	-1.77	-0.05
110	10.40	159	0.182	1.00	614		622	-8	0	-0.05	-0.40	-0.05
111	10.45	162	0.182	1.00	626		621	4	0	-0.05	0.21	-0.05
112	10.50	162	0.183	1.00	626		621	5	0	-0.05	0.23	-0.05
113	10.55	157	0.184	1.00	606		620	-14	-1	-0.05	-0.71	-0.06
114	10.60	157	0.185	1.00	606		620	-14	0	-0.06	-0.69	-0.06
115	10.65	160	0.186	1.00	618		620	-2	0	-0.06	-0.08	-0.06
116	10.70	163	0.187	1.00	629		619	10	0	-0.06	0.52	-0.06
117	10.75	164	0.188	1.00	633		619	15	1	-0.05	0.73	-0.05
118	10.80	165	0.188	1.00	637		618	19	0	-0.04	0.95	-0.04
119	10.85	171	0.189	1.00	660		618	43	2	-0.02	2.13	-0.03
120	10.90	171	0.190	1.00	660		617	43	1	-0.01	2.16	-0.01
121	10.95	163	0.191	1.00	629		617	13	1	0.00	0.64	0.00
122	11.00	157	0.192	1.00	606		616	-10	0	0.00	-0.50	-0.01
123	11.05	150	0.193	1.00	579		616	-37	-2	-0.02	-1.83	-0.02
124	11.10	151	0.194	1.00	583		615	-32	-1	-0.03	-1.61	-0.04
125	11.15	158	0.195	1.00	610		615	-5	0	-0.03	-0.24	-0.04
126	11.20	162	0.195	1.00	626		614	11	0	-0.03	0.56	-0.03
127	11.25	170	0.196	1.00	657		614	43	2	-0.01	2.13	-0.02
128	11.30	172	0.197	1.00	664		614	51	1	0.01	2.54	0.01
129	11.35	169	0.198	1.00	653		613	40	2	0.03	1.98	0.02
130	11.40	165	0.199	1.00	637		613	25	1	0.03	1.23	0.03
131	11.45	158	0.200	1.00	610		612	-2	0	0.03	-0.09	0.03
132	11.50	151	0.201	0.99	583		612	-28	-1	0.03	-1.42	0.02
133	11.55	153	0.202	0.99	591		611	-20	-1	0.01	-1.01	0.01
134	11.60	157	0.202	0.99	606		611	-4	0	0.01	-0.22	0.01
135	11.65	162	0.203	0.99	626		610	15	1	0.02	0.77	0.02
136	11.70	158	0.204	0.99	610		610	0	0	0.02	0.02	0.02
137	11.75	159	0.205	0.99	614		609	5	0	0.02	0.24	0.02
138	11.80	166	0.206	0.99	641		609	32	1	0.03	1.62	0.03
139	11.85	170	0.207	0.99	657		608	48	2	0.06	2.41	0.05
140	11.90	178	0.208	0.99	688		608	80	2	0.08	3.98	0.08
141	11.95	178	0.209	0.99	688		608	80	4	0.13	4.00	0.12
142	12.00	171	0.209	0.99	661		607	54	1	0.14	2.68	0.14
143	12.05	178	0.210	0.99	688		607	81	4	0.19	4.05	0.17
144	12.10	181	0.211	0.99	699		606	93	2	0.21	4.65	0.21

Appendix I

	A	B	C	D	E	F	G	H	I	J	K	L
145	12.15	185	0.212	0.99	715		606	109	5	0.27	5.45	0.26
146	12.20	186	0.213	0.99	719		605	113	3	0.30	5.67	0.30
147	12.25	183	0.214	0.99	707		605	102	5	0.36	5.11	0.35
148	12.30	181	0.215	0.99	699		604	95	2	0.39	4.75	0.39
149	12.35	182	0.216	0.99	703		604	99	5	0.44	4.97	0.43
150	12.40	190	0.216	0.99	734		603	131	3	0.48	6.54	0.48
151	12.45	188	0.217	0.99	726		603	123	6	0.54	6.17	0.53
152	12.50	175	0.218	0.99	676		603	74	2	0.56	3.68	0.56
153	12.55	171	0.219	0.99	661		602	59	3	0.60	2.94	0.59
154	12.60	164	0.220	0.99	634		602	32	1	0.61	1.61	0.60
155	12.65	167	0.221	0.99	645		601	44	2	0.63	2.21	0.62
156	12.70	172	0.222	0.99	665		601	64	2	0.65	3.20	0.64
157	12.75	183	0.223	0.99	707		600	107	5	0.71	5.35	0.69
158	12.80	190	0.223	0.99	734		600	135	3	0.74	6.73	0.74
159	12.85	188	0.224	0.99	727		599	127	6	0.81	6.36	0.80
160	12.90	192	0.225	0.99	742		599	143	3	0.85	7.16	0.86
161	12.95	188	0.226	0.99	727		598	128	6	0.92	6.41	0.91
162	13.00	181	0.227	0.99	700		598	102	2	0.95	5.08	0.95
163	13.05	181	0.228	0.99	700		597	102	5	1.01	5.10	0.99
164	13.10	178	0.229	0.99	688		597	91	2	1.03	4.55	1.03
165	13.15	172	0.230	0.99	665		597	68	3	1.07	3.41	1.06
166	13.20	170	0.230	0.99	657		596	61	1	1.09	3.05	1.08
167	13.25	170	0.231	0.99	657		596	61	3	1.12	3.07	1.11
168	13.30	174	0.232	0.99	673		595	77	2	1.14	3.87	1.14
169	13.35	178	0.233	0.99	688		595	93	4	1.19	4.67	1.18
170	13.40	182	0.234	0.99	703		594	109	3	1.22	5.46	1.23
171	13.45	182	0.235	0.99	704		594	110	5	1.29	5.49	1.27
172	13.50	180	0.236	0.99	696		593	102	2	1.31	5.12	1.31
173	13.55	181	0.236	0.99	700		593	107	5	1.37	5.34	1.36
174	13.60	187	0.237	0.99	723		592	131	3	1.41	6.53	1.41
175	13.65	192	0.238	0.99	742		592	150	7	1.49	7.52	1.47
176	13.70	197	0.239	0.99	762		591	170	4	1.54	8.51	1.54
177	13.75	193	0.240	0.99	746		591	155	7	1.62	7.76	1.61
178	13.80	189	0.241	0.99	731		591	140	3	1.66	7.01	1.67
179	13.85	196	0.242	0.99	758		590	168	8	1.75	8.38	1.74
180	13.90	201	0.243	0.99	777		590	187	4	1.81	9.37	1.81
181	13.95	207	0.243	0.99	800		589	211	10	1.92	10.56	1.90
182	14.00	213	0.244	0.99	824		589	235	6	1.99	11.74	2.00
183	14.05	211	0.245	0.99	816		588	228	11	2.11	11.38	2.09
184	14.10	201	0.246	0.99	777		588	189	5	2.17	9.47	2.17
185	14.15	196	0.247	0.99	758		587	171	8	2.26	8.53	2.24
186	14.20	196	0.248	0.99	758		587	171	4	2.31	8.55	2.31
187	14.25	199	0.249	0.99	769		586	183	9	2.41	9.15	2.39
188	14.30	201	0.250	0.99	777		586	191	5	2.46	9.56	2.47
189	14.35	205	0.250	0.99	793		585	207	10	2.57	10.36	2.55
190	14.40	207	0.251	0.99	800		585	215	5	2.63	10.77	2.64
191	14.45	212	0.252	0.99	820		585	235	11	2.76	11.76	2.74
192	14.50	219	0.253	0.99	847		584	263	6	2.84	13.14	2.85
193	14.55	226	0.254	0.99	874		584	290	14	3.00	14.52	2.97
194	14.60	229	0.255	0.99	886		583	302	7	3.08	15.12	3.09
195	14.65	233	0.256	0.99	901		583	318	15	3.25	15.92	3.22
196	14.70	226	0.257	0.99	874		582	292	7	3.34	14.59	3.35
197	14.75	224	0.257	0.99	866		582	285	14	3.49	14.23	3.46
198	14.80	231	0.258	0.99	893		581	312	7	3.58	15.60	3.59
199	14.85	243	0.259	0.99	940		581	359	17	3.78	17.95	3.74
200	14.90	244	0.260	0.99	944		580	363	9	3.88	18.17	3.89
201	14.95	241	0.261	0.99	932		580	352	17	4.07	17.61	4.04
202	15.00	234	0.262	0.99	905		579	326	8	4.16	16.28	4.17
203	15.05	227	0.263	0.99	878		579	299	14	4.33	14.95	4.30
204	15.10	226	0.264	0.99	874		579	296	7	4.41	14.78	4.42
205	15.15	239	0.264	0.99	924		578	346	16	4.60	17.32	4.56
206	15.20	247	0.265	0.99	955		578	378	9	4.70	18.89	4.72
207	15.25	247	0.266	0.99	955		577	378	18	4.91	18.92	4.87
208	15.30	244	0.267	0.99	944		577	367	9	5.01	18.36	5.03
209	15.35	251	0.268	0.99	971		576	395	19	5.23	19.74	5.19
210	15.40	251	0.269	0.99	971		576	395	9	5.34	19.76	5.35
211	15.45	253	0.270	0.99	979		575	403	19	5.56	20.17	5.52
212	15.50	260	0.271	0.99	1006		575	431	10	5.68	21.55	5.70
213	15.55	262	0.271	0.99	1014		574	439	21	5.92	21.96	5.88
214	15.60	264	0.272	0.99	1021		574	447	11	6.04	22.37	6.07
215	15.65	260	0.273	0.99	1006		573	432	21	6.28	21.62	6.24
216	15.70	262	0.274	0.99	1014		573	441	10	6.40	22.03	6.43
217	15.75	259	0.275	0.99	1002		573	430	20	6.64	21.48	6.60

	A	B	C	D	E	F	G	H	I	J	K	L
218	15.80	259	0.276	0.99	1002		572	430	10	6.76	21.50	6.78
219	15.85	263	0.277	0.99	1018		572	446	21	7.01	22.30	6.97
220	15.90	257	0.278	0.99	994		571	423	10	7.12	21.16	7.14
221	15.95	264	0.278	0.99	1022		571	451	21	7.37	22.54	7.33
222	16.00	275	0.279	0.99	1064		570	494	12	7.51	24.70	7.53
223	16.05	275	0.280	0.99	1064		570	494	24	7.78	24.72	7.74
224	16.10	295	0.281	0.99	1142		569	572	14	7.94	28.61	7.97
225	16.15	301	0.282	0.99	1165		569	596	28	8.27	29.80	8.22
226	16.20	296	0.283	0.99	1146		568	577	14	8.43	28.86	8.46
227	16.25	290	0.284	0.99	1122		568	554	26	8.73	27.72	8.69
228	16.30	289	0.284	0.99	1118		567	551	13	8.88	27.55	8.92
229	16.35	294	0.285	0.99	1138		567	571	27	9.20	28.54	9.15
230	16.40	285	0.286	0.99	1103		567	536	13	9.35	26.82	9.37
231	16.45	288	0.287	0.99	1115		566	549	26	9.65	27.43	9.60
232	16.50	303	0.288	0.99	1173		566	607	14	9.82	30.36	9.85
233	16.55	299	0.289	0.99	1157		565	592	28	10.14	29.61	10.10
234	16.60	313	0.290	0.99	1212		565	647	15	10.32	32.34	10.37
235	16.65	330	0.291	0.99	1277		564	713	34	10.71	35.66	10.66
236	16.70	333	0.291	0.99	1289		564	725	17	10.91	36.26	10.96
237	16.75	332	0.292	0.99	1285		563	722	34	11.31	36.09	11.26
238	16.80	326	0.293	0.99	1262		563	699	17	11.50	34.96	11.55
239	16.85	323	0.294	0.99	1250		562	688	33	11.88	34.40	11.83
240	16.90	318	0.295	0.99	1231		562	669	16	12.07	33.46	12.11
241	16.95	316	0.296	0.99	1223		562	662	31	12.43	33.09	12.38
242	17.00	326	0.297	0.99	1262		561	701	17	12.63	35.05	12.67
243	17.05	339	0.298	0.99	1312		561	752	36	13.04	37.60	12.99
244	17.10	343	0.298	0.99	1328		560	768	18	13.25	38.39	13.30
245	17.15	350	0.299	0.99	1355		560	795	38	13.69	39.77	13.63
246	17.20	343	0.300	0.99	1328		559	769	18	13.90	38.44	13.95
247	17.25	340	0.301	0.99	1317		559	758	36	14.32	37.89	14.26
248	17.30	347	0.302	0.99	1344		558	785	19	14.54	39.27	14.59
249	17.35	357	0.303	0.99	1382		558	825	39	14.99	41.23	14.93
250	17.40	365	0.304	0.99	1413		557	856	20	15.23	42.80	15.28
251	17.45	369	0.305	0.99	1429		557	872	41	15.71	43.60	15.65
252	17.50	355	0.305	0.99	1375		556	818	19	15.93	40.92	15.98
253	17.55	344	0.306	0.99	1332		556	776	37	16.36	38.81	16.30
254	17.60	350	0.307	0.99	1355		556	800	19	16.58	40.00	16.64
255	17.65	362	0.308	0.99	1402		555	847	40	17.05	42.35	16.99
256	17.70	376	0.309	0.99	1456		555	902	21	17.30	45.08	17.36
257	17.75	392	0.310	0.99	1518		554	964	46	17.83	48.21	17.76
258	17.80	394	0.311	0.99	1526		554	972	23	18.10	48.62	18.16
259	17.85	389	0.312	0.99	1507		553	953	45	18.62	47.67	18.55
260	17.90	387	0.312	0.99	1499		553	946	22	18.88	47.31	18.95
261	17.95	391	0.313	0.99	1515		552	962	46	19.41	48.11	19.34
262	18.00	395	0.314	0.99	1530		552	978	23	19.68	48.91	19.75
263	18.05	387	0.315	0.99	1499		551	948	45	20.21	47.39	20.14
264	18.10	407	0.316	0.99	1577		551	1026	24	20.49	51.29	20.57
265	18.15	424	0.317	0.99	1643		550	1092	52	21.09	54.60	21.02
266	18.20	436	0.318	0.99	1689		550	1139	27	21.41	56.95	21.49
267	18.25	461	0.319	0.99	1786		550	1236	59	22.09	61.82	22.00
268	18.30	465	0.319	0.99	1802		549	1252	30	22.43	62.62	22.52
269	18.35	462	0.320	0.99	1790		549	1241	59	23.12	62.07	23.03
270	18.40	468	0.321	0.99	1813		548	1265	30	23.47	63.25	23.56
271	18.45	495	0.322	0.99	1918		548	1370	65	24.22	68.51	24.12
272	18.50	532	0.323	0.99	2061		547	1514	36	24.64	75.70	24.75
273	18.55	564	0.324	0.99	2185		547	1639	78	25.54	81.93	25.43
274	18.60	606	0.325	0.99	2348		546	1802	43	26.04	90.09	26.17
275	18.65	640	0.326	0.99	2480		546	1934	92	27.11	96.71	26.97
276	18.70	661	0.326	0.99	2561		545	2016	48	27.66	100.80	27.81
277	18.75	679	0.327	0.99	2631		545	2086	99	28.81	104.32	28.67
278	18.80	694	0.328	0.99	2689		544	2145	51	29.40	107.25	29.56
279	18.85	694	0.329	0.99	2690		544	2146	102	30.59	107.28	30.45
280	18.90	695	0.330	0.99	2693		544	2150	51	31.18	107.50	31.34
281	18.95	695	0.331	0.99	2694		543	2150	102	32.36	107.52	32.23
282	19.00	681	0.332	0.99	2639		543	2097	50	32.94	104.84	33.09
283	19.05	647	0.332	0.99	2508		542	1965	93	34.03	98.27	33.91
284	19.10	618	0.333	0.99	2395		542	1854	44	34.54	92.68	34.67
285	19.15	598	0.334	0.99	2318		541	1777	84	35.52	88.83	35.41
286	19.20	589	0.335	0.99	2283		541	1742	41	36.00	87.11	36.13
287	19.25	571	0.336	0.99	2213		540	1673	80	36.92	83.65	36.82
288	19.30	562	0.337	0.99	2179		540	1639	39	37.37	81.93	37.50
289	19.35	523	0.338	0.99	2027		539	1488	71	38.19	74.40	38.11
290	19.40	482	0.339	0.99	1869		539	1330	32	38.56	66.48	38.66

	A	B	C	D	E	F	G	H	I	J	K	L
291	19.45	456	0.339	0.99	1768		538	1229	58	39.24	61.47	39.17
292	19.50	434	0.340	0.99	1683		538	1145	27	39.55	57.23	39.65
293	19.55	420	0.341	0.99	1628		538	1091	52	40.15	54.54	40.10
294	19.60	414	0.342	0.99	1605		537	1068	25	40.45	53.40	40.54
295	19.65	423	0.343	0.99	1640		537	1103	52	41.06	55.17	41.00
296	19.70	432	0.344	0.99	1675		536	1139	27	41.37	56.94	41.47
297	19.75	433	0.345	0.99	1679		536	1143	54	42.00	57.16	41.94
298	19.80	432	0.346	0.99	1675		535	1140	27	42.31	56.99	42.41
299	19.85	415	0.346	0.99	1609		535	1074	51	42.91	53.72	42.86
300	19.90	390	0.347	0.98	1512		534	978	23	43.18	48.90	43.26
301	19.95	386	0.348	0.98	1497		534	963	46	43.71	48.15	43.66
302	20.00	389	0.349	0.98	1509		533	975	23	43.98	48.76	44.06
303	20.05	391	0.350	0.98	1516		533	983	47	44.52	49.17	44.47
304	20.10	401	0.351	0.98	1555		532	1023	24	44.80	51.13	44.89
305	20.15	404	0.352	0.98	1567		532	1035	49	45.37	51.74	45.32
306	20.20	397	0.353	0.98	1540		532	1008	24	45.65	50.41	45.74
307	20.25	402	0.353	0.98	1559		531	1028	49	46.21	51.40	46.16
308	20.30	408	0.354	0.98	1582		531	1052	25	46.50	52.59	46.60
309	20.35	416	0.355	0.98	1614		530	1083	52	47.10	54.17	47.05
310	20.40	415	0.356	0.98	1610		530	1080	26	47.40	54.00	47.49
311	20.45	419	0.357	0.98	1625		529	1096	52	48.00	54.80	47.95
312	20.50	427	0.358	0.98	1656		529	1128	27	48.31	56.38	48.41
313	20.55	424	0.359	0.98	1645		528	1116	53	48.93	55.82	48.88
314	20.60	433	0.360	0.98	1680		528	1152	27	49.25	57.59	49.35
315	20.65	442	0.360	0.98	1715		527	1187	56	49.90	59.37	49.84
316	20.70	448	0.361	0.98	1738		527	1211	29	50.24	60.56	50.35
317	20.75	463	0.362	0.98	1796		527	1270	60	50.94	63.49	50.87
318	20.80	475	0.363	0.98	1843		526	1317	31	51.30	65.84	51.42
319	20.85	496	0.364	0.98	1924		526	1399	67	52.07	69.94	51.99
320	20.90	498	0.365	0.98	1932		525	1407	33	52.46	70.36	52.58
321	20.95	503	0.366	0.98	1952		525	1427	68	53.25	71.35	53.17
322	21.00	491	0.367	0.98	1905		524	1381	33	53.63	69.05	53.74
323	21.05	477	0.367	0.98	1851		524	1327	63	54.36	66.36	54.29
324	21.10	467	0.368	0.98	1812		523	1289	31	54.71	64.45	54.82
325	21.15	456	0.369	0.98	1770		523	1247	59	55.40	62.34	55.34
326	21.20	435	0.370	0.98	1688		522	1166	28	55.72	58.29	55.82
327	21.25	423	0.371	0.98	1642		522	1120	53	56.34	55.99	56.28
328	21.30	396	0.372	0.98	1537		521	1015	24	56.62	50.77	56.70
329	21.35	385	0.373	0.98	1494		521	973	46	57.16	48.66	57.11
330	21.40	374	0.374	0.98	1452		521	931	22	57.41	46.55	57.49
331	21.45	378	0.374	0.98	1467		520	947	45	57.93	47.36	57.88
332	21.50	387	0.375	0.98	1502		520	983	23	58.21	49.13	58.29
333	21.55	388	0.376	0.98	1506		519	987	47	58.75	49.35	58.70
334	21.60	382	0.377	0.98	1483		519	964	23	59.02	48.21	59.10
335	21.65	379	0.378	0.98	1471		518	953	45	59.54	47.65	59.49
336	21.70	354	0.379	0.98	1374		518	857	20	59.78	42.83	59.85
337	21.75	350	0.380	0.98	1359		517	841	40	60.24	42.07	60.19
338	21.80	339	0.380	0.98	1316		517	799	19	60.46	39.96	60.52
339	21.85	340	0.381	0.98	1320		516	804	38	60.90	40.18	60.86
340	21.90	349	0.382	0.98	1355		516	839	20	61.14	41.96	61.20
341	21.95	336	0.383	0.98	1305		515	789	38	61.57	39.46	61.53
342	22.00	337	0.384	0.98	1309		515	794	19	61.79	39.68	61.86
343	22.05	342	0.385	0.98	1328		515	813	39	62.24	40.67	62.20
344	22.10	340	0.386	0.98	1320		514	806	19	62.46	40.31	62.53
345	22.15	340	0.387	0.98	1320		514	807	38	62.91	40.33	62.86
346	22.20	331	0.387	0.98	1285		513	772	18	63.12	38.61	63.18
347	22.25	333	0.388	0.98	1293		513	781	37	63.55	39.03	63.51
348	22.30	335	0.389	0.98	1301		512	789	19	63.77	39.44	63.83
349	22.35	344	0.390	0.98	1336		512	824	39	64.22	41.21	64.17
350	22.40	361	0.391	0.98	1402		511	891	21	64.47	44.54	64.54
351	22.45	359	0.392	0.98	1394		511	884	42	64.95	44.18	64.91
352	22.50	362	0.393	0.98	1406		510	896	21	65.20	44.78	65.28
353	22.55	359	0.394	0.98	1394		510	885	42	65.69	44.23	65.64
354	22.60	368	0.394	0.98	1429		509	920	22	65.94	46.00	66.02
355	22.65	372	0.395	0.98	1445		509	936	45	66.46	46.80	66.41
356	22.70	374	0.396	0.98	1453		509	944	22	66.72	47.22	66.80
357	22.75	389	0.397	0.98	1511		508	1003	48	67.27	50.16	67.22
358	22.80	395	0.398	0.98	1535		508	1027	24	67.55	51.35	67.64
359	22.85	410	0.399	0.98	1593		507	1086	52	68.15	54.29	68.09
360	22.90	424	0.400	0.98	1647		507	1141	27	68.47	57.03	68.56
361	22.95	424	0.401	0.98	1647		506	1141	54	69.10	57.06	69.04
362	23.00	439	0.401	0.98	1706		506	1200	29	69.43	60.00	69.53
363	23.05	446	0.402	0.98	1733		505	1228	58	70.10	61.38	70.04

	A	B	C	D	E	F	G	H	I	J	K	L
364	23.10	454	0.403	0.98	1764		505	1259	30	70.45	62.96	70.56
365	23.15	456	0.404	0.98	1772		504	1268	60	71.15	63.38	71.09
366	23.20	442	0.405	0.98	1718		504	1214	29	71.48	60.68	71.59
367	23.25	448	0.406	0.98	1741		503	1238	59	72.17	61.88	72.10
368	23.30	435	0.407	0.98	1691		503	1188	28	72.49	59.38	72.59
369	23.35	425	0.408	0.98	1652		503	1149	55	73.13	57.46	73.07
370	23.40	428	0.408	0.98	1663		502	1161	28	73.45	58.07	73.55
371	23.45	417	0.409	0.98	1621		502	1119	53	74.06	55.96	74.01
372	23.50	394	0.410	0.98	1531		501	1030	24	74.35	51.51	74.44
373	23.55	387	0.411	0.98	1504		501	1004	48	74.90	50.18	74.85
374	23.60	390	0.412	0.98	1516		500	1016	24	75.18	50.79	75.27
375	23.65	393	0.413	0.98	1528		500	1028	49	75.75	51.39	75.70
376	23.70	385	0.414	0.98	1497		499	997	24	76.02	49.87	76.11
377	23.75	387	0.415	0.98	1504		499	1006	48	76.58	50.28	76.53
378	23.80	369	0.415	0.98	1435		498	936	22	76.84	46.81	76.91
379	23.85	338	0.416	0.98	1314		498	816	39	77.29	40.81	77.25
380	23.90	322	0.417	0.98	1252		497	754	18	77.49	37.72	77.56
381	23.95	327	0.418	0.98	1271		497	774	37	77.92	38.72	77.88
382	24.00	320	0.419	0.98	1244		497	748	18	78.13	37.38	78.19
383	24.05	323	0.420	0.98	1256		496	760	36	78.55	37.99	78.51
384	24.10	322	0.421	0.98	1252		496	756	18	78.75	37.82	78.82
385	24.15	318	0.421	0.98	1237		495	741	35	79.16	37.07	79.13
386	24.20	305	0.422	0.98	1186		495	691	16	79.35	34.57	79.41
387	24.25	293	0.423	0.98	1139		494	645	31	79.71	32.26	79.68
388	24.30	282	0.424	0.98	1097		494	603	14	79.88	30.15	79.93
389	24.35	273	0.425	0.98	1062		493	568	27	80.19	28.42	80.16
390	24.40	274	0.426	0.98	1066		493	573	14	80.35	28.64	80.40
391	24.45	274	0.427	0.98	1066		492	573	27	80.66	28.66	80.64
392	24.50	273	0.428	0.98	1062		492	570	14	80.82	28.50	80.87
393	24.55	271	0.428	0.98	1054		491	563	27	81.13	28.13	81.11
394	24.60	257	0.429	0.98	1000		491	509	12	81.27	25.43	81.32
395	24.65	254	0.430	0.98	988		491	497	24	81.55	24.87	81.52
396	24.70	248	0.431	0.98	965		490	475	11	81.68	23.73	81.72
397	24.75	236	0.432	0.98	918		490	428	20	81.91	21.42	81.90
398	24.80	231	0.433	0.98	899		489	410	10	82.03	20.48	82.07
399	24.85	227	0.434	0.98	883		489	394	19	82.24	19.72	82.23
400	24.90	233	0.435	0.98	907		488	418	10	82.36	20.91	82.40
401	24.95	228	0.435	0.98	887		488	399	19	82.58	19.97	82.57
402	25.00	233	0.436	0.98	907		487	419	10	82.69	20.96	82.74
403	25.05	232	0.437	0.98	903		487	416	20	82.92	20.79	82.91
404	25.10	218	0.438	0.98	848		486	362	9	83.02	18.09	83.06
405	25.15	213	0.439	0.98	829		486	343	16	83.21	17.15	83.21
406	25.20	207	0.440	0.98	806		486	320	8	83.30	16.00	83.34
407	25.25	210	0.441	0.98	817		485	332	16	83.48	16.61	83.48
408	25.30	215	0.442	0.98	837		485	352	8	83.58	17.61	83.62
409	25.35	220	0.442	0.98	856		484	372	18	83.79	18.61	83.78
410	25.40	222	0.443	0.98	864		484	380	9	83.89	19.02	83.93
411	25.45	215	0.444	0.98	837		483	354	17	84.09	17.68	84.08
412	25.50	208	0.445	0.98	810		483	327	8	84.18	16.35	84.21
413	25.55	203	0.446	0.98	790		482	308	15	84.35	15.40	84.34
414	25.60	208	0.447	0.98	810		482	328	8	84.44	16.39	84.48
415	25.65	213	0.448	0.98	829		481	348	17	84.63	17.39	84.62
416	25.70	213	0.449	0.97	829		481	348	8	84.72	17.42	84.77
417	25.75	211	0.449	0.97	821		480	341	16	84.91	17.05	84.91
418	25.80	212	0.450	0.97	825		480	345	8	85.01	17.27	85.05
419	25.85	216	0.451	0.97	841		480	362	17	85.21	18.08	85.20
420	25.90	217	0.452	0.97	845		479	366	9	85.31	18.29	85.35
421	25.95	206	0.453	0.97	802		479	324	15	85.49	16.18	85.48
422	26.00	196	0.454	0.97	763		478	285	7	85.56	14.26	85.60
423	26.05	186	0.455	0.97	724		478	247	12	85.70	12.33	85.70
424	26.10	194	0.456	0.97	756		477	278	7	85.78	13.91	85.82
425	26.15	197	0.456	0.97	767		477	290	14	85.94	14.52	85.94
426	26.20	201	0.457	0.97	783		476	307	7	86.02	15.33	86.07
427	26.25	200	0.458	0.97	779		476	303	14	86.19	15.16	86.19
428	26.30	205	0.459	0.97	798		475	323	8	86.28	16.16	86.33
429	26.35	201	0.460	0.97	783		475	308	15	86.45	15.40	86.45
430	26.40	204	0.461	0.97	795		474	320	8	86.54	16.01	86.59
431	26.45	200	0.462	0.97	779		474	305	15	86.70	15.26	86.71
432	26.50	196	0.463	0.97	764		474	290	7	86.78	14.50	86.83
433	26.55	184	0.463	0.97	717		473	244	12	86.92	12.19	86.93
434	26.60	185	0.464	0.97	721		473	248	6	86.99	12.41	87.04
435	26.65	191	0.465	0.97	744		472	272	13	87.14	13.60	87.15
436	26.70	188	0.466	0.97	733		472	261	6	87.21	13.04	87.26

	A	B	C	D	E	F	G	H	I	J	K	L
437	26.75	190	0.467	0.97	740		471	269	13	87.36	13.45	87.37
438	26.80	194	0.468	0.97	756		471	285	7	87.44	14.26	87.49
439	26.85	192	0.469	0.97	748		470	278	13	87.59	13.89	87.60
440	26.90	189	0.469	0.97	737		470	267	6	87.66	13.33	87.71
441	26.95	181	0.470	0.97	705		469	236	11	87.79	11.80	87.81
442	27.00	174	0.471	0.97	678		469	209	5	87.85	10.46	87.89
443	27.05	177	0.472	0.97	690		468	221	11	87.97	11.07	87.99
444	27.10	179	0.473	0.97	698		468	230	5	88.04	11.48	88.08
445	27.15	188	0.474	0.97	733		468	265	13	88.18	13.26	88.19
446	27.20	174	0.475	0.97	678		467	211	5	88.24	10.56	88.28
447	27.25	171	0.476	0.97	667		467	200	10	88.35	10.00	88.36
448	27.30	165	0.476	0.97	643		466	177	4	88.40	8.85	88.43
449	27.35	166	0.477	0.97	647		466	181	9	88.50	9.07	88.51
450	27.40	170	0.478	0.97	663		465	198	5	88.55	9.88	88.59
451	27.45	174	0.479	0.97	678		465	214	10	88.67	10.68	88.68
452	27.50	167	0.480	0.97	651		464	187	4	88.72	9.34	88.76
453	27.55	163	0.481	0.97	636		464	172	8	88.82	8.58	88.83
454	27.60	165	0.482	0.97	643		463	180	4	88.87	9.00	88.90
455	27.65	176	0.483	0.97	686		463	223	11	88.99	11.17	88.99
456	27.70	180	0.483	0.97	702		462	239	6	89.06	11.97	89.09
457	27.75	182	0.484	0.97	710		462	248	12	89.19	12.39	89.20
458	27.80	174	0.485	0.97	679		462	217	5	89.25	10.85	89.29
459	27.85	170	0.486	0.97	663		461	202	10	89.36	10.10	89.37
460	27.90	169	0.487	0.97	659		461	198	5	89.42	9.92	89.45
461	27.95	171	0.488	0.97	667		460	207	10	89.53	10.34	89.54
462	28.00	178	0.489	0.97	694		460	235	6	89.60	11.73	89.63
463	28.05	177	0.490	0.97	690		459	231	11	89.72	11.56	89.73
464	28.10	169	0.490	0.97	659		459	200	5	89.78	10.02	89.81
465	28.15	155	0.491	0.97	605		458	146	7	89.86	7.32	89.87
466	28.20	153	0.492	0.97	597		458	139	3	89.90	6.95	89.93
467	28.25	158	0.493	0.97	616		457	159	8	89.99	7.95	90.00
468	28.30	163	0.494	0.97	636		457	179	4	90.04	8.95	90.07
469	28.35	172	0.495	0.97	671		456	215	10	90.15	10.73	90.16
470	28.40	178	0.496	0.97	695		456	238	6	90.22	11.92	90.26
471	28.45	187	0.497	0.97	730		456	274	13	90.37	13.71	90.37
472	28.50	187	0.497	0.97	730		455	275	7	90.45	13.73	90.49
473	28.55	193	0.498	0.97	753		455	299	14	90.61	14.93	90.61
474	28.60	199	0.499	0.97	777		454	322	8	90.74	16.12	90.74
475	28.65	196	0.500	0.97	765		454	311	15	90.87	15.56	90.87
476	28.70	200	0.501	0.97	781		453	327	8	90.96	16.37	91.01
477	28.75	198	0.502	0.97	773		453	320	15	91.14	16.00	91.14
478	28.80	201	0.503	0.97	785		452	332	8	91.23	16.61	91.28
479	28.85	208	0.504	0.97	812		452	360	17	91.43	18.00	91.43
480	28.90	212	0.504	0.97	828		451	376	9	91.53	18.81	91.58
481	28.95	223	0.505	0.97	871		451	420	20	91.76	20.98	91.75
482	29.00	223	0.506	0.97	871		451	420	10	91.88	21.00	91.93
483	29.05	230	0.507	0.97	898		450	448	21	92.13	22.39	92.11
484	29.10	233	0.508	0.97	910		450	460	11	92.25	23.01	92.30
485	29.15	223	0.509	0.97	871		449	422	20	92.49	21.08	92.48
486	29.20	228	0.510	0.97	890		449	442	10	92.61	22.08	92.66
487	29.25	230	0.511	0.97	898		448	450	21	92.86	22.49	92.85
488	29.30	227	0.511	0.97	886		448	439	10	92.98	21.93	93.03
489	29.35	228	0.512	0.97	890		447	443	21	93.22	22.15	93.21
490	29.40	228	0.513	0.97	890		447	444	11	93.34	22.18	93.40
491	29.45	224	0.514	0.97	875		446	428	20	93.58	21.42	93.57
492	29.50	217	0.515	0.97	848		446	402	10	93.69	20.08	93.74
493	29.55	217	0.516	0.97	848		445	402	19	93.91	20.11	93.91
494	29.60	211	0.517	0.97	824		445	379	9	94.02	18.96	94.06
495	29.65	201	0.517	0.97	785		445	341	16	94.20	17.03	94.20
496	29.70	200	0.518	0.97	781		444	337	8	94.30	16.86	94.34
497	29.75	202	0.519	0.97	789		444	346	16	94.49	17.28	94.49
498	29.80	199	0.520	0.97	777		443	334	8	94.58	16.72	94.62
499	29.85	202	0.521	0.97	789		443	347	16	94.77	17.33	94.77
500	29.90	195	0.522	0.97	762		442	320	8	94.86	15.98	94.90
501	29.95	187	0.523	0.97	731		442	289	14	95.02	14.45	95.02
502	30.00	173	0.524	0.97	676		441	235	6	95.08	11.73	95.12
503	30.05	174	0.524	0.97	680		441	239	11	95.21	11.95	95.22
504	30.10	177	0.525	0.97	692		440	251	6	95.28	12.57	95.32
505	30.15	184	0.526	0.97	719		440	279	13	95.44	13.96	95.43
506	30.20	190	0.527	0.97	743		439	303	7	95.52	15.16	95.56
507	30.25	195	0.528	0.97	762		439	323	15	95.70	16.16	95.69
508	30.30	188	0.529	0.97	735		439	296	7	95.78	14.81	95.82
509	30.35	179	0.530	0.97	700		438	262	12	95.93	13.08	95.92

	A	B	C	D	E	F	G	H	I	J	K	L
510	30.40	163	0.531	0.97	637		438	200	5	95.98	9.98	96.01
511	30.45	158	0.531	0.96	618		437	180	9	96.08	9.02	96.08
512	30.50	152	0.532	0.96	594		437	158	4	96.12	7.88	96.15
513	30.55	154	0.533	0.96	602		436	166	8	96.21	8.29	96.22
514	30.60	152	0.534	0.96	594		436	158	4	96.26	7.92	96.28
515	30.65	152	0.535	0.96	594		435	159	8	96.35	7.95	96.35
516	30.70	145	0.536	0.96	567		435	132	3	96.38	6.61	96.40
517	30.75	141	0.537	0.96	551		434	117	6	96.45	5.85	96.45
518	30.80	135	0.538	0.96	528		434	94	2	96.47	4.70	96.49
519	30.85	131	0.538	0.96	512		433	79	4	96.52	3.94	96.52
520	30.90	134	0.539	0.96	524		433	91	2	96.54	4.55	96.56
521	30.95	136	0.540	0.96	532		433	99	5	96.60	4.97	96.60
522	31.00	134	0.541	0.96	524		432	92	2	96.62	4.60	96.64
523	31.05	137	0.542	0.96	536		432	104	5	96.68	5.21	96.68
524	31.10	136	0.543	0.96	532		431	101	2	96.71	5.04	96.72
525	31.15	137	0.544	0.96	536		431	105	5	96.76	5.26	96.77
526	31.20	137	0.545	0.96	536		430	106	3	96.79	5.28	96.81
527	31.25	141	0.545	0.96	552		430	122	6	96.86	6.09	96.86
528	31.30	141	0.546	0.96	552		429	122	3	96.89	6.12	96.91
529	31.35	140	0.547	0.96	548		429	119	6	96.96	5.94	96.96
530	31.40	141	0.548	0.96	552		428	123	3	96.99	6.16	97.01
531	31.45	141	0.549	0.96	552		428	124	6	97.06	6.19	97.06
532	31.50	142	0.550	0.96	556		427	128	3	97.10	6.41	97.12
533	31.55	137	0.551	0.96	536		427	109	5	97.16	5.45	97.16
534	31.60	131	0.552	0.96	513		427	86	2	97.18	4.31	97.20
535	31.65	122	0.552	0.96	477		426	51	2	97.21	2.57	97.22
536	31.70	118	0.553	0.96	462		426	36	1	97.22	1.81	97.23
537	31.75	123	0.554	0.96	481		425	56	3	97.25	2.81	97.26
538	31.80	126	0.555	0.96	493		425	68	2	97.27	3.42	97.28
539	31.85	132	0.556	0.96	517		424	92	4	97.32	4.62	97.32
540	31.90	131	0.557	0.96	513		424	89	2	97.35	4.45	97.36
541	31.95	129	0.558	0.96	505		423	82	4	97.39	4.08	97.39
542	32.00	126	0.559	0.96	493		423	70	2	97.41	3.52	97.42
543	32.05	126	0.559	0.96	493		422	71	3	97.45	3.54	97.45
544	32.10	129	0.560	0.96	505		422	83	2	97.47	4.16	97.49
545	32.15	125	0.561	0.96	489		421	68	3	97.51	3.40	97.51
546	32.20	129	0.562	0.96	505		421	84	2	97.53	4.21	97.55
547	32.25	134	0.563	0.96	525		421	104	5	97.59	5.21	97.59
548	32.30	133	0.564	0.96	521		420	101	2	97.62	5.04	97.63
549	32.35	136	0.565	0.96	533		420	113	5	97.68	5.65	97.68
550	32.40	131	0.565	0.96	513		419	94	2	97.71	4.69	97.72
551	32.45	130	0.566	0.96	509		419	90	4	97.76	4.52	97.76
552	32.50	130	0.567	0.96	509		418	91	2	97.78	4.55	97.79
553	32.55	134	0.568	0.96	525		418	107	5	97.84	5.35	97.84
554	32.60	138	0.569	0.96	541		417	123	3	97.87	6.16	97.89
555	32.65	138	0.570	0.96	541		417	124	6	97.94	6.19	97.94
556	32.70	132	0.571	0.96	517		416	101	2	97.97	5.04	97.98
557	32.75	135	0.572	0.96	529		416	113	5	98.03	5.65	98.03
558	32.80	138	0.572	0.96	541		415	125	3	98.07	6.26	98.08
559	32.85	146	0.573	0.96	572		415	157	7	98.15	7.85	98.15
560	32.90	147	0.574	0.96	576		415	161	4	98.20	8.07	98.21
561	32.95	145	0.575	0.96	568		414	154	7	98.28	7.70	98.28
562	33.00	137	0.576	0.96	537		414	123	3	98.32	6.16	98.33
563	33.05	130	0.577	0.96	509		413	96	5	98.37	4.81	98.37
564	33.10	124	0.578	0.96	486		413	73	2	98.39	3.66	98.40
565	33.15	128	0.579	0.96	502		412	89	4	98.44	4.47	98.44
566	33.20	127	0.579	0.96	498		412	86	2	98.46	4.30	98.47
567	33.25	132	0.580	0.96	517		411	106	5	98.52	5.30	98.51
568	33.30	135	0.581	0.96	529		411	118	3	98.55	5.92	98.56
569	33.35	139	0.582	0.96	545		410	134	6	98.63	6.72	98.62
570	33.40	139	0.583	0.96	545		410	135	3	98.67	6.75	98.68
571	33.45	145	0.584	0.96	569		410	159	8	98.75	7.95	98.74
572	33.50	146	0.585	0.96	572		409	163	4	98.80	8.17	98.81
573	33.55	151	0.586	0.96	592		409	184	9	98.90	9.18	98.88
574	33.60	150	0.586	0.96	588		408	180	4	98.95	9.00	98.96
575	33.65	139	0.587	0.96	545		408	137	7	99.02	6.87	99.02
576	33.70	128	0.588	0.96	502		407	95	2	99.05	4.74	99.06
577	33.75	121	0.589	0.96	475		407	68	3	99.09	3.39	99.08
578	33.80	121	0.590	0.96	475		406	68	2	99.11	3.41	99.11
579	33.85	126	0.591	0.96	494		406	88	4	99.16	4.42	99.15
580	33.90	129	0.592	0.96	506		405	101	2	99.18	5.03	99.19
581	33.95	134	0.593	0.96	526		405	121	6	99.25	6.04	99.24
582	34.00	126	0.593	0.96	494		404	90	2	99.27	4.49	99.28

	A	B	C	D	E	F	G	H	I	J	K	L
583	34.05	124	0.594	0.96	486		404	82	4	99.32	4.12	99.31
584	34.10	124	0.595	0.96	487		404	83	2	99.34	4.15	99.35
585	34.15	125	0.596	0.96	490		403	87	4	99.39	4.37	99.38
586	34.20	125	0.597	0.96	490		403	88	2	99.42	4.39	99.42
587	34.25	120	0.598	0.96	471		402	69	3	99.45	3.44	99.45
588	34.30	119	0.599	0.96	467		402	65	2	99.47	3.27	99.47
589	34.35	114	0.600	0.96	447		401	46	2	99.50	2.31	99.49
590	34.40	107	0.600	0.96	420		401	19	0	99.50	0.96	99.50
591	34.45	104	0.601	0.96	408		400	8	0	99.51	0.39	99.50
592	34.50	106	0.602	0.96	416		400	16	0	99.51	0.81	99.51
593	34.55	107	0.603	0.95	420		399	21	1	99.52	1.03	99.52
594	34.60	115	0.604	0.95	451		399	53	1	99.54	2.63	99.54
595	34.65	125	0.605	0.95	491		398	92	4	99.59	4.61	99.58
596	34.70	124	0.606	0.95	487		398	89	2	99.61	4.44	99.62
597	34.75	118	0.607	0.95	463		398	66	3	99.65	3.29	99.64
598	34.80	109	0.607	0.95	428		397	31	1	99.66	1.55	99.66
599	34.85	104	0.608	0.95	408		397	12	1	99.66	0.59	99.66
600	34.90	104	0.609	0.95	408		396	12	0	99.67	0.61	99.67
601	34.95	103	0.610	0.95	404		396	9	0	99.67	0.44	99.67
602	35.00	108	0.611	0.95	424		395	29	1	99.68	1.45	99.68
603	35.05	105	0.612	0.95	412		395	18	1	99.69	0.88	99.69
604	35.10	104	0.613	0.95	408		394	14	0	99.69	0.71	99.69
605	35.15	103	0.613	0.95	405		394	11	1	99.70	0.54	99.70
606	35.20	101	0.614	0.95	397		393	3	0	99.70	0.17	99.70
607	35.25	106	0.615	0.95	416		393	23	1	99.71	1.17	99.71
608	35.30	104	0.616	0.95	409		392	16	0	99.72	0.81	99.72
609	35.35	101	0.617	0.95	397		392	5	0	99.72	0.24	99.72
610	35.40	98	0.618	0.95	385		392	-7	0	99.72	-0.33	99.72
611	35.45	95	0.619	0.95	373		391	-18	-1	99.71	-0.89	99.71
612	35.50	98	0.620	0.95	385		391	-6	0	99.71	-0.28	99.71
613	35.55	99	0.620	0.95	389		390	-1	0	99.71	-0.06	99.71
614	35.60	103	0.621	0.95	405		390	15	0	99.71	0.75	99.71
615	35.65	104	0.622	0.95	409		389	19	1	99.72	0.97	99.72
616	35.70	104	0.623	0.95	409		389	20	0	99.73	1.00	99.73
617	35.75	108	0.624	0.95	424		388	36	2	99.75	1.81	99.74
618	35.80	109	0.625	0.95	428		388	41	1	99.76	2.03	99.76
619	35.85	108	0.626	0.95	425		387	37	2	99.78	1.86	99.78
620	35.90	103	0.627	0.95	405		387	18	0	99.78	0.90	99.78
621	35.95	98	0.627	0.95	385		386	-1	0	99.78	-0.06	99.78
622	36.00	97	0.628	0.95	381		386	-5	0	99.78	-0.23	99.78
623	36.05	97	0.629	0.95	381		386	-4	0	99.78	-0.21	99.78
624	36.10	95	0.630	0.95	374		385	-12	0	99.78	-0.58	99.77
625	36.15	94	0.631	0.95	370		385	-15	-1	99.77	-0.75	99.77
626	36.20	95	0.632	0.95	374		384	-11	0	99.76	-0.53	99.76
627	36.25	98	0.633	0.95	385		384	2	0	99.77	0.08	99.76
628	36.30	105	0.634	0.95	413		383	30	1	99.78	1.49	99.78
629	36.35	112	0.634	0.95	441		383	58	3	99.81	2.89	99.80
630	36.40	109	0.635	0.95	429		382	46	1	99.82	2.32	99.82
631	36.45	103	0.636	0.95	405		382	23	1	99.83	1.16	99.83
632	36.50	97	0.637	0.95	382		381	0	0	99.83	0.01	99.83
633	36.55	98	0.638	0.95	386		381	5	0	99.83	0.23	99.83
634	36.60	100	0.639	0.95	393		380	13	0	99.84	0.65	99.84
635	36.65	102	0.640	0.95	401		380	21	1	99.85	1.06	99.84
636	36.70	104	0.641	0.95	409		380	30	1	99.86	1.48	99.86
637	36.75	94	0.641	0.95	370		379	-9	0	99.85	-0.46	99.85
638	36.80	85	0.642	0.95	334		379	-44	-1	99.84	-2.21	99.84
639	36.85	82	0.643	0.95	323		378	-55	-3	99.81	-2.77	99.81
640	36.90	86	0.644	0.95	338		378	-39	-1	99.80	-1.96	99.80
641	36.95	93	0.645	0.95	366		377	-11	-1	99.79	-0.56	99.79
642	37.00	99	0.646	0.95	390		377	13	0	99.80	0.64	99.80
643	37.05	101	0.647	0.95	398		376	21	1	99.81	1.06	99.81
644	37.10	97	0.648	0.95	382		376	6	0	99.81	0.30	99.81
645	37.15	95	0.648	0.95	374		375	-1	0	99.81	-0.07	99.81
646	37.20	103	0.649	0.95	406		375	31	1	99.82	1.53	99.82
647	37.25	104	0.650	0.95	409		375	35	2	99.84	1.75	99.83
648	37.30	103	0.651	0.95	406		374	32	1	99.85	1.58	99.85
649	37.35	101	0.652	0.95	398		374	24	1	99.86	1.21	99.86
650	37.40	96	0.653	0.95	378		373	5	0	99.86	0.25	99.86
651	37.45	92	0.654	0.95	362		373	-10	0	99.85	-0.52	99.86
652	37.50	95	0.654	0.95	374		372	2	0	99.85	0.10	99.86
653	37.55	100	0.655	0.95	394		372	22	1	99.87	1.11	99.87
654	37.60	98	0.656	0.95	386		371	15	0	99.87	0.74	99.87
655	37.65	94	0.657	0.95	370		371	-1	0	99.87	-0.03	99.87

	A	B	C	D	E	F	G	H	I	J	K	L
656	37.70	98	0.658	0.95	386		370	16	0	99.87	0.79	99.88
657	37.75	102	0.659	0.95	402		370	32	2	99.89	1.60	99.89
658	37.80	106	0.660	0.95	418		369	48	1	99.91	2.41	99.91
659	37.85	110	0.661	0.95	433		369	64	3	99.94	3.22	99.94
660	37.90	112	0.661	0.95	441		369	73	2	99.96	3.64	99.97
661	37.95	109	0.662	0.95	430		368	61	3	100.00	3.07	99.99
662	38.00	102	0.663	0.95	402		368	34	0	100.00	0.86	100.00
663	38.05	102	0.664	0.95	402		367	35				
664	38.10	100	0.665	0.95	394		367	27				
665	38.15	100	0.666	0.95	394		366	28				
666	38.20	100	0.667	0.94	394		366	28				
667	38.25	101	0.668	0.94	398		365	33				
668	38.30	102	0.668	0.94	402		365	37				
669	38.35	102	0.669	0.94	402		364	38				
670	38.40	105	0.670	0.94	414		364	50				
671	38.45	113	0.671	0.94	446		363	82				
672	38.50	112	0.672	0.94	442		363	79				
673	38.55	108	0.673	0.94	426		363	63				
674	38.60	102	0.674	0.94	402		362	40				
675	38.65	100	0.675	0.94	394		362	33				
676	38.70	101	0.675	0.94	398		361	37				
677	38.75	102	0.676	0.94	402		361	42				
678	38.80	106	0.677	0.94	418		360	58				
679	38.85	109	0.678	0.94	430		360	70				
680	38.90	110	0.679	0.94	434		359	75				
681	38.95	119	0.680	0.94	470		359	111				
682	39.00	123	0.681	0.94	485		358	127				
683	39.05	120	0.682	0.94	474		358	116				
684	39.10	115	0.682	0.94	454		357	96				
685	39.15	112	0.683	0.94	442		357	85				
686	39.20	116	0.684	0.94	458		357	101				
687	39.25	118	0.685	0.94	466		356	110				
688	39.30	123	0.686	0.94	486		356	130				
689	39.35	128	0.687	0.94	505		355	150				
690	39.40	119	0.688	0.94	470		355	115				
691	39.45	116	0.689	0.94	458		354	104				
692	39.50	116	0.689	0.94	458		354	104				
693	39.55	121	0.690	0.94	478		353	124				
694	39.60	124	0.691	0.94	490		353	137				
695	39.65	131	0.692	0.94	517		352	165				
696	39.70	130	0.693	0.94	513		352	161				
697	39.75	127	0.694	0.94	502		351	150				
698	39.80	117	0.695	0.94	462		351	111				
699	39.85	117	0.696	0.94	462		351	112				
700	39.90	116	0.696	0.94	458		350	108				
701									8624		12084	
702												

Raw Intensity vs Scattering Angle (Annealed @ 300°C/5 min.)

ITX: Normalized Intensity vs Scattering Angle (Annealed @ 300°C/5 min.)
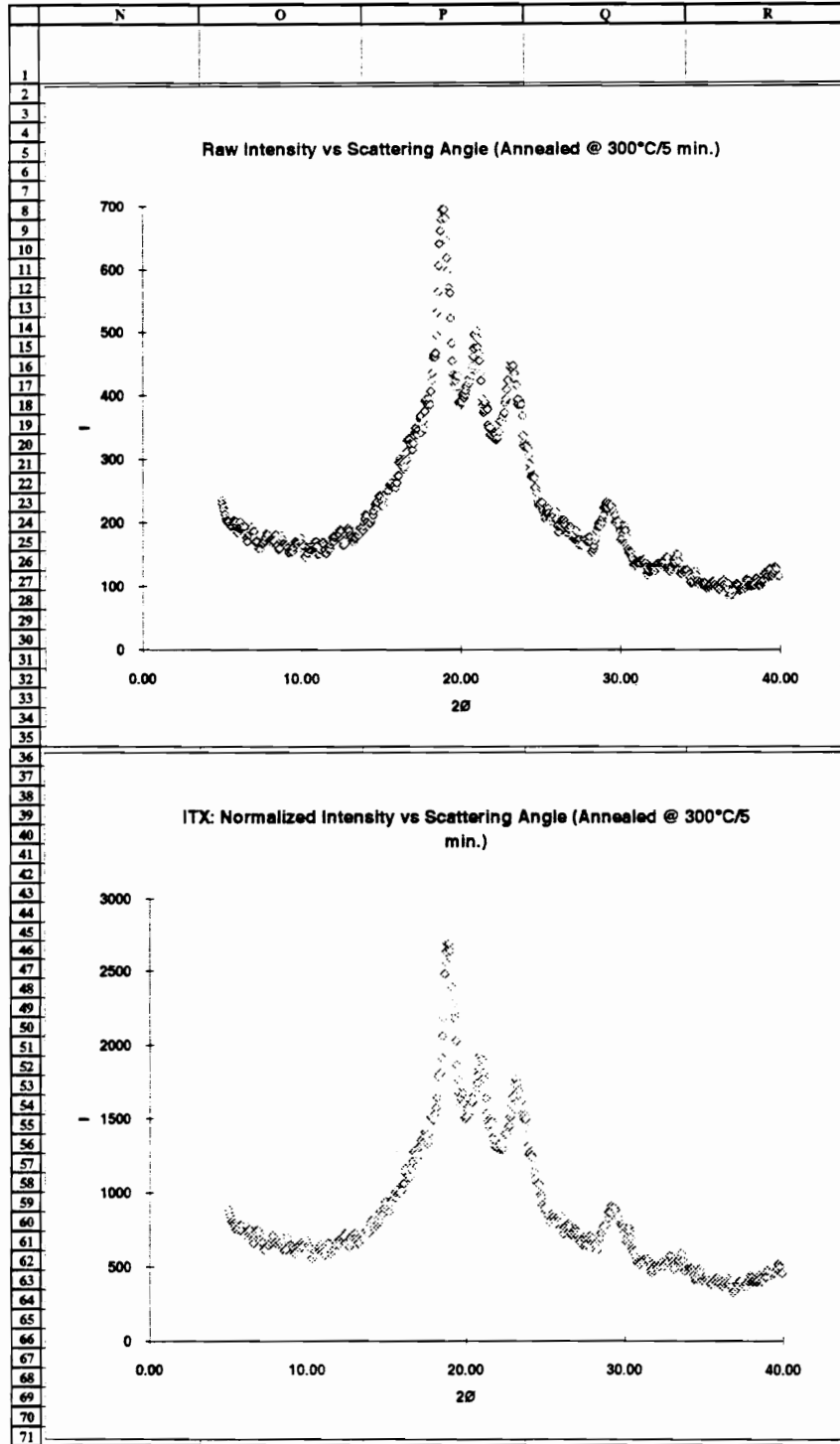
REFERENCES

1. *Engineered Materials Handbook: Composites*, Volume 3, Dostal C. A., Ed.; ASM International: Ohio, 1987.

2. Cogswell, F. N. *SAMPE Quarterly* 33-37 (1983).

3. *International Encyclopedia of Composites*, Volume 6, Lee S. M., Ed.; VCH: New York (1991).

4. Nguyen, H. X. and Ishida, H. *Polymer Composites* **8** (2), 57-73 (1987).

5. Rigby, R. B., *27 th National SAMPE Symposium* 747-752 (1982).

6. Lee, Y. and Porter, R. S. *Polym. Eng. Sci.* **26** (9), 633-639 (1986).

7. Blundell, D. J., Chalmers, J. M. Mackenzie, M. W. and Gaskin, W. F. *SAMPE Quarterly* **16** (4), 22-30 (1985).

8. Mijovic, J. and Gsell, T. C. *SAMPE Quarterly* **21** (1), 42-46 (1990).

9. Bassett, D. C., Olley, R. H. and Al Raheil, A. M. *Polymer* **29**, 1745-1754 (1988).

10. Schultz, J. M. *Polym. Eng. Sci.* **24** (10), 770-785 (1984).

11. Jonas, A. and Legras, R. *Polymer* **32** (15), 2691-2706 (1991).

12. Kumar, S., Anderson, D. P., Adams, W. W., *Polymer* **27**, 329-336 (1986).

13. Dean, D., Miyase, A. and Geil, P. H., *J. Thermoplastic Comp. Mat.* **5**, 136-151 (1992).

14. Cebe, P., Chung, S. Y., and Hong, S.-H. *J. App. Polym. Sci.* **33**, 487-503 (1987).

15. Orchard, G. A. J. and Ward, I. M. *Polymer* **33** (19), 4207-4209 (1992).

16. Jar, P.-Y., Cantwell, W. J. and Kausch, H. H. *Comp. Sci Tech.* **43**, 299-306 (1992).

17. Velisaris, C. N. and Seferis, J. C. *Polym. Eng. Sci.* **26** (22), 1574-81 (1986).

18.   Vautey, P. SAMPE *Quarterly 23-28* (1990).

19.   Samuels, R. J. *Structured Polymer Properties*, John Wiley: New York, 1974.

20.   Deslandes, Y., Kay, M., Sabir, N.-F., and Suprunchuk, T. *Polymer Composites* **10** (5), 360-366.

21.   Marand, H. and Prasad, A. *Macromolecules* **25** (6), 1731-36 (1992).

22.   Tung, C. M. and Dynes, P. J., *J. Appl. Polym. Sci.*, **33**, 505 (1987).

23.   Lawrence, W. E. and Seferis, J. C. *Polym. Comp.* **13** (2), 86-95 (1992).

24.   Jonas, A. and Legras, R. *Macromolecules* **26** (4),813-824 (1993).

25a.   Parvatareddy, H., Lesko, J. J., Dillard, D. A., and Reifsnider, K. L., *J. Comp. Matls.*, accepted 1/95

25b.   Wang, J. Z., Parvatareddy, H., Chang, T., Iyengar, N., Dillard, D. A., and Reifsnider, K. L., *J. Comp. Sci. & Tech.*, accepted 3/95

25c.   Parvatareddy, H.,Wang, J. Z., Dillard, D. A., Ward, T. C. and Rogalski, M. E., *J. Comp. Sci. & Tech.*, accepted 4/95

26.   Price, W., *Advanced Materials* **12** (9), 3 (1990).

27.   Price, W., Anderson, D. P., and Carlin, D. M., *35th International SAMPE Symposium* 35, 46-58 (1990).

28.   Cebe, P. and Hong, S. D., *Polymer* **27**, 1183-1192 (1986).

29.   Hay, J. N., Kemmish, D. J., Langford, J. I. and Rae, A. I. M. *Polym. Comm.* **25**, 175-178 (1984).

30.   Lovinger, A. J. and Davis, D. D. *J. Appl. Phys.*, **58**(8), 2843-2853 (1985).

31.   Wang, J. et al, *Macromolecules* **25,** 6943-6951 (1992).

32.   Rogalski, M. E., Boeing Commercial Airplane Group, Seattle, WA., private communication.

33.   Blundell, D. J. and Osborn, B. N. *Polymer* **24,** 953-958 (1983).

34. Carlier, V., Devaux, J., Legras, R. and McGrail, P. T. *Macromolecules* **25** (24), 6646-6650 (1992).

35. Blundell, D. J. *Polymer* **33** (18), 3773-3776 (1992).

36. Zhang, Z. and Zeng, H. *Makromol. Chem.* **193**, 1745-1752 (1992).

37. Olley, R. H., Basset, D. C. and Blundell, D. J. *Polymer* **27**, 344-48 (1986).

38. Blundell, D. J., Crick, R. A., Fife, B., Peacock, J., Keller, A. and Waddon, A., *J. Mat. Sci.* **24**, 2057-64 (1989).

39. Devaux, J., Delimoy, D., Daoust, D., Legras, R., Mercier, J. P., Strazielle, C. and Nield, E. *Polymer* **26**, 1994-2000 (1984).

40. Ogale, A. A., and McCullough, R. L. *Comp. Sci. Tech.* **30**, 137-148 (1987).

41. Nishino, T., Tada, K. and Nakamae, K. *Polymer* **33** (4), 736-743 (1992).

42. Plummer, C. J. G. and Kausch, H.-H. *Polymer* **34** (2), 305-311 (1993).

43. Stober, E. J., Seferis, J. C. and Keenan, J. D. *Polymer* **25**, 1845-1852 (1984).

44. Xu, J., Zhang, Z., Xiong, X and Zeng, H. *Polymer* **33** (20) 4432-4434 (1992).

45. Wolf, C. J., Bornmann, J. A. and Grayson, M. A. *J. Polym. Sci.: Pt. B: Polym. Phys.* **29**, 1533-1539 (1991).

46. Wolf, C. J., Bornmann, J. A. Grayson, M. A. and Anderson, D. P. *J. Polym. Sci.: Pt. B: Polym. Phys.* **30**, 251-257 (1992).

47. Prime, R. B. and Seferis, J. C. *J. Polym. Sci. Pt. C: Polym. Lett.* **24**, 641-644 (1986).

48. Sasuga, T. and Hagiwara, M. *Polymer* **27**, 821-826 (1986).

49. Sasuga, T. and Hagiwara, M. *Polymer* 501-505 (1985).

50. Cheng, S. Z. D. Cao, M.-Y. and Wunderlich, B. *Macromolecules* **19** (7) 1868-1876 (1986).

51.   David, L. and Etienne, S. *Macromolecules* **25** (17), 4302-4308 (1992).

52.   Hinkley, J. A., Eftekhari, A, Crook, R. A., Jensen, B. J. and Singh, J. J. *J. Polym. Sci. Pt. B: Polym. Phys.* **30**, 1195-1198 (1992).

53.   Jonas, A., Legras, R. and Devaux, J. *Macromolecules* **25** (21), 5841-5850 (1992).

54.   Jonas, A. and Legras, R. *Macromolecules* **26** (3), 526-538 (1993).

55.   Lee, Y. and Porter, R. S. *Macromolecules* **20** (6), 1336-41 (1987).

56.   Chalmers, J. M., Gaskin, W. F. and Mackenzie, M. W. *Polymer Bulletin* **11**, 433-435 (1984).

57.   Lovinger, A. J. and Davis, D. D. *Macromolecules* **19** (7), 1861-1867 (1986).

58.   Carpenter, J. F. *SAMPE Journal* 36-39 (1988).

59.   Nguyen, H. X. and Ishida, H. *J. Polym. Sci. Pt. B: Polym Phys.* **24**, 1079-1091(1986).

60.   Wang, J., Alvarez, M., Zhang, W., Wu, Z., Li, Y. and Chu, B. *Macromolecules* **25** (25), 6943-6951 (1992).

61.   Hsiao, B. S. *Polymer Preprints* **32** (3), 471-2 (1991).

62.   Cebe, P., Lowry, L., Chung, S. Y., Yavrouian, A. and Gupta, A. *J. App. Polym. Sci.* **34**, 2273-2283 (1987).

63.   Cebe, P. *Polymer Composites* **9** (4), 271-279 (1988).

64.   Magill, J. H. *Polymer* **3**, 221-233 (1961).

65.   Ostberg, G. M. K. and Seferis, J. C. *J. App. Polym. Sci.* **33**, 29-39 (1987).

66.   Schultz, J. M. *J. Mat. Sci.* **25** (8), 3746-3752 (1990).

67.   Kemmish, D. J. and Hay, J. N. *Polymer* **26**, 905-912 (1985).

68.   Konnecke, K., *J. Macromol. Sci.-Phys.* **B33** (1), 37-62 (1994).

69. Schultz, J. M. *Thermoplastic Composite Materials* Carlsson, L. A.; Ed., Elsevier: B. V. (1991).

70. Hsiao, B. S., Chang, I. Y. and Sauer, B. B. *ANTEC '91* 2084-2087 (1991).

71. Folkes, M. J. and Hardwick, S. T. *J. Mat. Sci. Letters* **3**, 1071-73 (1984).

72. Cebe, P., Lowry, L., Chung, S. Y., Yavrouian, A. and Gupta, A. *J. App. Polym. Sci.* **34**, 2273-2283 (1987).

73. Lee, K. and Weitsman, Y., *J. Comp. Matls.*, **25**, 1143-1157 (1991).

74. Buynak, C. F. and Moran, T. J., *SAMPE Journal* , 35-39 (1988).

75. Saiello, J., Kenny, J. and Nicolais, L., *J. Mat . Sci.* **25**, 3493-3496 (1990).

76. Talbott, M. F. and Springer, G. S., *J. Comp. Matls.*, **21**, 1056-1081 (1987).

77. Peacock, J. A., Fife, B., Nield, E. and Barlow, C. Y. *Composite Interfaces,* Ishida, H. and Koenig, J. L. Eds.; Elsevier: New York, 1986.

78. Bergenn, W. R. and Rigby, R. B., *CEP*, 36-38 (1985).

79. Arzak, A., Eguiazabal, J. I. and Nazabal, J. *J. Mat. Sci.* **26,** 5939-5944 (1991).

80. Hay, J. N. *Prog. Colloid Polym. Sci.* **87**, 74-77, (1992).

81. Malik, T. M. *J. Appl. Polym. Sci.* **46**, 303-310 (1992).

82. Carlier, V. , Devaux, J., Legras, R., Bunn, A. and McGrail, P. T., *Polymer* **35**(2), 415-22 (1994).

83. Carlier, V. , Devaux, J., Legras, R., and McGrail, P. T., *Polymer* **35**(2), 423-9 (1994).

84. Lovell, D. R. and Green, G. E., *Composite Materials in Aircraft Structures,* Middleton, D. H.; Ed., Longman: New York, (1990).

85. Caramaro, L., Chabert, B., Chauchard, J. and Vu-Khanh, T. *Polym. Eng . Sci.* **31** (17), 1279-1285.

86. Lopez, L. C. and Wilkes, G. L., *J. Thermoplastic Comp. Matls.*, **4**, 58-71 (1991).

87.   Devaux, E. and Chabert, B., *Polymer Comm.* **32**(15), 464-468 (1991).

88.   Desio, G. P. and Rebenfeld, L., *J. App. Polym. Sci.* **39**, 825-835 (1990).

89.   Carvalho, W. S. and Bretas, R. E. S., *Eur. Polym. J.* **26**(7), 817-821 (1990).

90.   Ishida, H. and Bussi, P., *Macromolecules* **24** (12),3569-3577 (1991).

91.   Frisch, H. L., *J. Elastoplastics*, **3**, 214-221 (1971).

92.   He, T. and Porter, R. S., *J. App. Polym. Sci.* **35**, 1945-1953 (1988).

93.   Thomason, J. L. and Van Rooyen, A. A., *J. MatSci.* **27**, 889-896 (1992).

94.   Thomason, J. L. and Van Rooyen, A. A., *J. MatSci.* **27**, 897-907 (1992).

95.   DePorter, J. K., Baird, D. G. and Wilkes, G. L. *J. Mac. Sci. Rev. Mac. Chem. Phys.* **C33** (1), 1-79 (1993).

96.   Fatou, J. G., In *Encyclopedia of Polymer Science and Engineering* Supplement Volume, John Wiley: New York, 231-296 (1989).

97.   Mandelkern, L., In *Comprehensive Polymer Science* Volume 1, Booth, C. and Price, C. Eds., Pergamon: Oxford, 363-414 (1989).

98.   Binsbergen, F. L. In *Progress in Solid State Chemistry* Volume 8, McCaldin, J. O. and Somorjai, G. Eds., Pergamon: Oxford, Chapter 4 (1973).

99.   La Mer, V. K. *Ind. Eng. Chem.* **44** (6), 1270-1277 (1952).

100.   Wunderlich, B., *Macromolecular Physics: Volume 2-Crystal Nucleation, Growth, Annealing,* Academic: New York (1976).

101.   Fisher, J. C., Hollomon, J. H. and Turnbull, D. *J. Appl. Phys.* 19, 775-784 (1948).

102.   Fisher, J. C., and Turnbull, D. *J. Appl. Phys.* **17**(1), 71-73 (1949).

103.   Van Krevelen, D. W., *Chimia* **32** (8) 279-294 (1978).

References

104. Hoffman, J. D., Davis, G. T., and Lauritzen, J. I. Jr. *Treatise on Solid State Chemistry: Volume 3 Crystalline and Noncrystalline Solids* Hannay, N. B. Ed.; Plenum: New York-London (1976).

105. Magill, J. H., *J. Appl. Phys.* **35**, 3249 (1964).

106. Avrami, M. *J. Chem. Phys.* **7**, 1103 (1939).

107. Avrami, M. J. *J. Chem. Phys.* **8**, 212 (1940).

108. Avrami, M. J. *J. Chem. Phys.* **9**, 177 (1941).

109. Price, F. P. *J. Appl. Phys.* **36** (10), 3014-3016 (1965).

110. Grenier, D and Prud'homme, R. E. *J. Polym. Sci.: Polym. Phys. Ed.* **18**, 1655-1657 (1980).

111. Cheng, S. Z. D. and Wunderlich, B. *Macromolecules* **21**, 3327-28 (1988).

112. Escleine, J. M., Monasse, B., Wey, E., and Haudin, J. M. *Colloid & Polymer Sci.* **262** (5), 366-373 (1984).

113. Billon, N., Escleine, J. M. and Haudin J. M., *Colloid Polym. Sci.* **267** (8), 668-680 (1989).

114. Billon, N. and Haudin, J. M., *Colloid Polym. Sci.* **267** (12), 1064-1076 (1989).

115. Mehl, N. A. and Rebenfeld, L., *J. App. Polym. Sci.* **57**, 187-199 (1995).

116. McDaniels, T. ICI Thermoplastic Composites Technical Service, private communication.

117. Hermans, P. H., and Weidinger, A., *J. Appl. Phys.*, **58**, 491-506 (1947).

118. Hermans, P. H., and Weidinger, A., *J. Polym. Sci.*, **4**, 709-723 (1949).

119. Hermans, P. H., and Weidinger, A., *J. Polym. Sci.*, **5**(5), 565-568 (1950).

120. Hermans, P. H., and Weidinger, A., *J. Polym. Sci.*, **5**(3), 269-281 (1950).

121. Weidinger, A., and Hermans, P. H., *Makrol. Chem.*, **50**(98), 98-115 (1961).

122. Hermans, P. H., and Weidinger, A., *Makrol. Chem.*, **44**(46), 24-36 (1961).

123. Challa, G., Hermans, P. H., and Weidinger, A., *Makrol. Chem.*, **56**(169), 169-178 (1962).

124. Alexander, L. E., *X - Ray Diffraction Methods in Polymer Science*, Krieger: Florida, (1985).

125. Swokowski, E. W., *Calculus with Analytic Geometry*, PWS Kent: Boston, Ch. 5., (1988).

126. Lopez, L. C., Ph. D. Thesis, Virginia Polytechnic Institute and State University, Blacksburg, VA p. 88. (1987).

127. Khanna, Y. P. and Reimschuessel, A. C., *J. Appl. Polym. Sci.* **35**, 2259-2268 (1988).

128. Khanna, Y. P., Reimschuessel, A. C., Banerjie, A. and Altman, C. *Polym. Eng. Sci.* **28** (24) 1600-1606 (1988).

129. Khanna, Y. P., Kumar, R. and Reimschuessel, A. C. *Polym. Eng. Sci.* **28** (24) 1607-1611 (1988).

130. Khanna, Y. P., Kumar, R. and Reimschuessel, A. C. *Polym. Eng. Sci.* **28** (24) 1612-1615 (1988).

131. Jorda, R. and Wilkes, G. L. *Polymer Bulletin* **19**, 409-415 (1988).

132. Schultz, J. M. *J. MatSci.* **25** (8), 3746-3752 (1990).

133. Weeks, J. *J. Res., Pt. A.*, **67A** (5), 441-451 (1963).

134. Schultz, J. M. *Thermoplastic Composite Materials* Carlsson, L. A.; Ed., Elsevier: B. V. (1991).

135. Mettler TA300 System Operating Instructions Manual, p. 64.

136. Risch, B. G., Ph. D. Thesis, Virginia Polytechnic Institute and State University, Blacksburg, VA (1994).

137. Park, H. C. and Mount, E. M. III In *Encyclopedia of Polymer Science and Engineering* Volume 7, John Wiley: New York, 88-107 (1985).

138.   Mandelkern, L., *Crystallization of Polymers*, McGraw-Hill: New York, (1964).

139.   Schmitz, P. et al. In *Ullmann's Encyclopedia of Industrial Chemistry* , Fifth Edition Volume A11, W. Gerhartz, Ed., VCH: New York, 85-111 (1988).

140.   Adams, R. D. and Wake, W. C. *Structural Adhesive Joints in Engineering* Elsevier Applied Science: London, (1984).

141.   Allen, K. W. *Proceedings of the 10th Annual Meeting of the Adhesion Society, Inc.* [Williamsburg, VA], L. H. Sharpe, Ed., Gordon and Breach: New York (1987).

142.   Meyer, F. J. In *Encyclopedia of Polymer Science and Engineering* Volume 1, John Wiley: New York, 518-546 (1985).

143.   Landrock, A. H. *Adhesives Technology Handbook* Noyes:New Jersey (1985).

144.   Anderson, G.P., In *Encyclopedia of Physical Science and Technology* Second Edition, Volume 1 Meyers, R. A.; Ed., Academic: San Diego, 269-287 (1992).

145.   Gent, A. N. and Hamed, G. R. In *Encyclopedia of Polymer Science and Engineering* Volume 1, John Wiley: New York, 476-518 (1985).

146.   Haller, W. et al. In *Ullmann's Encyclopedia of Industrial Chemistry* , Volume A1, VCH: New York, 221-267 (1985).

147.   Packham, D. E. in *Aspects of Adhesion 7*, Alner, D. J. and Allen, K. W., Eds., Transcripta: London (1973).

148.   Venables, J. D. In *Adhesion 7* Allen, K. W. Ed., Applied Science: London (1983) [141].

149.   Maxwell, J. W. *Trans. Am. Soc. Mech. Engs.* **67**, 104 (1945) cited in [141].

150.   Voyutskii, S. S., *Autohesion and Adhesion of High Polymers* , Vakula, V., Ed., Interscience: New York (1963) cited in [141].

151.   Vasenin, R. M. *Adhesives Age* **8** (5) 21 (1965).

152.   Vasenin, R. M. *Adhesion, Fundamentals and Practice* McLaren: London (1969) in [146].

153.   Sung, N. H., *Polymer Eng. Sci.* **19**, 810 (1979).

154. Wu, S., *Polymer Interface and Adhesion* Dekker: New York (1982).

155. Derjaguin, B. V. et al. in *Proc. 2nd Int. Congr. Surface Activity Div.* VI(c), 595 (1957) in [141].

156. Kinlock, A. J. and Young, R. J. *Fracture Behavior of Polymers* Applied Science: London (1983).

157. In *Engineered Materials Handbook: Volume 3 - Adhesives and Sealants* Brinson, H. F.;Ed., ASM International: USA, (1990).

158. Gauthier, M. M. In *Engineered Materials Handbook: Volume 3 - Adhesives and Sealants* Brinson, H. F.;Ed., ASM International: USA, 73-39 (1990).

161. Packham, D. E. In *Engineered Materials Handbook: Volume 3 - Adhesives and Sealants* Brinson, H. F.;Ed., ASM International: USA, 406-427 (1990).

162. Webster, H. F. Ph. D. Dissertation, Virginia Polytechnic Institute and State University, Blacksburg, VA 1992.

163. Dillard, D. A. In *Engineered Materials Handbook: Volume 3 - Adhesives and Sealants* Brinson, H. F.;Ed., ASM International: USA, 313-314 (1990).

164. Sharp, L. H. In *Engineered Materials Handbook: Volume 3 - Adhesives and Sealants* Brinson, H. F.;Ed., ASM International: USA, 33-38 (1990).

165. Zalucha, D. J. In *Engineered Materials Handbook: Volume 3 - Adhesives and Sealants* Brinson, H. F.;Ed., ASM International: USA, 39-43 (1990).

166. Minford, J. D. In *Durability of Structural Adhesives* Kinlock, A. J. Ed., Barking Applied Science, 135-214 (1983).

167. Eisenberg, A. *Macromolecules* **3** (2), 147-154 (1970).

168. Lundberg, R. D. In *Encyclopedia of Polymer Science and Engineering* Volume 8, John Wiley: New York, 393-423 (1987).

169. Longworth, R., In *Developments in Ionic Polymers-1* Wilson, A. D. and Prosser, H. J., Eds., Applied Science: London, 53-172 (1983).

170. McKnight, W. J. and Earnest, T. R. *J. Polym. Sci.: Macromol. Rev.* **16**, 41-122 (1981).

171. Gilby, G. W. in *Developments in Rubber Technology*, Vol. 3, Whelan, A. and Lee, K. S., Eds., Applied Science: London (1982).

172. Hatzinikolaou, T. A., Ph. D. thesis, University of Bath (1985) cited in [161].

173. Ward, I. M., Structure and Properties of Oriented Polymers, John Wiley & Sons: New York (1975).

174. Engel, L., Klingele, H, Ehrenstein, G. W. and Schaper, H. *An Atlas of Polymer Damage*, Prentice-Hall: New Jersey (1981).

175. Schreiber, H. P. Proceedings from the Adhesion Society Meeting, Clearwater, FL (1992).

176. Kambour, R. P. *Macromol. Rev.* **7** (1) (1973) in [156].

177. Sternstein, S. S. and Rosenthal, J. *Toughness and Brittleness of Plastics*, Deanin, R. D. and Crugnola, A. M. Eds., ACS: Washington (1976) in [156].

178. Farrar, N.R. and Kramer, E. J. Polymer **22**, 691 (1981).

179. Hoh, G., Sadik, S. A., and Gates, J. A. In *1989 Polymers, Laminations and Coatings Conference* 361-366 (1989).

180. Hatch, J. E. Ed., *Aluminum Properties and Physical Metallurgy*, American Society for Metals: Metals Park, OH (1984).

181. Anderson, G. P., Bennett, S. J. and DeVries, K. L. *Analysis and Testing of Adhesive Bonds*, Acadamic Press: New York (1977).

182. Adams, R. D. and Harris, J. A., *Int. J. Adhesion and Adhesives* **7** (2), 69-80 (1987).

183. Perkin-Elmer PHI Model 5400 ESCA system operating manual.

184. Wilkes, G. L., "Rheo-Optical Properties", chapter in *Encyclopedia of Polymer Science & Engineering*, Vol. 14, 2nd Edition, John Wiley & Sons (1988).

185. Read, B. E. In *Structure and Properties of Oriented Polymers* Ward, I. M. Ed., Applied Science: London, 150-186 (1975).

186. Aggarwal, S. L. and Sweeting, O. J., *Chemical Reviews*, Vol. 57, 665-742 (1957).

187. Filbey, J. A. and Wightman, J. P., *J. Adhesion* **20**, 283-291 (1987).

188. Hunston, D. L., Bitner, J. L., Rushford, J. L., Oroshnik, J. and Rose, W. S. *Elastomers and Plastics* **12**, 133-149 (1980).

VITA

Pamela Anne Percha was born in Mt. Pleasant, Michigan on June 3, 1955, the daughter and first of four children of Leonard Joseph and Marjorie Jane Kuznicki Percha. The family moved to Midland, Michigan in 1960 because of the excellent reputation of the local schools, and Pamela completed her elementary and secondary education within the Midland Public School system, graduating with distinction from Midland High School in 1973. That fall she entered the University of Michigan, leaving for financial reasons with an incomplete degree in chemistry. In 1978, Pamela was hired by The Dow Chemical Company where she worked up from the hourly position of Operating Technician to the position of Associate Chemical Technologist within Dow Central Research. She attended classes part-time during this period to complete her degree, and graduated from the University of Michigan with a B. S. in Chemistry in August 1989. On the advice of several respected mentors including: Mr. T. O. Ginter, Dr. W. H. Howell, Ms. C. A. Hutter and Dr. J. K. Rieke, she left Dow in August 1989 to pursue a Ph.D. at Virginia Polytechnic Institute and State University in the Chemistry Department. In September 1990, after returning to Dow as a graduate summer intern, Pamela joined the research group of Dr. Garth L. Wilkes in Chemical Engineering and the MESc program. She was awarded a fellowship from The Adhesive and Sealant Council in 1991, 1992, 1993 and 1994. The author was awarded her degree of Doctor of Philosophy in Materials Engineering Science in May 1995. After the completion of her work at VPI&SU, the author will join 3M as a Senior Materials Engineer in the Corporate Research Analytical & Properties Research Laboratory in St. Paul, Minnesota.